VISIT…

Nanomechanics of Materials and Structures

Edited by
T.-J. Chuang, P.M. Anderson,
M.-K. Wu and S. Hsieh

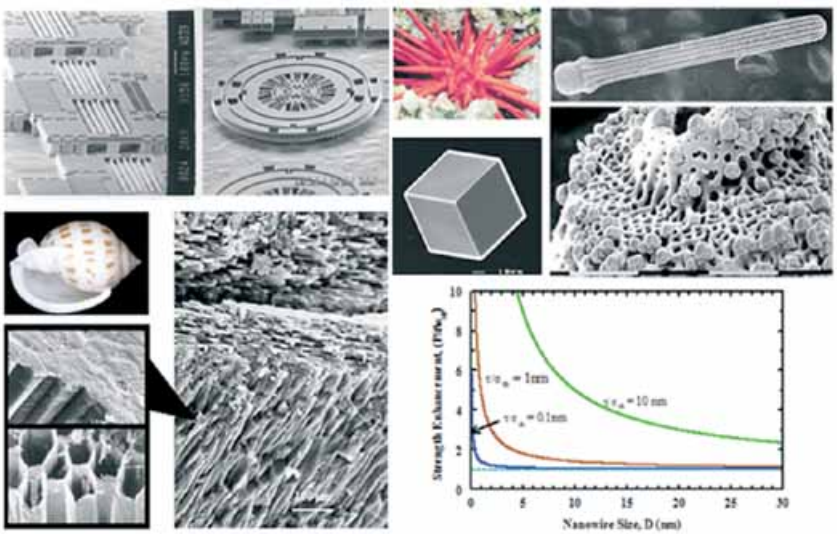

Springer

NANOMECHANICS OF MATERIALS AND STRUCTURES

Nanomechanics of Materials and Structures

Edited by

T.-J. Chuang
National Institute of Standards and Technology, Gaithersburg, Maryland, U.S.A.

P.M. Anderson
Ohio State University, Columbus, Ohio, U.S.A.

M.-K. Wu
National Science Council, Taipei, Taiwan, ROC

and

S. Hsieh
Asylum Research Corporation, Santa Barbara, CA, U.S.A.

Springer

A C.I.P. Catalogue record for this book is available from the Library of Congress.

ISBN-10 1-4020-3950-6 (HB)
ISBN-13 978-1-4020-3950-8 (HB)
ISBN-10 1-4020-3951-4 (e-book)
ISBN-13 978-1-4020-3951-5 (e-book)

Published by Springer,
P.O. Box 17, 3300 AA Dordrecht, The Netherlands.

www.springer.com

Printed on acid-free paper

All Rights Reserved
© 2006 Springer
No part of this work may be reproduced, stored in a retrieval system, or transmitted
in any form or by any means, electronic, mechanical, photocopying, microfilming, recording
or otherwise, without written permission from the Publisher, with the exception
of any material supplied specifically for the purpose of being entered
and executed on a computer system, for exclusive use by the purchaser of the work.

Printed in the Netherlands.

Table of Contents

Preface ix

Summary of Group Discussions 1

Nano Mechanics/Materials Research
Ken P. Chong 13

An ab-initio study of mechanical behavior for $(A\ell O)_n$ Nanorods
X. Song, Q. Ge and S. C. Yen 23

Phase Field Modeling of Solidification and Melting of a Confined Nano-particle
J. Slutsker, A. L. Roytburd, G. B. McFadden, and J. A. Warren . . 33

Friction-Induced Nucleation of Nanocrystals
S. Guruzu, G. Xu, and H. Liang 45

Modeling of Carbon Nanotubes and Their Composites
Chunyu Li and Tsu-Wei Chou 55

On the Tensile Strength of a Solid Nanowire
Tze-jer Chuang 67

Fracture Nucleation in Single-Wall Carbon Nanotubes
H. Jiang, Y. Huang , P. Zhang and K. C. Hwang 79

Multiscale Modeling of a Germanium Quantum Dot in Silicon
V.K. Tewary and D.T. Read 89

Nanomechanics of Biological Single Crystals
Joanna Aizenberg 99

Nano/Micro Fluidic Systems: Design, Characterization, and Biomedical Applications
Fan-Gang Tseng 109

Mechanical Characterization of a Single Nanofiber: Experimental Techniques
E. P. S. Tan and C. T. Lim 121

Atomistic studies of Flaw Tolerant Nanoscale Structural Links in Biological Materials: Natures principle of material design
Markus J. Buehler and Huajian Gao 139

Towards the Integration of Nano/Micro Devices Using MEMS Technology
Weileun Fang, Jerwei Hsieh, and Hung-Yi Lin 151

Atomic Scale Mechanisms of Stress Production in Elastomers
A.F. Bower and J.H. Weiner 161

Dynamic Indentation of Polymers Using the Atomic Force Microscope
H. Y. Hou, N. K. Chang and S. H. Chang 171

Fabrication and Simulation of Nanostructures on Silicon by Laser Assisted Direct Imprint Technique
F-B Hsiao, Y-C Lee, C-P Liu, C-H Chuang, C-P Jen, D-B Wang, and C-Y. Lin 181

Structure and Stress Evolution due to Medium Energy Ion Bombardment of Silicon
N. Kalyanasundaram, M. C. Moore, J. B. Freund , and H. T. Johnson 191

Mechanics of Nanostructures
R. Ruoff and P. Pugno 199

Residual Stresses in Nano-Film/Substrate Systems
Sanboh Lee 205

Nanomechanics of Crack Front Mobility
Ting Zhu, Ju Li and Sidney Yip. 217

Finite Temperature Coupled Atomistic/Continuum Discrete Dislocation Dynamics Simulation of Nanoindentation
Behrouz Shiari and Ronald E. Miller 225

Static Atomistic Simulations of Nanoindentation and Determination of Nanohardness
Yeau-Ren Jeng and Chung-Ming Tan 235

Electric Field-Directed Patterning of Molecules on a Solid Surface
W. Hong and Z. Suo 245

Dynamics of Dislocations in Thin Colloidal Crystals
P. Schall, I. Cohen, D. A. Weitz, and F. Spaepen 255

Mesoscopic Length Scales for Deformed Nanostructures
W.M. Mook, M.D. Chambers, C.R. Perrey, C.B.Carter, R.E. Miller, W.A. Curtin and W.W. Gerberich 263

Rough Surface Plasticity and Adhesion across Length Scales
Yan-Fei Gao and Allan F. Bower 277

Modeling the Effect of Texture on the Deformation Mechanisms of Nanocrystalline Materials at the Atomistic Scale
M.-J. Caturla and T. G. Nieh 289

Modeling the Tribochemical Aspects of Friction and Gradual Wear of DLC Films
Feodor M. Borodich, Chad S. Korach, and Leon M. Keer 299

Subject Index 309

Author Index 313

PREFACE

This book is derived from the proceedings of the International Workshop on Nanomechanics held at Asilomar Conference Grounds in Pacific Grove, California on July 14-17, 2004. Approximately 70 leading experts from academia, government and industrial sectors in semiconductors, computers, communication, information technology, defense, energy, transportation and aerospace attended the Workshop (see the workshop photo taken on July 16, 2004). The main objective was to convene leading researchers in the nanotechnology community to assess the current state-of-the-art and disseminate recent progress, critical issues, barriers to applications, and directions for future research in nanomechanics.

Miniaturization of structural components and functional devices such as electronic, optical, mechanical and electric-magnetic parts has been a recent trend, and the pace has accelerated over the past few years. Advances in micromanufacturing, semiconductor processing (e.g., etching, lithography, grafting, etc.), sensors, actuators and microprocessors have opened up a revolutionary path to the development of new technologies such as micro-electro-mechanical systems (MEMS), nano-electro-mechanical systems (NEMS), micro-engines, smart structures, smart controllers, lab-on-a-chip devices, and even bio-medical sensing devices which can detect, analyze, decide and activate appropriate functions in real time.

The above-mentioned devices, structures, or systems, have one issue in common. In order to perform their assigned functions, they must maintain their structural integrity and be reliable and durable during their entire designed service life. Thus, strength, durability, and time-dependent mechanical property degradation are major concerns for design engineers and device manufacturers, even though the parts are designed for electronic, magnetic, optical or other functions.

Nanomechanics address the mechanics of structures and materials at the nanometer size scale. It differs from conventional mechanics in many aspects. As the size of the entity shrinks, new features and phenomena emerge from conventional mesomechanics. For example, surface properties can dominate over bulk properties. As a result, physical-mechanical properties are known to be distinctly different for nanoscale components. For example, the melting point of a metal decreases with smaller sample

size. On the other hand, strength and yield point are often enhanced as sample size reduces to nanometer range. Secondly, as the volume of the entity reduces, line and area defects (e.g., dislocations, impurities, grain boundaries, etc.) are confined to smaller volumes, resulting in increased hardness and other mechanical properties relative to bulk sample. Third, as the size shrinks to atomic range, quantum effects become substantial and particle mechanics principles cease to operate. Conventional continuum mechanics approaches such as finite element methods have given way to atomistic modeling techniques such as molecular dynamics and Monte Carlo method. Finally, in the atomic size range, interaction forces usually negligible in traditional mechanics become important such as van der Waal forces and static charge forces. Those forces will affect adhesion, friction and bonding across nanosurfaces.

Nanomechanics is a new emerging field that contains many sub-fields such as contact mechanics, nanotribology, thermodynamics, kinetics and nanoindentation. Current research efforts are wide-spread in many disciplines including biology, engineering, physics, electronics, chemistry, materials science and surface science. The issues in each field have different communities working on them. This leads to barriers in communication that hinder exchange of ideas and research. This public forum provided a valuable opportunity for these communities to exchange information and ideas to facilitates progress. It was the objective of this workshop to invite leading international researchers from these communities to share common technical themes, discuss common issues, identify and address areas and problems to enable nanotechnologies.

In addition to the oral sessions and eight poster presentations, the workshop also included four breakout discussion sessions that covered areas of phase transformations and thermodynamics; biological and polymeric materials; plasticity and wear; and nanostructures. The discussions were focused on basic theories, modeling and simulation methods, experimental techniques, potential applications and topic that merit future research. A summary of the major findings from the four breakout discussion sessions is documented in the following article.

Oral presentations were organized into six sessions: (A) Research Overview; (B) Phase Transformations and Thermodynamics; (C) Nanotubes, Nanowires and Nanostructures; (D) Bio/Polymer Materials; (E) Quantum Dots, Thin Films and Nanostructures; (F) Plasticity and Wear.

In the Research Overview session, K. Chong presents a snap shot of his mechanics and materials program at NSF. He points out that the transcendent technologies are the primary drivers of the new economy of the twenty first century and they include nanotechnology, as well as enabling and supporting mechanical and civil infrastructure systems and materials. Research opportunities in nanomechanics of structures and materials, including multi-scale modeling, carbon nano-tubes, coatings, and fire-

resistant materials are outlined. In the session on Thermodynamics and Phase Transformations, X. Song *et al*. presents first principles approach based on DFT to study the mechanical behavior of the linear $(A\ell O)_n$ nanorods with n spanning from 1 to 10, from which a force-strain curve is obtained for all nanorods. The mechanical response of the two shortest nanorods is like that of ductile aluminum, but longer nanorods deform like brittle aluminum oxide. All cases demonstrate a much higher compressive than tensile strength. J. Slusker *et al.* presents a phase field model that includes the stress field during non-isothermal solidification of a one-component system. The model was applied to solidification and melting of confined spherical volumes. The results identify specific boundary and initial conditions for which the evolution of a spherically symmetric system results in isothermal steady states with a time-independent distribution of phase. The model can be applied to simulate the process of "writing" to electronic media that exploits an amorphous-to-crystalline phase change for recording information. S. Guruzu, *et al*. report an experimental investigation of friction-induced nucleation of nanocrystals. They examine a series of interfacial interactions, including pressing, light sliding, and heavy sliding. Nucleation of crystalline features are predicted only under certain sliding conditions. Compressing with heavy sliding is predicted to cause either melting or severe wear. It is thus feasible to use a friction-stimulation process combined with phase transformation to generate nanostructured materials.

In the session of Nanotubes and Nanowires, C. Li and T.-W. Chou review recent advancements in the multiscale modeling of carbon nanotubes and their composites. The basic tool is the molecular structural mechanics method developed by the authors, which has been successfully applied to simulate the static and dynamic properties of carbon nanotubes. Then, the nanotube/polymer composite is analyzed by combining the continuum finite element method with molecular structural mechanics. Potential application of molecular structural mechanics is to study thermal properties of nanotubes and composites. T.-J. Chuang presents a simple theory on the strength of a solid nanowire based on a simple derivation in mechanics principle, without relying on tedious *ab initio* molecular dynamics calculations. It shows that the measured tensile strength contains two terms: the material's intrinsic bond breaking strength and the surface stress (or surface tension) contribution. It further shows that as the size of the nanowire diminishes, the surface stress effect is enhanced, such that a simple functional relationship can be established in the nanoscale regime: $\sigma \infty 1/D$ where σ is strength and D is the diameter of the nanowire. Due to the fact that the values of surface stress are ~ 1.0 N/m, this translates into substantial strength enhancement for ***all*** nanowires with diameters below 30 nm. H. Jiang, *et al*. presents an atomistic-based continuum theory for carbon nanotubes by incorporating the

interatomic potential directly into the continuum analysis through the constitutive model. The theory accounts for the effect of carbon nanotube chirality, and is applied to study fracture nucleation in carbon nanotubes by modeling it as a bifurcation problem. Good agreements with the molecular dynamics simulations. V.K. Tewary and D. T. Read present a method for multiscale modeling of a quantum dot in a semiconductor solid containing a free surface. The method is based on the use of lattice-statics and continuum Green's functions integrated with classical molecular dynamics. The method can model a large crystallite containing, for example, a million atoms without excessive CPU effort and it connects nanoscales seamlessly to macroscales. An example is given to calculate the lattice distortion around a Ge quantum dot in Si.

In the session of Biological and Polymer Materials, J. Aizenberg examines a few examples of ceramic materials in which the organic framework is stiffened by inorganic particles. Organisms also form a different type of composite in which the host is a inorganic single crystal and the guests are proteins deliberately occluded into the crystal. The best-studied examples, to date, are biogenic calcites, and in particular those formed by the echinoderms. In vitro experiments with calcite crystals grown in the presence of echinoderm intracrystalline proteins and mollusk shell proteins show that these macromolecules are occluded inside the crystal on specific planes that are oblique to the cleavage planes, and their presence significantly improves the mechanical properties of the crystal host. F.-G. Tseng describes three examples employing surface tension for fluid manipulation, precise dosage control, and powerless operation at the micro/nano scale. The first example is a fluidic network system employing surface tension for enzyme batch-immobilization and bio assay in parallel. The second system, a 3-in-1 micro/nano protein arrayer, utilizes passive surface tension force for protein array formation and protein assay processes. The third system, a powerless droplet manipulation system, employs surface hydrophobicity gradient for droplet manipulation. All three examples demonstrate efficient and precise fluid control in micro/nano scale. E.P.S. Tan and C.T. Lim discuss biodegradable polymeric nanofibrous scaffolds used extensively for tissue engineering. The stiffness of the individual nanofibers in these scaffolds can determine not only the structural integrity of the scaffold, but also the various functions of living cells seeded on it. Therefore, there is a need to study the nanomechanical properties of these individual nanofibers. Experimental techniques to test single polymeric nanofibers - namely tensile, three-point bend and indentation testing at the nanoscale are presented. M. Buehler and H. Gao discussed fundamental design concepts of nanoscale structural links in biological materials and focus on verification of these concepts via atomistic simulations. They demonstrate via atomistic simulations the principle of flaw tolerance by size reduction. Application is made to the evolution of the bulk nanostructure of

bone-like materials and the surface nanostructure of gecko. A.F. Bower and J.H. Weiner outline a series of molecular dynamics computations that reveal an intimate connection at the atomic scale between difference stress (which resists stretches) and pressure (which resists volume changes) in an idealized elastomer, in contrast to the classical theory of rubber elasticity. The model predicts behavior that is in good agreement with experimental data for the influence of pressure on the difference stress induced by stretching solithane. H.Y. Hou, *et al*. demonstrate the applicability of using Atomic Force Microscope (AFM) to measure surface property of polymeric materials. During penetration by the AFM tip, the sample surface was simultaneously undergoing an oscillation at smaller amplitude (3-5 nm) by a piezoelectric actuator. The results show that the technique is a powerful method for polymer characterization with nanometer spatial resolution. W. Fang, *et al.* introduce a technology platform MUMPs as the first fabrication platform for MEMS. Many promising MEMS devices have been realized through the MUMPs platform. Presently, other platforms such as SCREAM, SUMMIT, MPW, and CMOS-MEMS have been successfully explored or still under investigation. Two fabrication platforms, MOSBE and BELST, are discussed. Finally, F.-B. Hsiao, et al. propose a new nano-patterning technology, namely laser assisted direct imprinting (LADI). Using silicon as the target material and utilizing a single KrF excimer laser pulse (248nm wavelength and 30ns pulse duration) as a heating source, they demonstrate the fabrication of a positive quartz mold within micro-level and nano-level trenches by combination of conventional photolithography and novel focused ion beam (FIB) machining. The results show that the magnitude of imprinting pressure and the laser characteristics can affect the thickness of the melted layer on the substrate surface and the morphology of the resulting nanostructures.

In the session of Quantum Dots and Thin Films, H. T. Johnson, et al. investigate sputtering, stress evolution and surface evolution due to ion bombardment of silicon. Impact due to argon ions at normal incidence with beam energies of 500eV and 700eV are simulated using Molecular Dynamics (MD). Stresses are calculated using a force balance method and approach 1.7GPa and 1.3GPa in the 700eV and 500eV cases respectively after about 125 impacts. Continuum descriptions of the damaged surface are obtained from atomistic coordinate data using a silicon probe atom method. R. Ruoff and M. Pugno present a theory of quantized fracture mechanics for a defective nanotube. Comparison of strength prediction on the defective nanotube with atomistic simulations and experimental data clearly shows that materials are sensitive to flaws at nanoscale. S. Lee derives residual stresses in elastic multi-layer film/elastic substrate systems and obtained closed-form solutions. General solutions of visco-elastic film/elastic substrate and elastic film/viscoelastic substrate are obtained.

In the final session of Plasticity and Wear, T. Zhu, et al. study the nanomechanics of crack front mobility. Minimum energy paths for unit advancement of a crack front are determined by reaction pathway sampling, thus providing the reaction coordinates for the analysis of crack tip mechanics in ductile and brittle materials. Results are compared on activation energy barrier and atomic displacement distributions for a atomically sharp crack in Cu, where one observes the emission of a partial dislocation loop, and in Si, where crack front extension evolves in a kink-like fashion. B. Shiari and R.E. Miller perform simulations of nanoindentation in a hexagonal aluminum single crystal using a finite temperature coupled atomistic/continuum discrete dislocation (CADD) method. The method captures, at the same time, the atomistic mechanisms and the long-range effects without the computational cost of full atomistic simulations. Y.-R. Jeng and C.-M. Tan develop a nonlinear finite element formulation to analyze nanoindentation using an atomistic approach, which is conducive to observing the deformation mechanisms associated with the nanoindentation cycle. The simulation results of the current modified finite element formulation indicate that microscopic plastic deformation of the thin film is caused by instabilities in the crystalline structure, and that the commonly used procedure for estimating the contact area in nanoindentation testing is invalid when the indentation size falls in the nanometer regime. W. Hong and Z. Suo develop a phase field model to simulate the molecular motion and patterning under the combined actions of dipole moments, intermolecular forces, entropy, and electrodes. By varying the voltages of the electrodes individually, it is possible to program molecular patterning, direct an island to move in a desired trajectory, or merge several islands into a larger one. P. Schall, *et al*. investigated dislocation dynamics in thin colloidal crystals. Suspensions of μm-size colloidal particles form structures similar to those formed by atoms (vapor, liquid, glass, crystal). Since they can be observed optically in real time on the particle scale, colloids can be used to study the dynamics of these structures Dislocations are introduced by lattice mismatch at the template or by deformation (e.g., indentation). Their strain fields are imaged by laser diffraction microscopy (geometrically similar to electron microscopy) and their cores by confocal optical microscopy. The critical thickness of the epitaxial crystal, the rate of introduction of the interfacial dislocations and their offset from the template can be accurately predicted by continuum dislocation theory. W.M. Mook, *et al*. discuss length scales for deformed nanostructures. They point out that defining mesoscopic length scales for deformed nanostructures requires a close coupling of theory and experiment. One approach is to mechanically probe single crystal nanospheres of the same size that can be evaluated computationally. This involves analyzing dislocation nucleation and its corresponding yield instability represented by either a displacement excursion or load drop. This is shown both for experimentally compressed

silicon nanospheres and theoretically simulated nanoindentation of silver. Y.-F. Gao and A. F. Bower study interacting rough surfaces at mesoscale and nanoscale. The multiscale nature of surface roughness, the structure- and size-sensitive material deformation behavior, and the importance of surface forces and other physical interactions give rise to very complex surface phenomena at mesoscale and nanoscale. They present a contact mechanics model based on the power spectral density function of the surface roughness. Also presented is a new scheme of modeling rough surface adhesion by using the Dugdale model and the self-affine fractal surface, which leads to a discussion of gecko adhesion. M.-J. Caturla and T.G. Nieh employ molecular dynamics simulations to show significant differences in the deformation behavior of nanocrystalline nickel with low and high angle grain boundaries. At a grain size of 12 nm, a low angle boundary sample shows enhanced dislocation activity and reduced strength with respect to a high angle boundary sample. However, at a smaller grain size of 4 nm, a low angle boundary sample shows a higher strength, revealing a change in deformation behavior. At this grain size, regardless the type of grain boundary, dislocation activity is negligible. L. Keer considers the friction and wear of DLC films. He focuses on physical and tribochemical processes that occur in sliding contact between the DLC coated slider and the counterpart and develops a model of the process, assuming a transient short-life high temperature field at the vicinities of contacting protuberances that may cause transformations of the surface. The model helps to explain how microscopic processes, such as the breaking and forming of interatomic bonds, may affect macroscopic phenomena, such as friction and wear.

The International Workshop on Nanomechanics was sponsored by the U.S. National Science Foundation, *Mechanics and Materials Program*, the National Science Council of Taiwan, *National Nanotechnology Program* and the National Institute of Standards and Technology (NIST), *Center for Theoretical and Computational Materials Science*. Their financial support is hereby acknowledged. Special thanks go to Ohio State University, NIST and the Taiwanese American Science and Technology Association of Maryland for providing logistical support at the workshop, accounting, and fund disbursement. We are also grateful to the Science and Technology Division, Taipei Economic and Cultural Representative Office, DC Office and San Francisco Office for their logistic support.

This material is based upon work supported by the National Science Foundation under Grant No. 0335083. Any opinions, findings, and conclusions or recommendations expressed in this material are those of the author(s) and do not necessarily reflect the views of the National Science Foundation.

We wish to express appreciation to the session chairs for leading the fruitful discussions in a timely fashion. Special thanks go to the chairs of the

four breakout sessions, who not only organized the discussion sessions but also provided summary reports which are the basis for the following article.

Finally, without the encouragement by Dr. Chin Hsieh, Deputy Director of the National Science Council during the initial planning stage of the workshop, this publication will not be possible. We also express our application to the editorial and production staff at Kluwer Academic Publishers, Inc., Dordrecht Office, especially Editor Nathalie Jacobs and Editor Anneke Pot for their support and patience.

Tze-jer Chuang
Gaithersburg, Maryland

Peter M. Anderson
Columbus, Ohio

Maw-Kuen Wu
Taipei, Taiwan

Shuchen Hsieh, copy editor
Asylum Research Corporation, Santa Barbara, CA 93117, U.S.A.

The participants at the **International Workshop on Nanomechanics**

SUMMARY OF GROUP DISCUSSIONS

Four breakout discussion sessions were held during the Workshop. They are: (1) Phase Transformations and Thermodynamics; (2) Biological and Polymeric Materials; (3) Plasticity and Wear; and (4) Nanostructures. Basic theories, modeling and simulation methods, experimental techniques, potential applications, and the barriers which merit future research were discussed in each session. This article summarizes the major findings from each discussion session.

The session on Phase Transformations and Thermodynamics was led by Professor Zhigang Suo of Harvard University. Participants included Wei Hong (Harvard University), Hong Liang (University of Alaska), Alexander Roytburd (University of Maryland), Julia Slutsker (NIST), Max Yen (Southern Illinois University), Sidney Yip (Massachusetts Institute of Technology), Yunzhi Wang (Ohio State University), and Ting Zhu (Harvard University).

The group discussion on Biological and Polymeric Materials was led by Dr. Markus J. Buehler of Max Planck Institute and Professor Suo Hung Chang of National Taiwan University. Participants included Alan Bower (Brown University), Fei-Bin Hsiao (National Cheng Kung University), Long-Sun Huang (National Taiwan University), Sanboh Lee (National Tsing Hua University), Ting-Kuo Lee (Academia Sinica), and Fan-Gang Tseng (National Tsing Hua University).

The session on Plasticity and Wear was led by Professor Frans Spaepen of Harvard University with written input from Professor Nix of Stanford University. Participants included Peter M. Anderson (Ohio State University), Robert Cammarata (Johns Hopkins University), William Gerberich (University of Minnesota), Yeau-Ren Jeng (National Chung Cheng University), Y. Huang (University of Illinois), Leon Keer (Northwestern University), K.-S. Kim (Brown University), T. G. Nieh (Lawrence Livermore National Lab.), Behrouz Shiari (Carleton University), and Vinod Tewary (NIST).

The discussion session on Nanostructures was chaired by Dr. Charles Barbour of Sandia National Lab. Participants included T.-J. Chuang (NIST), Wei-Leung Fang (National Tsing Hua University), Harley T. Johnson (University of Illinois), Chwee-Teck Lim (National Singapore

T. J. Chuang et al. (eds.), Nanomechanics of Materials and Structures, 1–12.
© 2006 *Springer. Printed in the Netherlands.*

University), Hung-Yi Lin (ITRI), and Rodney Ruoff (Northwestern University).

1. PHASE TRANSFORMATIONS AND THERMODYNAMICS

Several broad trends have emerged as we explore the mechanical behavior of nanostructures. The studies of phase transformation, fracture and deformation are converging. These phenomena appear to be distinct at the macroscopic scale. At a microscopic scale, however, they are variations of a single theme: the collective behavior of atoms. Also convergent are traditionally different disciplines such as thermodynamics, kinetics and mechanics. A unifying concept is the energy landscape, which contains both thermodynamic and kinetic information. External forces modify the energy landscape. Another unifying concept is to view structural evolution as a sequence of configurational changes driven by thermodynamic forces. In addition to more familiar forces of push and pull, other thermodynamic forces come from entropy, elasticity, electrostatics, phase separation, phase boundaries, van der Waals interactions, etc.

The presentations at the workshop sampled recent advances in the field. The energy landscape is a function of a large number of coordinates. A construction of the full energy landscape is prohibitively time-consuming for most phenomena of interest. Techniques now exist to compute the minimum energy path on the energy landscape, which connects one local minimum, via a saddle point, to another local minimum. Dislocation nucleation and crack extension have been studied this way. Thermodynamics and mechanics, in combination, have been used to study self-assembling nanostructures. The phase field model can now simulate realistic microstructures in alloys. Efforts are underway to link such microstructural simulations to thermodynamic data banks, and to the mechanical behavior of alloys. First principles methods have been used to study the energetics of atomic clusters, the structures that are far beyond the reach of continuum mechanics. Stress-induced phase transformations have been studied experimentally and theoretically. Phase transformation can give rise to large deformation, and is a basis for active structures. A continuum theory is presented to couple Stokes's creep with Herring's diffusion. In nanostructures, surface energy and surface stress often play prominent roles, as the fraction of atoms on the surface is large.

The participants also speculated on likely progress in coming years. Deformation localization will be studied at the atomic scale. First principles calculations will be more widely used to study electronic effects on

mechanical behavior. We will see more coupled actions of mechanics and chemistry. Few engineering problems are solved by computation alone. The pragmatic approach is to divide the labor between computation and measurement. Some quantities are easier to compute, others are easier to measure. A combination of computation and measurement solves problems economically. Of course what is easy changes with circumstances. As new tools and applications emerge, it behooves us to renegotiate a more economical division of labor. This is a time of renegotiation. Great progress will be made to link computations more intelligently across scales, and with experiments.

In a traditional mechanics education, thermodynamics and kinetics rarely play a part. This situation will change in coming years. The impetus comes from a confluence of new tools, new questions, and new applications. Affordable computers have opened new ways to study most phenomena. New instruments, such as the scanning tunneling microscope, have brought us to an intimate contact with individual atoms. Like traditional mechanics, traditional thermodynamics studies macroscopic structures. For nanostructures, we are interested in local processes. Many thermodynamic properties become size and shape dependent. Both mechanics and thermodynamics have long played active roles in manufacturing, such as metal forming, ceramic sintering, and rapid prototyping. Together, mechanics and thermodynamics will play active roles in nano-manufacturing.

2. BIOLOGICAL AND POLYMERIC MATERIALS

2.1 Introduction

The sessions on biological and polymeric materials covered the areas of fabrication, characterization and modeling. The talks covered questions related to fabrication methods such as imprinting approaches, fluidic control, organic-inorganic composites/structures at nanoscale (e.g. DNA-CNT complexes), mechanical properties of cells (e.g. diseases change properties), scale effects in biomaterials (length scale reduction for robustness), mechanics of single biomolecules, characterization, modeling (e.g. nano-indentation and fracture at nanoscale and in biomaterials), as well as sensing (MEMS, micro fluidics and biochip, or fluorescence microscopy using quantum dots). We outline some of the fields in more detail in the next sections.

2.2 Specific research topics

2.2.1 Fabrication and manufacturing

The workshop participants reported several techniques to create small-scale structures. Examples included nano-imprinting; LIGA (a German acronym for lithography, electroforming, and molding), classical techniques such as electron beam lithography and focused ion beam lithography; and self-assembly. Despite significant past progress in this area, tremendous opportunities and challenges still remain. In particular, even the most advanced nanofabrication techniques cannot yet emulate the widespread ability of biological systems to self-assemble. Advances in nanofabrication would enable a wide range of small-scale structures and materials to be created. Examples include DNA-CNT complex, neuroprobes, bio-molecular sensors, as well as integrated of micro- and nano devices in a complex apparatus such as a lab-on-a-chip.

MEMS and NEMS technologies are an important gateway to nanotechnology, as they may be used to combine top-down and bottom-up approaches. However, there is still significant need for further research in techniques to fabricate micro- and nano-structures. For example, it is still difficult to mass-produce many MEMS devices on scales that are routinely used to manufacture integrated circuits. Another issue discussed was reliability of the devices, which still poses a problem, particularly in designs that use sliding contacts. In the future, we envision that micron and submicron size MEMS / NEMS devices will play an increasing role to integrate nanomaterials and nanostructures for testing and applications.

2.2.2 Characterization techniques

Techniques such as SEM, (HR)TEM, X-ray scattering and AFM, confocal microscopy, as well as optical tweezers still play an important role in characterizing micro/nano scale materials. Other methods that were utilized are nano-indentation for characterization of polymers, and specially designed micro-channels for studying nano-/micro fluidic systems. In the future, MEMS devices could take over some part of the testing by serving as sensors and actuators. At the important interface of biology and materials science, bio-sensors based on functionalized surfaces may be the key to a number of promising applications. These methods are examples where concepts of mechanics, physics and chemistry are combined. Similar considerations apply for fluorescence microscopy using quantum dots.

2.2.3 Modeling and simulations

Available methods for modeling and simulation in the area of small-scale materials are atomistic methods (e.g. *ab initio* and MD), FEM/BEM based numerical tools, analytical continuum theory, as well as mesoscopic approaches. The workshop highlighted the importance of multi-physics and multi-scale simulations in treating biological and MEMS problems. An important goal for the future is thus the development of reliable, generally applicable multiscale and multi-physics simulation methods. Coupling of different length and time scales, along with development of software tools, is a critical and timely issue. Biology intrinsically operates on multiple scales.

Specific topics covered at the workshop included: fracture at nanoscale (organic versus/and inorganic); adhesion at nanoscale; size effects in biomaterials, and addressing the common "design objectives" in biomaterials. In this particular field, design for robustness was identified as a critical objective of nature's evolution over millions of years, and it was found for example in bulk and surface materials. Another important area is calculating material properties based on a fundamental perspective (e.g. at the quantum level), polymer properties based on atomistic calculations, and structural properties-functional relationship. It is critical to note that nature does not distinguish between formal scientific disciplines and therefore, the numerical studies that describe biological materials usually must be multi-disciplinary.

2.3 Summary

The session on biological and polymeric materials brought together a group of researchers who work in very diverse fields, including fabrication methods, nanoscale testing methods, nano- and multiscale computations, and observations and modeling of biological systems. Studying biological materials is a challenging, timely research opportunity. Investigations of such materials should involve a joint theory-simulation-experimental approach, combining scientists from various fields. We believe that understanding biology, and learning from nature could change engineering and science in the coming decades.

We have seen great progress in developing techniques to fabricate nanostructures, but this remains a rapidly evolving field, and much progress remains to be made before we can even begin to rival nanoscale structures observed in nature. This is clearly an area that will continue to require significant long term investment. Manipulating discrete elements of a nanosystem is a particular challenge. Progress in this area could be accelerated by providing mechanisms experimentalists to obtain access to novel fabrication tools. More could be done to establish shared facilities that can be used at low cost, and also to accelerate commercialization of

promising techniques. Mechanisms to permit postdocs and students to visit facilities and learn techniques would also be valuable.

Advances have also been made in developing methods to study material behavior at the nanoscale. Ex-situ microscopy is highly advanced and widely available; in-situ testing is more difficult, but advances continue to be made in this area. Quantitative measurements are very difficult, and other than nano-indentation, there are virtually no commercially available tools to measure material behavior at nanometer length scales.

Our ability to model systems at nanoscale has improved greatly with advances in computer power, and with the development of widely available codes such as VASP, DYNAMO for *ab initio* and molecular dynamic simulations, and many commercial and free finite element codes. Wide gaps remain in the length and time scales that can be resolved by *ab initio*, MD, and continuum simulations, however. Methods to simulate nanostructures with atomic or meso-scale resolution for realistic time scales, without undue reliance on phenomenological constitutive equations, are a particular problem. Even the most advanced atomic scale simulations of polymers, for example, can only simulate behavior of short chain molecules (500 atoms or so) over a few nanoseconds. An enormous challenge in this field, which would have particular applications to biological systems, is to connect chemistry to mechanics. Multi-scale simulations are one promising approach, but much more work needs to be done before this become more than an exploratory research tool. In addition, there is a critical need to develop experimental methods that can be used to validate nanoscale simulations. This means we need to develop techniques to measure atomic scale phenomena quantitatively. In this regard, two interesting, and very different, approaches were presented in the workshop: one is K.S. Kim's field projection method, which can be used to extract quantitative measures of stress and strain around defects from high resolution TEM images. The other is F. Spaepen's innovative use of a colloidal system to mimic the behavior of a hard-sphere simple liquid.

Studies of biological systems are extremely helpful to identify physical phenomena that can be exploited to design materials and systems at nanometer length-scales; and also to identify processes that are beyond our current understanding. Traditionally, biology, and also bio-mechanics, have aimed to provide a descriptive understanding of natural phenomena and living systems. We have learned a great deal from these studies, and we shall undoubtedly continue to do so. But to fully exploit the power of mechanics, we need to develop the ability to predict, rather than describe, the behavior of nano-scale systems. In this regard, it may be advantageous to design experiments and simulations that enable us to study phenomena of interest in isolation and under controlled conditions, rather than in the natural state. Four specific examples of specific phenomena that are

observed in nature and could be studied in this way were presented in the symposium:

(i) Crystal growth mediated by organic molecules;
(ii) Nanoscale mechanisms of adhesion;
(iii) Deformation mechanisms in biological bone-like materials;
(iv) Nanoscale composites based on organic molecules trapped in a crystal.

We envision that international collaboration could help to address some of the described issues and to achieve the long-term goals of utilizing the concepts of biology or biomaterials itself in technological applications. There are already numerous funding agencies that, for instance, offer specific programs for funding US-Taiwan collaboration, such as NSC agreements with NSF, NIST and AFOSR. The next step could be to identify strategies, develop key projects, and establish joint research and education programs. We believe there is necessity for a greater modeling effort for biomechanics problems, for instance in atomistic understanding. An example is the role of biomolecules trapped in single crystals (challenging because of time and length scale, and the interaction potential between different atom species). Also, we envision that combining MEMS devices with bio-problems may lead to development of efficient sensors (e.g. "lab on a chip" technologies). Linking simulation-experiment-theory, for example by joint studies carried out between different groups should also be a key aspect in future research, as for example in projects focusing on a fundamental problem such as functioning of muscles. Today, an important experimental limitation is how to handle small size samples for instance in clamping carbon nanotubes, handling biomolecules, or dealing with nanofluidics.

In summary, there is lots of room to find interesting materials, experimental techniques, and phenomena in nature: Nature has taken millions of years to develop very powerful concepts in building wonderful materials and eventually intriguing "machines" that we refer to as "life". We believe that future research at the bio-nano interface needs to focus on learning the fundamental principles that are exploited by nature in the design of living systems, rather than simply copying or describing natural systems themselves. This may eventually enable us to use them in manmade technology that would have similar superior features. Biology is nanotechnology by nature, and nano-mechanics is the key yet to be understood.

3. PLASTICITY AND WEAR

3.1 Theory

Progress in nanoscience and nanotechnology needs contributions from *all* the natural sciences: physics, chemistry, biology, and engineering. For researchers in materials science and in applied mechanics, there are many new opportunities and they bring *unique* expertise to the enterprise. These are some of the contributions that only they can provide:

(i) an understanding of microstructure and its relation to properties;

(ii) developing a phenomenological and theoretical understanding of the constitutive relations of mechanical behavior on the nanoscale;

(iii) connecting phenomena on the nanoscale, through the intervening scales, up to the macroscopic scale.

3.2 Experiment

The strong activity in analysis (theory and simulation) needs to be balanced by an increase in ***experimental*** work. Needed are experiments specifically designed to reveal underlying mechanics. Mechanical testing on the nanoscale is a challenge. New ways of fabricating samples (lithography, focused ion beam,...), new ways of loading them (AFM, optical tweezers, ...), new and more precise ways of measuring stress and strain, and new ways of observing the samples (high-resolution electron microscopy, AFM, atom probe, ...) *in* or *ex situ*, should be broadly considered. Different modes of deformation (tension, compression, shear, bending, wear) give complementary information. There is much room for clever and innovative experimentation.

There should be more testing as a function of strain rate and temperature to reveal underlying mechanisms. Nanoscale testing at elevated or low temperature is difficult, but solution of the experimental problems is particularly worthwhile given the broad kinetic window offered by variation in temperature.

Nanoindentation remains one of the main tools of the field. New ways should be found to make direct observations or *in situ* measurements of the area of contact between indenter and sample. Much can be learned as well from detailed comparison of the experimental load-displacement curves with the results of discrete dislocation simulations.

3.3 Modeling

Some aspects in the ***modeling*** of plasticity in nanostructured materials have received insufficient attention. An example is the modeling of "nonlinear" events in the kinetics of dislocation motion: formation of nodes, entanglement, or formation of cells. In the interest of computational efficiency, such events are treated as "black boxes": the initial and final states are specified, but the specific path between them is left unspecified. More specific rules and computational exploration of the kinetic path inside these "boxes" are highly desirable.

A further example is the use of dislocation theory with continuous space- and time-dependent variables, such as the dislocation density tensor and the velocity vector. This approach represents a length scale intermediate between those of discrete dislocation modeling and continuum mechanics. The main issue in the development of continuum dislocation theory is the appropriate averaging of the quantities in discrete dislocation modeling.

3.4 Surface effects

As sample size or microstructural length decrease, ***surfaces and interfaces*** become increasingly important, and they can have substantial effects on plasticity. For example, how is the nucleation of dislocations affected by the topology (roughness, steps), energy (including orientation), chemistry (including contamination) and stress of the surface? Is subsurface plasticity distinct from that in the bulk (e.g., is there a dislocation-free zone)? Under what conditions does the formation of stacking faults or twin boundaries become important alternative responses to shear loading?

3.5. Interfacial effects

The small ***volume*** of a sample or a grain limits the nucleation probability of dislocations. For quantum structures, which need to be defect-free to function, understanding these probabilities in detail is essential. In polycrystalline systems, nucleation of dislocations at grain boundaries, especially with limited area, remains largely unexplored. The shear of an entire small grain by the passing of the dislocation can be usefully considered as a "quantum event" in a description of the overall plasticity of nanosize polycrystals.

3.6 Fabrication methods

The ***fabrication*** of nanostructures is often a mechanical process or contains important mechanical steps. Clear examples are the production of very small grains by comminution or abrasive wear. The study of plasticity at very high strain rates can contribute to a quantitative understanding of these processes. Planarization is an essential ingredient of contemporary microfabrication; the chemical and mechanical processes in nanoplanarization remain a fruitful areas of technological and scientific research. There are many fascinating new areas of nanofabrication where the exploration of the mechanics has only just begun, such as nanowelding, nano-imprinting and stamping, and the many forms of adhesion on the nanoscale.

3.7 Plasticity in soft materials

The study of the plasticity of ***soft materials*** is well developed for polymers, but is only just beginning for colloids, membranes and many biological materials. It should be explored to what degree the insights from the more mature study of plasticity (experiments, theory, simulations) in metals and semiconductors can be transferred usefully to some of those soft materials.

4. NANOSTRUCTURES

First, the group recognized that there is a need to properly define what do we mean by "nanostructure" as opposed to "nanomaterial". For example, is a carbon nanotube a nanostructure or nanocrystalline material? With the nanostructure clearly defined in our minds, there are three ingredients that are needed for achieving the functionality offered by those devices or components: (1) Fabrication: innovative fabrication methods, either from the approach of top-down or bottom-up, are needed; in particular, the process should be reproducible and can be adapted to mass production in order to be economically feasible. (2) Characterization: this step is essential to understanding the properties and behaviors of the nanostructure in question so that its functionality either in isolation or as a whole can be assured. (3) Implementation: once the nanostructure is fully characterized in terms of its property and function, the final critical step would be to incorporate it into the system in such a way that it can be performed as it is designed for.

The discussions of the group concluded with the following major needs in the area of nanostructures:

(1) There is a need to establish an intimate connection between modeling and experiments. In order to enhance the reliable predictive capability in modeling, experimental ingredient must be incorporated in the model. A model without the support of experimental data is not sound. The predictions coming out from the model cannot be trusted. For instance, to establish a valid mechanics model for nanostructures, fundamental data base on constitutive laws must be available. Those data must come from performing well controlled strain/strain rate experiments.

(2) There is a need to promote close interactions between mechanicians and physical scientists. A well-defined physics-based model is superior to an empirical model. Moreover, the boundary conditions should be sufficiently controlled and understood. Those include thermal, electrical and mechanical boundary (e.g., joining, clamping to form building blocks). Meanwhile, the environmental effects need be controlled and understood. Those include mechanical environments such as floor noise, EM and acoustic perturbations; chemical environments such as relative humidity and surface chemistry.

(3) There is a need to improve control in nanomanipulation. Due to the size scale in nanometer range, the control and manipulations on those nanostructures pose a challenging task. It is unavoidable that the experimentalist will face the problems of control of interaction forces and force transduction across boundaries of dissimilar materials. The presence of adhesion forces, surface tension and van der Waals forces unique in nanomechanics further add to the complexity. With the newly developed nanomechanics tools such as AFM and SEM, the degree of difficulty in control mitigate a bit. But still, there is ample room for improvement in this area.

(4) There is a need to understand appropriate structural level in building blocks. For example, how does one define structural members or subunits for molecules? For a complex material system, how do we understand the joining and integration of dissimilar materials such as a laminate structure of soft-hard material integration? Eventually we will face unavoidably the scale-up problems, namely the need to integrate nanostructures up to human length scale (i.e., mm size scale and up).

The group also recognized that nanostructures are very sensitive to imperfections such as surface defects, vacancies and impurities. In particular, since most of the devices are designed to be serviced in air, surface defects in the form of oxides are often present inadvertently. Thus,

there is a need to impose greater focus on those surface oxides. It is recognized that traditional mechanics models which are centered on the bulk behaviors may not be applicable to nanostructures which are surface-eccentricted. For example, to model the strength of a nanorod, a special treatment incorporating the surface stress effect becomes the essential portion of the model. A result, as T.-J. Chuang shows, is that the strength of a solid nanowire is enhanced as compared to its counterpart of the same bulk material. On the other hand, we recognized that it may not make sense to reproduce 18^{th}-19^{th} century structures at the nanoscale. What is more important is to find a niche by taking advantages of new functionality.

For potential areas of application, the group identifies the following:

(1) It is possible to exploit the dual usage of the nanostructures. They can provide structural support; meanwhile they can also be used to measure properties of materials. Carbon nanotubes are good examples.

(2) It is possible to take advantage of coupled behavior to achieve mult-functionality of a nanostructure. For example, single and double wall nanotubes possess superior electrical-optical and mechanical-tribological properties that they can be used as a vital part in nano-motors, electron microscopy and AFM devices.

(3) It is known that nature provides biological parts with superior property through innovative design of nanostructures. By taking advantage of the unique properties that exist only for nanostructures, such as high strength and force transduction, it is possible to manipulate atoms from bottom-up so as to achieve the functionality we are looking for, where it is not achievable in ordinary structures.

(4) Finally, the control of mechanics at the nanoscale may evolve into advances in other fields. For example, bonding and orientation of carbon nanotubes can find a way to feed into optical spectroscopy studies.

NANO MECHANICS/MATERIALS RESEARCH

Ken P. Chong
Director of Mechanics & Materials, National Science Foundation, Arlington,VA 22230, U.S.A .Phone:(703)292-7008, Fax :(703)292-9053, E-mail : kchong@nsf.gov

Abstract: The transcendent technologies are the primary drivers of the new economy of the twenty first century and they include nanotechnology, microelectronics, information technology and biotechnology as well as the enabling and supporting mechanical and civil infrastructure systems and materials. Mechanics and materials are essential elements in all of the transcendent technologies. Nanotechnology is the creation of new materials, devices and systems at the molecular level - phenomena associated with atomic and molecular interactions strongly influence macroscopic material properties; with significantly improved mechanical, optical, chemical, electrical... properties. Research opportunities, education and challenges in mechanics and materials, including multi-scale modeling, nanomechanics, carbon nano-tubes, coatings, fire-resistant materials as well as improved engineering and design of materials are presented and discussed in this paper.

Key words: nano and micro mechanics; multi-scale modeling; nano tubes; coatings; strength

1. INTRODUCTION

Nanotechnology is the creation of new materials, devices and systems at the molecular level - phenomena associated with atomic and molecular interactions strongly influence macroscopic material properties [according to I. Aksay, Princeton]; with significantly improved mechanical, optical,

T. J. Chuang et al. (eds.), Nanomechanics of Materials and Structures, 13–22.
© 2006 *Springer. Printed in the Netherlands.*

chemical, electrical... properties. Nobelist Richard Feynman back in 1959 had the foresight to indicate "there is plenty of room at the bottom". National Science Foundation [NSF] Director Rita Colwell in 2002 declared "nanoscale technology will have an impact equal to the Industrial Revolution".

In the education area in order to do competitive research in the nanotechnology areas, engineers should also be trained in quantum mechanics, molecular dynamics, etc. The following lists some of the key topics across different scales. The author has been advocating a summer institute to train faculty and graduate students to be knowledgeable in scales much less than the micrometer. A NSF Summer Institute on Nano Mechanics and Materials has been established training about 140 faculty members, post doctors and some graduate students annually. For details see: http://tam.northwestern.edu/summerinstitute/Home.htm

10^{-12} m	QUANTUM MECHANICS [TB.DFT.HF…]*
10^{-9}	MOLECULAR DYN.[LJ…]; NANOMECHANICS; MOLECULAR BIOLOGY; BIOPHYSICS
10^{-6}	ELASTICITY; PLASTICITY; DISLOCATION…
10^{-3}	MECHANICS OF MATERIALS
10^{-0}	STRUCTURE ALALYSIS

MULTI-SCALE ANALYSES & SIMULATIONS...

*TB = TIGHT BINDING METHOD; DFT = DENSITY FTNAL THEORY;
HF = HATREE-FOCK APPROX; LJ = LENNARD JONES POTENTIAL

The National Science Foundation has supported basic research in engineering and the sciences in the United States for a half century and it is expected to continue this mandate through the next century. As a consequence, the United States is likely to continue to dominate vital markets, because diligent funding of basic research does confer a preferential economic advantage [**1**]. Concurrently over this past half century, technologies have been the major drivers of the U. S. economy, and as well, NSF has been a major supporter of these technological developments. According to the former NSF Director for Engineering, Eugene Wong, there are three *transcendental* technologies:

- Microelectronics – Moore's Law: doubling the capabilities every two years for the last 30 years; unlimited scalability; nanotechnology is essential to continue the miniaturization process and efficiency.
- Information Technology [IT] – NSF and DARPA started the Internet revolution about three decades ago; the confluence of computing and communications.
- Biotechnology – unlocking the molecular secrets of life with advanced computational tools as well as advances in biological engineering, biology, chemistry, physics, and engineering including mechanics and materials.

Efficient civil infrastructure systems as well as high performance materials are essential for these technologies. By promoting research and development at critical points where these technological areas intersect, NSF can foster major developments in engineering. The solid mechanics and materials engineering (M&M) communities will be well served if some specific linkages or alignments are made toward these technologies. Some thoughtful examples for the M&M and other engineering communities are:

- Bio-mechanics/materials
- Thin-film mechanics/materials
- Wave Propagation/NDT
- Nano-mechanics/materials
- Nano-electro-mech'cal (NEMS)
- Multi-scale Simulations/modeling
- Micro-electro-mechanical systems
- Smart materials/structures
- Designer materials
- Fire Retardant Materials and Structures

MEMs can be used as platforms for NEMS. Another product of the nanotechnology is carbon nano-tubes (CNT) which are self-assembled in deposition from C-rich vapors, consisted of honeycomb lattices of carbon rolled into cylinders; nm in diameter, micron in length. CNT have amazing properties:

- 1/6 the weight of steel; 5 times its Young's modulus; 100 times its tensile strength; 6 orders of magnitude higher in electrical conductivity than copper; CNT strains up to 15% without breaking
- 10 times smaller than the smallest silicon tips in Scanning Tunnel Microscope - STM [CNT is the world's smallest manipulator]
- CNT may have more impact than transistors
- ideal material for flat-screen TV [~2003]
- similar diameter as DNA
- bridge different scales in mesoscale - useful as bldg. blocks ~ e.g. nanocomposites; gases storage
- metallic or semiconducting
- as single-electron transistor; logic gate
- as RAM - on/off do not affect memory storage - no booting needed

Sources:[**2-5**]
CARBON NANOTUBES -THE FIRST 10 YEARS, NATURE, 2001.
MECHANICAL ENGINEERING, ASME, NOV. 2000
TECHNOLOGY REVIEW, MIT, MAR. 2002

Considerable NSF resources and funding will be available to support basic research related to nano science and engineering technologies. These opportunities will be available for the individual investigator, teams, small groups and larger interdisciplinary groups of investigators. Nevertheless, most of the funding at NSF will continue to support unsolicited proposals from individual investigator on innovative "blue sky" ideas in all areas including nano science and engineering technologies.

2. NANOTECHNOLOGY

2.1 Nanomechanics Workshop

Initiated by the author, with the organization and help of researchers from Brown [K. S. Kim, et al], Stanford, Princeton and other universities, a NSF Workshop on Nano- and Micro-Mechanics of Solids for Emerging Science and Technology was held at Stanford in October 1999. The following is extracted from the Workshop Executive Summary. Recent developments in science have advanced capabilities to fabricate and control material systems on the scale of nanometers, bringing problems of material behavior on the nanometer scale into the domain of engineering. Immediate applications of nanostructures and nano-devices include quantum electronic devices, bio-surgical instruments, micro-electrical sensors, functionally graded materials, and many others with great promise for commercialization. Recognizing that this area of nanotechnology is in its infancy, substantial basic research is needed to establish an engineering science base. Such a commitment to nano- and micro-mechanics will lead to a strong foundation of understanding and confidence underlying this technology based on capabilities in modeling and experiment embodying a high degree of rigor. The instruments and techniques available for multiple scales in experimental micro- and nano-mechanics are depicted in Fig. 1, courtesy of K. S. Kim of Brown University.

One of the key instruments in nanotechnology is the atomic force microscope [AFM]. However one of the limitation is: ***AFM SCAN SPEED ~1 HZ [TAKES ~10 MIN. FOR A SMALL IMAGE OF 1 MEGA-PIXELS]*** To improve the speed and performance of the atomic force microscope, more optimal control of the cantilever and more robust software to acquire and process the data as well as other improvements are needed.

IBM has also developed a portable AFM recently.

The potential of various concepts in nanotechnology will be enhanced, in particular, by exploring the nano- and micro-mechanics of coupled phenomena and of multi-scale phenomena. Examples of coupled phenomena discussed in this workshop include modification of quantum states of materials caused by mechanical strains, ferroelectric transformations induced by electric field and mechanical stresses, chemical reaction processes biased by mechanical stresses, and changes of bio-molecular conformality of proteins caused by environmental mechanical strain rates. Multi-scale phenomena arise in situations where properties of materials to be exploited in applications at a certain size scale are controlled by physical processes occurring on a size scale that is orders of magnitude smaller. Important problems of this kind arise, for example, in thermo-mechanical behavior of thin-film nanostructures, evolution of surface and bulk nanostructures caused by various material defects, nanoindentation, nanotribological responses of solids, and failure processes of MEMS structures. Details of this workshop report can be found by visiting http://en732c.engin.brown.edu/nsfreport.html.

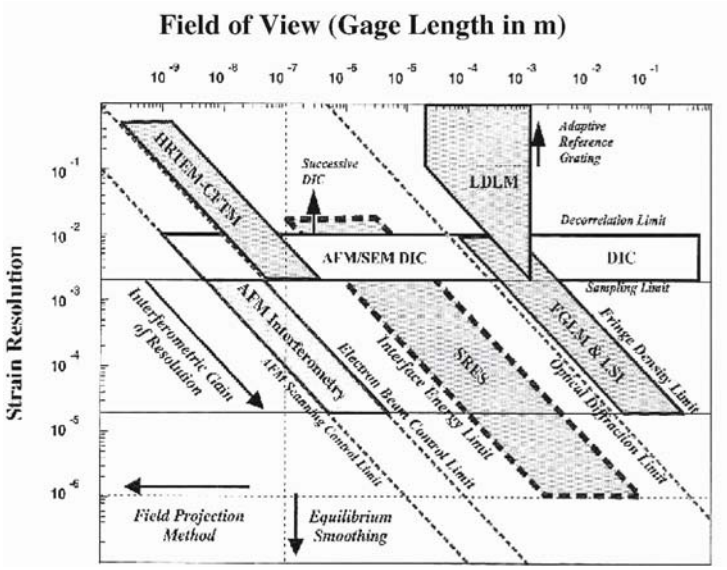

Figure 1. Instruments and techniques for experimental micro and nano mechanics [courtesy of K. S. Kim of Brown University], where HRTEM High Resolution Transmission Electron Microscopy; SRES Surface Roughness Evolution Spectroscopy; CFTM Computational Fourier Transform Moire; FGLM Fine Grating Laser Moiré; AFM Atomic Force Microscopy; LSI Laser Speckle Interferometry; SEM Scanning Electron Microscopy; DIC Digital Image Correlation ; LDLM Large Deformation Laser Moire.

2.2 Nanoscale Science and Engineering Initiatives

Coordinated by M. Roco [**6**], NSF recently announced a multi-year program [**7**] on collaborative research in the area of nanoscale science and engineering (NSE). This program is aimed at supporting high risk/high reward, long-term nanoscale science and engineering research leading to potential breakthroughs in areas such as materials and manufacturing, nanoelectronics, medicine and healthcare, environment and energy, chemical and pharmaceutical industries, biotechnology and agriculture, computation and information technology, improving human performance, and national security. It also addresses the development of a skilled workforce in this area as well as the ethical, legal and social implications of future nanotechnology. It is part of the interagency National Nanotechnology Initiative (NNI). Details of the NNI and the NSE initiative are available on the web at http://nano.gov.

The NSE competition will support Nanoscale Interdisciplinary Research Teams (NIRT), Nanoscale Exploratory Research (NER), Nanoscale Science and Engineering Centers (NSEC), Nano Undergraduate Education (NUE) and others. In addition, individual investigator research in nanoscale science and engineering will continue to be supported in the relevant NSF Programs and Divisions outside of this initiative. This NSE initiative focuses on seven high risk/high reward research areas, where special opportunities exist for fundamental studies in synthesis, processing, and utilization of nanoscale science and engineering. The seven areas are:

- Biosystems at the nanoscale
- Nanoscale structures, novel phenomena, and quantum control
- Device and system architecture
- Nanoscale processes in the environment
- Multi-scale, multi-phenomena theory, modeling and simulation at the nanoscale
- Manufacturing processes at the nanoscale
- Societal and educational implications of scientific and technological advances on the nanoscale

The National Nanotechnology Initiative started in 2000 ensures that investments in this area are made in a coordinated and timely manner (including participating federal agencies – NSF, DOD, DOE, DOC [including NIST], NIH, DOS, DOT, NASA, EPA and others) and will accelerate the pace of revolutionary discoveries now occurring. Current request of Federal agencies on NNI is about $710 million. The NSF share of the budget is around $220 million [on NSE, part of NNI].

3. CHALLENGES

The challenge to the mechanics and materials research communities is: How can we contribute to these broad-bases and diverse research agendas? Although the mainstay of research funding will support the traditional programs for the foreseeable future, considerable research funding will be directed toward addressing these research initiatives of national focus. At the request of the author, a NSF research workshop has been organized by F. Moon of Cornell University to look into the research needs and challenges facing the mechanics communities. A report with recommendations of research needs and challenges has been published in *Mechanics* [**8**], in August 2003.

Mechanics and materials engineering are really two sides of a coin, closely integrated and related. For the last decade this cooperative effort of the M&M Program has resulted in better understanding and design of materials and structures across all physical scales, even though the seamless and realistic modeling of different scales from the nano-level to the system integration-level (Fig. 2) is not yet attainable. ***The major challenges are the several orders of magnitude in time and space scales from the nano level to micro and to meso levels.*** The following list summarizes some of the major methods in bridging the scales, top down or bottom up, and their limitations.

- **FIRST PRINCIPLE CALCULATIONS - TO SOLVE SCHRODINGER'S EQ.**
  ***AB INITIO*, e.g. HATREE- FOCK APPROX., DENSITY FUNCTIONAL THEORY,…**
  - COMPUTIONAL INTENSIVE, O (N^4) – N is the number of orbitals.
  - UP TO ~ 3000 ATOMS

- **MOLECULAR DYNAMICS [MD] pico sec. range - DETERMINISTIC, e.g. W/ LENNARD JONES POTENTIAL**
  - MILLIONS TIMESTEPS OF INTEGRATION; TEDIOUS
  - UP TO ~ BILLION ATOMS FOR NANO-SECONDS

- **COMBINED MD & CONTINUUM MECHANICS [CM], e.g. MAAD[Northwestern U.]; LSU; BRIDGING SCALE; …**
  - PROMISING, but bridging time and space scales is the constraint...

- **INTERATOMIC POTENTIAL/CM – HUANG [U. of Illinois – UC]: EFFICIENT; MD STILL NEEDED IN TEMPERATURE, STRUCTURAL CHANGES, DISLOCATIONS…**

In the past, engineers and material scientists have been involved extensively with the characterization of given materials. With the

availability of advanced computing and new developments in material science, researchers can now characterize processes and design and manufacture materials with desirable performance and properties. One of the challenges is to model short-term nano/micro-scale material behavior, through meso-scale and macro-scale behavior into long-term structural systems performance, Figure 2. Accelerated tests to simulate various environmental forces and impacts are needed [**9**]. Supercomputers and/or workstations used in parallel are useful tools to solve this scaling problem by taking into account the large number of variables and unknowns to project micro-behavior into infrastructure systems performance, and to model or extrapolate short term test results into long term life-cycle behavior [**9, 10**]. Twenty-four awards were made totaling $7 million. A grantees' workshop was held recently in Berkeley and a book of proceedings has been published [**11**].

MATERIALS		**STRUCTURES**	**INFRASTRUCTURE**	
nano-level (10^{-9})	**micro-level (10^{-6})**	**meso-level (10^{-3})**	**macro-level (10^{+0})**	**systems-level (10^{+3}) m**
Molecular Scale	***Microns***	***Meters***		***Up to Km Scale***
***nano-mechanics**	***micro-mechanics**	***meso-mechanics**	***beams**	***bridges**
***self-assembly**	***micro-structures**	***interfacial-structures**	***columns**	*** lifelines**
***nanofabrication**	***smart materials**	***composites**	***plates**	***airplanes**

Figure 2. Physical scales in materials and structural systems [**12**]

Researchers at NIST and other places have been building nano-clay filled polymers with natural clay form platelet [less than 1 nm in thickness] and 1 to 5% by volume. These nano-clay filled polymers can dramatically improve fire resistance as well as mechanical properties. Metal oxide nanoparticles have also been used in coatings for protection of UV light, self-disinfecting surfaces, solar cells, indoor air cleaners, etc. Tremendous progress is also being made in micro and nano sensors. Researchers at UC–Berkeley have been working on “smart dust” sensors – with a target of a size of a cube 1mm on each side, capable of sensing [e.g. cracks in materials] and transmitting wirelessly the data collected. Using cantilevers coated with polymer layers and based on changes in surface tension, researchers at IBM – Zurich and Basel have developed the “artificial nose” to detect minute analytes [including wine] and air quality in the air [Fig. 3].

Figure 3. Micro cantilever detection mechanism [IBM – Zurich]

4. ACKNOWLEDGMENTS AND DISCLAIMER

The author would like to thank his colleagues and many members of the research communities for their comments and inputs during the writing of this paper. Information on NSF initiatives, announcements and awards can be found in the NSF website: www.nsf.gov. Parts of this paper have been presented elsewhere. This paper was written by a U.S. Government employee, hence it has no copyright, intended for wider dissemination. The opinions expressed in this article are the author's only, not necessarily those of the NSF.

REFERENCES AND BIBLIOGRAPHY

1. Wong, E. (1996). An Economic Case for Basic Research. *Nature* **381,** 187-188.
2. Reich, S., Thomsen, C., and Maultzsch, J. (2004). Carbon Nanotubes, Wiley-VCH.
3. Srivastava, D., Wei, C., and Cho, K. (2003). Nanomechanics of carbon nanotubes and composites. *Applied Mechanics Review*, 56, 215-230.
4. Qian, D., Wagner, G. J., Liu, W. K., Yu, M., and Ruoff, R. S. (2002). Mechanics of carbon nanotubes. *Applied Mechanics Review*, 55, 495-533.
5. Chong, K. P., "Research and Challenges in Nanomechanics" 90-minute Nanotechnology Webcast, ASME, Oct. 2002; archived in *www.asme.org/nanowebcast*
6. Iijima, S. (1991). Helical microtubes of graphite carbon. *Nature (London),* 354 (6348), 56-58. Interagency Working Group on Nano Science, Engineering and Technology (IWGN). (2000). *Nanotechnology Research Directions*. Kluwer Academic Publ. 37-44.
7. NSF. (2004). Nanoscale Science and Engineering. *NSF 03-043*, National Science Foundation, Arlington, VA.
8. Boresi, A. P., Chong, K. P. and Saigal, S. (2002). *Approximate Solution Methods in Engineering Mechanics*, John Wiley, New York.
9. NSF. (1998). Long Term Durability of Materials and Structures: Modeling and Accelerated Techniques. *NSF 98-42,* National Science Foundation, Arlington, VA.

10. Chong, K. P. (1998, 1999). Smart Structures Research in the U.S. *Keynote paper, Proc. NATO Adv. Res. Workshop on Smart Structures*, held in Pultusk, Poland, 6/98, *Smart Structures,* Kluwer Academic Publ. 37-44 (1999).
11. Monteiro, P. J. M., Chong, K. P., Larsen-Basse, J. and Komvopoulos, K., Eds. (2001). *Long-term Durability of Structural Materials*, Elsevier, Oxford, UK.
12. Boresi, A. P. and Chong, K. P. (2000). *Elasticity in Engineering Mechanics*, John Wiley, New York.
13. a.Asif, S. A. S., Wahl, K. J., Colton, R. J., and Warren, O. L. (2001). Quantitative Imaging of Nanoscale Mechanical Properties Using Hybrid Nanoindentation and Force Modulation. *J. Appl. Phys.* **90**, 5838-5838.
14. Bhushan, B., Kulkarni, A. V., Banin, W., and Wyrobek, J. T. (1996). Nanoindentation and Picoindentation Measurements Using a Capacitive Transducer System in Atomic Force Microscopy. *Phil. Mag. A* **74**, 1117-1128.
15. VanLandingham, M. R., Villarrubia, J. S., Guthrie, W. F., and Meyers, G. F. (2001). Nanoindentation of Polymers: An Overview. *Macromolecular Symposia* **167**: *Advances in Scanning Probe Microscopy of Polymers*, V. V. Tsukruk and N. D. Spencer, Eds., 15-44.

AN AB-INITIO STUDY OF MECHANICAL BEHAVIOR FOR $(A\ell O)_n$ NANORODS

X. Song[1], Q. Ge[2], S. C. Yen[1]
[1]*Materials Technology Center, Southern Illinois University, Carbondale, IL 62901*
[2]*Department of Chemistry and Biochemistry, Southern Illinois University, Carbondale, IL 62901; Email: xiaolan@siu.edu, Qge@chem.siu.edu, myen@siu.edu*

Abstract: A first principles approach based on DFT was used to study the mechanical behavior of the linear $(A\ell\text{-}O)_n$ nanorods with n spanned 1 to 10. The minimum-energy configurations for the nanostructures are first found by fully relaxing the coordinates of the atoms. Virtual tension and compression tests were then conducted by applying a series of tensile/compressive deformations to the relaxed structures and calculating the corresponding forces required to maintain the equilibrium of the deformed nanorods. Hence, A force-strain curve is obtained for all the nanorods. The mechanical response of the two shortest nanorods is like that of the ductile aluminum, but the other longer nanorods deform like the brittle aluminum oxide. All the nanorods demonstrate a much higher compressive strength than tensile strength.

Key words: first principles, mechanical property, alumina nanorods

1. INTRODUCTION

The distinct anisotropic morphology and high aspect ratio of the nanorods make them one of the most important building blocks to develop nanodevices for electronic, mechanical, or other functional materials applications [**1-3**]. Their one dimensional morphology and large surface areas are advantageous in the alignment and functionalization procedures to assemble nanoparticles into new micro electrical-mechanical system (MEMS) or nano electrical-mechanical system (NEMS) devices. Considering the importance of the aluminum oxide in electronics, optics,

T. J. Chuang et al. (eds.), Nanomechanics of Materials and Structures, 23–32.
© 2006 *Springer. Printed in the Netherlands.*

biomedical, and mechanical engineering applications, there has been an emerging interest to fabricate this material in the form of nanorods [**4-8**]. Alumina nanorod arrays have been successfully synthesized by etching a porous anodic alumina (PAA) membrane with straight nanochannels. In order to explore the industry applications of the alumina nanorods, it is very important to investigate the mechanical properties of this new strongly anisotropic nanomaterial.

In the present study, a systematic study of the linear (AlO)n structures with n in the range of 1-10 is performed using the density functional theory (DFT) based first principles approach. The linear $(A\ell O)_n$ structures are the thinnest alumina nanorods containing only one atom in the cross section. The simplicity of the linear structure allows an unambiguous definition of the uniaxial deformation, and thus a virtual tension/compression test to investigate the mechanical behavior of these nanoparticles. It is a challenging task to measure the mechanical response of the small nanoparticles experimentally, although the atomic force microscope may provide some information. The empirical methods, such as molecular dynamics simulation, could also be non-applicable since the potential energy functions developed for the bulk materials are likely to fail in correctly describing the interatomic interactions in the nanoparticles, which have different structures from the bulk material. The first principles approach used in this study makes it possible to have an accurate and quantitative understanding in the mechanical properties of the small nanoparticles. We note that the linear structures studied here are not the most stable structures of aluminum oxide with the same compositions. However, they are metastable and could be prepared under controlled conditions. This simple system offers a good opportunity for studying the effect of particle size on their stability and mechanical properties.

The paper is organized as follows. Section 2 describes the computational method used in this work. The results of the virtual tension and compression tests are presented in Sec. 3, and the conclusions are then summarized in Sec. 4.

2. METHOD

Ten straight $(A\ell O)_n$ nanorods investigated in this work have a linear structure as shown in Fig. 1. Ten structures with n increased from 1 to 10 were systematically studied. The nanorods were placed in a periodically repeated supercell, with the nearest distance between replicas larger than 10 Å. The calculations were performed using the Vienna Ab-initio Simulation Package (VASP) [**9**], which is based on DFT with a plane wave basis set.

The projector augmented wave (PAW) method [**10**] was adopted to describe the electron-ion interactions in electronic structure, total energy, and force calculations. The exchange and correlation energies were calculated using the Perdew-Wang 91 form of the generalized gradient approximation [**11**]. A plane wave cutoff energy of 500 eV was used in our calculations.

The minimum-energy configurations of the nanorods are first found by fully relaxing the coordinates of the atoms. The stability of these linear (AlO)n nanorods is examined by calculating their formation energies. The reaction to form the *(AlO)n* nanorod from the aluminum (Al) and oxygen (O) atoms is shown in Equation (1):

$$nAl+nO \rightarrow (AlO)_n \tag{1}$$

The total energy of one aluminum atom (E_{Al}) was calculated to be -0.177 eV, and that of one oxygen atom (E_O) -1.901 eV. Thereby, the total formation energy of the nanorod (in eV) is calculated by

$$E_f = n \times (E_{Al} + E_O) - E_{(AlO)_n} \tag{2}$$

where $E_{(AlO)_n}$ represents the total energy of the nanorod. The formation energy per AlO unit ($\overline{E}_f$) is defined as:

$$\overline{E}_f = E_f / n \tag{3}$$

According to the definition, the systems with positive formation energy ($\overline{E}_f > 0$) are stable, and the larger value of formation energy indicates higher stability. All the nanorods studied here are found to be energetically stable.

Fig. 1. The linear structure of the nanorods

Virtual uniaxial tension and compression experiments were then conducted to investigate the mechanical behavior of these fully relaxed nanorods. In the tests, displacements ($\pm d$) are applied to a fully relaxed nanorod with an original length of l , and the amount of the strain (ε) in the nanorod is equal to d/l . The two atoms at both ends of the nanorod are fixed to maintain the deformed length of $l \pm d$. Next the minimum-energy

configuration in the presence of constraints is found by allowing the remaining atoms to move until the total energy attains a minimum value, and the external forces applied to maintain the equilibrium of the deformed nanorods can be evaluated using the well known Hellmann-Feynman force theorem [**12, 13**]. The force-strain relations are used to characterize the mechanical property of the nanorods. The force, instead of stress is used in this study because of the following two reasons: 1) at the nanoscale, the definition of the stress is ambiguous due to a lack of accurate definition of the cross sectional area. 2) It is justified to assume that the nanorods investigated in this study have similar cross sections, which contain only one atom. Furthermore, the breaking mechanisms of the nanorods under tension and compression are also investigated by monitoring the change of the bond lengths during the loading procedure.

3. RESULTS

With formation energies larger than zero, all the ten nanorods studied here are energetically stable with reference to the single aluminum and oxygen atoms. Their lengths are in the range of 0.16 – 3.26 nm. The size effects on the formation energy ($\overline{E}_f$) of the nanorods are presented in Fig. 2. The formation energy, thereby the stability of the nanorods, is found to increase when the size of the rods increases.

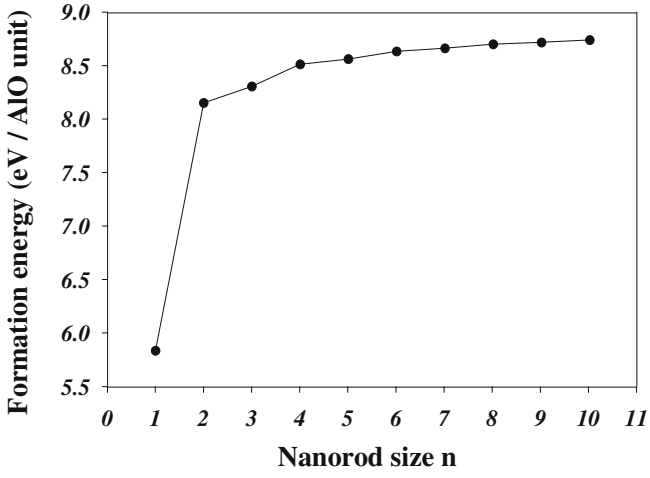

Fig. 2. The formation energies of the nanorods as a function of the number of $(A\ell O)_n$ units.

The results of the virtual tension tests are presented in Fig. 3 and Fig. 4. The forces are plotted as a function of the tensile strain applied to the nanorods. The two shortest nanorods, $(AlO)_1$ and $(AlO)_2$, have a force-strain curve typical of ductile material like aluminum. From the curves we can identify three different ways in which the material behaves, depending on the amount of strain induced in the material. The first portion of the curves is linear, and this might represents an elastic behavior. With a further load applied, the curves rise continuously, but become flatter until a maximum force is reached. The rise in the curves in this manner is usually called strain hardening. Then the force-strain diagrams tend to curve downward, and it often indicates a decrease in the cross-sectional area, called necking in the macroscopic mechanical test. When *n* is in the range of 3–10, the nanorods are more like the brittle material, exhibiting little or no yielding before failure. Interesting odd-even effect is also observed in the virtual tension tests for these brittle nanorods. As shown in Fig. 3, when *n* is an odd number, the maximum force sustainable by the nanorod decreases with the increase of the rod length until n reaches 7, and the tensile response of $(AlO)_9$ has little difference with that of $(AlO)_7$. However, Fig. 4 shows that the nanorods containing even number of AlO units, namely 4, 6, 8, and 10, have almost the same force-strain diagram under the tensile load. It is also noted that $(AlO)_3$, $(AlO)_5$, $(AlO)_7$ and $(AlO)_9$ are capable to support larger tensile load than $(AlO)_2$, $(AlO)_4$, $(AlO)_6$, and $(AlO)_8$.

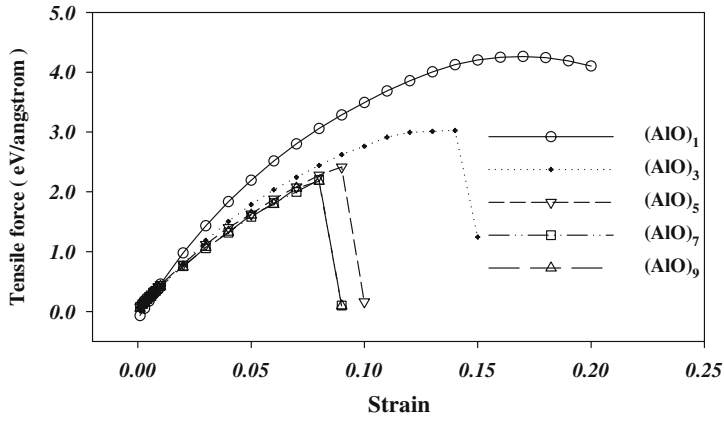

Fig. 3. The results of virtual tension tests for the (AlO)n nanorods, where n is an odd number.

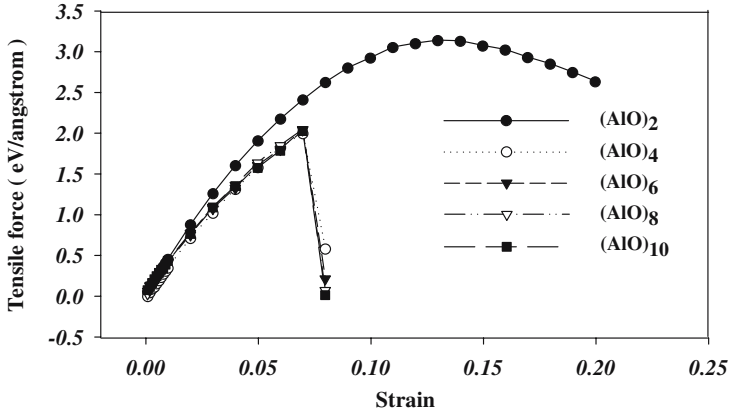

Fig. 4. The results of virtual tension tests for the (AlO)n nanorods, where n is an even number.

In order to investigate the breaking mechanisms of the ductile and brittle nanorods under tension, the change of the bond lengths with the increase of the strain is studied. Here we use $(AlO)_2$ and $(AlO)_4$ as two examples to show the different failure mechanisms in ductile and brittle nanorods. Fig. 5 and Fig. 6 display the tensile force and lengths of the bonds as a function of the strain for the ductile $(AlO)_2$ and brittle $(AlO)_4$, respectively. For $(AlO)_2$, when the strain is less than 0.04, the lengths of all the three bonds increase with similar rate, and this corresponds to the linear portion of the force-strain curve. When the strain increases from 0.04 to 0.13, the length of the first bond increases more sharply while the increase in the lengths of the other two bonds slows down. In this phase, strain hardening might occur and the force-strain curve rises with a decreasing slope. The maximum force is reached at the strain of 0.13. After that, the first bond continues to elongate at a large rate, but the lengths of the other two bonds decrease steadily. This phenomenon indicates that the first bond will break and lead to the failure of the $(AlO)_2$ nanorod eventually. As shown in Fig. 6, the bonds in the brittle $(AlO)_4$ respond to the tensile force differently. Before the nanorod fails, a long linear portion, with the strain spanned 0 to 0.05, is observed in all the bond length-strain curves, and thereby force-strain curve. When the strain increases from 0.05 to 0.07, the slope of the force-strain curve decreases a little, and it can be attributed to an accelerated elongation of the fourth bond. When the strain changes from 0.07 to 0.08, the force applied to the nanorod decreases suddenly, and indicates the failure of the nanorod. At the same time, the length of the fourth bond increases sharply, jumping from 1.98Å to 2.60 Å, while the lengths of all the other bonds decrease. This shows that the $(AlO)_4$ nanorod is broken into two $(AlO)_2$ rods.

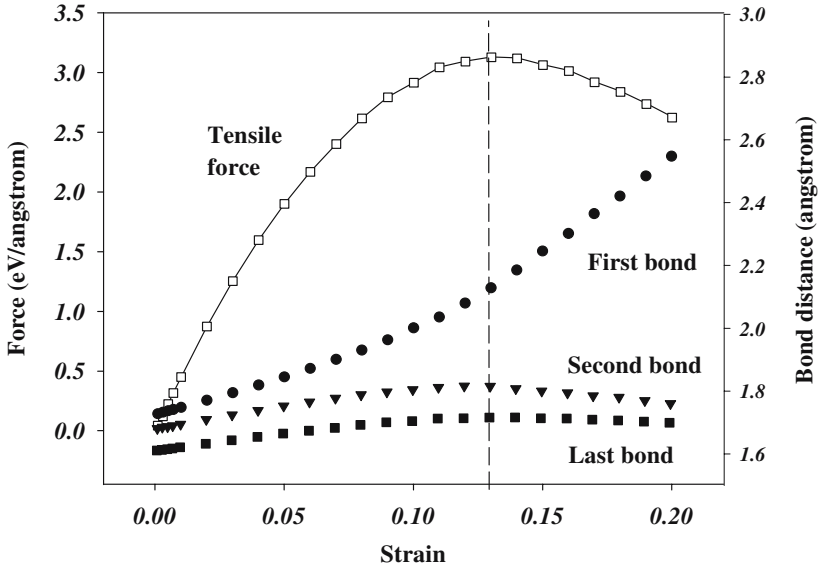

Fig. 5. The change of bond distances in $(AlO)_2$ during the tensile loading procedure.

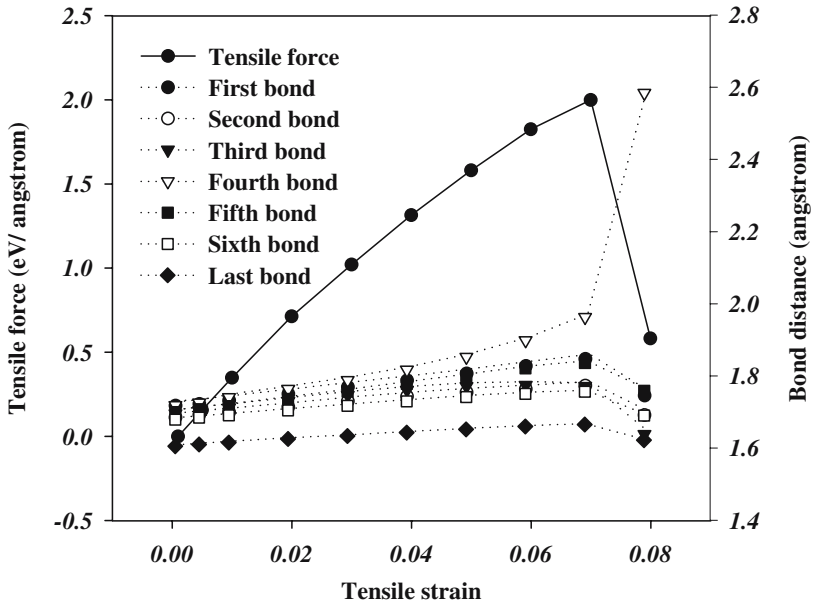

Fig. 6. The change of bond distances in $(AlO)_4$ during the tensile loading procedure.

The compression test results are shown in Fig. 7. All the nanorods are found to behave similarly under the compressive load. The forces increase with the strain linearly when the compressive strain is small, but the slope of the curves increases with the further increase of the strain, indicating the strengthening of the material under compression. The change of bond lengths for $(AlO)_4$ under compression is shown in Fig. 8 to demonstrate the breaking mechanism of the nanorods subject to compressive force. It is observed that all the bonds shorten steadily and the difference in the bond lengths become negligible eventually. Therefore, it might be appropriate to predict that the nanorods will collapse under compression due to the simultaneous failure in all the bonds.

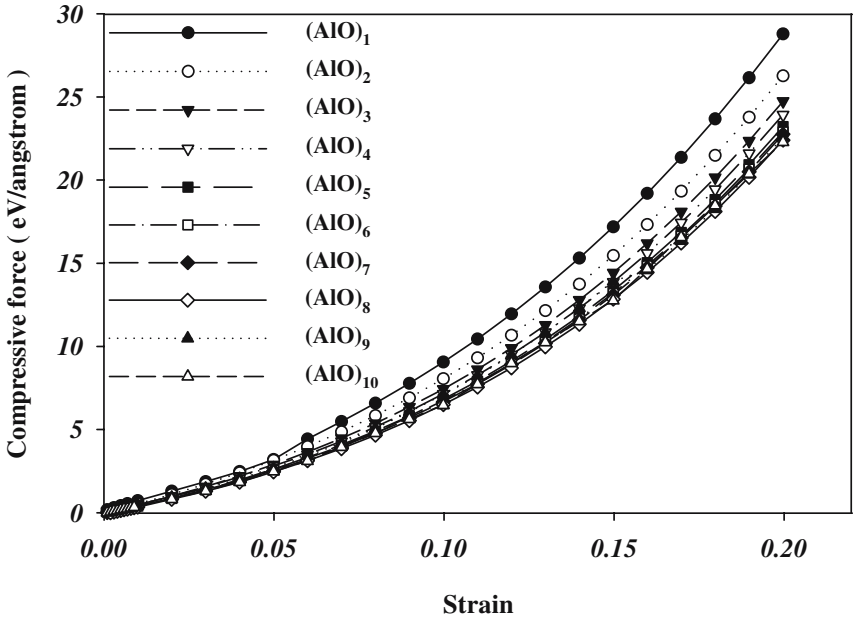

Fig. 7. The results of virtual compression test for the(AlO)n nanorods.

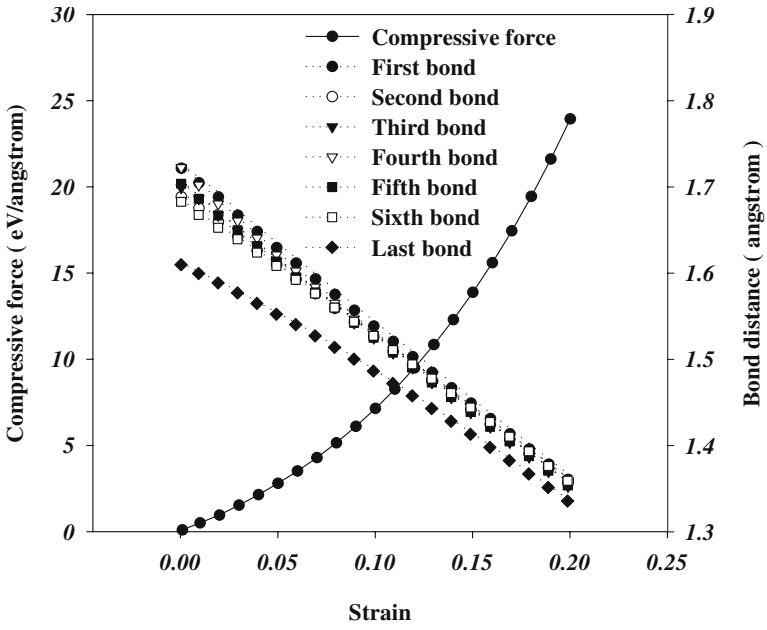

Fig. 8. The change of bond distances in $(AlO)_4$ during the compressive loading procedure.

4. CONCLUSIONS

We have investigated the stability and mechanical properties of ten linear (AlO)n nanorods with n spanned 1 to 10. The DFT calculations have shown that these nanorods are energetically stable with reference to the aluminum and oxygen atoms. Our investigation has revealed the size dependence of the stability and properties for the nanorods. The stability of the nanorods increases with the rod length. The results of the virtual tension and compression tests show that the two shortest nanorods are ductile materials while the other longer nanorods are brittle. Like the bulk Al_2O_3 material, the compressive strength of the nanorods is much higher than the tensile strength. The breaking mechanisms of the nanorods are investigated by tracking the change of the bond lengths during the loading procedure. Under the tension load, one of the Al-O bonds elongate with the accelerated rate while the lengths of the other bonds increase a little, or even decrease. The breakage of the highly elongated bond will result in the failure of the nanorods. However, when subject to the compressive force, all the bond distances decrease monotonously and the difference in the bond lengths become negligible eventually. Hence it might be appropriate to predict that

the collapse of the nanorods under compression will be caused by the simultaneous failure in all the bonds.

ACKNOWLEDGMENTS

X. Song acknowledges the financial support from Materials Technology Center of Southern Illinois University Carbondale (SIUC), and thanks Professor Lichang Wang at the Department of Chemistry and Biochemistry for useful discussions. Q. Ge acknowledges the start-up fund from SIUC.

REFERENCES

1. Patzke, R. G., Krumeich, F., and Nesper, R., 2002, “Oxidic Nanotubes and Nanorods – Anisotropic Modules for a Future Nanotechnology,” *Angew. Chem. Int. Ed.*, **41**(14), pp. 2446-2461.
2. Limmer, S. J., and Cao, G., 2003, “Sol-Gel Electrophorectic Deposition for the Growth of Oxide Nanorods,” *Adv. Mater.* **15**(5), pp. 427-431.
3. Huynh, W. U., Dittmer, J. J., and Alivisatos, A. P., 2002, “Hybrid Nanorod-Polymer Solar Cells,” *Science*, **295** (5564), pp. 2425-2427
4. Tian, YT; Meng, GW; Gao, T; Sun, SH; Xie, T; Peng, XS; Ye, CH; Zhang, LD, 2004, “Alumina Nanowire Arrays Standing on a Porous Anodic Alumina Membran,” *Nanotechnology* **15**(1), pp. 189-191.
5. Pang, YT; Meng, GW; Zhang, LD; Shan, WJ; Zhang, C; Gao, XY; Zhao, AW; Mao, YQ, 2003, “Electrochemical Synthesis of Ordered Alumina Nanowire Arrays,” *J. of Solid State Electrochem.***7**(6), pp. 344-347.
6. Yuan, ZH; Huang, H; and Fan SS, 2202, “Regular Alumina Nanopillar Arrays,” *Adv. Mater.* **14**(4), pp. 303-306.
7. Xiao, ZL; Han C. Y., Welp, U., Wang, HH; Kwork K. W., Willing G. A., Hiller J. M., Cook R. E., Miller D. J., and Crabtree W. G., 2002, “Fabrication of Alumina Nanotubes and Naowires by Etching Porous Alumina Membranes,” *Nano Lett.* **2**(11), pp. 1293-1297.
8. Zhou, J; Deng, SZ; Chen, J; She, JC; Xu, NX, 2002, “Synthesis of Crystalline Alumina Nanowires and Nanotrees,” *Chem. Phys. Lett.* **365**(5-6), pp. 505-508.
9. Kresse, G., Hafner, J., 1993, "Ab initio molecular dynamics for liquid metals," *Phys. Rev. B* **47**(1), pp. 558-561.
10. Kresse, G., Joubert, J., 1999, "From ultrasoft pseudopotentials to the projector augmented-wave method," *Phys. Rev. B* **59**(3), pp. 1758-1775.
11. Perdew, J. P., Chevary, J. A., Vosko, S. H., Jackson, K. A., Pederson, M. R., Singh, D. J., Fiolhais, C., 1992, "Atoms, molecules, solids, and surfaces: Applications of the generalized gradient approximation for exchange and correlation," *Phys. Rev. B* **46** (11), pp 6671-6687.
12. Nielsen, O. H., and Martin M. R., “Quantum-Mechanical Theory of Stress and Force,” 1985, *Phys. Rev. B.* **32**(6), pp. 3780-3791.
13. Kresse, G., and Furthmüller, J., 2003, VASP the Guide, http://cms.mpi.univie.ac.at/VASP/

PHASE FIELD MODELING OF SOLIDIFICATION AND MELTING OF A CONFINED NANO-PARTICLE

J. Slutsker, A. L. Roytburd*, G. B. McFadden**, and J. A. Warren
Materials Science and Engineering Laboratory, National Institute of Standards and Technology, 100 Bureau Drive, Gaithersburg,MD 20899
**Department of Materials Science and Engineering, University of Maryland, College Park,MD 20742*
***Mathematics and Computational Science Division, National Institute of Standards and Technology, 100 Bureau Drive, Gaithersburg,MD 20899*
Phone: (301)975-5160, fax: (301)975-4553, email: julias@nist.gov

Abstract: A phase field model that includes the stress field during non-isothermal solidification of a one-component system has been developed. The model has been applied to solidification and melting of confined spherical volumes. It has been shown that at some boundary and initial conditions the evolution of a spherically symmetric system results in isothermal steady states with a time-independent distribution of phase. The temperature interval of two-phase stability decreases with the sphere radius. The presented model can be applied to simulate the process of "writing" to electronic media that exploit an amorphous-to-crystalline phase change for recording information.

Key words: phase field modeling, solidification, nano-volumes, phase change recording

1. INTRODUCTION

Melting and solidification into either a crystalline or amorphous state in nano-volumes are basic mechanisms of modern phase change recording. This process exploits an amorphous-to-crystalline phase change to record information onto electronic media such as DVDs. Due to the density difference between phases, transformations in confined volumes are accompanied by internal stresses. Thus, it is necessary to take into account the effect of internal stress during phase change recording. In this proceedings we propose to model this "writing" process by considering melting and solidification in a confined volume.

T. J. Chuang et al. (eds.), Nanomechanics of Materials and Structures, 33–43.
© 2006 *Springer. Printed in the Netherlands.*

To simulate melting/solidification we employ a phase field model, which is an effective approach for the analysis and prediction of the evolution of complex microstructures during phase transformations. This approach has been particularly successful when it has been applied to solidification problems (see e.g. [**1-3**]). For single-component system the phase field method requires solving two equations: the time dependent Ginsburg-Landau phase field equation and the equation of heat transfer.

Another area where the phase field method has been successfully applied is solid/solid phase transformations. In this case, isothermal conditions are usually considered, and the problem is reduced to solving the phase field equation together with equations of elasticity for strain and stress fields. Most of the published works in this area consider a homogeneous solid, neglecting the difference between the elastic properties of the phases (e.g. [**4-6**]). Including elastic inhomogeneity in a phase field model presents a separate challenge. In [**7**] this has been done for systems with an elastic inhomogeneity that does not evolve with time.

The main goal of this work is to develop a phase field model that accounts for the stresses that develop during non-isothermal solidification of a one-component system. These stresses can be external or internal, i.e. they can arise as a result of boundary conditions at the external surface or they can be a result of elastic interactions between phases. Thus, the phase field model should take into account the simultaneous evolution of three fields: a phase field, a temperature field and a stress/strain field.

2. GENERAL DEVELOPMENT OF THE PHASE FIELD MODEL

In this paper we present a phase field model of non-isothermal first order transformation in one-component system in the presence of stress. The phase transformation is characterized by an order parameter, $\eta(x_i, t)$, a function of position and time. The free energy of the two-phase system is

$$F = \int_V \left[f(\eta(x_i,t),T(x_i,t)) + \frac{\beta}{2}(\nabla\eta(x_i,t))^2 + e(\varepsilon_{jk}(x_i,t),\eta(x_i,t)) \right] dV \quad (1)$$

where $f(\eta,T)$ is the free energy density. It characterizes the transformation from an initial phase characterized by with the order parameter $\eta_0^{(1)}$ to the product phase with order parameter $\eta_0^{(2)}$. The temperature corresponding to thermodynamic equilibrium between the bulk phases is T_0 (Fig.1).

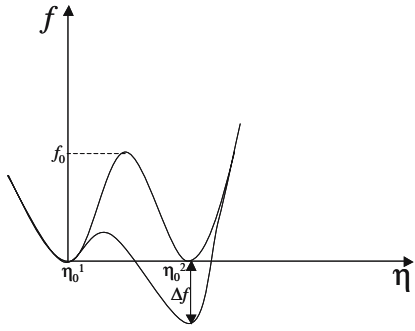

Figure 1. Free energy characterizing the transformation from the initial phase, η_0^1 to the product phase η_0^2 and its dependence on temperature.

$f(\eta,T)$ is a double well function where the difference in energy between the two minima, Δf, depends on temperature. The second term in Eq.(1) is a gradient energy contribution associated with interfaces, where β is a gradient energy coefficient. The third term is an elastic energy density of the two-phase system, depending on the strain field $\varepsilon_{jk}(x_i,t)$. Thus, the free energy of the two-phase system depends on three time-dependent fields: the order parameter, η, the temperature, T and the strain field, ε_{jk}.

The order parameter satisfies the time dependent Ginsburg-Landau equation

$$\frac{\partial \eta}{\partial t} = -M_\eta \frac{\delta F}{\delta \eta} \tag{2}$$

where M_η is a kinetic coefficient. The temperature field satisfies the equation of heat conduction with a source term [1]

$$\frac{\partial T}{\partial t} = \nabla \cdot (D \nabla T) + \frac{q}{c}\frac{d\eta}{dt} \tag{3}$$

where D is the thermal diffusivity, q is the latent heat, and c is the heat capacity.

Assuming that elastic equilibrium is attained faster than the local equilibration of the order parameter, we neglect inertial effects for the elastic field. Then the displacement field is determined by the equations of a mechanical equilibrium:

$$\frac{\delta F}{\delta u_i} = \frac{\partial}{\partial x_j}\frac{\delta F}{\delta \varepsilon_{ij}} = \frac{\partial \sigma_{jk}}{\partial x_j} = 0 \tag{4}$$

where u_i are the components of the displacement field, and the total strain tensor ε_{ik} is given by:

$$\varepsilon_{ik} = \frac{1}{2}\left(\frac{\partial u_i}{\partial x_k} + \frac{\partial u_k}{\partial x_i}\right) \tag{5}$$

The stress, σ_{ik}, according to Hook's law is:

$$\sigma_{ik} = C_{iklm}(\eta)(\varepsilon_{ik} - \varepsilon_{ik}^0(\eta)) \tag{6}$$

where $C_{iklm}(\eta)$ is the elastic modulus tensor, which generally depends on the order parameter, η, and therefore can be different in each phase. $\varepsilon_{ik}{}^0(\eta)$ is a stress-free or self-strain tensor accompanying the phase transition, and ε_{ik}-$\varepsilon_{ik}{}^0(\eta)$ is an elastic strain tensor. The elastic energy density at fixed order parameter can be expressed in terms of these strains by

$$e_{el} = \frac{1}{2}(\varepsilon_{ik} - \varepsilon_{ik}^0(\eta))C_{iklm}(\eta)(\varepsilon_{lm} - \varepsilon_{lm}^0(\eta)) \tag{7}$$

In the isotropic case the elastic energy depends on the bulk modulus, K, and shear modulus, μ:

$$e_{el} = \frac{K}{2}[\varepsilon_{ll} - \varepsilon_{ll}^0(\eta)]^2 + \mu\{[\varepsilon_{ik} - \varepsilon_{ik}^0(\eta)] - \frac{1}{3}\delta_{ik}[\varepsilon_{ll} - \varepsilon_{ll}^0(\eta)]\}^2 \tag{8}$$

Solving the equations (2), (3) and (4) with appropriate boundary and initial conditions, one can find the evolution of order parameter, temperature and stress/strain during the transformation.

For our description of a solid- liquid transformation we will use a double well function, $f(\eta)$ with two symmetric minima at $\eta_0{}^{(1)}=0$ and $\eta_0{}^{(2)}=1$, corresponding to the liquid and solid phases, respectively. Specifically,

$$\begin{aligned} &f(\eta,T) = f^0(\eta) + \Delta f p(\eta) \\ &\Delta f = q\frac{T - T_0}{T_0} \qquad p(\eta) = \eta^3(10 - 15\eta + 6\eta^2) \\ &\Delta f = f(1,T) - f(0,T) \\ &f^0(\eta) = 16 f_0 \eta^2(1-\eta)^2 = f(\eta, T_0) \end{aligned} \tag{9}$$

where f_0 characterizes the height of the energy barrier between liquid and solid. The interpolation function, $p(\eta)$, ensures that the value of the order parameter at the minima of $f(\eta)$ are fixed for all temperatures [**1**].

To treat liquid-solid transitions in the framework of the theory of coherent two-phase systems we assume that the shear modulus of the liquid, μ, is equal to zero, i.e. $\mu(\eta)=p(\eta)\ \mu_0$ [**8,9**][*)]. For simplicity we assume the

[*)] The dependence of shear modulus $\mu=\mu_0 p(\eta)$ is chosen instead of $\mu=\mu_0\eta$, for the same reasons that the temperature dependence of free energy density is chosen as $\Delta f p(\eta)$ instead of

bulk moduli, K, of both the liquid and solid phases are equal. To take into account a volume change due to the transformation the self-strain is introduced as a pure dilatation:

$$\varepsilon_{ik}^{0}(\eta) = \varepsilon^{0}(\eta)\delta_{ik} \,. \tag{10}$$

where $\varepsilon^0(\eta) = (1-p(\eta))\varepsilon_0$, i.e. $\varepsilon^0 = \varepsilon_0$ in the liquid and $\varepsilon_0 = 0$ in the solid.

3. A PHASE FIELD MODEL OF THE MELTING AND SOLIDIFICATION OF A CONFINED SPHERE

In this problem, spherical symmetry is assumed and thus the displacement has only a radial component. The equations of equilibrium, $\frac{\partial \sigma_{ik}}{\partial x_i} = 0$, in spherical coordinates is written

$$\frac{2}{r}\sigma_{\varphi\varphi} - \frac{1}{r^2}\frac{d}{dr}(r^2\sigma_{rr}) = 0 \,. \tag{11}$$

Using the relationships:

$$\varepsilon_{rr} = \frac{du}{dr}, \varepsilon_{\varphi\varphi} = \varepsilon_{\theta\theta} = \frac{u}{r} \tag{12}$$

and the constitutive law for stress in the isotropic case:

$$\sigma_{rr} = K(\varepsilon_{ll} - \varepsilon_{ll}^{0}(\eta)) + \frac{4}{3}\mu(\eta)(\varepsilon_{rr} - \varepsilon_{\varphi\varphi})$$

$$\sigma_{\varphi\varphi} = \sigma_{\theta\theta} = K(\varepsilon_{ll} - \varepsilon_{ll}^{0}(\eta)) - \frac{2}{3}\mu(\eta)(\varepsilon_{rr} - \varepsilon_{\varphi\varphi}) \tag{13}$$

$\varepsilon_{ll}^{0}(\eta) = 3\varepsilon^{0}(\eta)$, the equation of equilibrium (11) can be rewritten in terms of the displacement[*)]:

$$(K + \frac{4}{3}\mu(\eta))\frac{d\varepsilon_{ll}}{dr} + \frac{4}{3}\frac{d\mu(\eta)}{dr}(\frac{du}{dr} - \frac{u}{r}) = K\frac{d\varepsilon_{ll}^{0}(\eta)}{dr} \,. \tag{14}$$

The displacement field *u(r)* can be found as a solution of Eq.(14). The elastic energy of the solid-liquid system (Eq.(7)) can be expressed through the displacement using the relations, Eq.(12):

Δf η. The function p(η) ensures that the minima η=0 and η=1 stay in place for all stresses as well as temperatures.

*) This equation coincides with equilibrium equation used in [**14**], where the ordering in radially stressed sphere has been considered only for the case where shear modulus does not depend on order parameter.

$$E = \frac{1}{2}\int_V [K(\frac{du}{dr} + 2\frac{u}{r} - \varepsilon_{ll}^0(\eta))^2 + \frac{4}{3}\mu(\eta)(\frac{du}{dr} - \frac{u}{r})^2]dV \,. \qquad (15)$$

Inserting the elastic energy into Eq.(1), the free energy for the spherical solid/liquid system including the elastic energy can be written as

$$F = 4\pi\int_0^R [f(\eta,T) + \frac{\beta}{2}(\frac{d\eta}{dr})^2 + \frac{1}{2}K(\frac{du}{dr} + \frac{2u}{r} - \varepsilon_{ll}{}^0(\eta))^2 + \frac{2}{3}\mu(\eta)(\frac{du}{dr} - \frac{u}{r})^2]r^2 dr \,. \qquad (16)$$

The order parameter, η should satisfy the time dependent Ginsburg-Landau evolution equation Eq.(2):

$$\frac{\partial\eta}{\partial t} = -M_\eta\left[\begin{array}{l}\frac{\partial f}{\partial\eta} - \frac{\beta}{r^2}\frac{d}{dr}(r^2\frac{d\eta}{dr}) - K(\frac{du}{dr} + \frac{2u}{r} - \varepsilon_{ll}{}^0(\eta))\frac{d\varepsilon_{ll}{}^0(\eta)}{d\eta} \\ + \frac{2}{3}\frac{d\mu(\eta)}{d\eta}(\frac{du}{dr} - \frac{u}{r})^2\end{array}\right] \qquad (17)$$

while the temperature field should satisfy the equation of heat conduction (Eq.(3)) which in spherical coordinates becomes:

$$\frac{\partial T}{\partial t} = D(\frac{\partial^2 T}{\partial r^2} + \frac{2}{r}\frac{\partial T}{\partial r}) + \frac{q}{c}\frac{\partial\eta}{\partial t} \qquad (18)$$

To perform simulations we introduce the following dimensionless parameters: $\tilde{T} = \frac{T}{T_0}; \tilde{r} = \frac{r}{R}; \tilde{u} = u/R; \tau = t\frac{D}{R^2}; \tilde{f} = f/f_0; M = \frac{DM_\eta f_0}{R^2}$; $Q = \frac{q}{f_0}$, $\overline{Q} = \frac{q}{cT_0}$ and $\tilde{\beta} = \frac{\beta}{R^2 f_0}$. The dimensionless parameter, *M*, describes how fast the order parameter approaches equilibrium relative to the thermal field, i.e. it can be considered as a relaxation time parameter.

Using the postulated dependence of shear modulus on order parameter, $\mu(\eta)=\mu_0 p(\eta)$, where $\mu_0=\mu_s/K$ (μ_s is the shear modulus of the solid), and the dependence of self-strain on order parameter: $\varepsilon_{jk}{}^0(\eta)=\varepsilon_0(1-p(\eta))\delta_{jk}$, the equilibrium equation (15) becomes:

$$(1 + \frac{4}{3}\mu_0 p(\eta))\frac{d\varepsilon_{ll}}{dr} + \frac{4}{3}\mu_0\frac{dp(\eta)}{dr}(\frac{du}{dr} - \frac{u}{r}) = -3\varepsilon_0\frac{dp(\eta)}{dr} \qquad (19)$$

In the next section we present numerical solutions of equations (17), (18) and (19) for the problems of solidification and melting of a confined sphere from the outer surface.

4. SIMULATION RESULTS

We consider a sphere of radius R, with prescribed zero displacement at the surface (r=R). To initiate melting and/or solidification of the sphere from the surface we fix the temperature, T_s, and the order parameter, η, at the surface. Fixing the order parameter at the surface allows one to sidestep the problem of nucleation. The calculations have been done for a sphere using mesh of 1000 evenly spaced points 0.01 apart, yielding a sphere of radius R=10. The dimensionless gradient coefficient is $\tilde{\beta}$ =0.002, and the following elastic properties were selected: dimensionless bulk modulus, $K\varepsilon_0^2/f_0$=0.22, Poisson ratio, ν=1/3, i.e. $\mu_0=\mu_s/K$=0.375; latent heat: q/f_0=2.5, q/cT_0=0.3. The simulations have been performed with a time step $\Delta\tau=10^{-6}$, and relaxation time parameter M=0.01.

Our first set of simulations examined the melting of a solid from the surface. The boundary conditions imposed at the surface are η=0 and $T = T_s>T_0$. The initial temperature of the bulk sphere is $T_{init}<T_0$. We analyze the process of melting for different surface temperatures T_s. At each temperature, the numerical solutions of Eqs.(19)-(21) describe the time evolution of the order parameter and temperature at each point of the sphere. The location of the solid/liquid interface is taken to be η=1/2.

Two examples of the evolution of the order parameter for the melting of sphere at initial temperature of the sphere T_{init}/T_0=0.7 are shown in Figs. 2 and 3. For T_s/T_0=1.3, melting results in the establishment of a two-phase coexistence of solid and liquid. At T_s/T_0=1.75, the final state is solely liquid. For these parameters, two-phase steady states exist up to the temperature T_s/T_0=1.65.

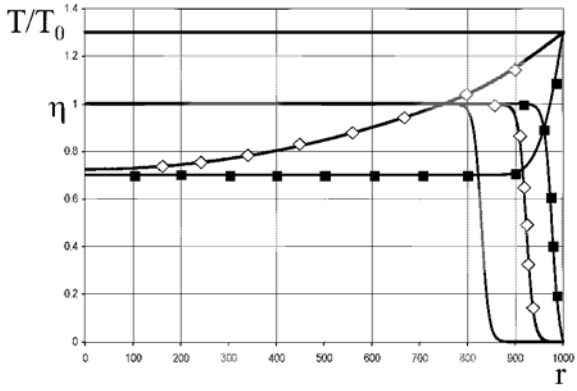

Figure 2. Evolution of the order parameter, η, and temperature, T/T_0 during the melting of a sphere. The temperature at the surface is fixed, T_s/T_0=1.3. The initial temperature of the sphere is T_{init}/T_0=0.7. At steady state (solid black lines), the temperature reaches the surface value everywhere, T_s/T_0, and solid and liquid phases coexist.

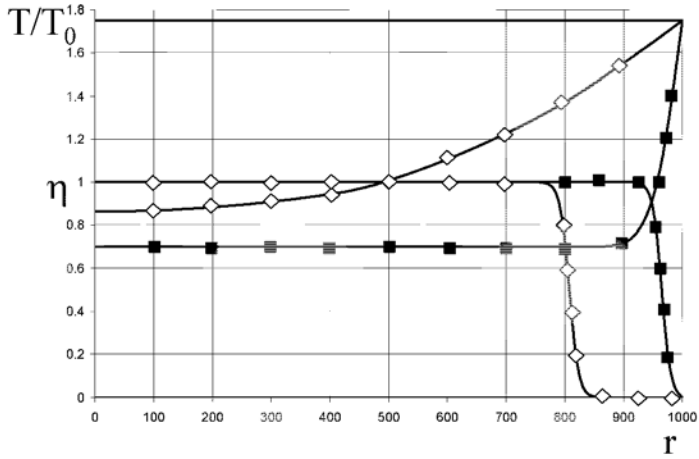

Figure 3. Evolution of the order parameter, η and temperature, T/T_0 during the melting of a sphere. The temperature at the surface is fixed atT_s/T_0=1.75. The initial temperature of the sphere is T_{init}/T_0=0.7. At steady state (solid black lines), the temperature reaches the surface value everywhere, T_s/T_0, but only the liquid phase is present .

The liquid volume fraction, α, increases from 0 to 0.84 as the temperature rises until T_s/T_0=1.65, when α jumps to 1 (Fig.4). Because the displacement at the surface is zero, the liquid is stressed.

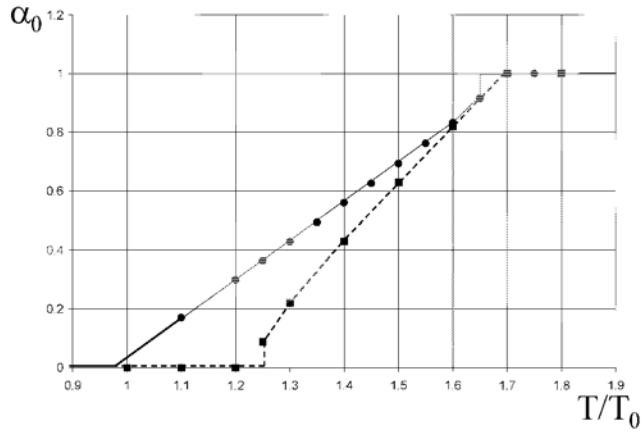

Figure 4. The dependence of an equilibrium fraction of liquid on temperature following from steady state results (equilibrium) of phase field simulation. Solid line: melting of solid sphere from the surface. Dotted line: solidification of liquid sphere from the surface.

We next consider solidification from the surface, i.e. the order parameter at the surface is prescribed to be η=1. In Figs.5 and 6 the solidification of the sphere is shown at an initial temperature of the sphere, T_{init}/T_0=1.8 and at two different surface temperatures (T_s/T_0= 1.5, 1.2, respectively). At T_s/T_0=

1.5, the final state is a solid/liquid mixture (Fig.5). At T_s/T_0 =1.2 the sphere is solidified completely (Fig.6).

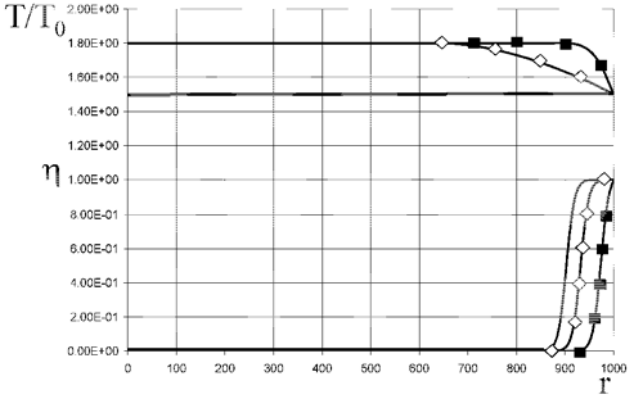

Figure 5. Evolution of order parameter, η and temperature, T/T_0 during the solidification of a sphere. The temperature at the surface is fixed, T_s/T_0=1.5. The initial temperature of the sphere is T_{init}/T_0=1.8. At steady state (solid black lines), the temperature reaches the surface value everywhere, T_s/T_0, and both phases coexist.

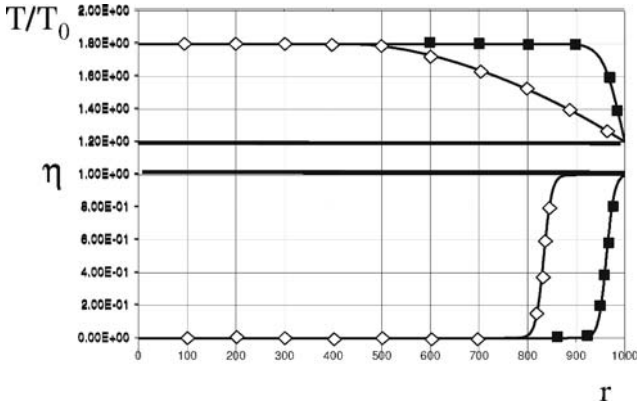

Figure 6. Evolution of order parameter, η, temperature, T/T_0 during the solidification of sphere. The temperature at the surface is fixed, T_s/T_0=1.2. The initial temperature of the sphere is T_{init}/T_0=1.8. At steady state (solid black lines), the temperature reaches the surface value everywhere, T_s/T_0, but only one phase is present .

Two-phase states occur at temperatures lower than T_s/T_0=1.7, as the liquid volume fraction, α, decreases from 1 to 0.1 as the temperature decreases to T_s/T_0=1.25. At this temperature the liquid phase disappears and the sphere becomes completely solid (Fig.4).

To demonstrate that the steady states represent equilibria, we have performed simulations of melting and solidification at uniform temperatures by solving Eqs. (19) and (21) with assumption that the thermal conductivity is infinitely large. These simulations lead to the same steady states, but are only determined by the temperature and the order parameter values at the surface and do not depend on the initial temperature.

The variation of two-phase stability with changing sphere radius is presented in Figure 7. The interval of two-phase stability decreases with the radius of the sphere.

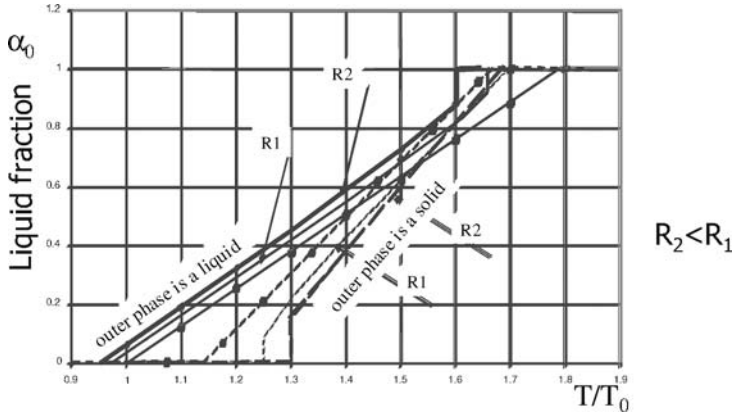

Figure 7. The dependence of equilibrium liquid fraction, α, on temperature at different sphere radii.

5. CONCLUSIONS

The following conclusions can be made from the results of the phase field modeling:

1. There is a temperature interval where two-phase equilibrium states persist during solidification and melting of confined sphere. Existence of the two phase state shows that "writing" requires overheating, of a magnitude that depends on the sphere radius.
2. Melting and solidification from the surface lead to different equilibrium states at the same temperature.
3. At some temperatures during melting and solidification the two-phase states lose stability at finite phase fractions. The stability interval decreases with sphere radius.

REFERENCES

1. W.J.Boettinger, J.A.Warren, C.Beckermann and A.Karma, *Annu.Rev.Mater.Res*., **163**, 2002
2. M. Grujicic, G. Cao, R.S. Miller, *Jour. of Mat. Synt. & and Proc.*, **10,** 191, 2002
3. H.S. Udaykumar, L. Mao, *Inter.Journ. of Heat & Mass Transfer* ,**45,** 4793, 2002
4. K.O. Rasmussen, T. Lookman, A. Saxena, A.R.Bishop, R.C.Albers, S. R. Shenoy *Phys. Rev. Lett*. **87**, 5704 , 2001.
5. A. Artemev, Y.Wang and A.G. Khachaturyan, *Acta Mater*. **48**, 2503, 2000.
6. J.Slutsker, A.Artemev and A.L.Roytburd, *J.Appl.Phys*, **91**, 9049, 2002.
7. Y.U.Wang, Y.M.Jin and A.G.Khachaturyan, *Appl.Phys.Lett*., **80**, 4513, 2002.
8. J.Muller and M.Grant, *Phys.Rev.Lett*. **82**, 1736, 1999
9. K.Kassner, C.Misbah, J.Muller, J.Kappey and P.Kohlert, *Phys.Rev.E*, **63**, 036117, 2001.

FRICTION-INDUCED NUCLEATION OF NANOCRYSTALS

S. Guruzu, G. Xu, and H. Liang
Department of Mechanical Engineering, Texas A&M University, College Station, TX 77843-3123

Abstract: Experimental investigation of friction induced nucleation of nanocrystals was conducted. A series of interfacial interactions were experimentally examined, including pressing, light sliding, and heavy sliding. Results showed that only under a certain sliding conditions, nucleation of crystalline features were formed. Compressing along with heavy sliding caused either melting or severe wear. This preliminary research demonstrated the feasibility of using a friction-stimulation process combined with phase transformation to generate nanostructured materials. The possible nucleation mechanisms are frictional energy induced melting and strain-related nucleation. It leads to the future study of nucleation theory.

Key words: wear, nanocrystals, phase transformation, asperity, nucleation.

1. INTRODUCTION

The development in microelectro mechanical systems (MEMS), the atomically ordered nanostructures such as Nano-MOSFETs, and tiny fluid power devices for bio-applications, etc., have challenged manufacturing precision products such as micro-pumps, micro-engines, and micro-robots [**1-14**]. There are existing methods, such as surface coatings, lithographic techniques, self-assembly, etc., developed to fabricate small devices. Yet, the synthesis of precisely defined artificial molecular architectures beyond 25 nm in length is often unattainable, due to solubility, material throughput, and characterization constraints [**15-20**]. Generating nanoscaled phases with

T. J. Chuang et al. (eds.), Nanomechanics of Materials and Structures, 45–54.
© 2006 *Springer. Printed in the Netherlands.*

desired size, shape, and crystal structure is critically important for nanotechnology development.

The motivation of this research is to investigate the doping/nucleation mechanisms of low-temperature systems through friction triggered atomic doping and nucleation. This paper reports our findings from experiments.

It has been widely accepted that friction activates the surface reaction sites by bond stretching, bond breaking, and reformation [**21-30**]. Using an AFM, experimental evidence supports the mechanism involving mechanical stimulation-enhanced mass transport of ions to nucleation sites [**31-32**]. Due to friction, spontaneous, heterogeneous nucleation produces nanodeposits on brushite surfaces.

In this research, effects of friction on interactions of Ga and Si are investigated. Doping Ga into Si, the surface and phase changes under the friction stimulation are studied. Due to the small nature of asperity contact, small features are expected to form that are potentially useful for nanoscale study. The doping takes place when Ga is rubbing against a Si substrate in ambient conditions. The Ga has a low melting point (29.78 ^{o}C) and Si has a high one (1410 ^{o}C). This material pair undergoes eutectic phase transformation at temperatures around 29 ^{o}C. Due to the low equilibrium concentration of Si, the eutectic phase formed during cooling will remain small in size. The numerical analysis method is used to understand the growth mechanisms of crystalline features.

2. EXPERIMENTAL PROCEDURE

2.1. Materials

Gallium is a soft metal with a low melting temperature (29.78^{o}C). With a boiling point of 2070^{o}C, Ga forms an equilibrium eutectic structure below 30^{o}C with low silicon concentration. A typical example is the gallium (Ga) and silicon (Si) system, as illustrated in Figure1 with a Ga-Si phase diagram[**33**]. Gallium forms a eutectic with small quantities of 5x10^{8} atom% Si at 29.8 ^{o}C and exists as a perfectly mixed liquid over a broad temperature and composition range. The eutectic phase contains only about 10 gallium atoms per million silicon atoms. Nanorods and nanowires have been obtained using a low-temperature vapor-liquid-solid synthesis method [**34-41**].

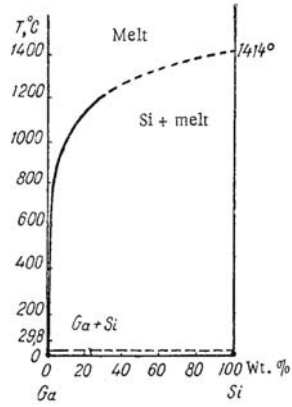

Figure1. Phase diagram of Silicon and Gallium

2.2 Experiments

Ga doping was conducted using basically two approaches: liquid Ga droplets on silicon substrates and solid Ga pin slides against Si disk Figure 2.

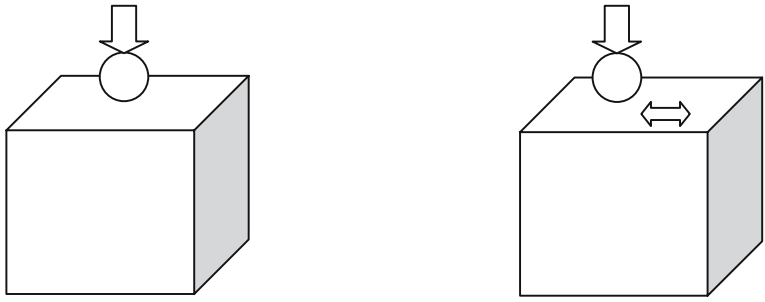

Figure 2. Ga is relative to Si. Left, 2a, A droplet of solid Ga sets on Si then pressed. Right, 2b, solid Ga pin slides against Si.

Figure 2a illustrates the pressing motion. A Ga particle is pressed by an AFM cantilever. Figure 2b is the sliding motion. A pin-on-disc tribometer is used in this setup. The pin is made of Ga and the disk is of single crystal Si.

The pin travels at a reciprocal motion within a length of 6 mm in one direction. The applied load is 200mN. The pin has a diameter of 4 mm. Experiments are conducted out at room temperature in dry conditions. Two tests were conducted at speeds of 700 and 1000 revolutions per minute.

Pressed particles and wear track were observed first using an optical microscope and an AFM. Surface analysis was conducted using an surface imaging software to obtain the physical dimension.

3. RESULTS AND DISCUSSIONS

Figure 3 shows the AFM imagine of a Si surface was pressed with Ga particles using an AFM cantilever. The total area of this image is 5 μm. Light colored particles are Ga particles. Their edges are rounded due to melting.

Figure 3. AFM image of Ga pressed into Si.

Sliding experiments were conduced. Figure 4 shows the Si surface after sliding by a Ga pin. At a speed of 140 mm/sec, there are crystal-like features (two bright triangle like) formed on the Si surface. A surface profile shows the height is around 250 nm and wide at indicated location is around 100 nm. A sliding experiment at higher speed, 200 mm/sec, was conducted. Figure 5 shows the AFM results. Here there are more features like those in Figure 4. In Figure 5, their sizes vary significantly.

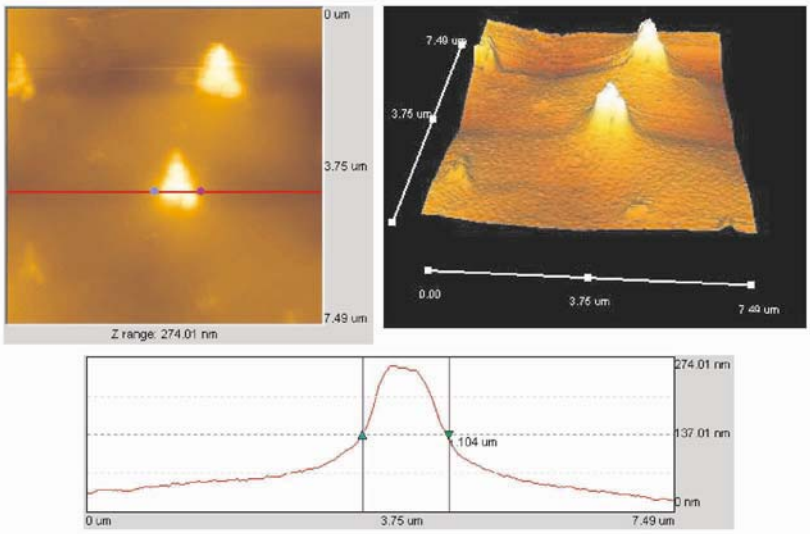

Figure 4. AFM analysis of Si surface after Ga slides on Si at speed of 140 mm/sec

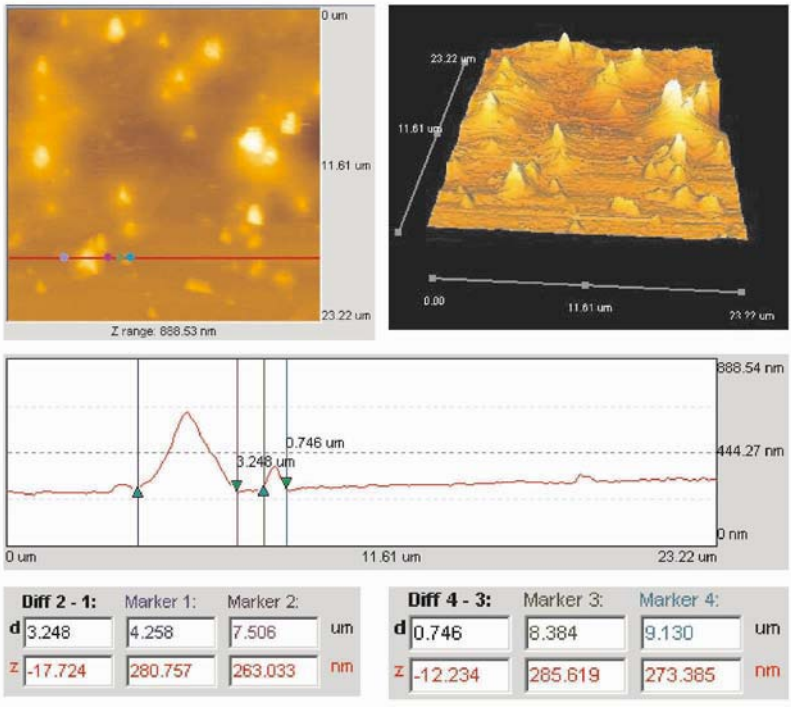

Figure 5. AFM analysis of Si surface after sliding with a Ga pin. Variation of sizes indicate the continuous nucleation and growth of crystals sliding at 200 mm/sec

These crystalline features are detected using a high resolution transmission electron microscope combined with X-ray, as shown in Figure 6. In this figure, the connection of the small feature to Si substrate is seen (circled area). Chemical analysis shows the composition is mostly Si. The physical separation between Si substrate and Ga is not clearly identified. Further down, there is no severe subsurface damage existing. The surface is roughened in a few nanometers that are within the physical range of islands observed on the top surface. It is concluded that islands are formed due to friction. According to the equilibrium phase diagram, Ga and Si form a low temperature eutectic structure (below 30 ^{o}C). It is likely that friction induced heating melt the Ga-Si system so that a certain number of nucleates appear. Without friction, such melting can only take place when temperature reaches the eutectic temperature in area where the Ga and Si are in contact.

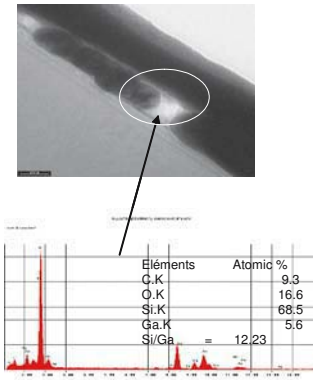

Figure 6. HR TEM analysis shows cross section (top) and many Ga over the bright area (bottom)

Continued sliding experiments with a much higher load were conducted. Si surface is shown in Figure 7. In this figure, the worn surface is clearly seen. Under this condition, the surface wear takes instead of nucleation of crystals.

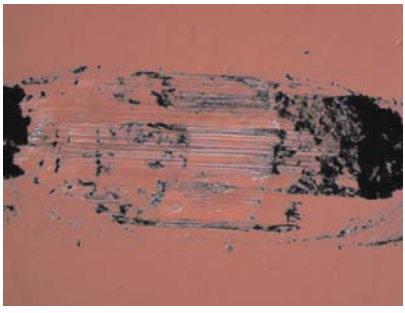

Figure 7. Sliding under sever sliding condition – wear appeared

Experiments have shown nucleation of nanometer length scale crystals form under a certain sliding conditions. No sliding or sliding with heavy load, no nucleation was observed. Table 1 is the summary of results.

Table 1. Summary of Statistical Measurement of Crystalline Features

Conditions	Speed (mm/sec)	Height/Diameter ratio
AFM pressing	-	0.01-0.11
Pin on disc sliding	140	0.24-0.31
Pin on disc sliding	200	0.08-1.58

The number of asperities, average area of each asperity, and the average gray scale of each asperity were obtained using the surface imaging software. The average gray scale value represents the average height of each asperity. The results of this analysis are shown in Table 2.

Table 2. Table showing values of average number of asperity, average height, average area, normal load and frictional load for 700 and 1000 rpm

Speed RPM	average number of asperities per 1000 μm^2	Average height (μm)	Average area (μm^2)	Normal load per asperity (μN)	Tangential force (μN)
700	35.65	0.273	0.479	9.468	6.628
1000	35.24	0.432	1.36	7.0348	4.924

Using the friction (tangential) force measured, the frictional energy over area of Ga/Si contact calculated was around 1.7 mJ, which was higher than the energy of a eutectic reaction between Ga-Si. The nucleation of crystalline phases of Ga-Si is thermodynamically possible. The nucleation under the conditions presented here, demonstrated, in experiments, is associated with the elastic strain energy through friction stimulation. This is similar to elastic train energy effects on nucleation in solids, proposed by Eshelby in 1951[**40**]. Future investigation is underway

4. SUMMARY

Experiments provide evidence of nucleation of crystalline features of Si due to friction stimulation. The formation of nanocrystals is due to frictional energy and reformation. Future study will focus on the strained crystal lattice and their effects on nucleation mechanisms.

ACKNOWLEDGMENTS

Authors are grateful for the financial support by the National Science Foundation (DMI 0300574) and the UAF graduate school fellowship. Assistance in TEM analysis by Jean-Michel Martin and Beatrice Vacher are greatly appreciated. Discussions and help on AFM provided by Milind Kulkarni and Sudeep Ingole are appreciated.

REFERENCES

1. R. Allan, "Special report - MEMS Designs Gear Up For Greater Commercialization - As new markets arise, MEMS and MST technologies move forward to overcome challenging packaging, testing, reliability, and manufacturing roadblocks," *Electronic Design*, **Vol. 48**, No. 12, p. 85, 2000.
2. G.D. Hutcheson and J.D. Hutcheson, "Technology and Economics in the Semiconductor Industry," *Scientific American*, Jan. 22, p.66-73, 1998.
3. R. Merz, F. B. Prinz, K. Ramaswami, M. Terk, and L. E. Weiss, "Shape Deposition Manufacturing," *Proc. Solid Freeform Fabrication Symposium*, edited by H. Marcus, J. J. Beaman, J. W. Barlow, K. L. Bourell and R. H. Crawford, The University of Texas, Austin, August, pp. 1-8, 1994.
4. H. Liang and S. Jahanmir, "Boric Acid as an Additive for Core-Drilling of Alumina," ASME Trans., *J. of Tribology*, **117** (1), pp. 65-73, 1995.
5. G. Dearnaley, "Ion Implantation and Ion Beam Mixing in Corrosion Science and Technology," Fundamental Aspects of Corrosion Protection by Surface Modification, *Proc. Int. Symp. Cosp. Corr. Div. Elec. Soc. & Euro. Fed. Corro*., ed. E. McCafferty, C.R. Clayton, J. Oudar, **Vol. 84-3**, pp. 1-14, 1984.
6. E. Wendler-Kalsch, "Corrosion Protection of Unalloyed and Low-Alloy Steels by Electrochemical Modification of Surface Oxide Films," Fundamental Aspects of Corrosion Protection by Surface Modification, *Proc. Int. Symp. Cosp. Corr. Div. Elec. Soc. & Euro. Fed. Corro*., ed. E. McCafferty, C.R. Clayton, J. Oudar, **Vol. 84-3**, pp.158-172, 1984.
7. E. D. Nicholas, "Friction Processing Technologies," *Advanced Materials & Processes*, June, pp.69-71, 1999.
8. H. S. Hong and M. F. Ashby, "Friction Heat Maps and Their Application," *MRS Bull.* **Vol.16 (10)**, pp.41-47, 1991.
9. Nam P. Suh, *Tribophysics*, Prentice-Hall, Englewood Cliffs, NJ, pp.356-382, 1986.
10. F. P. Bowden and D. Tabor, *The Friction and Lubrication of Solids*, Clarendon Press, Oxford, pp. 33-72, 1958.
11. K.E. Petersen, "Silicon as a Mechanical Material," *Proc. IEEE*, **Vol.70**, p.420-457, 1982.
12. J.H. Wohlgemuth, "Improvements in Cast Polycrystalline Silicon PV Manufacturing Technology," *AIP Conference Proceedings*, **Vol. 394**, p. 415, 1997.
13. T. Ohmi, "Trends for Future Silicon Technology," *Japanese J. App. Phys. Part 1*, **Vol. 33**, No. 12B, p. 6747, 1994.
14. C.M.A. Ashruf, P.J. French, P.M. Sarro, P.M.M.C. Bressers, J.J. Kelly, "Electrochemical Etch Stop Engineering for Bulk Micromachining," *Mechatronics*, **Vol.8**, p.595-612, 1998.
15. J.M. Tour, "Conjugated Macromolecules of Precise Length and Constitution. Organic Synthesis for the Construction of Nanoarchitectures"*Chem. Rev*.,**Vol. 96**, 1996, p.537-553.

16. G.M.Whitesides, J. P. Mathias, C. T. Seto, " Molecular Self-Assembly and Nanochemistry: A Chemical Strategy for the Synthesis of Nanostructures:.Additional Info: Engineering a Small World: From Atomic Manipulation to Microfabrication," *Science*, **254**, 1991, p.1312-1319.
17. C.A.Mirkin, R. L. Letsinger, R.C. Mucic, J.J. Storhoff, " A DNA-based Method for Rationally Assembling Nanoparticles into Macroscopic Materials" *Nature*, **382**, 1996, 607-609.
18. A.P. Alivisatos, K. P. Johnsson, X. Peng, T.E. Wilson, C.J.Loweth, M.P.Bruchez, P.G.Schultz, "Organization of 'nanocrystal molecules' using DNA"*Nature*, **382**, 609-611, 1996.
19. N.C. Seeman, "DNA Components for Molecular Architecture," *Acc. Chem. Res*., **30**, 357-363, 1997.
20. D.Bach, I.R. Miller, ""Biochim. Biophys. Acta, **114**, 311-325, 1966; (b) I.R. Miller, D. Bach, Biopolymers, **6**, 169-179, 1968, (c) P.L. Felgner, T.R. Gadek, M. Holm, R. Roman, H.W.Chan, M.Wenz, J.P. Northrop, G.M. Rigold, M.Danielsen, *Proc. Natl. Acad. Sci*. USA, 84, 7413, 1987; (d) H.J.Vollenweider, J.M.Sogo, H.H.Koller, *Proc. Natl. Acad. Sci*. USA, 72, 83-87, 1975.
21. E. Rabinowicz, "Polishing," *Sci. Am*., pp.91-99, 1968.
22. F.P. Bowden and D. Tabor, *The Friction and Lubrication of Solids*, Clarendon Press, Oxford, pp.33-72, 1958.
23. T. Ohmi, "Trends for Future Silicon Technology," Japanease *J. Appl. Phys*. Part 1, **Vol. 33**, No. 12B, p.6747, 1994.
24. Preston, "The Theory and Design of Plate Glass Polishing Machines," *J. Soc. Glass Tech*., **11**, p.214-256, 1927.
25. T.E. Fischer and W.M. Mullins, "Chemical Aspects of Ceramic Tribology," *J. Phs. Chem*., **96**, p.5690-5695, 1992.
26. H. Tomizawa and T.E. Fischer, *ASLE Trans*., **30**, p.41-46, 1986.
27. T.E. Fischer and H. Tomizawa, "Interaction of Tribochemistry and Microfracture in the Friction and Wear of Silicon Nitride," *Wear*, **105**, p.21, 1985.
28. Fischer, T.E., Liang, H. and Mullins, W.M., Tribochemical Lubricious Oxides on Silicon Nitride, New Directions in Tribology, L. Pope, L. Fehrenbacher, and W. Winer, eds., *Materials Research Society Symposium Proceedings*, **140**, pp.339-344, 1089.
29. T. Fischer, Tribochemistry, *Ann. Rev. Mater. Sci*. **18**, p.303-308, 1988.
30. Gerhard Heinicke, *Tribochemistry*, Carl Hanser, Munchen, 1984.
31. J.T. Dickinson, N.-S. Park, M-W. Kim, and S.C. Langford, "A Scanning Force Microscope Study of a Tribochemical System: Stress-Enhanced Dissolution," *Trib. Lett*. **3**, pp.69-80, 1997.
32. R. Hariadi, S. C. Langford, and J. T. Dickinson, "Controlling Nanometer-scale Crystal Growth on a Model Biomaterial with a Scanning Force Microscope", *Langmuir*, **18**, pp.7773-7776, 2002.
33. C.D. Thumoond and M. Kowalchik, *Bell Syst. Tech*. J. **39**, p.l169, 1960.
34. M.K. Sunkara, S. Sharma, and R. Miranda, G. Lian, and E.C. Dickey, "Bulk Synthesis of Silicon Nanowires Using a Low-temperature Vapor-Liquid-Solid Method," *App. Phys. Lett.*, **Vol. 79**, No. 10, p.1546-1548, 2001.
35. R.S. Wagner and W.C. Ellis,. *Appl. Phys Lett*., **4**, p.89, 1964.
36. J. Westwater, D.P. Gosain,S. Tomiya, S. Usui, and H. Ruda*, J. Vac. Sci. Technol*. B, **15**, p.554, 1997.
37. A.M. Morales and C.M. Liebe*r, Science*, **279**, p.208, 1998.
38. X. Duan and C. M. Lieber, *Adv. Mater*. **12**, p.298, 2000.

39. S.Q. Feng, D.P. Yu, H.Z. Zhang, Z.G. Bai, and Y. Ding, *J. Cryst. Growth*, **209**, p.513, 2000.
40. http://www.sunysccc.edu/academic/mst/ptable/Si.html last accessed on Apr. 26, 2003.
41. http://www.sunysccc.edu/academic/mst/ptable/Ga.html last accessed on Apr. 26, 2003.
42. J.D. Eshelby, "The Force on Elastic Singularity," *Phil. Trans. Roy. Soc. London*, Ser.A, Math. Phys. Sci., **vol. 244**, No. 877, Nov. 6, p.87-112, 1951.

MODELING OF CARBON NANOTUBES AND THEIR COMPOSITES

Chunyu Li and Tsu-Wei Chou
Department of Mechanical Engineering, University of Delaware, Newark, Delaware 19716, USA. Telephone: 302-831-1550; email: chou@me.udel.edu

Abstract: This paper reviews recent advancements in the multiscale modeling of carbon nanotubes and their composites. The basic modeling tool is the molecular structural mechanics method developed by the authors, which has been successfully applied to simulate the static and dynamics properties of carbon nanotubes. Then, the nanotube/polymer composite is analyzed by combining the continuum finite element method and the molecular structural mechanics approach. Finally, the potential application of molecular structural mechanics for studying the thermal properties of nanotubes and composites is introduced.

Key words: Carbon nanotube, Molecular structural mechanics, Nanocomposite, Atomistic modeling, Multiscale modeling, Nanomechanics.

1. INTRODUCTION

It has been theoretically and experimentally confirmed that carbon nanotubes possess exceptional high stiffness and strength. These properties as well as their high aspect ratio and low density suggest that carbon nanotubes may hold promise as reinforcements for nanocomposites [**1**]. The improvements in stiffness and strength due to the addition of carbon nanotubes in polymeric matrix materials have been demonstrated [**2-4**]. For the effective utilization of nanotubes as reinforcements, various attempts have been made in improving their dispersion and alignment in the composites. Polymeric matrix composites with well-dispersed and well-aligned nanotubes are now feasible [**5-9**]. Meanwhile, some efforts have also been devoted to the study of the load transfer between nanotubes and the

T. J. Chuang et al. (eds.), Nanomechanics of Materials and Structures, 55–65.
© 2006 *Springer. Printed in the Netherlands.*

matrix [**3, 4**]. Lordi and Yao [**10**] used force-field-based molecular mechanics to model the interactions between nanotubes and several different kind of polymers. Wise and Hinkley [**11**] used molecular dynamics simulation for addressing the local changes in the interface of a single-walled nanotube surrounded by polyethylene molecules. Odegard et al. [**12**] studied the effect of chemical functionalization on the mechanical properties of nanotube/polymer composites by using an equivalent-continuum modeling technique. However, due to the difficulty in modeling nanotube reinforced composites, studies on the load transfer between the matrix and nanotubes are still very limited.

In this paper, we introduce our multiscale modeling technique for simulating carbon nanotubes and their composites. This multiscale modeling technique is a combination of the atomistic molecular structural mechanics approach [**13**] and the continuum finite element method [**14**].

2. MOLECULAR STRUCTURAL MECHANICS APPROACH

The mechanical and physical properties of carbon nanotubes are highly size/structure dependent, and thus modeling of nanotubes at the atomistic scale is necessary. We developed the molecular structural mechanics approach [**13**] for modeling carbon nanotubes. The main concept of this approach is briefly outlined below.

In the molecular structural mechanics approach, a single-walled carbon nanotube is simulated as a space frame structure, with the covalent bonds and carbon atoms as connecting beams and joint nodes, respectively. If the beam elements simulating the covalent bonds are assumed to be of round section, then only three stiffness parameters, i.e., the tensile resistance *EA*, the flexural rigidity *EI* and the torsional stiffness *GJ*, need to be determined for deformation analysis. Based on the energy equivalence between local potential energies in computational chemistry and elemental strain energies in structural mechanics, a direct relationship between the structural mechanics parameters and the molecular mechanics force field constants can be established [**13**], i.e.,

$$\frac{EA}{L} = k_r, \frac{EI}{L} = k_\theta, \frac{GJ}{L} = k_\tau . \tag{1}$$

where L denotes the bond length, and k_r, k_θ and k_τ are the force field constants in molecular mechanics. The force field constants in our studies

are chosen as $k_r/2 = 469$ kcal mol^{-1} Å^{-2}, $k_\theta/2 = 63$ kcal mol^{-1} rad^{-2}, and $k_\tau/2 = 20$ kcal mol^{-1} rad^{-2}.

For simulations of van der Waals interactions between nested nanotube layers, a truss rod model was introduced [**15**]. This model is based on the Lennard-Jones "6-12" potential and the van der Waals force between two atoms in the nearest neighboring tube layers can be written as

$$F(r) = 24\frac{\varepsilon}{\sigma}\left[2\left(\frac{\sigma}{r}\right)^{13} - \left(\frac{\sigma}{r}\right)^{7}\right] \tag{2}$$

where, r is the interatomic distance, ε and σ are the Lennard-Jones parameters. The activation of a truss rod is determined by the distance between the two atoms in the neighboring tube layers. If the distance is less than 2.5σ, a truss rod is assumed to be activated.

3. STATIC PROPERTIES OF CARBON NANOTUBES

Using the molecular structural mechanics method, we can readily examine the elastic properties of carbon nanotubes. The basic elastic properties considered include axial Young's modulus, radial Young's modulus, circumferential Young's modulus and shear modulus [**13,14,19**]. In the calculations of these elastic moduli, different loading conditions, such as tension, torsion and hydrostatic pressure, are applied. The wall thickness is usually taken as the interlayer separation of graphite, 0.34 nm. The number of atoms involved in the calculations is in the range of 240~3500, depending on the nanotube diameter.

Figures 1 and 2 give examples of simulation results of elastic moduli of carbon nanotubes by using the molecular structural mechanics approach. These results indicate that the elastic moduli of carbon nanotubes are highly dependent on the tube diameter but the effects of tube chirality are relatively small.

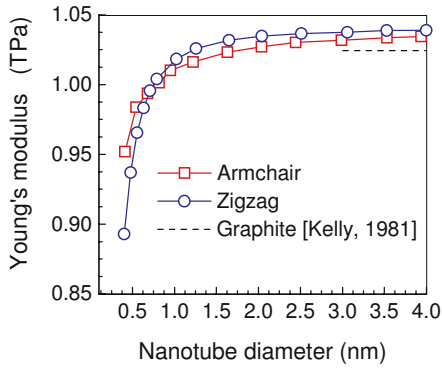

Figure 1 Young's moduli of single-walled carbon nanotubes [13]

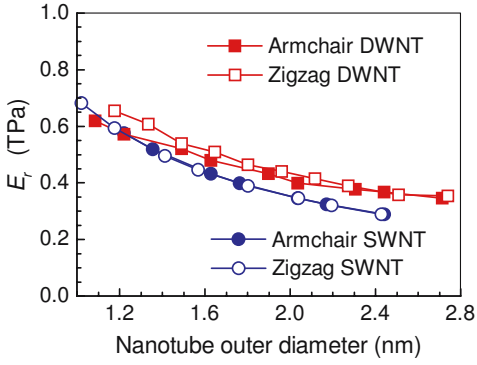

Figure 2 Radial moduli of single- and double-walled carbon nanotubes [14]

4. DYNAMIC PROPERTIES OF CARBON NANOTUBES

Although there are some studies in the literature regarding the use of carbon nanotubes as resonators [**17**] and oscillators [**18**], the vibrational properties of nanotubes are not well understood. There have been no reports on theoretical modeling of the dynamic properties of carbon nanotubes by molecular dynamics. Also, the continuum mechanics approach can not be readily applied for predicting the dynamic properties of carbon nanotubes because of the difficulty in distinguishing nanotube chirality and the uncertainty in defining the nanotube wall-thickness.

We studied dynamic properties of carbon nanotubes by employing the molecular structural mechanics approach [**19, 20**]. For determining the fundamental frequencies and vibrational modes of a carbon nanotube, we

simulate the nested tube layers by equivalent space frame structures and intertube van der Waals interactions by truss rods. According to the theory of structural dynamics, the equation of motion for the free vibration of an undamped structure is

$$[M]\{\ddot{y}\}+[K]\{y\}=\{0\}, \tag{3}$$

where $[M]$ and $[K]$ are, respectively, the global mass and stiffness matrices, and $\{y\}$ and $\{\ddot{y}\}$ are, respectively, the nodal displacement vector and acceleration vector.

The global stiffness matrix $[K]$ is assembled following the same procedure as that in simulating static properties. The global mass matrix $[M]$ can be assembled from the elemental mass matrix. By considering the atomistic feature of a carbon nanotube, the masses of electrons are neglected and the masses of carbon nuclei ($m_c = 1.9943\times10^{-26}$ kilogram) are assumed to be concentrated at the centers of atoms, i.e., the joints of beam members. Due to the extremely small radius ($r_c = 2.75\times10^{-5}$ Å) of the carbon atomic nucleus, the coefficients in the mass matrix corresponding to flexural rotation and torsional rotation, $\frac{2}{3}m_c r_c^{\,2}$, are assumed to be zero. Only the coefficients corresponding to translatory displacements are kept. Thus, the elemental mass matrix $[M]^e$ is given by

$$[M]^e = diag\left[m_c/3 \quad m_c/3 \quad m_c/3 \quad 0 \quad 0 \quad 0\right], \tag{4}$$

The factor 1/3 in the elements of the elemental mass matrix is introduced because the three bonds of a carbon atom connects with the three nearest neighboring atoms and it ensures that the nodal mass has the value of a single atom in the assembled global mass matrix $[M]$.

The orders of the global stiffness matrix and mass matrix are reduced by the static condensation method for more efficient computations. Then, the natural frequencies f and mode shapes are obtained from the solution of the eigenproblem

$$([K]_s-\omega^2[M]_s)\{y_p\}=0, \tag{5}$$

where $[K]_s$, $[M]_s$ are the condensed stiffness matrix and condensed mass matrix, respectively, $\{y_p\}$ is the displacement vector corresponding to the primary coordinates, i.e., the translatory displacements of carbon atoms, and $\omega = 2\pi f$ is the angular frequency.

The fundamental frequencies of carbon nanotubes depend on the tube diameter and length, as well as constraints on the nanotube ends. In our study, two forms of constraints, i.e., cantilevered and bridged, were analyzed [**19**]. The computational results of fundamental frequencies of single-walled carbon nanotubes are displayed in Fig. 3.

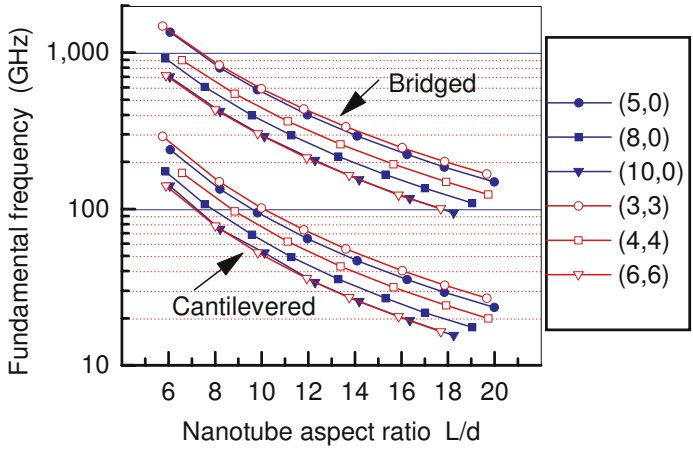

Figure 3 Fundamental frequencies of single-walled carbon nanotubes [19]

It is obvious from Fig. 3 that nanotubes possess very high fundamental frequencies. For nanotubes with diameters of 0.4~0.8 nm and length/diameter ratios of 6~20, the fundamental frequencies are in the ranges of 10~300 GHz and 100~1500 GHz, respectively, for cantilevered and bridged nanotubes. For the same aspect ratio, nanotubes with a smaller diameter have a higher fundamental frequency. Nanotube chirality does not have a significant effect on the fundamental frequency.

Our simulations also indicated that the fundamental frequency of a double-walled carbon nanotube is about 10% lower than that of a single-walled carbon nanotube with the same outer diameter and the same length [**24**]. The vibration modes associated with the fundamental frequencies are almost coaxial, and noncoaxial vibrations are excited at higher frequencies. Our simulations identify that the noncoaxial vibration initiates at the third resonant frequency, which is usually much higher than the first two lowest frequencies.

It can be concluded that the fundamental frequencies of both single-walled and double-walled carbon nanotubes are very high and are in the order of hundreds gigahertzs for the range of nanotube length studied. This level of fundamental frequency is much higher than the highest frequency nanomechanical resonator (~1.029 GHz) so far fabricated from SiC using optical and electron-beam lithography [**21**]. Thus, the high potential of using carbon nanotubes as nanomechanical resonators is unmistakable. Such high frequency mechanical nanodevices would facilitate the development of the fastest scanning probe microscopes, magnetic resonant force microscope and even mechanical supercomputers.

5. MULTISCALE MODELING OF CARBON NANOTUBE/POLYMER COMPOSITES

By combining the molecular structural mechanics approach with the finite element method, we proposed a multiscale modeling method for simulating deformation behavior of carbon nanotube/polymer composites [**22**]. In the method, the nanotube was modeled at the atomistic scale by the molecular structural mechanics method, and the matrix deformation was analyzed at the macroscopic scale by the continuum finite element method.

We have considered nanocomposites reinforced by single-walled carbon nanotubes. Two cylindrical unit cells were chosen as computational models. One is the discontinuous reinforcement model where the nanotube is entirely embedded in the matrix. Another is the continuous reinforcement model, where the length of the nanotube is assumed to be the same as the length of the surrounding polymer matrix. The first model is used for revealing the stress distribution around the interface, while the second is used in computing the effective modulus of nanotube/polymer composites.

Because the nanotube is modeled at the atomistic scale and the polymeric matrix is treated as a continuum, the modeling of the nanotube/polymer interface is rather difficult. We considered two limiting cases in interfacial load transfer capability. The case of low interfacial load transfer is approximated by the van der Waals interface. The case of high interfacial load transfer is simulated by a perfect interface, which may exist in covalently bonded nanotube/matrix interface.

For simulations of van der Waals interactions at the interface, the truss rod model is adopted, which was first developed for simulating the van der Waals forces between neighboring atomic layers of a multi-walled carbon nanotube (Fig.4a). At the nanotube/matrix interface, the activation of a truss rod is determined by the distance between an atom in the nanotube and a node in the finite element. For convenience in computation, we only consider the van der Waals interactions between the nanotube and the surface of the polymeric matrix immediately adjacent to the nanotube. This assumption may tend to underestimate the load transfer capability of the nanotube/polymer interface. For perfectly bonded interface, it is assumed that the outer surface of the nanotube coincides with the inner surface of the polymer matrix. But for matching the atoms in the nanotube and the nodes in the finite elements, the center of an atom in the nanotube is assumed to be located on the outer surface, not in the center of the tube wall (Fig.4b).

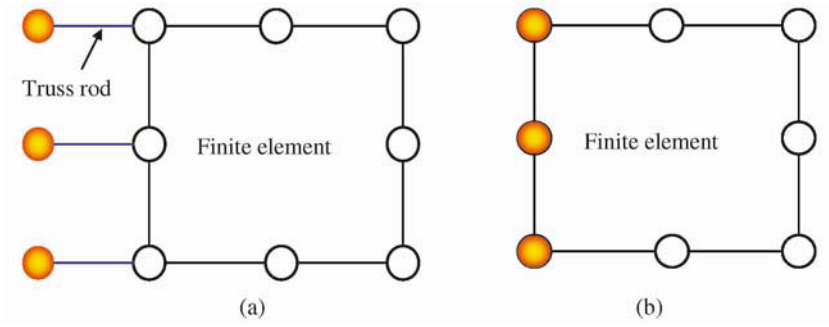

Figure 4 Nanotube/polymer interface treatment
(a) van der Waals interface and (b) perfect interface

The Young's modulus and Poisson's ratio of the polymer matrix are taken as 2.41 GPa and 0.35, respectively, for simulating an epoxy polymer. The nanotube is assumed to be zigzag type. The effective Young's moduli of nanotube/polymer composites are analyzed using the long-tube computational model. The nanotube/polymer interfacial bonding in this case is assumed to be van der Waals interaction. Our computational results indicate that the effective axial Young's modulus of nanotube/polymer composite follows the rule-of-mixtures.

Figure 5 displays the distributions of normalized shear stress in one quarter of the matrix material for perfect interface and van der Waals interface. It is observed that the maximum shear stresses occur at the vicinity of nanotube ends. The shapes of shear stress contours for the perfect interface and van der Waals interface cases are similar, but the maximum normalized shear stress in the former case is roughly twice as much as that of the latter case. Figure 6 shows the axial normal stress distributions in the polymeric matrix under isostrain and isostress loading conditions. It is observed that there are stress concentrations in the vicinity of the nanotube ends in both figures 5 and 6. The nature of stress concentrations in nanotube/polymer composites is similar to that in short fiber composites.

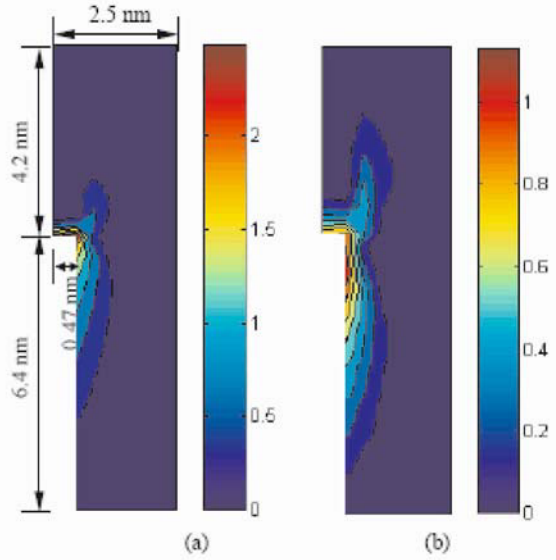

Figure 5 Shear stress distribution in polymer matrix [22]
(a) perfect bonding, isostrain, (b) van der Waals bonding, isostrain

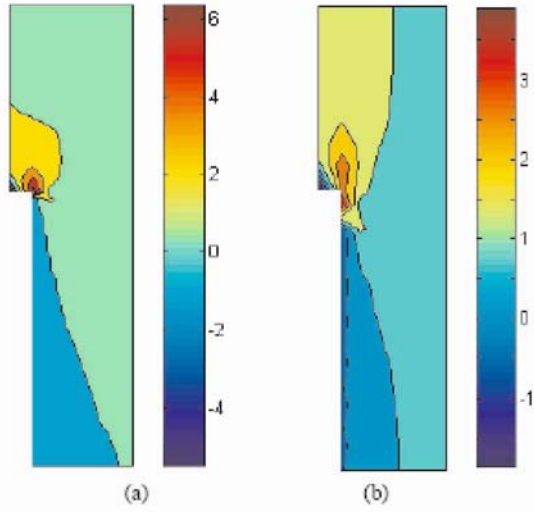

Figure 6 Axial stress distribution in polymer matrix [22]
(a) perfect bonding, isostrain, (b) van der Waals bonding, isostrain

6. THERMAL PROPERTIES OF CARBON NANOTUBES

The molecular structural mechanics approach has been extended to the study of thermal properties of carbon nanotubes. The vibrational modes of the nanotube are quantized according to the theory of quantum mechanics. The partition function is directly expressed by the vibrational frequencies of carbon atoms. Then, based on the theory of statistical thermodynamics, we have calculated the specific heat and the coefficients of thermal expansion of single-walled carbon nanotubes. Our computational predictions are in fair agreement with available experimental as well as theoretical results.

7. CONCLUSIONS

The molecular structural mechanics approach is an effective atomistic modeling technique for simulating carbon nanotubes. It has been used for the studies of static and dynamics properties of single- and multi-walled carbon nanotubes. It also has the potential of simulating thermal properties of carbon nanotubes as well as analyzing other nanomaterials. Its combination with the finite element method provides us with a unified capability of a multiscale modeling of carbon nanotube-reinforced composites.

ACKNOWLEDGMENTS

This work was supported by the National Science Foundation (NIRT Program, Grant No. 0304506) and the Army Research Office (Grant No. DAAD 19-02-1-0264).

REFERENCES

1. Thostenson ET, Ren ZF and Chou T-W, "Advances in the science and technology of carbon nanotubes and their composites: a review", *Comp Sci Tech*, **61**, 1899-1912 (2001)
2. Wagner HD, Lourie O, Feldman Y and Tenne R, "Stress-induced fragmentation of multiwall carbon nanotubes in a polymer matrix", *Appl Phys Lett*, **72**, 188-190 (1998).
3. Schadler LS, Giannaris SC and Ajayan PM, "Load transfer in carbon nanotube epoxy composites", *Appl Phys Lett*, **73**, 3842-3844 (1998).
4. Qian D, Dickey EC and Andrews R et al., "Load transfer and deformation mechanisms in carbon nanotube-polystyrene composites", *Appl Phys Lett*, **76**, 2868-2870 (2000).
5. Cooper CA, Ravich D and Lips D et al., "Distribution and alignment of carbon nanotubes and nanofibrils in a polymer matrix", *Comp Sci Tech*, **62**, 1105-1112 (2002).

6. Jin L, Bower C and Zhou O, "Alignment of carbon nanotubes in a polymer matrix by mechanical stretching", *Appl Phys Lett*, **73**, 1197-1199 (1998).
7. Haggenmueller R, Gommans HH and Rinzler AG et al., "Aligned single-wall carbon nanotubes composites by melt processing methods", *Chem Phys Lett*, **330**, 219-25 (2000).
8. Thostenson, ET, and Chou T-W, "Aligned Multi-Walled Carbon Nanotube-Reinforced Composites: Processing and Mechanical Characterization," *J. Phys. D: Appl Phys,* **35** (16), L77-L80 (2002).
9. Thostenson ET and Chou T-W, "On the Elastic Properties of Carbon Nanotube-Based Composites: Modeling and Characterization," *J Phys D: Appl Phys,* **36**, 573-582 (2003).
10. Lordi V and Yao N, "Molecular mechanics of binding in carbonnanotube-polymer composites", *Journal of Materials Research*, **15**, 2770–2779 (2000).
11. Wise K and Hinkley J, "Molecular Dynamics Simulations of Nanotube-Polymer Composites", *American Physical Society Spring Meeting*, Apr 12-16, 2001. Seattle, WA.
12. Odegard GM, Frankland SJV and Gates TS, "The effect of chemical functionaliz-ation on mechanical properties of nanotube/polymer composites", *44th AIAA Structure, Structures Dynamics, and materials Conference*, 2003-1701.
13. Li CY and Chou T-W, "A structural mechanics approach for the analysis of carbon nanotubes", *Int. J. Solids and Structures*, **40**, 2487-2499 (2002).
14. Zienkiewicz OC, *Finite Element Method*, 3rd edition. London: McGraw-Hill Book Co. Ltd., 1977.
15. Li CY and Chou T-W, "Elastic moduli of multi-walled carbon nanotubes and the effect of van der Waals forces", *Comp Sci Tech,* **63**, 1517-1524 (2003).
16. Li CY and Chou T-W, "Elastic properties of single-walled carbon nanotubes in transverse directions", *Physics Review B,* **69**, 073401/1-4 (2004).
17. Hunt BD et al., Nanotube Actuators and Oscillators, Interim Report, JPL Task 960 (2000).
18. Zheng Q and Jiang Q, "Carbon nanotubes as oscillators", *Phys Rev Lett.* **88**, 045503/1-3. (2002).
19. Li CY and Chou T-W, "Single-walled carbon nanotubes as ultrahigh frequency nanomechanical resonators", *Physics Review B,* **68**, 073405/1-4 (2003).
20. Li CY and Chou T-W, "Vibrational behaviors of multi-walled carbon nanotube-based nanomechancial resonators", *Appl Phys Lett*, **84**, 121-123 (2004).
21. Huang XMH, Zorman CA, Mehregany M and Roukes ML, "Nanodevice motion at microwave frequencies", *Nature(London)*, **421**, 496 (2003).
22. Li CY and Chou T-W, "Multiscale modeling of the interfacial load transfer in carbon nanotube/polymer composites", *J Nanosci Nanotech*, **3**, 423-430 (2004).

ON THE TENSILE STRENGTH OF A SOLID NANOWIRE

Tze-jer Chuang
National Institute of Standards and Technology, Gaithersburg, MD 20899 U.S.A.
Phone: (301)975-5773, fax: (301)975-5334, email: Chuang@nist.gov

Abstract: The present paper is concerned with the mechanical characterization of the measured tensile strength of a solid nanowire. As miniaturization is a general trend in nanotechnology, a variety of nanowires have been successfully fabricated/synthesized, including but not limited to Si, C, polymer DNA, MoSe, Au, Cu, TiC, Fe, Mo , NiAl and W. Mechanical strength is essential to maintaining the structural integrity in the multi-functional performance of those nanowires. A simple derivation in mechanics principle, without relying on tedious *ab initio* molecular dynamics calculations, is given which shows that the measured tensile strength contains two terms: the material's intrinsic bond breaking strength and the surface stress (or surface tension) contribution. It further shows that as the size of the nanowire diminishes, the surface stress effect is enhanced, such that a simple functional relationship can be established in the nanscale regime: $\sigma \alpha 1/D$ where σ is strength and D is the diameter of the nanowire. Generally speaking, depending on the ratio of surface stress to the intrinsic strength, the apparent tensile strength can be enhanced up to one order of magnitude in the nanometer size range. In addition to the mechanical strength, the surface tension plays a role in: tension/compression asymmetry; helical shapes of a nanobelt if surface stress is anisotropic; reduced melting point; stress-induced phase transformation under free external loading conditions. These phenomena will be discussed as direct evidence of the existence of the surface stress.

Key words: Mechanical strength; Nanowires; Size effect; Surface stress; Tension/compression asymmetry.

T. J. Chuang et al. (eds.), Nanomechanics of Materials and Structures, 67–78.
© 2006 *Springer. Printed in the Netherlands.*

1. INTRODUCTION

The present paper is concerned with the tensile strength of a solid nanowire. Nanowires and other one-dimensional systems (e.g., nanotubes) have recently been the focus of considerable research interest because they have great potential in a variety of applications like molecular electronics, diagnostic biosensors, and novel scanning microscopy probes [**1-3**]. A broad range of multicomponent nanowires has been successfully synthesized via chemical routes such as laser-assisted catalytic growth [**4**].The mechanical strength of the nanowires plays an important role in maintaining the structural integrity of the structures, devices or systems made from the nanowires even when they are primarily designed for performing other non-structural functions (such as electronic, photonic, magnetic, biological etc.).

Theoretically, the ideal strength of a solid nanowire can be investigated by using *ab initio* electronic structure methods based on the density functional theory [**5**]. Both un-relaxed and relaxed dimensions were considered in the calculations. However, this approach has a drawback in that it is material specific and tedious; thus, its complexity must rely on adequate computational power being available. It is therefore desirable to develop an alternative simple approach that does not rely on computers. The main objective of the current paper is to present a simple means to characterize the mechanical strength of a solid nanowire.

It is well-known that when the dimensions of a solid are comparable to atomic sizes, such that the surface to bulk ratio is enhanced, the contributions of the surface effects to the overall properties can no longer be neglected. Consequently, in evaluation of the mechanical strength of a solid nanowire, the role of surface stress must be taken into consideration. Hence, prior to the main derivations, we discuss briefly the origin of the surface stress in Section 2 from the standpoint of physics, thermodynamics and mechanics where we draw the distinction between surface energy/forces and surface stress/tension. With the knowledge of surface stress discussed in Section 2, we present a simple derivation in Section 3 on the measured tensile strength as a function of nanowire diameter, using simple mechanics principles. We find, as expected, that higher strengths are predicted with smaller sizes of nanowire for a given material and geometry. A functional relationship between the strength and the size is firmly established. In addition to the size effect on the mechanical strength, other interesting implications which are unique only in the nanometer size range are discussed including asymmetry in tension/compression behavior, and phase transformation under free standing conditions. These issues will be addressed in Section 4.

2. THE ROLE OF SURFACE STRESS

It is known that surface stresses exist at free surfaces of both solid and liquid phases. From a physical viewpoint, atoms outside the bulk are removed to form the surface. As a result, atoms on and near the surface must re-adjust from a non-relaxed to relaxed configuration. Surface stresses are then generated in order to maintain the relaxed configuration in equilibrium. From the standpoint of thermodynamics, surface free energy γ (unit in J• m^{-2}) is required to create a unit area of new free surface. Thus, γ is sensitive to atomic bonding forces or surface forces *normal* to the surface and adhesion forces. On the other hand, the surface stress tensor, $\tau_{\alpha\beta}$ (α,β=1,2) is related to deforming or stretching an element area of existing surface, dA. Its direction is in-plane or *parallel* to the surface tangent. To derive the relationship between γ and $\tau_{\alpha\beta}$ consider the energy balance before, (γdA), and after deformation, (γdA) + δ(γdA). We have $\delta(\gamma dA) = (\tau_{\alpha\beta} \bullet \delta\varepsilon_{\alpha\beta}) dA$, where the repeated index denotes summation. Now, since $\delta(\gamma\, dA) = \delta\gamma\, dA + \gamma\, \delta dA$, and $\delta dA = \delta_{\alpha\beta}\, \delta\varepsilon_{\alpha\beta}\, dA$, where $\delta_{\alpha\beta}$ is the Kronecker delta tensor, we obtain the well-known Shuttleworth equation [**6**]:

$$\tau_{\alpha\beta} = \gamma \bullet \delta_{\alpha\beta} + \frac{\partial \gamma}{\partial\, \varepsilon_{\alpha\beta}} \tag{1}$$

This equation illustrates that in the case of a fluid, surface stress state must be in hydrostatic tension and no shear stresses are allowed, because $\partial\gamma/\partial\varepsilon_{\alpha\beta}$=0. This can be explained in physical terms, namely, deforming an existing liquid surface versus creating a new surface will yield the same atomic state on the surface, because the underneath atoms can move freely to fill-up the surface "hole" when the surface is stretching to expand, resulting in the identical surface state or surface density. Thus, γ, which is the only parameter characterizing the surface state, is totally independent of the surface strains, i.e., $\partial\gamma/\partial\varepsilon_{\alpha\beta}$ = 0. Moreover, the magnitude of the surface tension (unit in force per unit length) is identical in numerical value to the surface free energy γ (unit in energy per unit area). In the case of a general solid, on the other hand, the situations are more complicated. The surface stress state in a solid, in general, consists of *in-plane* normal as well as *in-plane* shear stress components. Furthermore, the normal stress component can either be in tension (positive sign) or even in compression (negative sign). Also, the second term can dominate, and its magnitude can be up to three times as high as the first term. A literature survey indicates that γ is on the order of 1 J/m^2, whereas $\tau_{\alpha\beta}$ can vary from 1 N/m to 10 N/m depending on material and crystal orientation [**7-9**]. Other important consequences as derived from the virtual work principles in surface mechanics include [**10**]:

$$\tau_{\alpha\beta}\,\kappa_{\alpha\beta} = n_i\,\sigma_{ij}\,n_j \tag{2}$$

$$T_\beta = m_\alpha\,\tau_{\alpha\beta} \tag{3}$$

where T_β is the in-plane traction vector, m_α denotes the in-plane outward normal vector to the edge of the surface element, σ_{ij} denotes the bulk stress tensor (i,j=1,2,3), n_i is the out-of-plane normal vector to the surface, and $\kappa_{\alpha\beta}$ is the surface curvature tensor. Equation (3) in particular is quite useful in the derivation of the strength enhancement to be addressed in the following section.

3. EFFECT OF SURFACE STRESS ON THE STRENGTH OF A NANOWIRE

Consider an element of a straight solid nanowire with a cross-section area A, a total length L of the periphery enclosing A, which is subjected to a remote mechanical loading P loaded along the axial direction such that the apparent stress is P/A (Figure 1).

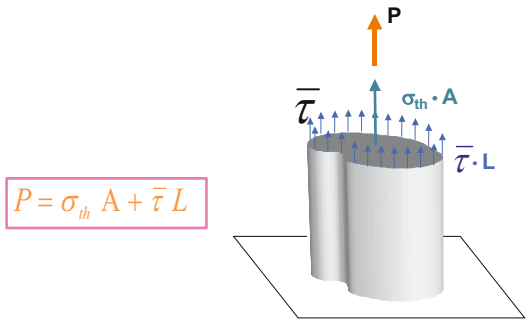

Figure 1. Free body diagram of a solid nanowire loaded by a remote force P. Here, A is cross-sectional area, L is periphery length, σ_{th} is bulk strength, and $\bar{\tau} \equiv \langle\tau\rangle$ is the averaged surface force per unit length.

When the load increases to its peak value where the nanowire breaks, P/A represents the measured tensile strength. In addition to the external load P

applied to the wire, the body also is subjected to the surface stresses applied around the periphery L in an amount in the axial direction:

$$\oint T_n(s,\theta)\, ds = \int_0^{2\pi} \int_0^L m_\alpha\, \tau_{\alpha\beta}\, m_\beta\, ds\, d\theta$$

where T_n is the magnitude of the traction vector in the axial direction, $T_n = m_\alpha\, \tau_{\alpha\beta}\, m_\beta$, θ is the orientation, defined as a polar angle, and ds is the element of arc length along the periphery of the cross-section. In deriving the above expression, Equation (3) has been used. The equilibrium conditions on the nanowire then demand that the external load must be equal to the sum of the surface force term plus the bulk term given by the bulk stresses in the interior of the nanowire (see Figure 1), namely,

$$P = \sigma_{th} \bullet A + \oint T_n(s,\theta)\, ds = \sigma_{th} \bullet A + \int_0^{2\pi} \int_0^L m_\alpha\, \tau_{\alpha\beta}\, m_\beta\, ds\, d\theta$$

where σ_{th} is the theoretical strength or bond breaking force of the bulk. We will have some more to say about this term in the Section 4. For the sake of discussion, we will further assume that the cross-section is a principal plane so that there are no shear stresses present along the periphery L. (Note: If shear stresses exist, bending moment will arise leading to a crooked rod as discussed in Section 4.). In this case, $T_z(s, \theta) = \tau_{zz}(s, \theta) = \tau(s, \theta)$, and we have: $P = \sigma_{th} \bullet A + \oint \tau(s,\theta)\, ds$ or

$$\frac{P/A}{\sigma_{th}} = 1 + \eta \left[\frac{<\tau>}{\sigma_{th}} \right] D^{-1} \qquad (4)$$

where $<\tau>$ is the averaged surface forces per unit length around L, $<\tau> \cdot L = \oint \tau\, ds$, and the shape factor $\eta = \lambda D$, where $\lambda = L/A$, D is the nanowire's characteristic size or diameter. In case of a non-circular rod, D is defined as the length of a straight edge. Note that η is a dimensionless scalar; that cannot be zero. Table 1 lists the values of a number of shape factor η for various cross-sectional shapes.

The left-hand side of Equation (4) is the normalized *measured* strength against the bulk strength, signifying the strength enhancement factor. If $<\tau> = 0$, then this factor equals unity and $P/A = \sigma_{th}$, so that there is no strength enhancement. To assess the relative strength enhancement, we plot, in Figure

2, Equation (4) on a graph of ($P/A/\sigma_{th}$) versus D for two typical cases: square cross-section and triangular cross-section, assuming $<\tau> = 1$ N/m and $\sigma_{th} = 1$ GPa. It can be seen from Figure 2 that since η for the triangular case is higher than the square case, the strength enhancement for the triangular cross-section is predicted to be higher than the square cross-section. For example, for a nanowire of diameter 5 nm, the square nanowire's strength is enhanced to 2 GPa, whereas the triangular nanowire is to 2.5 GPa, assuming the material's intrinsic strength is 1 GPa.

Table 1. η-shape factors for a variety of shapes of nanowire cross-sections.

Cross-Section	L/D	A/D^2	$\eta = (\lambda \cdot D)$
	3.0	0.433	6.93
	4.0	1.0	4.0
	5.0	1.72	2.9
	n	$\frac{n}{4}\cot\left(\frac{\pi}{n}\right)$	$4\tan\left(\frac{\pi}{n}\right)$
	π	π/4	4.0
	$\frac{\pi}{\sqrt{2}}\left(1+\gamma^{-2}\right)^{1/2}$	$\frac{\pi}{4\gamma}$	$2\sqrt{2\left(1+\gamma^2\right)}$

Note: (1) γ = aspect ratio (a/b) ≥ 1
(2) η = Shape Factor

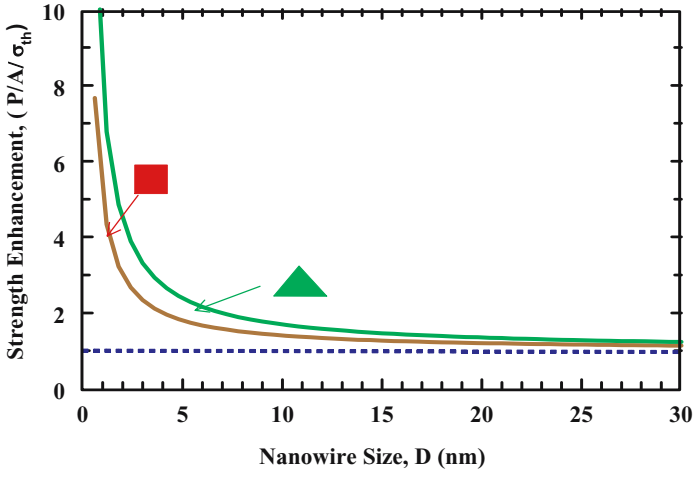

Figure 2. Plots of strength enhancement as a function of D for square and triangular rod with $\tau/\sigma_{th} = 1$ nm. It is seen that for a given D, the triangular cross-section is predicted to have higher strength.

As discussed earlier, the magnitude of surface stress in a solid can be different from its surface free energy in value. Further, they can vary from one crystal orientation to the other. Also, the sign could be positive in tension or negative in compression. The values of surface stress of a given solid can be as high as three times the value of its surface free energy [**7,9**]. Take pure gold as an example, the surface energy on the plane {110} is 0.95 J/m^2; but the surface stress in the ‹001› direction is 2.85 N/m, and 1.60 N/m in the ‹110› direction [**11**]. In general, the values of surface free energy of crystalline materials can vary from 0.5 to 3.0 J/m^2 , whereas the surface stress can vary from 1 to 10 N/m [**7-9**]. The typical bulk strength of metals or metal alloys is about 0.5 GPa to 1.0 GPa, whereas it is from 1 GPa to 10 GPa for ceramics and glasses. A more detailed discussion of the bulk strength will be addressed later. Thus, the ratio of the surface stress to the intrinsic bulk strength for most material is in the range from 0.1 nm to 20 nm. Figure 3 plots the normalized strength of a square rod as a function of D for three different ratios of $<\tau>/\sigma_{th}$ = 0.1 nm, 1 nm and 10 nm from Equation (4). It is shown that the strength increases with decreasing sizes proportional to the inverse of D. Of course, high surface stress yields higher measured strength. Since most materials possess values of $<\tau>/\sigma_{th}$ between 1 nm and 10 nm, it is predicted that noticeable strength enhancements will be realized for nanowires whose size is less than 30 nm in diameter

After obtaining the theoretical predictions for the size dependence of the tensile strength, it would be desirable to make a sensible comparison

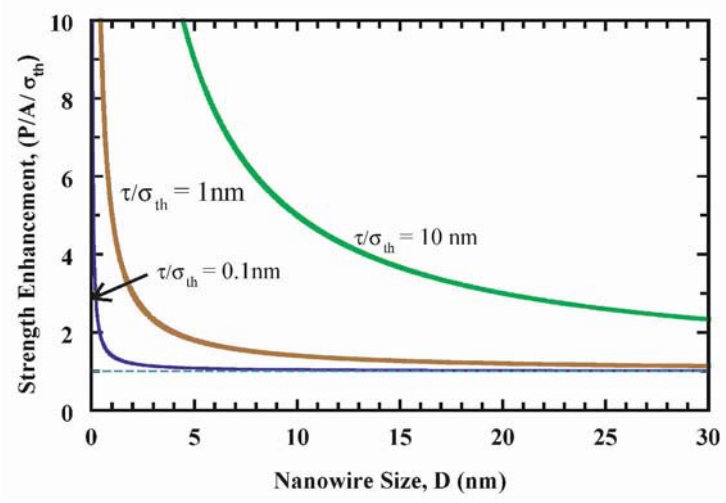

Figure 3. Plots of strength enhancement factor as a function of nanowire size in square cross-section for a trio of τ/σ_{th} = 0.1 nm, 1 nm and 10 nm. For a material with τ/σ_{th} = 10 nm, the strength can increase 10 times when the size D reduces to 5 nm in diameter. Nanowire sizes for most materials fall between 1nm and 10 nm.

between the current work and existing experimental data. Unfortunately, to the best knowledge of the author, no direct size-dependent strength data are yet available, although nanowire specimens with differing diameters have been successfully synthesized. Existing data are available, however, which indirectly infer a size-dependent strength from nanohardness measurements by nanoindentions on multi-layer thin films of metal alloys [**11**]. Figure 4 shows thickness dependent strength data, interpreted as measured hardness divided by 3, for three metal alloys in the range of layer thickness from 1 nm to 100 nm. It is seen that as the size of the layer thickness decreases, the strength does increase, in particular within the range between 1 nm to 50 nm, in qualitative agreement with the theoretical predictions. According to Figure 4, the critical size separation seems to be located at 50 nm. Above 50 nm the conventional models will apply, whereas below this level new concepts in nanomechanics are needed. These preliminary results only indicate that the general trend is consistent with the present simplistic theoretical predictions. A more rigorous empirical validation must await future experimental results carried out by direct uniaxial tensile loading of a well- prepared batch of nanowire specimens with systematically varying sizes.

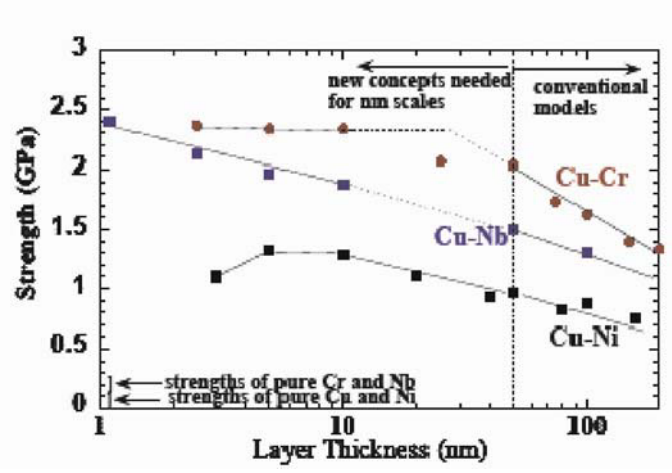

Figure 4. Strength (estimated as hardness divided by 3) vs. the layer thickness of three Cu-based multilayers. Note that significant increase in strength is observed as compared to strength of pure metals (estimated at 10 μm grain size to be 0.5 GPa). After Ref. [**11**].

4. DISCUSSION

We have presented a simplistic theory of the enhanced strength of a solid nanowire in the nanometer size scale range that does not use complicated *ab initio* atomic simulations. Based on the fact that typical values of surface stresses are in the range of 1 N/m to 10 N/m, and the materials bulk atomic bond-breaking strengths are on the order of 0.2 GPa to 10 GPa, The theory predicts that the nanowire strength can be as high as 10 times its bulk strength, depending on its cross-sectional geometry as well as materials properties such as crystal orientation, and ratio of surface stress to intrinsic strength. It should be noted that the bulk strength in the nano size range may already be higher than that in micrometer size or macro size scale. In conventional theory, the bulk strength is normally controlled by the size and density of defects such as cracks or dislocation core size. As the dimensions of the solid are reduced, the size and density of the defects must also be reduced, resulting in the enhanced bulk strength. More discussions on the bulk strength can be found in the literature such as Ref. [**12**].

In fact, property enhancement at the nanoscale is not limited to the mechanical strength. It is well known, for example, that the melting point is different in nano crystallites or nano particles as compared to the macroscopic size of the same material. Gold nano particles or clusters are observed to have their melting point reduced from 1000 °C to 800 °C when the particle size is reduced to 10 nm [**13-14**]. This is because the presence of the surface stress on the external surface exerts an internal pressure inside the interior of the particle according to Equation (2). Based on thermodynamic principles, the enhanced pressure leads to reduced melting temperature [**13-14**].

Another interesting phenomenon caused by the surface stress is the phase transformation induced in a solid nanowire under free external loading conditions. Figure 5 is the picture of a free standing Au nanowire showing the evolution of the phase transformation at (0.5, 10, 20, 30, 40 and 46) ps. [**15**]. It is seen that under the action of the surface stress as a driving force, the molecule dynamic simulations on the 1.83 nm x 1.83 nm wire at 100 K show that the phase transformation from face-centered-cubic (f.c.c) lattice to body-centered-tetragonal (b.c.t) lattice starts at the ends and propagates toward the center at a speed of 347 m/s. Examination of the free body of the nanowire shows that, since there is no external applied load, the only loading comes from the surface stresses. The bulk interior of the wire must then withstand *compressive* stresses in order to fulfill the equilibrium conditions. The magnitude of the residual compression in the bulk is high enough (estimated at about 1.6 GPa [**15**]) to trigger phase transformation. If the wire

length is long enough, this compression can also buckle the nanowire to form a crooked shape.

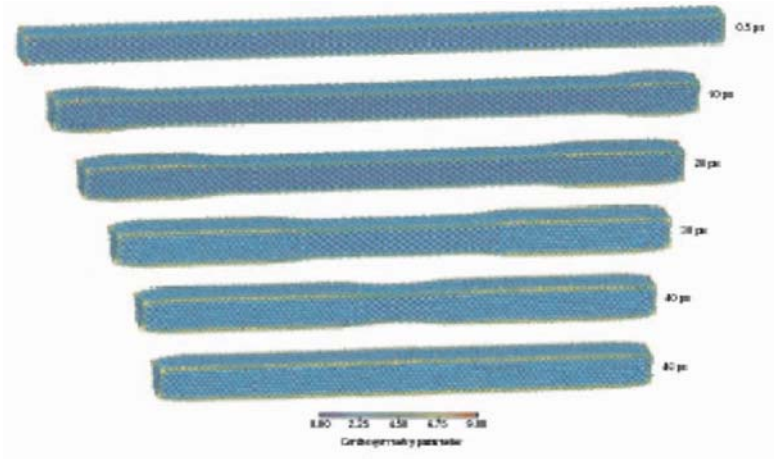

Figure 5. The dynamic progression of the phase transformation in a 1.83 nm x 1.83 nm nanowire at 100 K. Frames shown are configurations of the wire at (0.5, 10, 20, 30, 40 and 46) ps. (Courtesy K. Gall [15])

Further evidence for the existence of surface stress is the helical shape, similar to that of a telephone cord, demonstrated by nanobelts. Figure 6 shows SEM photos of as-synthesized ZnO nanobelts [**16**]. The authors suggested that the resulting helical shapes were due to the effect of surface electric charges. However, surface stresses on both surfaces of the nanobelt may play a role. Cahn and Hanneman [**17**] investigated surface tension effects on thin crystals. They concluded that if the surface stresses are unequal between the top and bottom surfaces, spontaneous bending will occur, leading to a curved shape. Similar conclusion may apply to the case of a nanobelt: if the surface stress tensor is anisotropic such that top and bottom surfaces possess unequal values of the surface stress, a bending moment will be established which leads to a helical shape.

Finally, it is worth mentioning that the presence of the surface stress in a solid nanowire will result in an asymmetry of the tensile/compressive strength. For the sake of discussion, let us suppose that the surface stress is tensile (positive sign), and the conventional tensile strength is identical to compressive strength in value, although the signs are different. In this case, as discussed earlier, under free external loading, the bulk is pre-stressed in

compression. Accordingly, the tensile strength must be the bulk strength plus this pre-stressed amount. On the other hand, the compressive strength will be the bulk strength less the pre-stressed amount. Therefore, the magnitude of the tensile strength will be twice of this pre-stressed amount *more than* the compressive strength, leading to the asymmetry of tensile/compressive strength. By the same token, it can be shown that compressive surface stress will also lead to asymmetry of tensile/compressive strength.

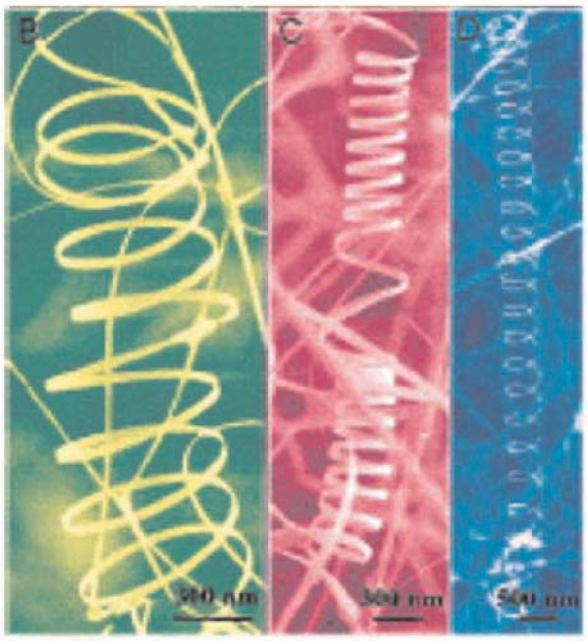

Figure 6. SEM images of as-synthesized ZnO nanobelts, showing helical nanostructure. The typical width of the nanobelt is about 30 nm, and the pitch distance is quite uniform. (Courtesy Z.L. Wang [16])

ACKNOWLEDGMENTS

We wish to thank Dr. Xiao-lei Wang of NIST for his help in preparing the sketch in Figure 1, Professor Ken Gall of the University of Colorado for the images of phase transformation of gold nanowire in Figure 5, and Professor Zhong Lin Wang of Georgia Institute of Technology for the nanobelt photos in Figure 6.

REFERENCES

1. Lieber CM "One-dimensional Nanostructures: Chemistry, Physics and Applications", *Solid State Commun*. **Vol. 107**, pp.607-616, 1998
2. Dekker C "Carbon Nanotubes as Molecular Quantum Wires", *Physics Today*, **Vol. 52**, [5] pp. 22-28, 1999.
3. Snoke D "Coherent Exciton Waves", *Science*, **Vol. 273**, pp. 1351-1352, 1996.
4. Duan X, Lieber CM "General Synthesis of Compound Semiconductor Nanowires", *Advanced Materials*, **Vol. 12** [4] pp. 298-302, 2000.
5. Friak M, Sob M, Vitek, V, "*Ab initio* study of the ideal strength and mechanical stability of transition metal disilicides", *Physical Review B*, **Vol. 68**, pp. 184101-1, 10, 2003.
6. Shuttleworth R., "The Surface Tension of Solids", *Proc. Phys. Soc*., **Vol. A63**, pp. 444-457, 1950.
7. Cammarata RC, Sieradzki K, "Surface and Interface Stresses", *Annu. Rev. Mater. Sci*., **Vol. 24**, pp. 215-234, 1994.
8. Ibach H, "The role of surface stress in reconstruction, epitaxial growth and stabilization of mesoscopic structures", *Surface Science Reports*, **Vol. 29**, pp. 193-263, 1997.
9. Cammarata RC, "Surface and interface stress effects in thin films", *Progress in Surface Science,* **Vol. 46**, pp. 1-38, 1994.
10. Rice JR, Chuang, T-J., "Energy Variations in Diffusive Cavity Growth*", J. Am. Ceram. Soc.* **Vol. 64** [1] pp.46-53, 1981.
11. Kung H, Misra A, Hoagland JD, Embury JD, Hirth JP, "Nano-Mechanics at LANL-Research currently supported by a new DOE-BES initiative", http://www.lanl.gov/mst/nano/docs/nanomechanics.pdf, 2004.
12. Gao H, Ji B, Jäger IL, Arzt E, Fratzl P, "Materials become insensitive to flaws at nanoscale: Lessons from nature", PNAS, **Vol. 100**, pp. 5597-5600, May 13, 2003.
13. Buffat Ph., Borel J-P, "Size effect on the melting temperature of gold particles", Physical Review A, **Vol. 13**, No.6, pp. 2287-2298, 1976.
14. Castro T, Reifenberger R, Choi E, Andres RP, "Size-dependent melting temperature of individual nanometer-sized metallic clusters", Physical Review B, **Vol. 42**, No. 13, pp. 8548-8556, 1990.
15. Diao J, Gall K, Dunn M, "Surface stress induced phase transformation in metal nanowires", *Nature*, Materials Advanced Online Publication, pp. 1-5, September, 2003
16. Kong XY, Wang ZL, "Spontaneous Polarization-induced nanohelixes, nanosprings and nanorings of piezoelectric nanobelts", *Nano Letters*, **Vol. 3**, No. 12, pp. 1625-1631, 2003.
17. Cahn JW, Hanneman RE, "(111) Surface tensions of III-V compounds and their relationship to spontaneous bending of thin crystals", *Surface Science*, **Vol. 1**, pp. 387-398, 1964.

FRACTURE NUCLEATION IN SINGLE-WALL CARBON NANOTUBES:

The Effect of Nanotube Chirality

H. Jiang[1], Y. Huang[1] , P. Zhang[2], K. C. Hwang[3]

[1]Department of Mechanical and Industrial Engineering, University of Illinois, Urbana, IL 61801, [2.]Department of Mechanical Engineering, University of Connecticut, Storrs,CT 06269,[3]Department of Engineering Mechanics, Tsinghua University, Beijing 100084, China, Email: huang9@uiuc.edu,Phone: (217) 265-5072, Fax: (217) 244-6534.

Abstract: We develop an atomistic-based continuum theory for carbon nanotubes by incorporating the interatomic potential directly into the continuum analysis through the constitutive model. The theory accounts for the effect of carbon nanotube chirality, and is applied to study fracture nucleation in carbon nanotubes by modeling it as a bifurcation problem. The results agree well with the molecular dynamics simulations.

Key words: Carbon nanotube, continuum analysis, interatomic potential, fracture nucleation, nanotube radius.

1. INTRODUCTION

There has been extensive research on carbon nanotubes (CNTs) since their first discovery [1] because of their superior materials properties [2-5]. Atomistic studies, such as molecular dynamics, have been used extensively to study the CNT properties. Molecular dynamics, however, is limited on both the length scale (~1μm) and time scale (~10^{-9} s). The purpose of the present study is to establish a continuum theory of CNTs based on the interatomic potential for carbon [6] in order to overcome these limits. We apply this atomistic-based continuum theory to study the effect of carbon nanotube chirality on fracture nucleation in CNTs.

T. J. Chuang et al. (eds.), Nanomechanics of Materials and Structures, 79–88.
© 2006 *Springer. Printed in the Netherlands.*

2. A CONTINUUM THEORY

2.1 The Interatomic Potential for Carbon

Brenner [6] suggested a multi-body interatomic potential for a carbon bond as

$$V(r_{ij}) = V_R(r_{ij}) - B_{ij}V_A(r_{ij}), \tag{1}$$

where i and j denote the two carbon atoms of the bond, r_{ij} is the bond length; V_R and V_A are the repulsive and attractive interactions pair terms, B_{ij} is a multi-body coupling term which results from the interaction between atoms i, j and their local environment. The detailed expressions of V_R, V_A and B_{ij} can be can be found in Brenner's [6] paper.

2.2 Single-Wall Carbon Nanotube Prior to Deformation

Jiang et al. [7] developed a method to take into accout the effect of CNT chirality in the continuum analysis. Such a method is briefly summarized here. Figure 1a shows a schematic diagram of a CNT with the diameter d_t.

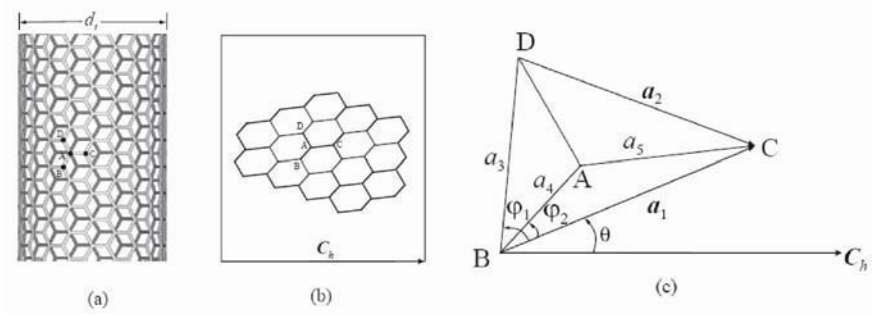

Figure 1. A carbon nanotube (CNT) prior to deformation. (a) a CNT; (b) a planar, "unrolled" CNT; (c) a representative atom (A) and its three nearest-neighbor atoms (B, C, and D).

Unlike a planar graphene sheet, a carbon atom and its three nearest-neighbor atoms on the CNT are not on a plane but form a tetrahedron because of the curvature effect. Since a CNT can be considered as a rolled graphene sheet, we map the CNT shown in Fig. 1a to a two-dimensional, planar sheet shown in Fig. 1b. The distance between each pair of carbon atoms in the "unrolled"

plane (Fig. 1b) is identical to the corresponding arc length on the CNT (Fig. 1a). It is important to point out that Fig. 1b is different from a graphene sheet since the bond lengths may not equal and the bond angles deviate from 120°.

Figure 1c shows a representative atom *A* in the "unrolled" plane along with its three nearest-neighbor atoms *B*, *C*, and *D*. These four atoms *A*, *B*, *C*, and *D* characterize the positions of all atoms on the planar sheet in Fig. 1b since all atoms essentially result from the in-plane translation of these four atoms due to periodicity in the atomic structure of the CNT. Therefore, the lengths and angles between these four atoms completely characterize the planar structure in Fig. 1b. Let $\boldsymbol{a}_1$ and $\boldsymbol{a}_2$ denote the vectors $\overrightarrow{BC}$ and $\overrightarrow{DC}$ in Fig. 1c, respectively, and a_1 and a_2 be the corresponding lengths. The length of *BD* is denoted by a_3, and the lengths of *AB* and *AC* are denoted by a_4 and a_5, respectively (Fig. 1c). With these five lengths $a_i\left(i=1,2,\cdots,5\right)$, all other lengths and angles in the "unrolled" plane can be completely determined.

In order to characterize the cylindrical structure of the CNT shown in Fig. 1a, it is necessary to prescribe the CNT diameter d_t and helicity together with these five lengthes $a_i\left(i=1,2,\cdots,5\right)$. The CNT diameter d_t and angle θ (Fig. 1) are related to the chirality $\left(n,m\right)$ of the CNT. Following the standard notation for CNTs, the chiral vector $\boldsymbol{C}_h$, whose length equals the circumference of the CNT, can always be expressed in terms of the base vectors $\boldsymbol{a}_1$ and $\boldsymbol{a}_2$ as (Fig. 1c) $\boldsymbol{C}_h = n\boldsymbol{a}_1 + m\boldsymbol{a}_2$, where *n* and *m* are integers, $n \geq |m| \geq 0$, and the pair $\left(n,m\right)$ is called the chirality of the CNT; $\left(n,0\right)$ and $\left(n,n\right)$ are called the zigzag and armchair CNTs, respectively. It can be found that the CNT diameter d_t and angle θ as well as the spatial coordinates of atoms *A*, *B*, *C*, and *D* can all be given in terms of these five lengths $a_i\left(i=1,2,\cdots,5\right)$. With these five lengths, the configuration of single-wall CNTs prior to deformation can be completerly characterized.

Once all bond lengths and angles are known (in terms of these five lengths $a_i\left(i=1,2,\cdots,5\right)$), the energy stored in a bond can be obtained from the interatomic potential for carbon (1). The energy associated with the representative atom *A* is $1/2\cdot\left(V_{AB}+V_{AC}+V_{AD}\right)$, which also depends on these five lengths $a_i\left(i=1,2,\cdots,5\right)$, where the factor $1/2$ results from the equal partition of the bond energy between the pair of atoms in each bond, V_{AB}, V_{AC} and V_{AD} are the energies stored in bonds *AB*, *AC*, and *AD*, respectively. These five lengths $a_i\left(i=1,2,\cdots,5\right)$ are determined by minimizing the energy in the representative atom *A*, i.e., $\partial\left[V_{AB}+V_{AC}+V_{AD}\right]/\partial a_i = 0, i=1,2,\cdots,5.$

2.3 Deformed Single-Wall Carbon Nanotubes

The continuum deformation measures of deformed CNTs can be related to the motion of many atoms via the Cauchy-Born rule [8], which equates the strain energy at the continuum level to the energy stored in atomic bonds. It also states that the atoms subject to a homogeneous deformation move according to a single mapping from the undeformed to deformed configurations. From the continuum level, this mapping is the deformation gradient $\boldsymbol{F} = \partial \boldsymbol{x} / \partial \boldsymbol{X}$, where $\boldsymbol{X}$ and $\boldsymbol{x}$ denote the positions of a material point in the undeformed and deformed configurations, respectively. A bond between a pair of atoms i and j in the undeformed configuration is described by a vector $\boldsymbol{r}_{ij}^{(0)} = r_{ij}^{(0)} \boldsymbol{n}_{ij}^{(0)}$, where $r_{ij}^{(0)}$ is the bond length and $\boldsymbol{n}_{ij}^{(0)}$ is unit vector of the bond direction. Upon deformation, the bond is described by

$$\boldsymbol{r}_{ij} = \boldsymbol{F} \cdot \boldsymbol{r}_{ij}^{(0)}. \tag{2}$$

Its length becomes $r_{ij} = \sqrt{\boldsymbol{r}_{ij} \cdot \boldsymbol{r}_{ij}} = r_{ij}^{(0)} \sqrt{1 + 2\boldsymbol{n}_{ij}^{(0)} \cdot \boldsymbol{E} \cdot \boldsymbol{n}_{ij}^{(0)}}$, where $\boldsymbol{E} = \frac{1}{2}\left(\boldsymbol{F}^T \cdot \boldsymbol{F} - \boldsymbol{I}\right)$ is the Green strain tensor and $\boldsymbol{I}$ is the second-order identity tensor. For a centrosymmetric lattice structure that has pair of bonds in the opposite directions ($\boldsymbol{r}$ and -$\boldsymbol{r}$) around each atom, the Cauchy-Born rule ensures the equilibrium of atoms because forces in the opposite, centrosymmetric bonds are always equal and opposite for arbitrarily imposed homogeneous deformation.

For CNTs, however, the Cauchy-Born rule cannot be applied because CNTs do not have a centrosymmetric lattice structure. Zhang et al. [9] modified the Cauchy-Born rule in order to ensure the equilibrium of atoms. Their method is extended in the following to account for the effect of CNT chirality. Figure 2 shows the plane "unrolled" from a deformed CNT. The hexagonal lattice can be decomposed into two triangular sub-lattices, marked by open circles and solid circles, respectively. Both the open-circle, and the solid-circle triangular sub-lattices in Fig. 2 possess centrosymmetry such that

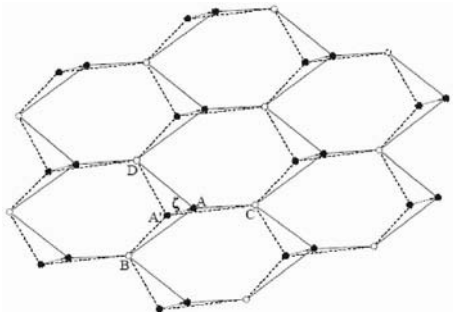

Figure 2. The decomposition of a hexagonal lattice, "unrolled" from a deformed carbon nanotube, to two triangular sub-lattices. There is a shift vector $\boldsymbol{\zeta}$ between two sub-lattices to ensure the equilibrium of atoms.

the atoms in these sub-lattices follow the Cauchy-Born rule. However, the solid-circle sub-lattice may undergo a shift with respect to the open-circle sub-lattice in order to ensure the equilibrium of atoms. This shift vector $\boldsymbol{\zeta}$ affects the lengths between atoms from two sub-lattices. For example, the vector $\boldsymbol{r}_{AB}$ in Fig. 2 is the sum of $\boldsymbol{F}\cdot\boldsymbol{r}_{AB}^{(0)}$ (Cauchy-Born rule) and the shift vector $\boldsymbol{\zeta}$,

$$\boldsymbol{r}_{AB}=\boldsymbol{F}\cdot\boldsymbol{r}_{AB}^{(0)}+\boldsymbol{\zeta}=\boldsymbol{F}\cdot\left(\boldsymbol{r}_{AB}^{(0)}+\boldsymbol{\xi}\right), \tag{3}$$

where we write $\boldsymbol{\zeta}=\boldsymbol{F}\cdot\boldsymbol{\xi}$, and $\boldsymbol{\xi}$ is an internal degree of freedom to be determined by the equilibrium of atoms. The length $\boldsymbol{r}_{AB}$ is then given by $r_{AB}=\sqrt{\mathbf{r}_{AB}\cdot\mathbf{r}_{AB}}=\sqrt{\left(\mathbf{r}_{AB}^{(0)}+\boldsymbol{\xi}\right)\cdot\left(\mathbf{I}+2\mathbf{E}\right)\cdot\left(\boldsymbol{r}_{AB}^{(0)}+\boldsymbol{\xi}\right)}$. Similar to Section 2.2, the bond lengths in the cylindrical configuration of a deformed CNT can also be obtained in terms of $\boldsymbol{E}$ and $\boldsymbol{\xi}$.

2.4 Strain Energy Density

Once the bond lengths and angles are known for the cylindrical configuration of the deformed CNT, the energy stored in each bond can be obtained from Brenner's [6] multi-body interatomic potential. The energy for each representative atom A (Fig. 2) is given by $\frac{1}{2}\left[V\left(r_{AB}\right)+V\left(r_{AC}\right)+V\left(r_{AD}\right)\right]$. The strain energy density W on the continuum level is the energy per unit area of the CNT surface, and is related to the interatomic potential by

$$W\left(\boldsymbol{E},\boldsymbol{\xi}\right)=\frac{V\left(r_{AB}\right)+V\left(r_{AC}\right)+V\left(r_{AD}\right)}{2\Omega_{\varepsilon}}, \tag{4}$$

where Ω_{ε} is the undeformed CNT surface area per atom.

The equilibrium of atoms is equivalent to the state of minimal energy. The internal degree of freedom $\boldsymbol{\xi}$ is determined by minimizing the strain energy density $W\left(\boldsymbol{E},\boldsymbol{\xi}\right)$ with respect to $\boldsymbol{\xi}$, i.e.,

$$\frac{\partial W}{\partial\boldsymbol{\xi}}=0. \tag{5}$$

This gives $\boldsymbol{\xi}$ in terms of the Green strain $\boldsymbol{E}$, i.e., $\boldsymbol{\xi}=\boldsymbol{\xi}\left(\boldsymbol{E}\right)$. The strain energy density is then written as $W=W\left[\boldsymbol{E},\boldsymbol{\xi}\left(\boldsymbol{E}\right)\right]$.

2.5 Stress and Incremental Modulus

The second Piola-Kirchhoff stress $\boldsymbol{T}$ is the work conjugate of the Green strain $\boldsymbol{E}$, and $\boldsymbol{T}$ is obtained from the derivative of the strain energy density W with respect to $\boldsymbol{E}$,

$$\boldsymbol{T} = \frac{dW}{d\boldsymbol{E}} = \frac{\partial W}{\partial \boldsymbol{E}} + \frac{\partial W}{\partial \xi} \cdot \frac{\partial \xi}{\partial \boldsymbol{E}} = \frac{\partial W}{\partial \boldsymbol{E}}. \tag{6}$$

The incremental modulus tensor $\boldsymbol{C}$ is obtained by taking the total derivative of the second Piola-Kirchhoff stress $\boldsymbol{T}$ with respect to $\boldsymbol{E}$ as

$$\boldsymbol{C} = \frac{d\boldsymbol{T}}{d\boldsymbol{E}} = \frac{\partial^2 W}{\partial \boldsymbol{E} \partial \boldsymbol{E}} - \frac{\partial^2 W}{\partial \boldsymbol{E} \partial \xi} \cdot \left(\frac{\partial^2 W}{\partial \xi \partial \xi} \right)^{-1} \cdot \frac{\partial^2 W}{\partial \xi \partial \boldsymbol{E}}. \tag{7}$$

2.6 Equilibrium Equations for Single-Wall Carbon Nanotubes

The equilibrium equation for a single-wall CNT has been established by Zhang et al. [9], and is given by

$$\begin{aligned}
&\frac{1}{R}\frac{\partial}{\partial \theta}(\boldsymbol{F}\cdot\boldsymbol{T})_{R\theta} - \frac{1}{R}(\boldsymbol{F}\cdot\boldsymbol{T})_{\theta\theta} + \frac{\partial}{\partial Z}(\boldsymbol{F}\cdot\boldsymbol{T})_{RZ} = 0,\\
&\frac{1}{R}(\boldsymbol{F}\cdot\boldsymbol{T})_{R\theta} + \frac{1}{R}\frac{\partial}{\partial \theta}(\boldsymbol{F}\cdot\boldsymbol{T})_{\theta\theta} + \frac{\partial}{\partial Z}(\boldsymbol{F}\cdot\boldsymbol{T})_{\theta Z} = 0,\\
&\frac{1}{R}\frac{\partial}{\partial \theta}(\boldsymbol{F}\cdot\boldsymbol{T})_{Z\theta} + \frac{\partial}{\partial Z}(\boldsymbol{F}\cdot\boldsymbol{T})_{ZZ} = 0,
\end{aligned} \tag{8}$$

where (R,θ,Z) denotes the cylindrical coordinates in the undeformed configuration.

3. FRACTURE NUCLEATION IN SINGLE-WALL CARBON NANOTUBES

Zhang et al. [10] studied fracture nucleation in single-wall CNTs. We follow the same approach but focus on the effect of CNT chirality on the fracture nucleation strains. Since the CNT undergoes uniform deformation prior to the first bond breaking in Yakobson et al.'s [11] MD simulations, and nonuniform deformation only steps in after the bond breaking, fracture nucleation in CNTs under tension is modeled as a bifurcation [10].

The deformation in armchair and zigzag CNTs under tension is uniform and axisymmetric prior to bifurcation, and is characterized by the non-vanishing components $F_{\theta\theta}$ and F_{ZZ} of the deformation gradient. The non-zero components of the Green strain are $E_{\theta\theta}$ and E_{ZZ}. The internal degree of freedom $\boldsymbol{\xi} = \boldsymbol{\xi}(E_{\theta\theta}, E_{ZZ})$ and the second Piola-Kirchhoff stress $\boldsymbol{T}$ are determined from Eqs. (5) and (6), respectively. We impose $T_{\theta\theta} = 0$ for uniaxial tension, which gives an implicit equation to determine $E_{\theta\theta}$ in terms of E_{ZZ}. The non-zero components of the incremental modulus $C_{\theta\theta\theta\theta}$, C_{ZZZZ}, $C_{\theta\theta ZZ} = C_{ZZ\theta\theta}$ are obtained from Eq. (7)

Let $\boldsymbol{U}$ denote the displacement, which is related to the deformation gradient $\boldsymbol{F}$ by $\boldsymbol{F} = \boldsymbol{I} + \boldsymbol{U}\boldsymbol{\nabla}$. At the onset of bifurcation, the increment of deformation is not uniform anymore. The non-uniform increment of deformation gradient $\dot{\boldsymbol{F}}$, Green strain increment $\dot{\boldsymbol{E}}$, and stress increment $\dot{\boldsymbol{T}}$ can be expressed with respect to the displacement increment $\dot{\boldsymbol{U}}$. Then the incremental form of the equilibrium equation can be written as (Zhang et al. [10])

$$
\begin{aligned}
&\left(T_{ZZ}\frac{\partial^2}{\partial Z^2} - \frac{1}{R^2}C_{\theta\theta\theta\theta}F_{\theta\theta}^2\right)\dot{U}_R - \frac{1}{R^2}C_{\theta\theta\theta\theta}F_{\theta\theta}^2\frac{\partial \dot{U}_\theta}{\partial\theta} - \frac{1}{R}C_{\theta\theta ZZ}F_{\theta\theta}F_{ZZ}\frac{\partial \dot{U}_Z}{\partial Z} = 0,\\
&\frac{1}{R^2}C_{\theta\theta\theta\theta}F_{\theta\theta}^2\frac{\partial \dot{U}_R}{\partial\theta} + \left[\frac{1}{R^2}C_{\theta\theta\theta\theta}F_{\theta\theta}^2\frac{\partial^2}{\partial\theta^2} + \left(T_{ZZ} + C_{\theta Z\theta Z}F_{\theta\theta}^2\right)\frac{\partial^2}{\partial Z^2}\right]\dot{U}_\theta + \frac{1}{R}(C_{\theta\theta ZZ} + C_{\theta Z\theta Z})F_{\theta\theta}F_{ZZ}\frac{\partial^2 \dot{U}_Z}{\partial\theta\partial Z} = 0,\\
&\frac{1}{R}C_{\theta\theta ZZ}F_{\theta\theta}F_{ZZ}\frac{\partial \dot{U}_R}{\partial Z} + \frac{1}{R}(C_{\theta\theta ZZ} + C_{\theta Z\theta Z})F_{\theta\theta}F_{ZZ}\frac{\partial^2 \dot{U}_\theta}{\partial\theta\partial Z} + \left[\frac{1}{R^2}C_{\theta Z\theta Z}F_{ZZ}^2\frac{\partial^2}{\partial\theta^2} + \left(T_{ZZ} + C_{ZZZZ}F_{ZZ}^2\right)\frac{\partial^2}{\partial Z^2}\right]\dot{U}_Z = 0.
\end{aligned}
\tag{9}
$$

The CNT is subjected to the axial displacement and vanishing shear stress tractions at the ends. Therefore, at the onset of bifurcation, the increments of the axial displacement and shear stress tractions vanish at both ends, which gives the incremental boundary conditions as

$$
\dot{U}_Z = \frac{\partial \dot{U}_R}{\partial Z} = \frac{\partial \dot{U}_\theta}{\partial Z} = 0 \text{ at } Z = 0 \text{ and } Z = L, \tag{10}
$$

where L is the length of the CNT.

The homogeneous governing equations (9) and boundary conditions (10) constitute an Eigenvalue problem for the displacement increment $\dot{\boldsymbol{U}}$. The Eigenvalue is the axial strain E_{ZZ}. In other words, Eqs. (9) and (10) have only the trivial solution $\dot{\boldsymbol{U}} = 0$ until the axial strain E_{ZZ} reaches a critical value $(E_{ZZ})_{critical}$ for bifurcation.

We first study the axisymmetric bifurcation, $\dot{U}_R = \dot{U}_R(Z)$, $\dot{U}_\theta = 0$, and $\dot{U}_Z = \dot{U}_Z(Z)$. The solution, satisfying the equilibrium equations (9) and homogeneous boundary condition (10), takes the form

$$\left[\dot{U}_R, \dot{U}_Z\right] = \left[\dot{U}_{Rm}^{(0)} \cos\frac{m\pi Z}{L}, \dot{U}_{Zm}^{(0)} \sin\frac{m\pi Z}{L}\right], \tag{11}$$

where $m = 1,2,3,\ldots$ is the Eigen mode number, $\left[\dot{U}_{Rm}^{(0)}, \dot{U}_{Zm}^{(0)}\right]$ is the corresponding eigenvector, and the superscript (0) denotes the axisymmetric bifurcation. This gives two homogeneous, linear algebraic equations for $\dot{U}_{Rm}^{(0)}$ and $\dot{U}_{Zm}^{(0)}$. The critical condition for bifurcation is then given by

$$f^{(0)} \equiv C_{\theta\theta\theta\theta}\left(C_{ZZZZ} + \frac{T_{ZZ}}{F_{ZZ}^2}\right) - C_{\theta\theta ZZ}^2 + \frac{T_{ZZ}}{F_{\theta\theta}^2}\left(C_{ZZZZ} + \frac{T_{ZZ}}{F_{ZZ}^2}\right)\left(\frac{m\pi R}{L}\right)^2 = 0. \tag{12}$$

The corresponding axial strain at bifurcation is denoted by $(E_{ZZ})_{critical}$.

For non-axisymmetric bifurcation, the displacement increment takes the form

$$\left[\dot{U}_R, \dot{U}_\theta, \dot{U}_Z\right] = \left[\dot{U}_R^{(n)}(Z)\cos n\theta, \dot{U}_\theta^{(n)}(Z)\sin n\theta, \dot{U}_Z^{(n)}(Z)\cos n\theta\right], \tag{13}$$

where $n = 1,2,3,\ldots$ is the wave number in the circumferential direction, $\dot{U}_R^{(n)}$, $\dot{U}_\theta^{(n)}$, and $\dot{U}_Z^{(n)}$ are functions of Z to be determined. The general solution of $\dot{U}_R^{(n)}$, $\dot{U}_\theta^{(n)}$, and $\dot{U}_Z^{(n)}$, satisfying the homogeneous boundary condition (10), takes the form

$$\left[\dot{U}_R^{(n)}, \dot{U}_\theta^{(n)}, \dot{U}_Z^{(n)}\right] = \left[\dot{U}_{Rm}^{(n)} \cos\frac{m\pi Z}{L}, \dot{U}_{\theta m}^{(n)} \cos\frac{m\pi Z}{L}, \dot{U}_{Zm}^{(n)} \sin\frac{m\pi Z}{L}\right], \tag{14}$$

where $m = 1,2,3,\ldots$ is the Eigen mode number in the axial direction, and $\left[\dot{U}_{Rm}^{(n)}, \dot{U}_{\theta m}^{(n)}, \dot{U}_{Zm}^{(n)}\right]$ is the corresponding eigenvector. The bifurcation condition is obtained as

$$f^{(n)} \equiv f^{(0)} + \frac{n^2 T_{ZZ}}{T_{ZZ} + C_{\theta Z\theta Z} F_{\theta\theta}^2}\left[C_{\theta\theta\theta\theta}\left(C_{ZZZZ} + \frac{T_{ZZ}}{F_{ZZ}^2}\right) - \left(C_{\theta\theta\theta\theta} + C_{\theta Z\theta Z}\right)^2 + C_{\theta Z\theta Z}\left(C_{\theta Z\theta Z} + \frac{T_{ZZ}}{F_{\theta\theta}^2}\right) + \left(n^2+1\right)C_{\theta\theta\theta\theta}C_{\theta Z\theta Z}\left(\frac{L}{m\pi R}\right)^2\right] = 0, \tag{15}$$

where $f^{(0)}$ is the function in (12) defined for axisymmetric bifurcation $n = 0$. The critical bifurcation strain $(E_{ZZ})_{critical}$ at the onset of bifurcation is determined from (15).

3.1 Bifurcation strain

The bifurcation strain is the minimal value of $(E_{ZZ})_{critical}$ among all wave numbers $n = 0,1,2,\ldots$. Table 1 shows the bifurcation strain for several armchair [(*n*,*n*)] and zigzag [(*n*,0)] CNTs. The length of CNTs is $L = 10nm$, while the diameter ranges from 0.7 to 4 *nm*. For armchair CNTs, the bifurcation strain is a constant 0.42, and is independent of CNT diameter. For zigzag CNTs, the bifurcation strain is not a constant anymore, but its variation is small (from 0.35 to 0.37). These bifurcation strains are all within the range of the breaking strains reported by Yakobson et al.'s [11] MD simulations for the same tube aspect ratio. Therefore, the bifurcation strain has essentially no dependence on the CNT diameter, and has a rather weak dependence on the CNT chirality.

Table 1. Bifurcation strain for armchair and zigzag carbon nanotubes under tension. The nanotube length is 10nm.

Armchair Carbon Nanotubes			Zigzag Carbon Nanotubes		
(*n*,*n*)	Diameter (nm)	$(E_{ZZ})_{critical}$	(*n*,0)	Diameter (nm)	$(E_{ZZ})_{critical}$
(5,5)	0.698	0.42	(9,0)	0.729	0.35
(10,10)	1.39	0.42	(18,0)	1.44	0.36
(20,20)	2.77	0.42	(36,0)	2.88	0.37
(30,30)	4.16	0.42	(50,0)	4.00	0.37

4. CONCLUDING REMARKS

We have proposed an atomistic-based continuum theory for carbon nanotubes (CNTs) from the interatomic potential. We have applied this theory to model fracture nucleation in single-wall CNTs under tension as a bifurcation problem. It is shown that the bifurcation strain has essentially no

dependence on the CNT diameter, and has a rather weak dependence on the CNT chirality. The results agree reasonably well with MD simulations without any parameter fitting.

ACKNOWLEDGMENTS

Y.H. acknowledges the support from NSF (CMS 0099909, CMS 0103257, CMS-0324643, and the Nano CEMMS Center DMI-0328162), Office of Naval Research (grant N00014-01-1-0205, Program Manager Dr. Y. D. S. Rajapakse), Alexander von Humboldt Foundation, and NSFC. K.C.H. acknowledges the support form NSFC.

REFERENCES

1. Iijima S. "Helical Microtubules of graphite carbon", *Nature*, **vol. 354**, pp. 56-58, 1991.
2. Srivastava D, Menon M, Cho KJ. "Computational Nanotechnology with Carbon Nanotubes and Fullerenes", *Computing in Science and Engineering*, **vol. 3**, pp. 42-55, 2001.
3. Qian D, Wagner GJ, Liu WK, Yu MF, Ruoff RS. "Mechanics of Carbon Nanotubes", *Applied Mechanics Review*, 2002.
4. Wong EW, Sheehan PE, Lieber CM. "Nanobeam Mechanics: Elasticity, Strength, and Toughness of Nanorods and Nanotubes", *Science*, **vol. 277**, pp. 1971-1975, 1997.
5. Yu MF, Lourie O, Dyer MJ, Moloni K, Kelly TF, Ruoff RS. "Strength and Breaking Mechanism of Multiwalled Carbon Nanotubes Under Tensile Load", *Science*, **vol. 287**, pp. 637-640, 2000.
6. Brenner DW. "Empirical Potential for Hydrocarbons for Use in Simulating the Chemical Vapor Deposition of Diamond Films", *Physical Review B*, **vol. 42**, pp. 9458-9471, 1990.
7. Jiang H, Zhang P, Liu B, Huang Y, Geubelle PH, Gao H, Hwang KC. "The Effect of Nanotube Radius on the Constitutive Model for Carbon Nanotubes", *Computational Materials Science*, **vol. 28**, pp. 429-442, 2003.
8. Born M, Huang K. "*Dynamical theory of the crystal lattices*", Oxford, Oxford University Press, 1954.
9. Zhang P, Huang Y, Geubelle PH, Klein PA, Hwang KC. "The Elastic Modulus of Single-Wall Carbon Nanotubes: A Continuum Analysis Incorporating Interatomic Potentials", *International Journal of Solids and Structures*, **vol. 39**, pp. 3893-3906, 2002.
10. Zhang P, Jiang H, Huang Y, Geubelle PH, Hwang KC. "An atomistic-based continuum theory for carbon nanotubes: analysis of fracture nucleation", *Journal of the Mechanics and Physics of Solids*, **vol. 52**, pp. 977-998, 2004.
11. Yakobson BI, Campbell MP, Brabec CJ, ernholc J. "High Strain Rate Fracture and *C*-Chain Unraveling in Carbon Nanotubes", *Computational Materials Science*, **vol. 8**, pp. 341-348, 1997.

MULTISCALE MODELING OF A GERMANIUM QUANTUM DOT IN SILICON[1]

V.K. Tewary and D.T. Read
National Institute of Standards and Technology, Boulder, CO 80305, USA
Phone:303-545-4415; Fax: 303-545-4413; Email: tewary@boulder.nist.gov

Abstract: A method is described for multiscale modeling of a quantum dot in a semiconductor solid containing a free surface. The method is based upon the use of lattice-statics and continuum Green's functions integrated with classical molecular dynamics. It fully accounts for the nonlinear discrete lattice effects inside and close to the quantum dot, discrete lattice structure of the host solid near the quantum dot and reduces asymptotically to the macroscopic continuum model near the free surface. Our method can model a large crystallite containing, for example, a million atoms without excessive CPU effort and it connects nanoscales seamlessly to macroscales. The method relates the physical processes such as lattice distortion at the atomistic level to measurable macroscopic parameters such as strains at a free surface in the solid. The method is applied to calculate the lattice distortion around a Ge quantum dot in Si. Preliminary numerical results are reported.

Key words: germanium in silicon; lattice Green's functions; molecular dynamics; multiscale modeling; quantum dots.

1. INTRODUCTION

Quantum dots in semiconductors have potential applications in powerful new devices such as a new generation of high output lasers, huge memories, and quantum computers. Currently there is a strong interest in elastic

[1] Contribution of National Institute of Standards & Technology, an agency of the US Government. Not subject to copyright in the USA.

T. J. Chuang et al. (eds.), Nanomechanics of Materials and Structures, 89–98.
© 2006 *Springer. Printed in the Netherlands.*

properties of quantum dots because the growth of quantum dots and their arrays are largely determined by the elastic strains [**1**] of the quantum dots. Free surfaces in the host solids play a relatively large role in nanostructures as compared to their role in ordinary solids. It is therefore necessary that a mathematical model for quantum dots accounts for the presence of free surfaces as well as the discrete atomistic configuration of the quantum dots. The atomistic structure of a solid needs to be modeled at sub nanometer scale whereas the surfaces can be modeled at the macroscopic scale.

We have developed a multiscale model that uses discrete-lattice theory to model the atomistic arrangements inside and around a quantum dot and continuum theory to model a free surface in the host solid in an integrated formalism. The quantum dot and its interfaces with the host solid are modeled by using the discrete-lattice theory and molecular dynamics. The near-field region of the host solid where nonlinear effects are negligible is modeled using lattice statics Green's function. Finally the free surface in the solid, assumed to be far away from the quantum dot, is modeled using the continuum theory by exploiting the property that the lattice statics Green's function reduces asymptotically to the continuum Greens function. Thus, our model bridges the length scales from sub-nano (inside the nanostructure) to nano scales (around the nanostructure) to macro scales near the free surface of the host solid by using the correspondence between the continuum and the lattice Green's functions. The model directly relates the lattice distortion to the measurable continuum parameters and will be referred to as the integrated Green's function molecular dynamics (GFMD) model.

Our GFMD model is generally applicable to nanomaterials but our main interest is in quantum dots and nanoislands. In particular, we consider homopolar semiconductors Ge and Si. This paper gives a brief review of our work on multiscale modeling of quantum nanostructures at NIST. More details will be published elsewhere.

2. INTEGRATED GREEN'S FUNCTION MOLECULAR DYNAMICS (GFMD) METHOD FOR MULTISCALE MODELING

Many papers have been published separately on lattice theory (see, for example, [**2,3**]) as well as continuum theory of defects [**4**]. For a review and other references, see [**5**]. The existing work on multiscale modeling of nanostructures is based upon purely numerical techniques using the finite-element method or molecular dynamics using computer simulation of the lattice structure (see, for example, [**6-8**], for a review and other references, see [**9**]). These techniques are accurate but CPU intensive. They require

massive computations for modeling a crystallite of a reasonable size for computer simulation and a fine enough mesh for the finite-element method. Hence they are not very convenient for quick parametric-design studies.

A semi-analytical method for calculating lattice distortions at the atomistic scale is the lattice statics Green's function (LSGF) method [**2,3**]. The advantage of the LSGF method is that it is computationally efficient. It can model a large crystallite without excessive CPU requirements. For example, calculation of LSGF in a million-atom model requires only a few seconds of CPU time on a 3 GHz desktop computer. One major limitation of the LSGF method is that it cannot be applied to the core of the strong defects or structural defects. This is because the LSGF method depends upon the use of the harmonic approximation and can not model large atomic displacements and their rearrangements in a lattice. These effects can be included in standard molecular dynamics (MD). This type of MD has been developed over the last 40 years, and has provided many original insights into the behavior of conventional solid materials.

The problem with MD is that it tries to simulate the whole crystallite on a computer. Unless special techniques [**6**] are used, it is limited to small crystallites (usually a few hundred to a few thousand atoms) due to CPU constraints. This is a serious limitation because too small a crystallite can introduce spurious size effects which will overshadow the genuine size effects associated with the nanostructures.

In an earlier paper, we presented [**10**] a multiscale Green's function (MSGF) method that integrates the LSGF method with the continuum model in the macroscopic limit and applied it to model point defects and extended defects in metals. The MSGF is based upon the well known fact [2,10] that the LSGF for a perfect lattice reduces asymptotically to the continuum Green's function (CGF). However, when the lattice has defects, its response is given by the defect-lattice Green's function that is a solution of the Dyson equation and does not reduce exactly to the CGF. In the MSGF method, we write the response of the defect lattice as a product of the perfect-lattice Green's function and an effective force called the Kanzaki force. The Kanzaki forces contain all the discrete-lattice effects and are localized near the defect. This relation is exact within the standard assumptions of the Green's-function method. We then use the asymptotic relationship between the perfect LSGF and the CGF to model the extended defects while retaining the atomistic effects exactly in the effective-force term.

In our new GFMD model the MSGF method is integrated with MD in the core of a nanostructure at the sub-nano scale. This integration makes our model truly multiscale by seamlessly linking length scales ranging from sub-nano to macro. By incorporating MD, our model accounts for the non-linear effects in the core of the nanostructure and provides a fast algorithm for

modeling a large crystallite. We are presently developing a billion-atom model crystallite containing a quantum nanostructure which would require less than about 60 minutes of CPU time on a standard desktop computer.

2.1 Theory

We consider a monatomic Bravais lattice with a quantum dot with its center at the origin. We assume a Cartesian frame of reference. We denote the lattice sites by vector indices **l, l'** etc. A vector index **l** has 3 components, denoted by l_1, l_2, and l_3. The three-dimensional (3D) force-constant matrix between atoms at **l** and **l'** is denoted by $\boldsymbol{\phi}^*(\mathbf{l}, \mathbf{l'})$. The force on atom **l** and its displacement from equilibrium position will be denoted, respectively, by **F**(**l**) and **u**(**l**), which are 3D column vectors. The displacement vectors **u**(**l**) at each lattice site give the relaxation of the lattice or the lattice distortion caused by the defect.

The force-constant matrix for each pair of atoms is 3×3. It is obtained from the potential energy of the lattice as follows:

$$[\boldsymbol{\phi}^*(\mathbf{l}, \mathbf{l'})]_{ij} = \partial^2 W / \partial x(\mathbf{l})_i \, \partial x(\mathbf{l'})_j, \tag{1}$$

where W is the potential energy of all atoms in the lattice, and **x**(**l**) is the radius vector of the atom **l**. Similarly, the force at the atom **l** due to the atom at the origin at a distance **x** is given by

$$[\mathbf{F}(\mathbf{l})]_i = -\partial W / \partial x(\mathbf{l})_i. \tag{2}$$

The derivatives in Eqns. (1) and (2) are evaluated at the equilibrium lattice sites of the corresponding perfect lattice. Following the method given in [2,3], we obtain

$$\mathbf{u}(\mathbf{l}) = \Sigma \; \mathbf{G}^*(\mathbf{l}, \mathbf{l'}) \, \mathbf{F}(\mathbf{l'}), \tag{3}$$

where **G*** is the defect lattice Green's function defined by

$$\mathbf{G}^* = [\boldsymbol{\phi}^*]^{-1}. \tag{4}$$

The sum in Eqn. (3) is over all lattice sites and Cartesian coordinates, which have not been shown explicitly for notational brevity.

In the representation of lattice sites, $\mathbf{G}^*$ and $\boldsymbol{\phi}^*$ are $3N \times 3N$ matrices, where N is the total number of lattice sites in the Born-von Karman supercell. For an infinite perfect lattice in equilibrium without defects, **F**(**l**) is 0 for all **l** and the force constant and the Green's function matrices have

translation symmetry. We denote these matrices by $\boldsymbol{\phi}$ and **G** respectively. When a defect is introduced in the lattice, **F(l)** becomes, in general, non-zero and the force constant matrix changes. So

$$\boldsymbol{\phi}^* = \boldsymbol{\phi} - \Delta\boldsymbol{\phi}, \tag{5}$$

where $\Delta\boldsymbol{\phi}$ denotes the local change in the force constant matrix $\boldsymbol{\phi}$. From eqs. (4) and (5), we obtain the following Dyson equation

$$\mathbf{G}^* = \mathbf{G} + \mathbf{G}\,\Delta\boldsymbol{\phi}\,\mathbf{G}^*, \tag{6}$$

where

$$\mathbf{G} = [\boldsymbol{\phi}]^{-1} \tag{7}$$

is the perfect lattice Green's function. In the same representation, we can write Eqn.(3) in the following matrix notation:

$$\mathbf{u} = \mathbf{G}^*\,\mathbf{F}. \tag{8}$$

Using Eqn.(6), we rewrite Eqn.(8) as

$$\mathbf{u} = \mathbf{G}\,\mathbf{F}^*, \tag{9}$$

where

$$\mathbf{F}^* = \mathbf{F} + \Delta\boldsymbol{\phi}\,\mathbf{u}. \tag{10}$$

Equation (9) gives the displacement in terms of the perfect-lattice Green's function and an effective force denoted by **F*,** the so called Kanzaki force [2]. From Eqn.(10), we can identify it as the force due to the defect on relaxed lattice sites, in contrast to **F,** which denotes the force at the unrelaxed original lattice site. Equation (9) is applicable to any point defect such as a vacancy, an interstitial, a substitutional impurity, or an aggregate of defects such as a quantum dot.

For the perfect lattice, **G(l,l')** has translation symmetry and therefore can be labeled by a single index **l-l'**. It is calculated by use of the Fourier representation

$$\mathbf{G}(\mathbf{l}) = (1/N)\,\Sigma_{\mathbf{q}}\,\mathbf{G}(\mathbf{q})\,\exp[\,\iota\mathbf{q}.\mathbf{x}(\mathbf{l})], \tag{11}$$

where $\iota = \sqrt{-1}$, N is the total number of atoms,

$$\mathbf{G}(\mathbf{q}) = [\boldsymbol{\phi}(\mathbf{q})]^{-1}, \tag{12}$$

$\boldsymbol{\phi}(\mathbf{q})$ is the Fourier transform of the force-constant matrix, and $\mathbf{q}$ is a vector in the reciprocal space of the lattice. For brevity of notation, we shall use the same symbol for a function and its Fourier transform, the distinguishing feature being the argument of the function. Since $\mathbf{G}(\mathbf{q})$ and $\boldsymbol{\phi}(\mathbf{q})$ are 3×3 matrices, Eqns. (11) and (12) can be used to calculate the perfect-lattice Green's function $\mathbf{G(l,l')}$.

We define the defect space as the vector space generated by $\mathbf{l,l'}$ for which $\Delta\boldsymbol{\phi}$ is non-vanishing. We solve the Dyson equation for the defect Green's function by using the matrix partitioning technique [2]. The reduced Dyson equation in defect space is given by

$$\mathbf{g}^* = \mathbf{g} + \mathbf{g}\,\Delta\boldsymbol{\phi}\,\mathbf{g}^*, \tag{13}$$

where $\mathbf{g}$, $\mathbf{g}^*$ are components of $\mathbf{G}$ and $\mathbf{G}^*$ in defect space. The matrices in Eqn.(13) are $3n \times 3n$ matrices, where n is the number of atoms in the defect space. For point defects, n is small so Eqn.(13) can be solved by direct matrix inversion as given below:

$$\mathbf{g}^* = (\mathbf{I} - \mathbf{g}\,\Delta\boldsymbol{\phi})^{-1}\mathbf{g}. \tag{14}$$

By definition, the force matrix defined by Eqn.(2) is nonvanishing only in the defect space. Using eqs. (8) and (13), we obtain for all atoms in the defect space

$$\mathbf{u} = \mathbf{g}^*\,\mathbf{F}. \tag{15}$$

In the GFMD method, we treat the whole defect space by using molecular dynamics and calculate $\mathbf{u}$ directly for atoms in defect space by iteration. In the first iteration, we keep the outer atoms of the defect space fixed at their original lattice sites and calculate the new equilibrium positions of the core atoms. This results into finite forces on the outer atoms. We then calculate the relaxed positions of the atoms by using LSGF. In the second iteration we keep the outer atoms fixed at the new relaxed positions and run molecular dynamics again to calculate the new equilibrium positions of the core atoms and the forces on the outer atoms. We find that the results converge to within 1% in 2-3 iterations.

After calculating $\mathbf{u}$ for all atoms in the defect space, we calculate the Kanzaki force in the defect space by using Eqn.(10). Then the displacement of all atoms in the solid is given in terms of the perfect-lattice Green's function by use of Eqn. (9). The Kanzaki force contains the full contribution of the discrete lattice structure in the defect space.

The perfect-lattice Green's function reduces [**2**] asymptotically to the continuum Green's function. For this purpose, we make **x(l)** and **q** continuous variables and replace the summation in Eqn. (11) by integration over the reciprocal space. In conformity with the continuum model notation, we replace **x(l)** by a continuous variable **x** for large x(**l**). In the limit $x \to \infty$,

$$\mathbf{G(x)} = (1/2\pi)^3 \int \mathbf{G}_c(\mathbf{q}) \exp(\iota \mathbf{q}.\mathbf{x})\, \mathbf{dq}, \tag{16}$$

where, keeping terms up to q^2 in $\boldsymbol{\phi}(\mathbf{q})$,

$$\mathbf{G_c(q)} = \mathrm{Lim}_{q\to 0}\, \mathbf{G(q)} = \mathrm{Lim}_{q\to 0}\, [\boldsymbol{\phi}(\mathbf{q})]^{-1} = [\boldsymbol{\Lambda}(\mathbf{q})]^{-1}. \tag{17}$$

In Eqn.(17), $\boldsymbol{\Lambda}$ is the Christoffel matrix, defined as follows:

$$\Lambda_{ij}(\mathbf{q}) = c_{ikjl}\, q_k\, q_l, \tag{18}$$

where i,j,k,l, etc. are Cartesian indices that assume the values 1-3, and **c** is the elastic constant tensor. Summation over repeated indices is implied.

Equation (9) is our master equation for multscale modeling. At large distances from the point defect, we replace **G** by the continuum Green's function defined by Eqn.(17) but use the lattice value of **F*** as defined in terms of the lattice Green's function by Eqns. (8) and (9). Thus the displacement field in our model at the position vector **x** is given by

$$\mathbf{u(x)} = \Sigma\, \mathbf{G_c(x-l')}\, \mathbf{F^*(l')}. \tag{19}$$

If the distance between the lattice sites in the defect space over which **F*** is distributed is much less than x, $\mathbf{G_c(x-l')}$ can be calculated in terms of the derivatives of the continuum Green's function.

We incorporate the effect of extended defects in $\mathbf{G_c}$ by imposing appropriate boundary conditions using the standard techniques of the continuum model. As an example, we consider a semi-infinite solid with a free surface. We choose a frame of reference in which the origin and the X- and Y- axes are on the free surface and the positive Z-axis points into the solid. The zero-traction boundary condition at the free surface, which is taken to be the plane at x_3=0, is given by

$$\tau_{i3}(\mathbf{x}) = c_{i3jk}\, e_{jk}(\mathbf{x}) = 0 \quad (x_3=0), \tag{20}$$

where

$$e_{jk} = \partial u_j(\mathbf{x})/\partial x_k. \tag{21}$$

The tensor **e** defined by Eqn.(21) has to be symmetrized to represent the conventional strain tensor.

Various computationally efficient representations of the continuum Green's function for anisotropic semi-infinite solids are available in the literature [**4,11-13**]. We use the delta-function representation for the continuum Green's function [**13**] that satisfies the boundary condition given by Eqn. (21). We add a virtual force term [**13**] to Eqn.(19), which is a solution of the homogeneous Christoffel equation as follows:

$$\mathbf{u(x)} = \Sigma\, \mathbf{G_c\,(x\text{-}l')\,F^*(l')} + \int \mathbf{G_h\,(x,x_s)\,f}(\mathbf{x}_s)\, d\mathbf{x}_s, \qquad (22)$$

where x_s is confined to the free surface of the solid, $\mathbf{f}_s$ is the virtual force, and $\mathbf{G}_h$ is the homogeneous Green's function, that is, a solution of the homogeneous Christoffel's equation. We determine the virtual force by imposing the boundary condition. The resulting Green's function thus includes the effect of the free surface as represented by the continuum model. The displacements are then calculated by using Eqn. (22) and the strains are calculated from Eqn. (21). A pure continuum model calculation of strain field due to quantum dots has been described in [**14**] which gives other references.

2.2 Results

In an earlier paper we have reported an application of the above method to a Au nanoisland in fcc Cu. Our work on Ge quantum dots in Si is in progress. Here we report some preliminary results on our calculations of lattice distortion due to a Ge quantum dot in Si. We modeled a Ge quantum dot consisting of 95 atoms and the host solid containing 14725 atoms. The relaxed configurations on (100) and (110) planes which show the lattice distortion are given, respectively, in Fig. (1) and Fig. (2). In these calculations we have used the modified embedded atom potential [**15**] which reproduces the physical parameters of silicon reasonably well. The results given in Figs. (1) and (2) do not yet include the effect of a large lattice and the contribution of the free surface which will be included in a later paper. We see from Figs. 1 and 2 that, as physically expected, the lattice distortion is anisotropic, is large near the interface between the quantum dot and the host lattice, and decreases with distance from the quantum dot. We are currently working on a million-atom model crystallite with a free surface. These results will be published elsewhere.

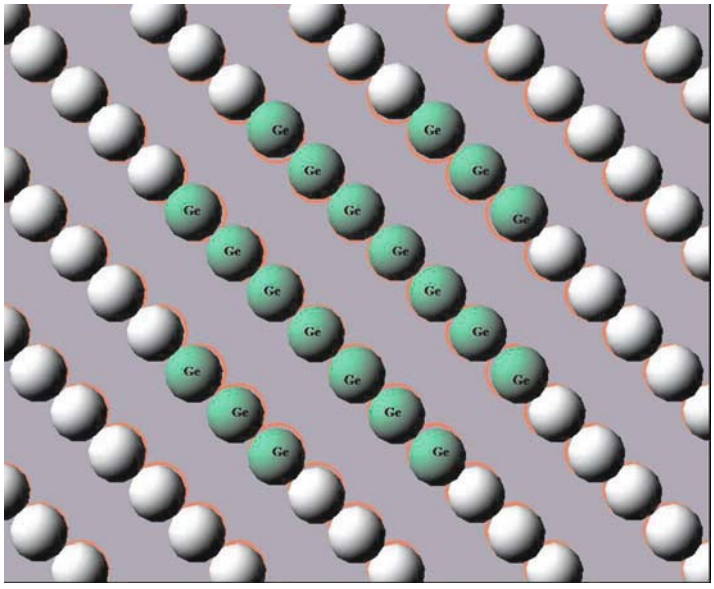

Figure 1. Equilibrium position of the atoms in and around Ge quantum dot in Si on the (0,0,1) plane. The empty circles denote the original lattice sites. Size of the circles is chosenarbitrarily for visualization. Ge atoms as marked, Si atoms unmarked.

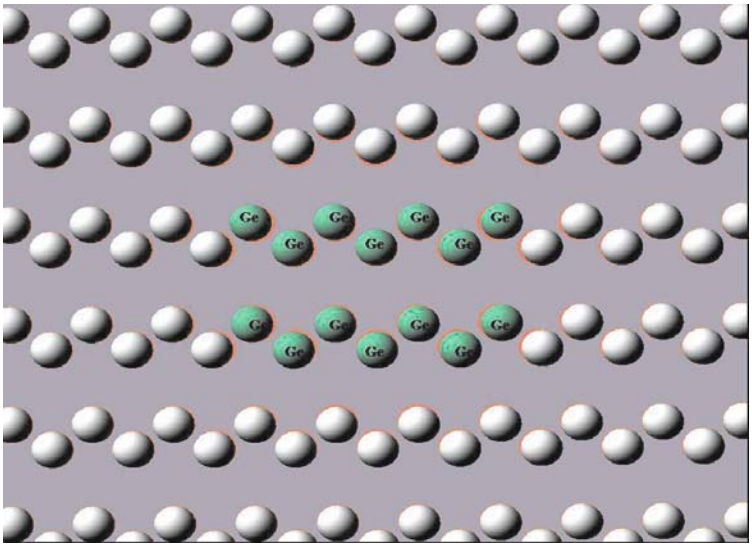

Figure 2. Same as in Fig. 1 on (110) plane.

3. CONCLUSIONS

An integrated Green's function molecular dynamics (GFMD) method has been described for calculating lattice distortion and strains due to a quantum dot in a semiconductor solid. The method accounts for nonlinear effects and discrete lattice effects in and close to the quantum dot, and the effect of a free surface. The method relates the discrete lattice distortion to macroscale continuum variables such as displacement fields and strains.

ACKNOWLEDGMENTS

This work was supported in part by the NIST ATP Program.

REFERENCES

1. Jain SC, Willander M, Maes H. "Stresses and strains in epilayers, stripes and quantum structures of III-V semiconductors", *Semicond. Sc. Tech.*, **11**, 641-671, 1996.
2. Tewary VK. "Green-function method for lattice statics", *Adv. Phys*., **22**, 757-810, 1973.
3. Thomson R, Zhou S, Carlsson AE, Tewary VK. "Lattice imperfections studied by use of lattice Green's functions", *Phys. Rev.*, **B46**, 10613-10622, 1992.
4. Ting TCT. *Anisotropic Elasticity*, Oxford, Oxford University Press, 1996.
5. Ortiz M, Phillips R. "Nanomechanics of defects in solids", *Adv. Applied Mech*., **36**, 1-79, 1999.
6. Vashishta P, Kalia RK, Nakano A. **"**Multimillion atom molecular dynamics simulations of nanostructures on parallel computers", *J. Nanoparticle Research*, **5**, 119-135, 2003.
7. Tadmor EB, Ortiz M, Phillips R. "Quasicontinuum analysis of defects in solids", *Phil. Mag.*, **A73**, 1529-1563, 1996.
8. Rao S, Hernandez C, Simmons JP, Parthasarathy TA, Woodward C. "Green's function based boundary conditions in two-dimensional and three-dimensional atomistic simulations of dislocations", *Phil. Mag*., **77**, 231-256, 1998.
9. Phillips R. "Multiscale modeling in the mechanics of materials", *Curr. Opin. Solid. St.*, M **3**, 526-532, 1998.
10. Tewary VK. "Multiscale Green's-function method for modeling point defects and extended defects in anisotropic solids: application to a vacancy and free surface in copper", *Phys. Rev.*, **B69**, article number 094109, 2004.
11. Pan E, Yuan FG. "Three-dimensional Green's functions in anisotropic bimaterials", *Int. J. Solids Struct*., **37**, 5329-5351, 2000.
12. Tewary VK. "Computationally efficient representation for elastostatic and elastodynamic Green's functions for anisotropic solids", *Phys. Rev.*, **B51**, 15695-15702, 1995.
13. Tewary VK. "Elastostatic Green's function for advanced materials subject to surface loading", *J. Eng. Maths.*, **49**, 289-304, 2004.
14. Yang B, Tewary VK. "Formation of a surface quantum dot near laterally and vertically neighboring dots", *Phys. Rev.*, **B 68**, article number 035301, 2003.
15. Baskes MI. "Modified embedded-atom potential for cubic materials and impurities", *Phys. Rev.*, **B46**, 2727-2742, 1993.

NANOMECHANICS OF BIOLOGICAL SINGLE CRYSTALS

The Role of Intracrystalline Proteins

Joanna Aizenberg

Bell Laboratories/Lucent Technologies, 600 Mountain Ave., Murray Hill, NJ 07974, USA; Tel.: (908)-582-3584; FAX: (908)-582-4868; E-mail: jaizenberg@lucent.com.

Abstract: Examples of ceramic materials in which the organic framework is stiffened by inorganic particles, are well known in nature and are produced synthetically by man. Organisms also form a different type of composite in which the host is a inorganic single crystal and the guests are proteins deliberately occluded into the crystal. The best-studied examples, to date, are biogenic calcites, and in particular those formed by the echinoderms. *In vitro* experiments with calcite crystals grown in the presence of echinoderm intracrystalline proteins and mollusk shell proteins show that these macromolecules are occluded inside the crystal on specific planes that are oblique to the cleavage planes, and their presence significantly improves the mechanical properties of the crystal host. Furthermore, the proteins also influence the crystal textural properties: the coherence length is reduced in directions perpendicular to the planes on which the proteins adsorb. This textural anisotropy is generally consistent with the gross morphology of the single crystal elements, suggesting that these proteins may also function in determining the shape of the crystal during growth. These novel single crystal-protein composites may be just one example of strategies used in nature for producing materials with special properties.

Key words: biomineralization, calcite, protein/crystal composite, crystal texture.

1. INTRODUCTION

Mineral formation by organisms is termed *biomineralization*. This is a diverse and widespread phenomenon involving various living creatures, from microorganisms to vertebrates [**1**]. Biominerals are usually different from the inorganic counterparts in their morphologies, mechanical

T. J. Chuang et al. (eds.), Nanomechanics of Materials and Structures, 99–108.
© 2006 *Springer. Printed in the Netherlands.*

properties, compositions and stabilities. This is a consequence of the differences in the environment of precipitation and, in particular, of the presence of an array of biological macromolecules [**2**].

The majority of mineralized tissues are constructed from crystalline materials. Inorganic crystals are used by organisms to fulfill different functions, the most common of which is to provide stiffness to their skeletal parts [**3**]. Although a wide variety of mineral types are used, most skeletons manufactured by organisms are made of the stable polymorphs of calcium carbonate - calcite and/or aragonite [**1**]. Calcite crystallizes in the trigonal centrosymmetric space group R-3c. The crystals of inorganic calcite develop in a typical rhombohedral morphology, expressing six {104} faces [**4**]. Cleavage readily occurs along these planes. This is a distinct disadvantage when using calcite as a structural material. Nevertheless many different organisms build their skeletons from calcite, and surprisingly, these possess remarkable strength and toughness [**5**].

Two main strategies are used by organisms for designing their calcitic skeletons. In the first strategy, crystals are used as stiffening agents in a preformed organic matrix. As a result, a composite material, such as mollusk shells, is formed (Fig. 1). This type of ceramic structure is widely employed by man in manufacturing synthetic composite materials [**6**].

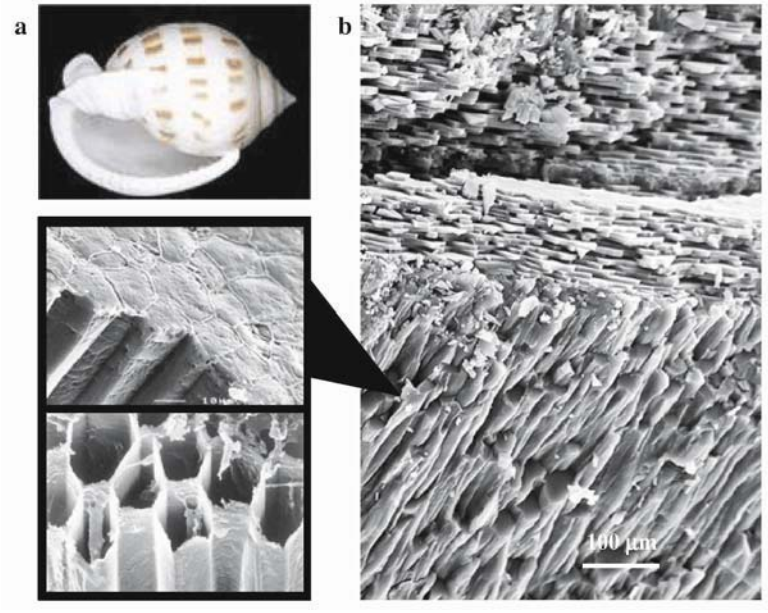

Figure 1. Natural ceramic material of a mollusk shell. a) Photograph of an entire mollusk shell; b) Scanning electron micrograph (SEM) of the interface between nacreous (top) and prismatic (bottom) layers of the shell. Insert shows higher magnification view of the prisms embedded in an organic envelope (top) and a demineralized organic envelope (bottom).

Many groups of organisms utilize a different strategy and produce a largely unknown composite structure – a unique fiber-reinforced composite material [**7-13**]. This tactic is used by organisms that build their skeletons out of large single crystals, e.g. echinoderms, calcareous sponges, foraminifera, etc. [**1**]. The basic concept of combining a stiff component with a pliant one still applies, but the roles are reversed. In these peculiar composites, the host is a single crystal and the guests are macromolecules, deliberately occluded into the single crystal along specific crystal planes. This type of composite is not (yet) exploited in synthetic materials.

In both cases, exceptional mineralized tissues that are adapted for specific mechanical functions are produced. Hence, there must be strong biological control over the calcite formation and the modification of its inherently poor mechanical properties. In this paper we outline the structural and nanomechanical features of such composite materials.

2. ECHINODERM SKELETON

The best known and possibly the most striking examples of skeletal elements composed of single crystals are found among the echinoderms, a class of organisms including sea urchins, brittle stars and sea stars (Fig. 2a). It has long been known, initially from polarized light experiments and subsequently from X-ray diffraction studies and epitaxial overgrowth experiments, that the tests, plates, ossicles and spines of these animals are built of discrete, sometimes huge, convoluted single crystals of calcite (Fig. 2b-d) [**1, 14, 15**]. Mechanical tests confirmed that they are much more resistant to fracture than synthetic calcite. Furthermore, they fracture like amorphous materials, revealing the curved glassy surfaces typical of the so-called conchoidal fracture, unlike the sharp fracture steps composed of the {104} cleavage planes of pure synthetic calcite crystals (Fig. 2e,f) [**16, 17**].

It was suspected decades ago that besides the extraneous control macromolecules, an additional protein fraction that is totally enclosed within the mineral phase, might be present. This was confirmed by the observation that some macromolecules are not extractable without prior demineralization, or are protected from destruction by oxidizing agents [**1**]. Since then the presence of intramineral proteins has been extensively documented, especially in biogenic single calcite crystals [**1, 7-13, 18**]. It has been shown, that many macromolecules involved in mineral formation in diverse and heterogeneous processes have one common chemical property – the ability to interact with the mineral ions in solution or with the surfaces of the solid phase [**8**]. This results from the presence of different charged groups, such as carboxylate, phosphate and/or sulfate [**1**]. Much less

information is available with regard to the precise disposition of these proteins in the biocrystals and their function. Some investigators suggested that these macromolecules are non-specifically trapped in the mineral during crystal growth, while others observed continuous sheaths of organic material inside biogenic crystals [**1**]. The low amounts of macromolecules in biogenic calcite crystals – only up to 0.1 wt. % – makes it difficult to characterize their position by direct techniques; but the location of these molecules itself indicates that they are in intimate contact with the mineral phase, and therefore are expected to influence the growth and properties of the biocrystals.

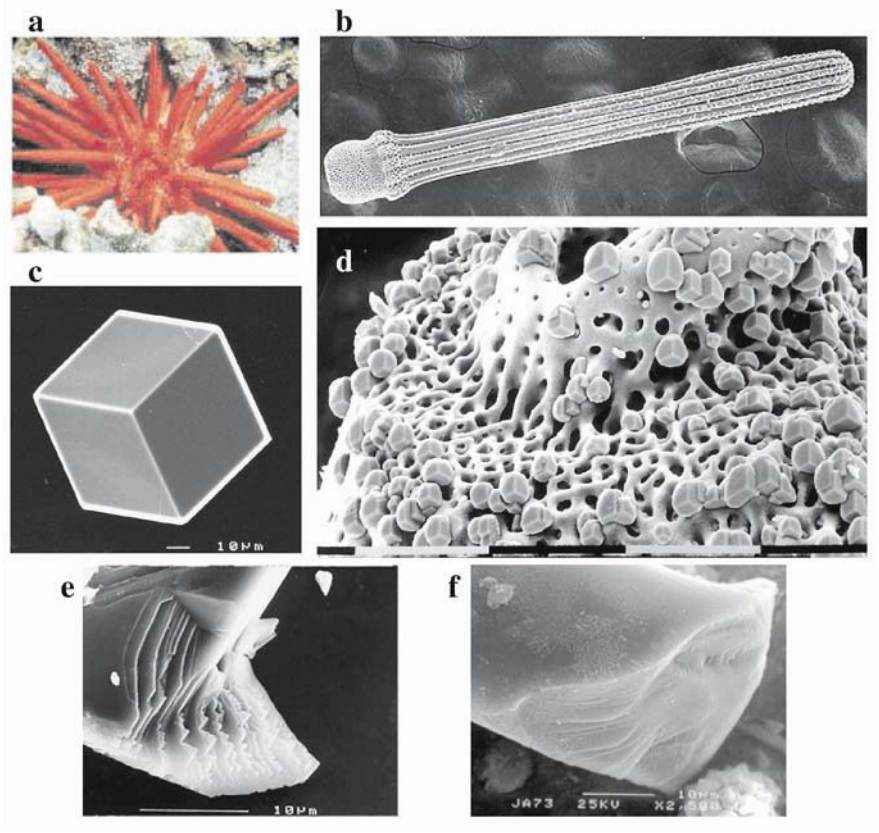

Figure 2. Biogenic and synthetic calcite crystals. a) Photograph of a sea urchin; b) SEM of a sea urchin spine – the entire spine is a single calcite crystal elongated in the *c*-axis direction; c) Typical synthetic calcite crystal – a rhombohedron faceted by the {104} cleavage planes of calcite; d) Echinoderm skeletal element epitaxially overgrown by synthetic calcite crystals from solution [**15**]. Note that newly formed rhombohedra are all co-aligned showing that the biological substrate is a single crystal; e) Fracture surface of a synthetic calcite crystal; f) Conchoidal fracture of a biogenic calcite crystal.

3. IN VITRO CRYSTAL GROWTH ASSAYS

One possible way to investigate macromolecule control over the formation of biogenic minerals is by simulating macromolecule-mineral interactions in synthetic precipitates. *In vitro* crystallization in the presence of additives in solution, such as macromolecules extracted from within biominerals, makes it possible to observe the effect they have on growing crystals [**7-13, 15, 19-21**]. The mechanism of such interactions is schematically illustrated in Fig. 3. The exposed crystal surfaces have different chemical and physical characteristics. The additives, when interacting with a synthetic crystal, recognize certain matching crystallographic planes and bind to them. Once adsorbed to the surface, they are overgrown and are consequently occluded within the crystal. Such specific adsorption poisons the recognized planes and slows down the growth of the crystal in the perpendicular direction. The resulting altered morphology of the synthetic crystal is an expression of different growth rates in the various crystallographic directions, modulated by the adsorbed additives. Thus, the interacting faces might be more pronounced or newly-developed, and molecular details of the surfaces that are recognized by the additives can be studied.

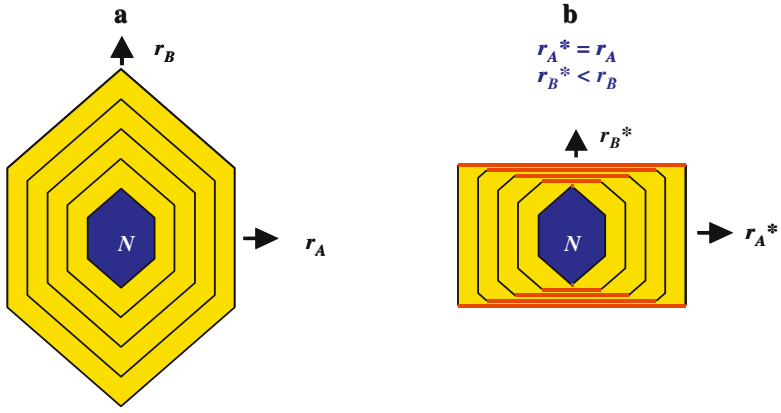

Figure 3. Mechanism of the crystal shape modulation by specific growth inhibitors. a) Equilibrium crystal shape. Crystal growth rates, *r*, in the directions [A] and [B] are indicated; b) Crystal morphology modified by the addition of an additive specific to the crystal plane {B}. Growth rate in the [B] direction is reduced, resulting in the formation of a differently shaped crystal with the newly developed {B} faces that were absent in a pure crystal.

We grew synthetic calcite in the presence of macromolecules extracted from different biogenic calcite crystals and monitored the induced morphological changes (Fig. 4) [**12, 13**]. Organic macromolecules extracted from sea urchin spines altered the morphology of the regular {104} calcite

rhombohedra (Fig. 4a) and produced crystals elongated in the *c*-axis direction (Fig. 4b). From these morphological changes we can infer that the proteins specifically interacted with the {hk0} calcitic planes, which are roughly parallel to the *c*-axis. This orientation is consistent with the elongation direction of the "mother" biocrystal (see Fig. 2b).

Organic molecules extracted from mollusk shells were fractionated and the major protein fraction was used in crystal growth assays [**12**]. Crystals grown in its presence were flattened in the *c*-axis direction (Fig. 4c). This morphological change suggested that the proteins were specifically adsorbed onto the {001} plane of calcite. This direction of intercalation is consistent with the so-called "growth lines" in mollusk prisms that are generally oriented perpendicular to the *c*-axis direction and correspond to the etched organic material.

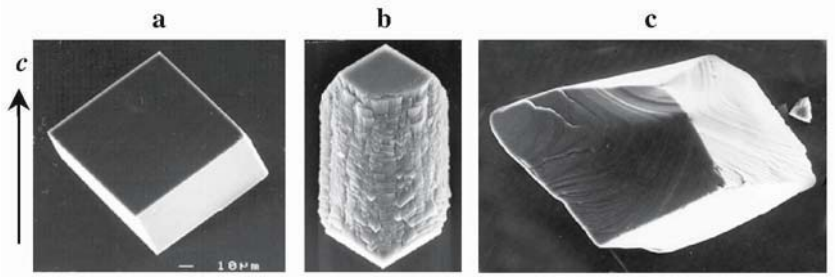

Figure 4. Morphologies of synthetic calcite crystals. The orientation of the *c* crystallographic axis is indicated. a) Pure calcite crystal; b) Elongated crystal grown in the presence of macromolecules extracted from sea urchin spines; c) Flattened crystal grown in the presence of mollusk shell proteins.

The significance of morphological changes in synthetic crystals in terms of reconstructing events that occurred during biological crystal formation should not be, however, overestimated, as the relevance of observations *in vitro* to processes that take place *in vivo* needs always to be demonstrated.

4. COHERENCE LENGTH MEASUREMENTS OF CRYSTAL PERFECTION

It has not been possible to date to directly image the macromolecules within the skeletons. However, it is possible to indirectly study the positions occupied by the macromolecules within the mineral, by monitoring the parameters of crystal perfection [**10-11, 13**]. This approach is based on the fact that the intracrystalline macromolecules are orders of magnitude larger than a unit cell of calcite. They cannot therefore be incorporated inside the perfectly coherent lattice in the form of a solid solution. They must reside at

the boundaries between domains of perfect structure, stabilizing existing imperfections or creating new ones. This means that they reduce the degree of perfection of the material, i.e. affect crystal texture. The defect distribution caused by protein intercalation inside the crystal can be characterized by means of diffraction behavior of the crystals [**22**]. Calcite crystals, including those with occluded proteins, are extremely well ordered crystals, and hence it is necessary to study their texture using highly collimated synchrotron X-ray radiation. The coherence length can be evaluated from the width of the diffraction peak in the ω/2θ mode by applying the Scherrer formula or modifications thereof. Synchrotron studies of biogenic and synthetic crystal/macromolecule composites demonstrate a direct crystallographic correlation between morphological changes induced by anisotropic occlusion of proteins and crystal texture (Fig. 5) [**10-11, 13**].

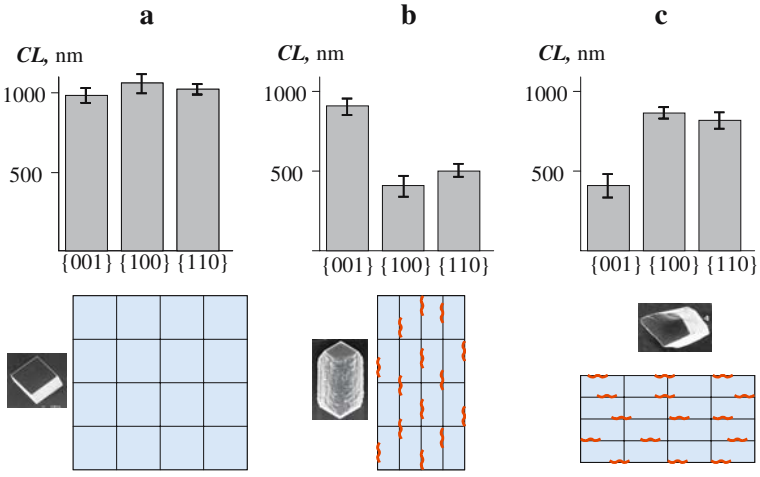

Figure 5. Textural parameters of synthetic calcite crystals. Top: Coherence lengths (*CL*) measured in 3 perpendicular directions: [001], [100] and [110]. Bottom: Schematic presentation of the crystal viewed as a combination of corresponding "perfect" domains. Macromolecule are indicated by bold wiggly lines. a) Pure calcite crystal; b) Elongated crystal grown in the presence of macromolecules extracted from sea urchin spines; c) Flattened crystal grown in the presence of mollusk shell proteins.

Pure calcite crystals showed highly isotropic texture with the coherence lengths of the perfect domains in the micron range (Fig. 5a). The crystals grown in the presence of sea urchin spine proteins showed a marked (~50%) reduction in coherence length in the *a,b*-plane, relative to the *c* direction (Fig. 5b). Therefore, intercalation of sea urchin spine macromolecules inside synthetic crystals is very selective on planes parallel to the *c* axis, in agreement with the observed morphological changes. Acidic proteins from the mollusk shells selectively reduced the coherence lengths of the perfect domains in the *c*-axis direction by ~50%. This type of textural anisotropy

suggests that selective protein adsorption occurs on the {001} planes of calcite (Fig. 5c).

A similar textural anisotropy was detected in their "parent" biological crystals [**10, 11**]. It was found that the domain lengths of sea urchin spines were reduced in the direction perpendicular to the c crystallographic axis, as would be expected from the in vitro observations of crystal-protein interactions. An exactly opposite anisotropic effect was detected in single calcitic prisms from a mollusk: the coherence lengths were decreased in the *c*-axis direction.

These results showed that single calcite crystals in the presence of specialized macromolecules form a unique composite tissue, in which macromolecules are selectively occluded in an orderly fashion within a crystal host.

5. MECHANICAL PROPERTIES OF PROTEIN-REINFORCED SINGLE CRYSTALS

The presence of the occluded polymers does not destroy the integrity of the crystal, but can change the material properties of the mineral. In this way, nature has overcome, at least in part, the problem of using commonplace materials that do not possess optimal mechanical properties, for constructing mineralized hard parts. Differently aligned crystal domains encountered by the crack propagation front cause the crack to deviate from the original cleavage planes. Hence, the organisms may control mechanical properties of their skeletal elements by lowering the degree of crystal perfection, i.e. by affecting crystal texture [**7, 9, 16-18, 23**].

Synthetic calcite crystals, grown in the presence of proteins extracted from within sea urchin spines and tests, also cleaved with conchoidal fracture, characteristic of biogenic calcites (Fig.2f), which is very different from the typical flat surfaces of cleaved pure crystals (Fig. 2e). Mechanical tests performed by microindentation produced stress-strain curves indicative of increased plasticity and reduced brittleness of the crystals with occluded protein, relative to those of pure calcite [**23**]. The estimated material toughness of the crystals with intercalated proteins was one order of magnitude higher than that of pure calcite.

It is clear that macromolecules occluded inside the biogenic and synthetic calcite crystals are responsible for the improved mechanical properties. The molecular mechanism of this specific reinforcement is, however, not as obvious. We proposed that the proteins, introduced along planes that are oblique to the cleavage planes of calcite (note that the {001} and the {hk0} planes, at which proteins adsorption is detected, form an angle of ~45° with

the {104} cleavage planes of calcite) strengthen the material against failure by both absorbing and deviating the advancing cracks (Fig. 6). One or more of the mechanisms well known in materials science may be involved, namely plastic yield of the material remote from the crack tip, plastic deformation at the crack tip, increase in area of the fracture surface and dissipation of energy by deformation of the polymer itself [**4**].

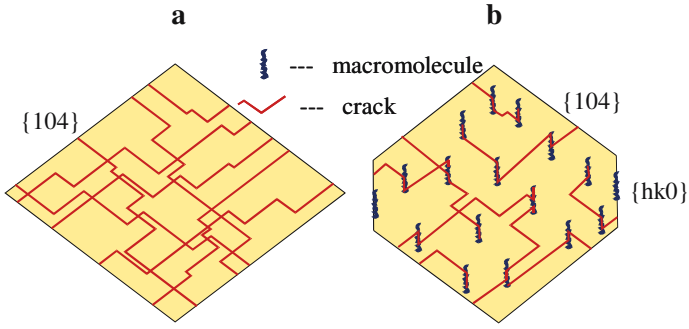

Figure 6. Schematic presentation of crack propagation in pure calcite (a) and the crack-arresting function of specific intracrystalline macromolecules positioned oblique to the cleavage planes (b).

The cases that we have investigated all involve calcite as a crystalline matrix, although we suspect that the same novel strategy may be used for different crystals. The mere fact that organisms from many completely different taxonomic groups control the distribution of organic matter and dislocations in the crystal is an indication in itself that they must derive important benefits. One benefit certainly relates to the improvement of mechanical properties – a feature that to our knowledge has not been utilized in the production of improved synthetic crystal containing materials.

ACKNOWLEDGMENTS

I thank Lia Addadi, Steve Weiner, Leslie Leiserowitz and Amir Berman for their involvement in this project.

REFERENCES

1. Lowenstam, H.A.; Weiner, S. *On Biomineralization*; Oxford University Press, New-York, 1989.
2. Simkiss, K.; Wilbur, K. M. *Biomineralization. Cell Biology and Mineral Deposition*, Academic Press: San Diego, 1989.
3. Wainwright, S. A.; Biggs, W. D.; Currey, J. D.; Gosline, J. M. *Mechanical Design in Organisms*; John Wiley & Sons: New York, 1976.

4. Lippmann, F. *Sedimentary Carbonate Minerals*; Springer-Verlag: Berlin, 1973.
5. Emlet, R.B. "Echinoderm calcite: A mechanical analysis of larval spicules". *Biol. Bull.* **163**, 264-275, 1982.
6. Weiner, S., Addadi, L. "Design strategies in mineralized biological materials." *J. Mater. Chem*. **7**, 689-702, 1997.
7. Berman, A.; Addadi, L.; Weiner, S. "Interactions of sea urchin skeleton macromolecules with growing calcite crystals – A study of intracrystalline proteins." *Nature* **331**, 546-548, 1988.
8. Addadi, L.; Weiner, S. "Control and design principles in biological mineralization". *Angew. Chem.* **31**, 153-169, 1992.
9. Berman, A.; Addadi, L.; Kvick, A.; Leiserowitz, L.; Nelson, M.; Weiner, S. "Intercalation of sea urchin protein in calcite: Study of a crystalline composite material". *Science* **250**, 664-667, 1990.
10. Berman, A.; Hanson, J.; Leiserowitz, L.; Koetzle, T. F.; Weiner, S.; Addadi, L. "Biological control of crystal texture: A widespread strategy for adapting crystal properties to function". *Science* **259**, 776-779, 1993.
11. Aizenberg, J.; Hanson, J.; Koetzle, T. F.; Leiserowitz, L.; Weiner, S.; Addadi, L. "Biologically induced reduction in symmetry: A study of crystal texture of calcitic sponge spicules". *Chem. Eur. J.* **7**, 414-422, 1995.
12. Albeck, S.; Aizenberg, J.; Addadi, L.; Weiner, S. "Interactions of various skeletal intracrystalline components with calcite crystals". *J. Am. Chem. Soc.* **115**, 11691-11697, 1993.
13. Aizenberg, J.; Hanson, J.; Koetzle, T. F.; Weiner, S.; Addadi, L. "Control of macromolecule distribution within synthetic and biogenic single calcite crystals". *J. Am. Chem. Soc.* **119**, 881-886, 1997.
14. Donnay, G.; Pawson, D. L. "X-ray diffraction studies of echinoderm plates". *Science*, **166**, 1147-1149, 1969.
15. Aizenberg, J.; Albeck, S.; Weiner, S.; Addadi, L. "Crystal-protein interactions studied by overgrowth of calcite on biogenic skeletal elements." *J. Cryst. Growth* **142**, 156-164, 1994.
16. Towe, K. M. "Echinoderm calcite: Single crystal or polycrystalline aggregate". *Science* **157**, 1048-1050, 1967.
17. Nissen, H. "Crystal orientation and plate structure in echinoid skeletal units". *Science* **166**, 1150-1153, 1969.
18. Currey, J. D. In *Skeletal Biomineralization: Patterns, Processes and Evolutionary Trends*; Carter, J. G., Ed.; Van Nostrand Reinhold: New York, 1991; pp 11-26.
19. Addadi, L.; Weiner, S. "Interactions between acidic proteins and crystals: Stereochemical requirements in biomineralization". *Proc. Natl. Acad. Sci. (USA)* **82**, 4110-4114, 1985.
20. Mann, S.; Archibald, D. D.; Didymus, J. M.; Douglas, T.; Heywood, B. R.; Meldrum, F. C.; Reeves, N. J. "Crystallization at inorganic-organic interfaces - Biominerals and biomimetic synthesis". *Science* **261**, 1286-1292, 1993.
21. Didymus, J. M.; Oliver, P.; Mann, S.; DeVries, A. L.; Hauschka, P. V.; Westbroek, P. "Influence of low-molecular-weight and macromolecular organic additives on the morphology of calcium-carbonate". *J. Chem. Soc. Faraday Trans.* **89**, 2891-2900, 1993.
22. Klug, H. P.; Alexander, L. E. *X-ray Diffraction Procedures*; Wiley-Interscience: New York, 1974.
23. Addadi, L.; Aizenberg, J.; Albeck, S.; Berman, A.; Leiserowitz, L.; Weiner, S. "Controlled occlusion of proteins: A tool for modulating the properties of skeletal elements". *Mol. Cryst. Liq. Cryst*. **248**, 185-198, 1994.

NANO/MICRO FLUIDIC SYSTEMS

Design, Characterization, and Biomedical Applications

Fan-Gang Tseng

Engineering and System Science Department, National Tsing Hua University, Taiwan, ROC
Phone:886-3-5715131; Fax:886-3-5720724; Email:fangang@ess.nthu.edu.tw

Abstract: This paper introduces three examples employing surface tension in micro/nano scale for fluid manipulation, precise dosage control, and powerless operation. Surface tension force, a line force, in micro scale is equally important as surface forces, such as friction or drag force. However, it becomes dominant in nanoscale when compared to surface or volume forces owing to scale effect. Therefore, the employment of surface tension would be effective and powerful in micro/nano fluidic systems. The first example will be a fluidic network system employing surface tension for enzyme batch-immobilization and bio assay in parallel. The second system, a 3-in-1 micro/nano protein arrayer, utilizes passive surface tension force for protein array formation and protein assay processes. The third system, a powerless droplet manipulation system, employs surface hydrophobicity gradient for droplet manipulation. All three examples demonstrate efficient and precise fluid control results in micro/nano scale.

Key words: Surface tension, Lab on A Chip, Micro Total Analysis System, micro/nano fluidics, micro array.

1. INRODUCTION

When forces with different power relationship of length (L) are compared in various length scales, we can find three important intersections among line forces (~L^1, such as surface tension force), surface forces (~L^2, such as friction or drag force), and volume forces (~L^3, such as inertia force). They would be roughly in meter scale for volume forces and surface forces, mm scale for volume forces and line forces, and μm scale for surface forces and line force. That is, volume forces would be dominant when length scale

T. J. Chuang et al. (eds.), Nanomechanics of Materials and Structures, 109–119.
© 2006 *Springer. Printed in the Netherlands.*

larger than meter size, surface forces would be the most significant in the scale between μm and mm rage, and line forces would be the most resound in nanoscale. As a result, the employment of surface tension force (a line force) would be effective and efficient when compared to others in micro/nano scale. This paper introduces three examples employing surface tension in micro/nano scale for fluid manipulation, precise dosage control, and powerless operation, including a fluidic network system employing surface tension for enzyme batch-immobilization and bio assay in parallel; a 3-in-1 micro/nano protein arrayer, utilize passive surface tension force for protein array formation and protein assay processes; and a powerless droplet manipulation system, employs surface hydrophobicity gradient for droplet manipulation. Following sections detail the operation principles, fabrication processes, and characterization of the three surface tension driven micro/nano fluidic systems.

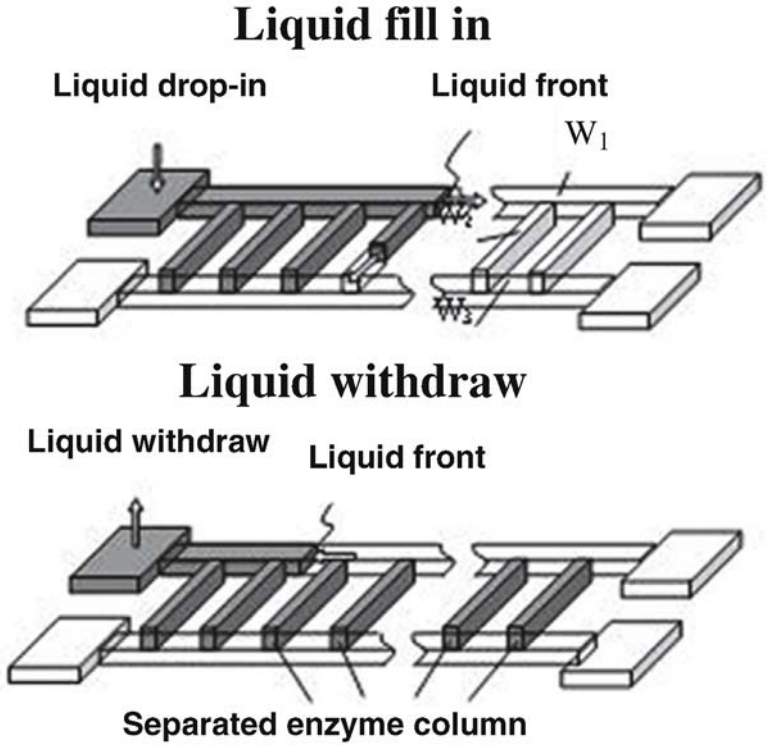

Figure 1. Fluid flow into each vertical channel by surface tension.

2. HAND HELD FLUIDIC NETWORK SYSTEMS

2.1 Introduction

The development and application of microchip system for the monitoring of multiple blood contents have become an important trend in modern blood analysis [**1**]. Chip system provides the major advantages of fewer amounts of regents, fast sensing response, automation, high throughput and portability [**2**]. Among different blood sensing methods, enzyme based systems have been widely employed for their high selectivity to specific targets and reliable characteristics [**3-5**]. The reactions for various enzymes were commonly carried out either by *in-situ* mixing of blood and reagents in micro fluidic system [**2**] or by manual application of enzyme layer on the electrode arrays [**4**]. However, those techniques either greatly reducing the ability of high throughput fabrication and analysis, limiting the accuracy of enzyme amount, posing cross contamination issue, or increasing the complexity and system size of the detection system. Thus, a surface tension driven fluidic system is introduced in this paper to solve the aforementioned issues for batch enzyme immobilization and multiple blood contents sensing.

2.2 Enzyme batch Immobilization

The design of the fluid network for enzyme immobilization is shown in Fig. 1. H-shaped micro channel was employed for enzyme immobilization with precise position and volume definition. When enzyme solutions touched one end of the top open trench (trenches has been treated with PEI and GA for enzyme boning), surface tension force drove the solution into each of the channel with precise volume control by the channel geometry. The channel width, designed following W1=W3>W2, allow the solution fully filled into each vertical branch without touch the bottom channel [**6**].

To quickly verify the functionality of the fluid network system, DI water was dropped onto one corner of the H-shaped channel, and the result demonstrated the feasibility for liquid precisely fill into each vertical channel. The extra liquid was drawn out by sponge to leave liquid appear only in the vertical channels. The visualized flow image is shown in Fig. 2. The deposition uniformity in each channel has been verified by fluorescence detection from Cy3 labeled protein immobilized on the electrode of each channel, and the deviation is within 10%.

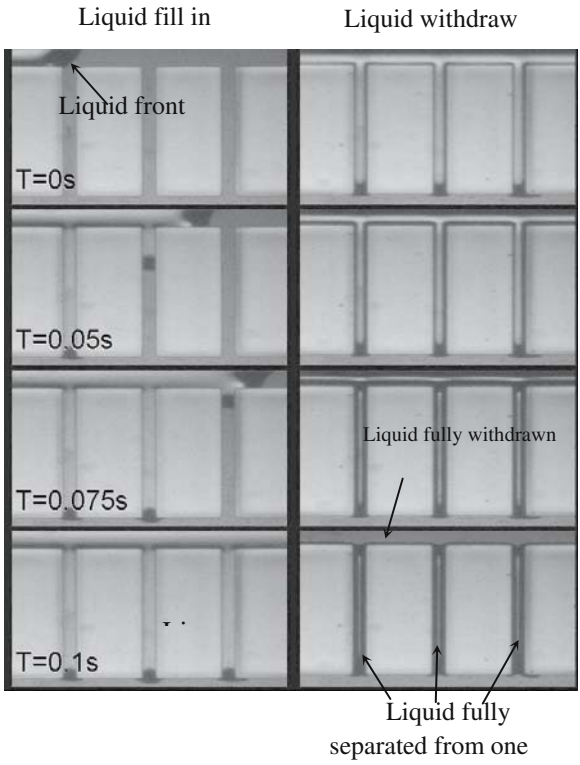

Fig. 2 Successive visualized pictures illustrated the process for liquid fill into each vertical channel

3. 3-IN-1 MICRO/NANO PROTEIN ARRAYER

3.1 Introduction

The development and application of protein arrays have become an important trend in modern biomedical diagnoses because of micro-array's ability of massive parallel process [**7**]. Protein micro arrays have become powerful tools in biochemistry and molecular biology. Array-based technology involves two principal processes: transferring hundreds of biosamples onto substrates, and immobilizing the biosamples on the substrates. "Micro contact printing" [**7-10**] is one of the microarray technology to simultaneously and rapidly imprint a vast number of bio-reagents in a short time. The conventional way to produce micro arrays utilized a needle array and computerized robot system to select and spot numerous bio reagents [**9**]. This arraying system has the drawbacks of high

cost, large size variation, and serial and long spotting process, which may malfunction proteins from dry-out. As a result, "Micro contact printing" [**7-10**] has been becoming an emerging technology to simultaneously and rapidly imprint a vast number of bio-reagents in a short time. Among various micro printing schemes, a new type microarrayer has been proposed by us recently [**11**] by employing micro stamping method to simultaneously immobilize hundreds of proteins in parallel. However, because of the short distance among stamping heads, it becomes necessary to employ a filler chip [**12**] for protein fill-in in batch instead of fill in individually. The combination of the batch fill-in and batch arraying process enable a rapid and high throughput formation of protein array to prevent proteins from de-naturization during the array process.

By employing the three-in-one chip system as mentioned above, parallel protein array formation and detection process can be realized, as shown in Fig. 3. Proteins can be loaded and preserved as a library in each fill-in reservoir in the micro filling chip before real application. When protein diagnosis/screen desired, the micro array stamper can be filled in proteins in parallel from the filling chip by piercing the needle array on the top of the stamper into the membrane of the filling chip at once. Protein array can then be formed simultaneously by the gentle contact between the stamper and bio reaction chip. The formed protein array is now ready for parallel bio reaction. Micro optical detection system is setup on the bottom of the bioreaction chip for parallel protein detection. Thus high throughput protein diagnosis/screen process can be finished in hours including bioreaction process for hundreds to thousands of proteins at one time.

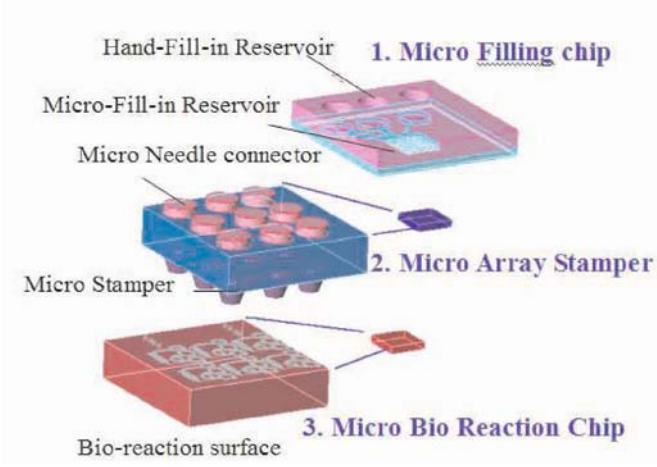

Fig. 3 integration of chip system

3.2 Biochip System Design

3.2.1 Micro Filling Chip

The operational concept of protein filler chip to perform batch fill-in process for micro arrayer is shown in Fig. 4. After we dispensing different proteins in the filler chip, parallel protein fill-in process can be carried out by directly contact the filler chip with the arrayer chip, thus tens to hundreds of proteins can be transferred by capillary force from the filler into the arrayer chip in seconds. This process can be repeated to fill another arrayer chip until the empty of the filler chip. The Filler chip is not only employed for protein filling purpose, but also applied to preserve the stored protein library permanently by sealing the top and bottom surface with PDMS thin film until the need for arrayer feeding.

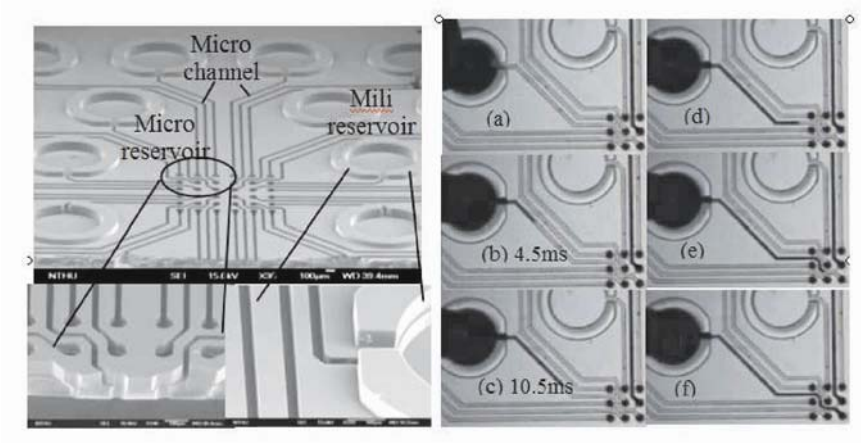

Fig. 4 Micro filler chip and filling test

The filler chip contains mili-reservoirs on the chip top for protein sample dispensing, micro reservoirs on the bottom for holding protein solutions, and micro channels connecting each mili-reservoir to the corresponding micro reservoir. Protein samples can be filled-in by capillary force from individual mili-reservoir to the corresponding micro-reservoir automatically without external power. To fill in protein solutions vertically and allow proteins arranged on a two-dimensional array, three-dimensional fluidic structures are desired.

3.2.2 Micro Stamper Chip

As shown in Fig. 5, the stamper chip can be used to spot different kinds of biosamples simultaneously and expanded to stamp hundreds of different biosamples. The micro stamper comprises micro-needles, micro-stamp array, and a microchannel array connecting the reservoirs and micro-stamp array. Different proteins could be dispensed into different channels and driven by capillary force to the tips of the micro stamps through the micro channels. The protein-filled micro stamper was then brought into contact with the bio-assay chip to generate sample arrays for further bio processing. Elastomeric polydimethylsiloxane (PDMS) is used to fabricate the micro stamps, so conformal contact can be achieved on rough surfaces. The uniform fluoresent spot of stamping result and the picture of the PDMS stamper was shown in the Fig. 5.

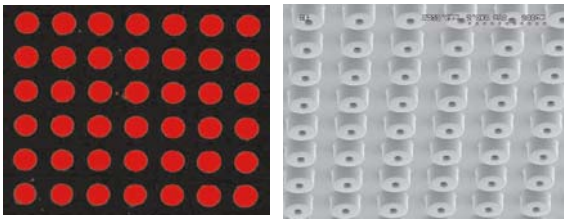

Fig. 5 Fluoresent stamp result and uniform PDMS micro stamper array

3.3 Droplet size versus wettability

The surface properties of bioreaction chip greatly affect the stamped droplet size. Thus, surfaces with different wetting properties were prepared by glass slide, APTS (aminopropyltrimethoxysilane) and BS^3 (bis-sulfo-succinimidyl suberate) on silde, APTS and DSC (N, N'-disuccinimidyl carbonate) on slide, and Su8 photo resist (MicroChem) coating on slide. The surface peak roughness is ranged from 73.8nm to 148nm. The deformation of the elastic stamper, which is made of PDMS, can make a conformal contacting with the substrate. The effect of surface roughness to the stamped feature size can be ignored. The hydrophilic properties of those surfaces have been characterized ranging from 18° to 78°, respectively on different surface coating. PBS buffer with 30% glycerol and 1% Cy3 dye is used as the stamping fluid in experiment. Both fluorescent and optical microscope images are used to measure the stamping feature size.

The stamped spot size varies with the different substrate wettability as shown in the Fig. 6. On the Su8 coating substrate, the printed spot size is 47 μm, which is much smaller than that on the glass substrate of 123 μm.

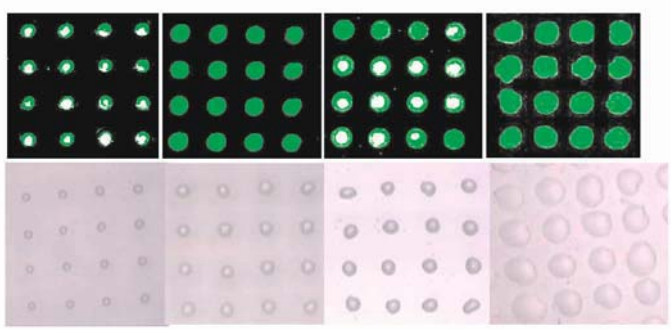

Figure 6. Drop features on different substrate observed from optical microscope and fluorescent image (a)Su8 photo resist (b) APTS+DSC (c) APTS+BS^3 (d) Glass

4. POWERLESS VAPOR-CONDENSATION AND DROPLET-COLLECTION/REMOVAL DEVICE

4.1 Introduction

Recently, μDMFC has attracted considerable attentions due to its potential to be a portable high energy power source [**13**]. However, different from macrosized fuel cells, micro fuel cell does not generate great enough energy for external pump or active valve system to support the operations such as fuel/air supply and waste removal. As a result, self-contained and powerless operation becomes important design strategy in micro fuel cell system. In this paper, a powerless waste management system for μDMFC is developed to separate gas/vapor, condensate droplet, collect small droplets into large ones, and remove large droplets into waste tank spontaneously and powerlessly, by simply employing condensation, surface tension/temperature gradient, and capillary force naturally without external energy.

4.2 Design and Experimental

The design of this waste management device is schematically shown in Fig. 7, consisting of a semicircle zone with wettability gradient in radial direction, polymer capillary guide channels, and gas exhaust holes. When vapor /gas mixtures arrives the vicinity of the hydrophobic gas-exhaust holes, vapor condensates as small droplets and gas (such as CO_2) exhausts from the micro holes [**14**]. When droplets accumulated large enough to generate enough surface tension gradient across the droplet toward the radial direction, droplets can then move automatically into micro channels, and are taken away into the waste tank. The fabrication process features DRIE etched exhaust holes, SU-8 resist structured micro channels, and, Diffusion-controlled silanization of octadecyltrichlorosilane on SiO_2 surface [**15**] to produce wetability gradient with hydrophobic center and hydrophilic border on the semicircle region.

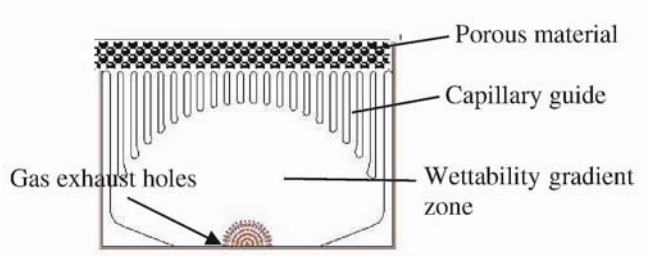

Fig. 7 Conceptual schematic of the chip

4.3 Characterization of droplet movement

The moving velocity of various sized droplets have been tested and simulated on this device, and experiments show that the average velocity is in the order of 1.5-2 cm/sec. Larger droplets move slightly faster, however, droplets stop moving when size smaller than 0.3μL. Vapor condensation and droplet collection/removal testing is demonstrated as shown in Figure 8. In this experiment, droplets do not move (Fig. 8a) until the condensed size larger than 500 μm in diameter (Fig. 8b). The moving droplets will coalesce with droplets in front of them and forming even larger droplets thus gradually increasing the moving speed (Fig. 8c) until touching the micro

channels. The micro channels then suck in all the large droplets (Fig. 8d-f), deliver them into waste tank (not shown in this paper), and dry out the semicircle surface for the next droplet condensation/collection/removal process. This device can effectively remove liquid in a speed of 5.8 μL/s, fast enough to manage waste solution generated from micro fuel cell process (~0.65μL /s).

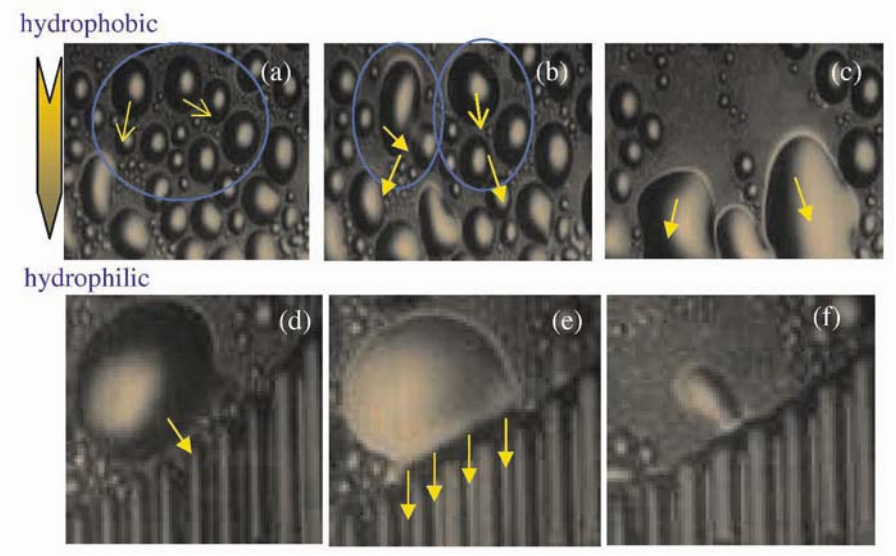

Fig. 8 Powerless droplet movement sequence

5. CONCLUSIONS

This paper presents three micro/nano fluidic systems employed only surface tension force for fluid manipulation, precise dosage, and powerless operation in high efficiency and precision. The designs, characterizations and applications are reviewed in detail and the three systems demonstrated their applicability to biomedical assays and micro fuel cells.

ACKNOWLEDGMENTS

We appreciate the financial support from National Science Council, Taiwan, for project funding and travel expenses.

REFERENCES

1. S. C. Jakeway, A. J. de Melto and E. L. Russel, Fresnius *J. Anal. Chem.* **Vol. 366**, pp. 525-539, 2000.
2. M. Seki, et. al, 1st IEEE-EMBS STC. on *Microtechnologies in Medicine & Biology*, Lyon, France , Oct. 12-14, , 2000.
3. W. E. Morf and N. F. de Rooij, *Sensors & Actuators B* **Vol. 44**, pp. 538-541, 1997.
4. H. Frebel, et al., *Sensors and actuators B* **Vol. 43**, pp. 87-, 1999.
5. Alice J. Cunningham, John Wiley & Sons, 1998.
6. R. Aoyama, M. Seki, J. W. Hong, T. Fujii, and I. Endo, IEEE Transducers'01, Munich, Germany, June 10-14, 2001.
7. S.C. Lin. et al., Fresnius *J. Anal. Chem.*, **Vol. 371**, pp. 202-208, 2001.
8. F.G. Tseng, et al., *Sensors and Actuators B*, **Vol. 83**, p. 22-29, 2002.
9. Kane, R.S. et al., *Biomaterials*, **Vol. 20**,p.2363-2376, 1999.
10. F.G. Tseng, et al, *Sensors and Actuators A*, **Vol. 97-98**, p131-138, 2002
11. S.C. Lin, et al., *IEEE MEMS'03*, Kyoto, Japan. p299-302, Jan. 2003
12. F.G. Tseng, et al., μTAS, Squaw Valley CA, USA, p639-643, Oct. 2003
13. Chang-Chien, A. et al, *Journal of Power Sources*, **Vol 112**, p 410-418, Nov., 2002.
14. De-Sheng Men, Joonwon Kim, CJ Kim, *IEEE MEMS'03,*pp.534-537, Kyoto, Japan, Jan. 2003.
15. Susan Daniel, Manoj K. Chaudhury, John C. Chen, *Science*, **Vol 291**, 633-636 , 2001.

MECHANICAL CHARACTERIZATION OF A SINGLE NANOFIBER

Experimental Techniques

E. P. S. Tan and C. T. Lim*

*Division of Bioengineering and Department of Mechanical Engineering, National University of Singapore, Singapore, 9 Engineering Drive 1, Singapore 118424. Tel: (65) 6874 7801, Fax: (65) 6779 1459, * email: ctlim@nus.edu.sg*

Abstract: Biodegradable polymeric nanofibrous scaffolds have been used extensively for tissue engineering. The stiffness of the individual nanofibers in these scaffolds can determine not only the structural integrity of the scaffold, but also the various functions of the living cells seeded on it. Therefore, there is a need to study the nanomechanical properties of these individual nanofibers. However, mechanical testing of these fibers individually at the nanoscale can pose great challenges and difficulties. Here, we present experimental techniques to test single polymeric nanofibers - namely tensile test, three-point bend test and indentation test at the nanoscale. For demonstration of the nano tensile test, we proposed the use of a nano tensile tester to perform pull test of a single nanofiber. For three-point bend test, a nanofiber is suspended across a microsized groove etched on a silicon wafer. An AFM tip is then used to apply a point load on the mid-span of the suspended nanofiber. For nanoindentation test, a nanofiber is deposited on a mica substrate and an AFM tip is used to indent the nanofiber. Mechanical properties such as Young's modulus, stress and strain at break of a single ultrafine fiber can then be obtained from these tests.

Key words: Nanomechanical characterization, polymer nanofibers, tensile test, three-point bend test, nanoindentation.

T. J. Chuang et al. (eds.), Nanomechanics of Materials and Structures, 121–137.
© 2006 *Springer. Printed in the Netherlands.*

1. INTRODUCTION

Biodegradable polymeric nanofibrous scaffolds have been widely used for engineering artificial tissues such as nerve [**1**], cardiac [**2**] and blood vessel [**3**] tissues. Although factors such as biocompatibility, suitable porosity and sufficient surface area for cell attachment [**4**] are vital for the survival and growth of cells seeded within or on the scaffold, mechanical properties of the scaffold are just as important.

Studies have shown that the stiffness of the scaffold can affect various cellular functions at the micro level such as cell growth, differentiation and motility [**5-7**]. The scaffold should also have the structural integrity and mechanical strength to maintain the desired shape before the new tissue is fully regenerated [**4**]. Therefore, there is a need to study the nanomechanical properties of individual nanofibers that make up the entire scaffold.

The difficulty in isolating and handling single ultrafine fibers is one of the main challenges experienced in the mechanical testing of single nanofibers. Devices that are able to measure the minute forces and deformations involved in the mechanical tests are also required. These issues are now addressed by the nanomechanical characterization techniques of single nanofibers proposed here - namely tensile test, three-point bend test and indentation test performed at the nanoscale. Mechanical properties such as Young's modulus, stress and strain at break of a single ultrafine fiber can then be obtained from these tests.

2. TENSILE TEST

We have previously performed tensile tests of a single nanofiber using three approaches. The first approach involves the innovative use of a nanoindenter to perform pull test of a single ultrafine fiber [**8**]. The second approach requires one end of the nanofiber to be attached to a piezo-resistive atomic force microscope (AFM) cantilever tip and the other end to a movable optical microscope stage [**9**]. The AFM tip acts a force sensor while the microscope stage is used to stretch the nanofiber. The third approach which will be presented here uses a nano tensile tester [**10**].

Due to the difficulty in manipulating and gripping single nanofibers, the most feasible way of conducting tensile tests of such samples is to collect the as-fabricated fibers on a jig or frame that can be directly mounted on a tensile tester. Here, aligned electrospun microsized polycaprolactone (PCL) fibers are used to demonstrate the tensile test using nano tensile tester. These fibers are first produced by collecting the fibers on two parallel,

conductive strips [**11**]. A commercial nano tensile testing system (Nano Bionix System, MTS, TN, USA) is used to conduct the tensile test.

2.1 Methodology

2.1.1 Collection of aligned fibers

The fibers are first fabricated using an electrospinning apparatus as shown in Fig. 1 from 7.5 wt% PCL (Mn 80,000) (Aldrich, MO, USA) polymer solution with chloroform and methanol in the ratio of 3:1 (w/w) as the solvent. A flow rate of 0.5 ml/h and potential difference of 9–10 kV between the spinneret and the grounded collector are used to electrospin the fibers for a few seconds to obtain several strands of fiber deposited across the frame. An aluminum frame with parallel strips is placed 60° to the horizontal grounded collector. A cardboard frame with 10 mm gap between the parallel strips is attached onto the aluminum frame for fiber collection. Double-sided tape is placed on this cardboard frame to attach the as-collected fibers to the frame. Individual fibers are partitioned with cardboard strips as shown in Fig. 2. The isolated portions are cut along the discontinuous lines to prepare single fibers for tensile test.

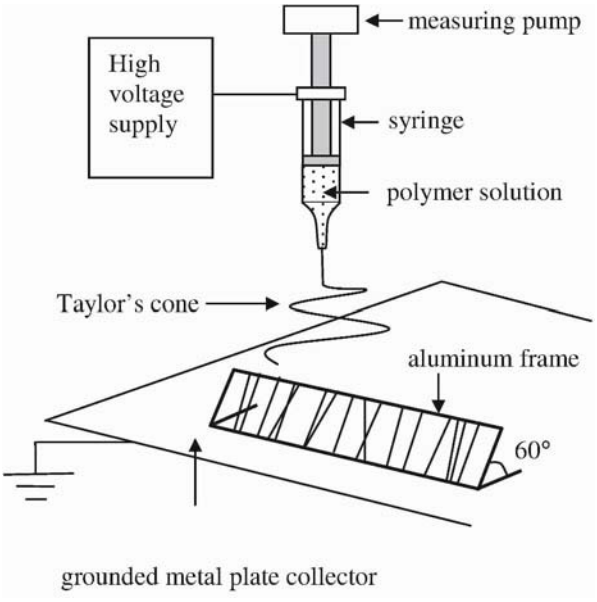

Figure 1. Illustration of the electrospinning apparatus.

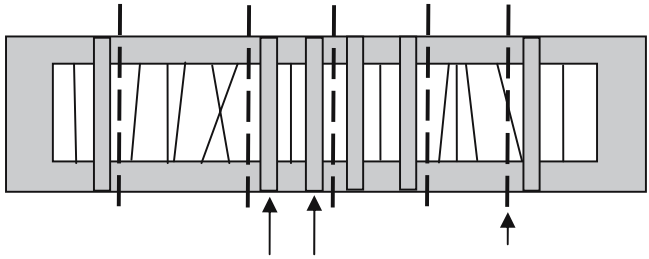

Figure 2. Cardboard frame being partitioned for the isolation of single nanofibers for tensile test [10].

2.1.2 Tensile test of a single ultrafine fiber

The diameters of individual ultrafine fibers are measured from the optical images taken using an inverted microscope (Leica DM IRB, Germany). Fiber alignment is also checked under the microscope. The gauge length is determined by the gap between the parallel strips of the cardboard frame (10 mm). The samples are mounted on the nano tensile tester as shown in Fig. 3. The cardboard partitions are cut along the discontinuous lines (Fig. 3) before stretching the fiber. Ten samples are stretched to failure at a strain rate of 1%/s at room temperature.

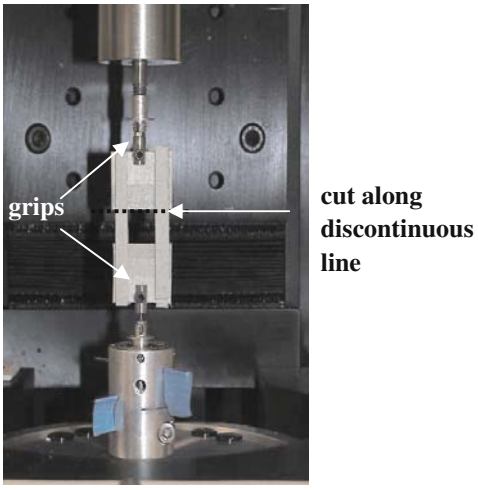

Figure 3. Sample mounted on the nano tensile tester (NanoBionix, MTS, USA) [**10**].

2.1.3 Results and Discussion

The stress-strain curves for PCL fibers at various fiber diameters is shown in Fig. 4. Electrospun PCL fibers are found to exhibit a tensile modulus of 120 ± 30 MPa, tensile strength of 40 ± 10MPa, strain at break of 200 ± 100% strain, yield stress of 13 ± 7MPa and yield strain of 20 ± 10% strain. The mechanical properties were found to vary with fiber diameter as shown in Fig. 4. Both tensile strength and yield stress decrease with increase in fiber diameter. The strain at break is found to increase with increase in fiber diameter whereas yield strain is found to decrease with an increase in fiber diameter. There is no apparent correlation between Young's modulus (E) and fiber diameter. The variation of the mechanical properties with fiber diameter is only significant for tensile strength and yield stress at a level of significance of 0.05.

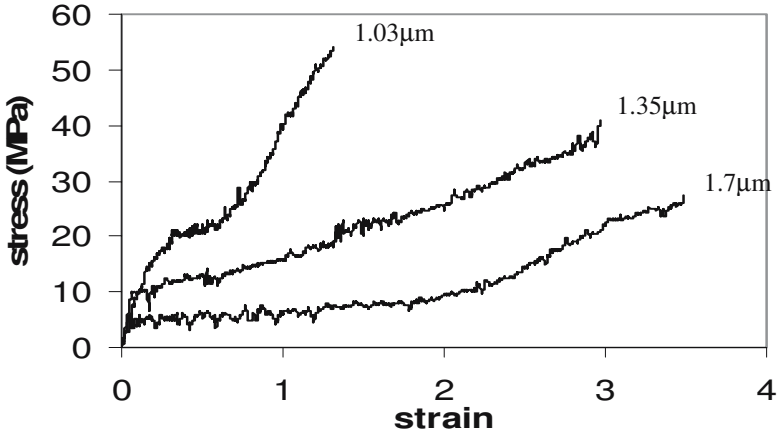

Figure 4. Plot of stress vs. strain for electrospun PCL fibers at various fiber diameters [**10**].

The electrospun PCL fibers exhibited low strength and stiffness but high ductility. This behavior is typical of polymers with glass transition temperature (T_g) below room temperature, which is the case for PCL [**12**]. At room temperature, the molecular chains have high mobility, thus enabling the chains to disentangle or slip past each other easily when a small force is applied.

The variation of mechanical properties with fiber diameter observed in this study is similar to the effect of cold drawing observed in gravity and melt spun fibers. As the polymer jet travels from the capillary to the grounded frame during the electrospinning process, the bending instability caused the jet to become narrower. The narrowing of the jet during its travel

is similar to the drawing process of gravity and melt spun fibers. The process of drawing reduces fiber diameter and provides a higher molecular chain orientation along the fiber axis. In support of this view, molecular chain and crystallite orientation with respect to the fiber axis has been observed in nonwoven electrospun PCL scaffold [**13**]. Certain portions of the polymer jet could have traveled a longer distance before reaching the grounded frame since the bending instability is not a static process. The 'draw ratio' increases as a result of this longer distance traveled. The process of drawing usually results in higher strength and stiffness but lower ductility as shown in Fig. 4. The smaller fibers exhibited higher strength and lower ductility, indicating that a higher 'draw ratio' is applied. The Young's modulus however, is observed not to be affected by the drawing process for the range of diameters studied here.

3. THREE-POINT BEND TEST

In order to perform three-point bend test of single nanofibers, individual fibers have to be suspended over a hole/groove and both fiber ends have to be fixed. As such a configuration is required, most suspended nanofibers are produced by microfabrication process [**14-18**] or electropolymerization process [**19,20**]. Polymeric biomaterials have been prepared from a suspension of the material in water and placing a drop of the liquid to a substrate [**21**]. For this test method to be applicable for polymeric nanofibers, the nanofibers have to be fabricated in the form of a two-dimensional mesh. Poly(L-lactic acid) (PLLA) nanofibers produced by the phase separation method is used to demonstrate this method [**22**].

3.1 Methodology

3.1.1 Sample preparation

PLLA with M_w~100,000 (Polysciences, Inc.) was dissolved in tetrahydrofuran (THF) to form a dilute polymer solution (0.5%wt/v). The solution was heated to 60 °C and stirred continuously with a magnetic stirrer until a homogeneous solution is obtained. A drop of the polymer solution is deposited on a mica slide placed in a glass petri-dish, which is prefrozen at -30 °C for 1 h. Liquid-liquid phase separation occurred when the drop of polymer solution is quenched as it comes into contact with the mica slide, thus forming a two dimensional gel. The mica slide with the gel is then placed back in the freezer for 2 h. THF is extracted from the gel by

immersing it in de-ionized water at 4 °C for one day. The water is changed three times within the day to remove all traces of THF, leaving behind a two-dimensional network of PLLA nanofibers. A silicon wafer with 4 μm wide and 2.5 μm deep grooves is placed in the glass petri dish with the PLLA film floating on the water surface. The water from the petri dish is removed using a pipette. This resulted in the deposition of the film on the silicon wafer. The film is then freeze dried under vacuum for one day. Nanofibers produced by this method have diameters in the range of 50–500 nm and lengths of several micrometers.

3.1.2 Three-point bend test of a single nanofiber

The elastic modulus of the PLLA nanofiber is obtained by performing a nanoscale three-point bend test on a single nanofiber suspended over the etched groove in a silicon wafer using atomic force microscopy (AFM) (Dimension 3100, Digital Instruments). An AFM cantilever tip is used to apply a small deflection at the midway along its suspended length using the force mode. The scanning electron microscope (SEM) (JEOL JSM-5500) image, AFM image and schematic diagram of the suspended nanofiber are shown in fig. 5.

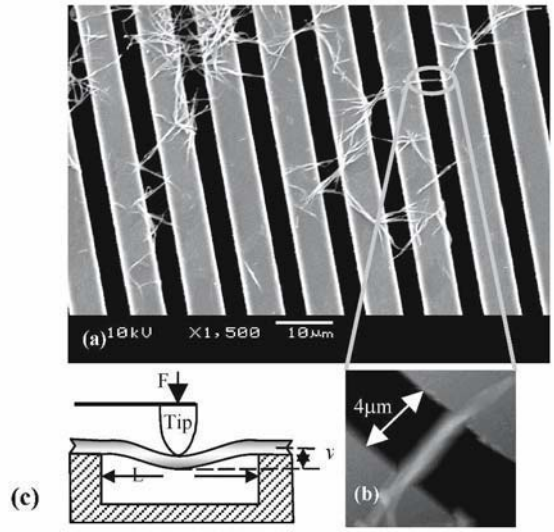

Figure 5. Nanofibers suspended over etched grooves of silicon wafer [**22**]. a) Electron micrograph of PLLA nanofibers deposited onto the silicon wafer, b) AFM contact mode image of a single nanofiber (400nm diameter) suspended over an etched groove, c) Schematic diagram of a nanofiber with mid-span deflected by an AFM tip.

The nanofiber is assumed to be a prismatic elastic beam with both ends fixed but undergoing pure bending as the force is applied (negligible shear deformation). The adhesion between the fiber and the silicon substrate was found to satisfy the assumption that both ends of the nanofibers are fixed as the fiber ends are found to remain in place even after the test is conducted. The AFM is used to apply a maximum load of 15 nN at the midspan of the nanofiber with a loading rate of 1.8 μm/s. The cantilever used in this experiment has a nominal spring constant of 0.15 N/m. The elastic modulus is found from beam bending theory [**23**] for a three-point bending of a beam with two ends fixed as

$$E = \frac{PL^3}{192vI} \tag{1}$$

where P is the maximum force applied, L is the suspended length, ν is the deflection of the beam at mid-span, and I is the second moment of area of the beam (where $I = \pi D^4/64$ and D is the beam diameter). An example of the force plot and the method of obtaining the deflection at mid-span of the fiber (ν) are shown in fig.6. A reference curve is first obtained by measuring the cantilever deflection over the Z-piezo displacement on a silicon wafer. The loading and unloading curves are obtained by using the AFM tip to deflect the mid-span of the nanofiber. The deflection of the fiber, v, is the difference between the loading and the reference curve.

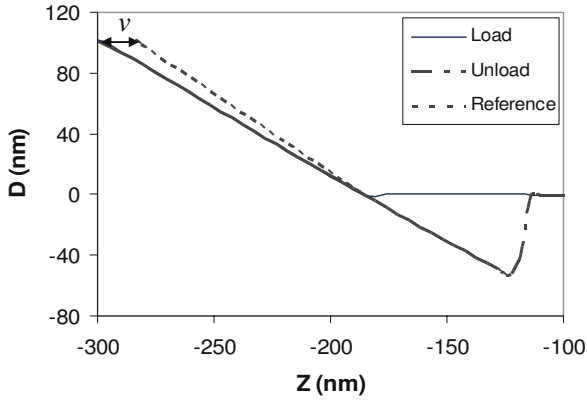

Figure 6. Force curve of suspended PLLA nanofiber. Plot of cantilever deflection (D) vs vertical displacement of the z-piezo (Z) [**22**].

The force curves of loading and unloading cycles coincide perfectly for the tests performed here thus indicating that the deformation of the nanofiber is purely elastic. In order for the elastic beam theory to be valid, the slope of

the deflection curve of the beam should be less than 5º for small deflection. This has been satisfied at the maximum load as the maximum slope of deflection curve is only 0.5°.

3.2 Results and Discussion

The elastic modulus of the PLLA nanofiber is found to be 1.0 ± 0.2 GPa for fibers with diameter less than 350nm. The elastic modulus appears to decrease as diameter of the nanofiber increases beyond 350nm (Fig. 7). This is due to the significance of shear deformation as *L/D* ratio decreases The value of elastic modulus obtained is in the lower range of reported values of between 1 to 10 GPa for bulk PLLA [**24**]. This is possibly due to the difference in the processing methods and molecular weight of the polymer used.

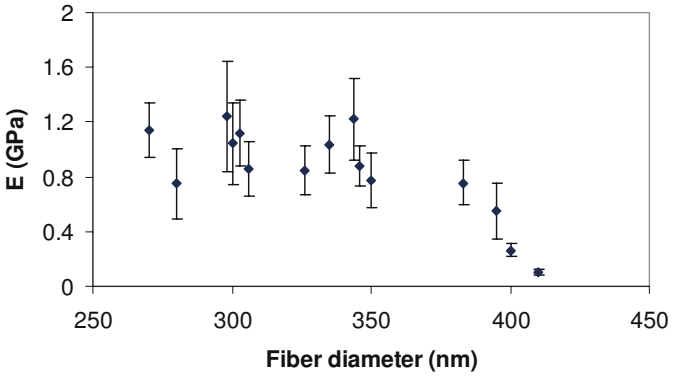

Figure 7. Variation of elastic modulus with fiber diameter [**22**].

Although consistent modulus values have been obtained for fibers with small diameter, there is a need to examine the assumptions used when calculating the elastic modulus. The simplifying assumption that the nanofiber is a prismatic beam is not true as the nanofiber diameter varies along the length. However, as the variation of diameter is small, the average nanofiber diameter as measured on the portions lying on the silicon wafer is taken to be the representative diameter. Another concern is the possibility of an indentation being made on the nanofiber by the AFM tip during the deflection. Force curves obtained on portions of the fiber lying on the substrate show that the maximum force applied in the bend test is not sufficient to cause an indent, i.e. the loading and reference force curves

coincide. Thus it can be safely assumed that the force applied to deflect the nanofiber did not cause any indentation.

4. NANOINDENTATION

Of all the nanomechanical characterization techniques mentioned, nanoindentation is perhaps the most convenient to perform as the sample can be prepared for testing simply by depositing the nanofibers on a hard and flat substrate, with sufficient adhesion between the substrate and fibers. Unlike the previous two methods, nanoindentation involves localized deformation. Thus the analysis of mechanical properties obtained is not as straight forward. In the present work, elastic nanoindentation of PLLA nanofibers produced by the phase separation method as mentioned above is performed using the AFM to obtain the elastic modulus.

4.1 Methodology

4.1.1 Issues concerning nanoindentation of nanofibers

Although the AFM is the most suitable device for probing mechanical properties of soft polymeric nanofibers, there are a number of issues that have to be considered.

Effect of Underlying Substrate. The elastic modulus values obtained using the Hertzian model are often overestimated when the samples probed are relatively thin (<200nm) [**25, 26**].

Ambiguous Tip Shape and Cantilever Spring Constant. Nominal tip radius and cantilever spring constants have often been used for the calculation of elastic modulus for convenience. However, the actual values usually deviate from the nominal values. This introduces some error in the calculation of elastic modulus, which is dependent on these two factors.

Fiber Surface Roughness. All real surfaces have a certain roughness. The asperities act like a compliant layer on the surface of the body, such that contact is extended over a larger area than it would be if the surfaces were smooth. As a result, the contact pressure for a given load will be reduced [**27**].

Curvature of Fiber Surface. Unlike most nanoindentation studies whereby the surface of the sample is flat, the curved surface of the fiber has to be taken into account of when using Hertz theory of elastic contact.

Non-Perpendicular Loading. The AFM tip is not perpendicular to the sample surface, thereby causing slip and friction between the AFM tip and the sample surface during indentation [**28**]. The angle the cantilever makes with respect to the horizontal is approximately 10° [**29**] and the correction factor for the load applied is cos10°, which is almost equal to 1. Thus the

non-perpendicular load factor is not significant. The slippage of AFM tip can be detected by non-coincidence of the loading and unloading force curves for elastic indents.

Adhesion Force. In a high humidity atmosphere (>70% relative humidity), the effects of adhesion due to the capillary effect of water condensation between tip and sample becomes significant [**30**]. Such adhesion force have to be accounted for as shown in a study by Park et al [**31**].

4.1.2 Sample Preparation

PLLA nanofibers are prepared as mentioned in section 3.1.1, except that the fibers are now deposited on freshly cleaved mica instead of silicon wafer.

4.1.3 Nanoindentation of a single nanofiber

Nanoindentation of PLLA nanofibers are carried out with the above factors in mind. A dehumidifier is used to keep the relative humidity of the environment to <60% to minimize the effect of adhesion forces. Nominal spring constants of the cantilevers are used for the calculation of the force applied. Cantilevers with nominal spring constants of 0.7-8N/m are used to produce indents shallow enough to prevent plastic deformation. The maximum force applied is in the range of 40-110nN to produce indents of 3-7nm deep at a loading rate of 0.5-1.8μm/s. The tip shape of the AFM probes are characterized by scanning a test grating (TGT1, Nano Technology Instruments) with an array of sharp tips (<10nm tip curvature radius) and analyzing the scanned image using the tip characterization option of the Scanning Probe Image Processor software (SPIP) (Image Metrology). Tip radii vary in the range of 20-60nm.

Hertz theory of normal contact of elastic solids is used to analyze the force-indentation data [**32**]. The nanofiber is modeled as a cylinder and the AFM tip is modeled as a sphere. The relative elastic modulus, E_r is given by

$$E_r = \sqrt{\frac{9P^2}{16R_e\delta^3}} \tag{2}$$

where P is the force applied, δ is the indentation depth, and R_e is the equivalent radius for a spherical indenter in contact with an infinitely long cylinder. R_e is given by

$$R_e = \sqrt{\frac{R_t^2 R_f}{R_t + R_f}} \tag{3}$$

Where R_t is the AFM tip radius and R_f is the radius of the nanofiber. The elastic modulus of the nanofiber, E_f is related to the relative elastic modulus E_r by the following relation

$$E_f \approx E_r(1-\nu_f^{\,2}) \tag{4}$$

where ν_f is the Poisson ratio of the nanofiber and the value is taken to be 0.33 as the properties of PLLA are similar to polystyrene [**33**]. Ten force curves are obtained from each sample along the length of the fiber. An example of the force plot and the method of obtaining the indentation depth (δ) are shown in Fig. 8.

The absence of indentation marks upon observation of indentation area after force measurements and the coincidence of the force curves of loading and unloading cycles indicated that the deformation of the nanofiber by the AFM tip is elastic.

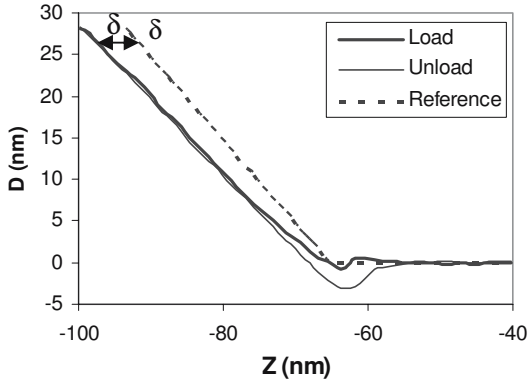

Figure 8. Plot of cantilever deflection (D) vs vertical displacement of the Z-piezo (Z). A reference curve is obtained by measuring the cantilever deflection over the Z-piezo displacement on a silicon wafer. The loading and unloading curves are obtained by using the AFM tip to indent the nanofiber. Indentation depth, δ, is the difference between the loading/unloading and reference curve.

The roughness of the nanofiber surface is taken from an area of 50x50nm, which is slightly larger than the largest contact area obtained in the experiment (largest contact diameter is 30nm). Ten fibers are used for roughness calculations and five readings are taken from each fiber. The RMS roughness (Rq) is used to determine the correction required (due to surface roughness) for the calculated modulus values. Rq, the standard distribution of the height values within a given area [**27**], is found to be 1.1 ± 0.6 nm.

4.2 Results and Discussion

The elastic modulus is found to vary with fiber diameter as shown in Fig. 9. The higher values obtained for small diameter fibers is likely due to the influence of the hard substrate on the deformation behavior of the fiber as shown in other studies on thin polymeric films [25, 26]. The elastic modulus values appear to level off for fibers with diameter > 250nm, indicating that the substrate effect is not significant beyond a certain fiber diameter. The elastic modulus of PLLA nanofiber was found to be 0.7 ± 0.2GPa, excluding fibers with diameter < 250nm. As the nanoindentation depth is of the same order as the surface roughness, the variation in modulus values obtained for each fiber is larger than that of the three-point bend test [**22**].

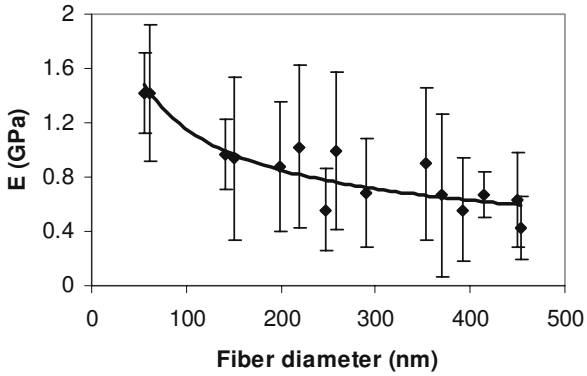

Figure 9. Variation of elastic modulus with fiber diameter for nanoindentation of PLLA nanofiber

As mentioned earlier, the presence of asperities on the fiber surface results in the increase in contact area and reduction of contact pressure for a given load. This results in an underestimation of the elastic modulus values. In order to determine if the effect of surface roughness is significant, a non-dimensional parameter, α, has to be determined:

$$\alpha = \sigma_s \left(\frac{16 R_e E_r^{\ 2}}{9 P^2} \right)^{1/3} \tag{5}$$

where σ_s is the RMS roughness obtained experimentally. The Hertz theory for smooth surfaces can be used with only a few percent error provided the parameter α is less than 0.05 [**27**]. The α for this study is calculated to be 0.28, thus correction has to be made for the elastic modulus values obtained.

A second non-dimensional parameter, μ, defined by Greenwood and Tripp [34] is given by:

$$\mu = \frac{8}{3}\eta_s \sigma_s (2R/\kappa_s)^{1/2} \tag{6}$$

where η_s is the asperity density and κ_s is the mean curvature of the summits of the asperities. Both parameters are very sensitive to the sampling interval when the topography of the surface is mapped. Thus an absolute value for μ cannot be obtained. However, Greenwood and Tripp obtained two values of μ which bracket a wide range of practical rough surfaces. The two parameters, α and μ are then used to determine the correction required. The ratio of effective contact radius (experimental), a^* to the Hertz radius (theoretical), a_0 are influenced by the surface roughness as shown in Fig. 10. For $\alpha = 0.28$ and μ within the range of 4 to 17, the ratio of a^*/a_0 is between 1.14 to1.18 (as indicated by the arrows). Since E is proportional to $1/a^3$, the elastic modulus value after roughness correction (experimental value is 0.7GPa) is approximately 1GPa. This result after roughness correction agrees well with that obtained from the three-point bend test.

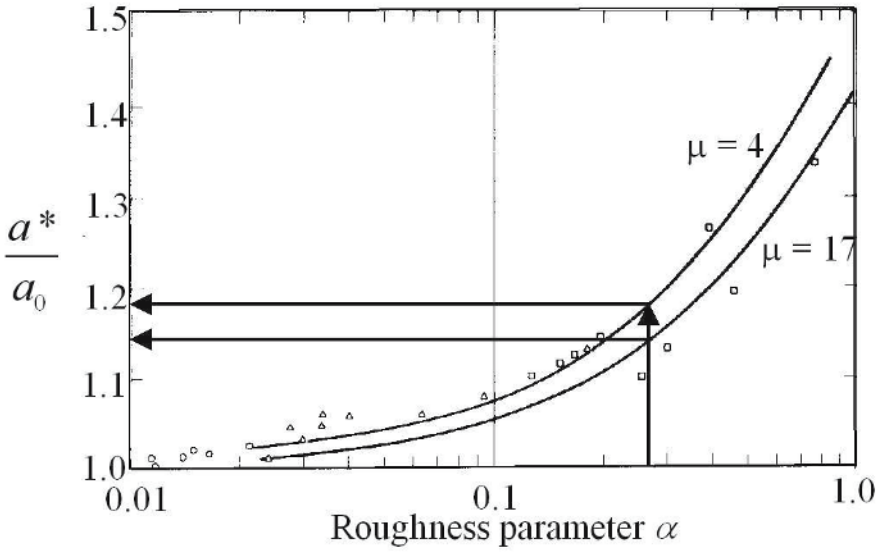

Figure 10. Influence of the surface roughness on the effective contact radius a^* compared with the Hertz radius a_0 [**27**].

5. CONCLUSIONS

In summary, the methods to characterize polymeric nanofibers by tensile test, three-point bend test and indentation test at the nanoscale have been presented. Tensile test is the most convenient test to perform and provides the most information about the mechanical properties of the polymer in question. This is possible provided that the fibers are continuous and direct deposition of fibers on a frame can be made. For shorter fibers of a few microns in length, the latter two methods are more feasible. However, only the elastic modulus value can be obtained. The mechanical properties obtained for individual nanofibers are useful in the design of tissue engineered scaffolds. Processing or fabrication parameters can be optimized to obtain nanofibers with mechanical properties that match closely to the natural tissues.

REFERENCES

1. Yang F, Murugan R, Ramakrishna S, Wang X, Ma YX, Wang S. "Fabrication of nano-structured porous PLLA scaffold intended for nerve tissue engineering", *Biomaterials*, **25**, pp. 1891-1900, 2004.
2. Shin M, Ishii O, Sueda T, Vacanti JP. "Contractile cardiac grafts using a novel nanofibrous mesh", *Biomaterials*, **25**, pp. 3717-3723, 2004.
3. Xu CY, Inai R, Kotaki M, Ramakrishna S. "Aligned biodegradable nano.brous structure: a potential scaffold for blood vessel engineering", *Biomaterials*, **25**, pp. 877-886, 2004.
4. Ma PX, Langer R. "Fabrication of Biodegradable Polymer Foams for Cell Transplantation and Tissue Engineering", *Tissue Engineering Methods and Protocols*, J.R. Morgan and M.L. Yarmush, Editors. Humana Press. pp. 47-56, 1999.
5. Ingber DE, "*Mechanical and Chemical Determinants of Tissue Development*, in *Principles of Tissue Engineering*", R.P. Lanza, R. Langer, and J. Vacanti, Editors. Academic Press. pp. 101-110, 2000.
6. Opas M, "Expression of the Differentiated Phenotype by Epithelial-Cells Invitro is Regulated by Both Biochemistry and Mechanics of the Substratum",. *Developmental Biology*, **131**, 2, pp. 281-293, 1989.
7. Vernon RB, Angello JC, Iruelaarispe ML, Lane TF, Sage EH. "Reorganization of Basement-Membrane Matrices by Cellular Traction Promotes the Formation of Cellular Networks Invitro", *Laboratory Investigation*, **66**, 5, pp. 536-547, 1992.
8. Tan EPS, Ng SY, Lim CT. "A novel approach to tensile testing of micro- and nanoscale fibers", *Review of Scientific Instruments*, **75**, 8, pp. 2581-2585, 2004.
9. Tan EPS, Lim CT. "Tensile Testing of a nanofiber using an AFM Cantilever Tip ", 2004. (*submitted*)
10. Tan EPS, Ng SY, Lim CT. "Tensile Testing of a Single Ultrafine Polymeric Fiber", *Biomaterials*, 2004. (*in press*)
11. Li D, Wang YL, Xia YN. "Electrospinning of polymeric and ceramic nanofibers as uniaxially aligned arrays". *Nano Letters*, **3**, 8, pp. 1167-1171, 2003.

12. Coombes AGA, Rizzi SC, Williamson M, Barralet JE, Downes S, Wallace WA. "Precipitation casting of polycaprolactone for applications in tissue engineering and drug delivery", *Biomaterials*, **25**, pp. 315-325, 2004.
13. Lee KH, Kim HY, Khil MS, Ra YM, Lee DR. "Characterization of nano-structured poly(ε -caprolactone) nonwoven mats via electrospinning", *Polymer*, **44**, pp. 1287-1294, 2003.
14. Sundararajan S, Bhushan B, Namazu T, Isono Y. "Mechanical property measurements of nanoscale structures using an atomic force microscope", *Ultramicroscopy*, **91,** 1-4, pp. 111-118, 2002.
15. Demczyk BG, Wang YM, Cumings J, Hetman M, Han W, Zettl A, Ritchie RO. "Direct mechanical measurement of the tensile strength and elastic modulus of multiwalled carbon nanotubes", *Materials Science and Engineering A-Structural Materials Properties Microstructure and Processing*, **334,** 1-2, pp. 173-178, 2002.
16. Kim GT, Gu G, Waizmann U, Roth S. "Simple method to prepare individual suspended nanofibers", *Applied Physics Letters*, **80**, 10, pp. 1815-1817, 2002.
17. Salvetat JP, Briggs GAD, Bonard JM, Bacsa RR, Kulik AJ, Stockli T, Burnham NA, Forro L. "Elastic and Shear Moduli of Single-Walled Carbon Nanotube Ropes", *Phys. Rev. Lett.*, **82**, 5, pp. 944-947, 1999.
18. Tombler TW, Zhou C, Alexseyev L, Kong J, Dai H, Liu L, Jayanthi CS, Tang M, Wu SY. "Reversible electromechanical characteristics of carbon nanotubes under local-probe manipulation", *Nature*, **405**, pp. 769-772, 2000.
19. Duvail JL, Retho P, Godon C, Marhic C, Louarn G, Chauvet O, Cuenot S, Pra NLDD, Demoustier-Champagne S. "Physical properties of conducting polymer nanofibers", *Synthetic Metals*, **135**, 1-3, pp. 329-330, 2003.
20. Cuenot S, Demoustier-Champagne S, Nysten B. "Elastic Modulus of Polypyrrole Nanotubes", *Physical Review Letters*, **85**, 8, pp. 1690-1693, 2000.
21. Xu W, Mulhern PJ, Blackford BL, Jericho MH, Templeton I. "A New Atomic Force Microscopy Technique for the Measurement of the Elastic Properties of Biological Materials", *Scanning Microscopy*, **8**, 3, pp. 499-506, 1994.
22. Tan EPS and Lim CT. "Physical properties of a single polymeric nanofiber", *Applied Physics Letters*, **84**, 9, pp. 1603-1605, 2004.
23. Ugural AC. "Stresses in beams, in Mechanics of Materials", McGraw-Hill, pp. 152-213, 1993.
24. Lu L, Mikos AG. *Polymer Data Handbook*, Oxford University Press, pp. 631-632, 1999.
25. Chizhik SA, Gorbunov VV, Luzinov I, Fuchigami N, Tsukruk VV. "Surface force spectroscopy of elastomeric nanoscale films", *Macromolecular Symposia*, **167**, pp.167-175, 2001.
26. Domke J, Radmacher M. "Measuring the elastic properties of thin polymer films with the atomic force microscope". *Langmuir*, **14**, 12, pp. 3320-3325, 1998.
27. Johnson KL. *Contact Mechanics*. Cambridge University Press, pp. 397-423, 1992.
28. Li X, Gao H, Murphy CJ, Caswell KK. "Nanoindentation of Silver Nanowires", *Nano Letters*, **3**, 11, pp. 1495-1498, 2003.
29. Bischel MS, Vanlandingham MR, Eduljee RF, Gillespie JW, Schultz JM. "On the use of nanoscale indentation with the AFM in the identification of phases in blends of linear low density polyethylene and high density polyethylene", *Journal of Materials Science*, **35**, 1, pp. 221-228, 2000.
30. Sumomogi T, Hieda K, Endo T, Kuwahara K. "Influence of atmosphere humidity on tribological properties in scanning probe microscope observation", *Applied Physics A Materials Science & Processing*, **66**, pp. 299-303, 1998.

31. Park JG, Lee SH, Kim B, Park YW. "Electrical resistivity of polypyrrole nanotube measured by conductive scanning probe microscope: The role of contact force", *Applied Physics Letters*, **81**, 24, pp. 4625-4627, 2002.
32. Johnson KL. *Contact Mechanics*, Cambridge University Press, pp. 84-106, 1992.
33. Garlotta D. "A Literature Review of Poly(Lactic Acid)", *Journal of Polymers and the Environment*, **9**, 2, pp. 63-84, 2001.
34. Greenwood JA, Tripp JH. "The elastic contact of rough spheres", *Trans. ASME, Series E, Journal of Applied Mechanics*, **34**, 153, pp. 417-420, 1967.

ATOMISTIC STUDIES OF FLAW TOLERANT NANOSCALE STRUCTURAL LINKS IN BIOLOGICAL MATERIALS

Nature's principle of material design

Markus J. Buehler and Huajian Gao

Max Planck Institute for Metals Research, Heisenbergstrasse 3, D-70569 Stuttgart, Germany. Phone: 47-711-86-2310; Fax: 47-865-2312; Email:, hjgao@mf.mpg.de

Abstract: This paper discusses fundamental design concepts of nanoscale structural links in biological materials and focuses on verification of these concepts via atomistic simulations. Bone-like biological materials have achieved superior mechanical properties through hierarchical composite structures of mineral and protein, with the most basic structural units designed at a characteristic nanoscale. Gecko and many insects have developed hierarchical surface structures to achieve extraordinary adhesion capabilities through evolution, with basic structural units also at nanoscale. We argue that choosing a characteristic nanometer scale for the structural links in these materials plays a critical role in allowing the biological systems to achieve their superior properties. In both systems, restricting the characteristic dimension of the basic structure components to nanometer scale prevents crack-like flaws from propagating to break the desired structural link. We demonstrate via atomistic simulations the principle of flaw tolerance by size reduction which may have had a governing influence on the evolution of the bulk nanostructure of bone-like materials and the surface nanostructure of gecko. The present study is part of an on-going effort in our research group on learning how nature designs materials and structures at nanoscale. Biology is nanotechnology by nature, and nanomechanics plays a key role in understanding the basic engineering principles used in nature.

Key words: Flaw-tolerance, structural link, continuum, atomistic, fracture, adhesion.

T. J. Chuang et al. (eds.), Nanomechanics of Materials and Structures, 139–150.
© 2006 *Springer. Printed in the Netherlands.*

1. INTRODUCTION

In this article, we discuss fundamental design concepts of structural links in biological bulk and surface materials and focus on verification of these concepts using atomistic simulation. Once characteristic materials length scales are reduced to nanoscale, mechanical properties often change dramatically. Nanomechanics is a subfield of nanoscience that deals with the mechanical behavior of materials and structures with characteristic length scales between 1 nm and 100 nm. What distinguishes nanomechanics from large-scale mechanics? Materials in nanoscale confinement often display novel mechanisms with substantially different behavior. One prominent example is that the weak van der Waals (vdW) interactions, which usually play a minor role in classical, "macroscopic" engineering, may become crucial in engineering of nanoscale-scale devices.

Nature is the unrivaled master in building and using nanodevices to perform different tasks from energy transport to assembling machines via complex control systems far beyond what human beings have ever been able to create. Therefore, biology could substantially lead the development of engineering at small scales. An important aspect in this area is controlling mechanical behaviors of nanoscale materials and devices. In this paper, we discuss how nature creates tough materials and efficient adhesion systems. We illustrate that by studying nature's design principles, it is possible to extract novel engineering concepts.

In studies of microstructures of bone-like materials, it has been discovered that these materials exhibit a generic nanostructure characterized by staggered mineral platelets embedded in a soft matrix material consisting of proteins (see Figure 1, left); see e.g., [**1-4**]. Although the matrix material is as soft as human skin, and the mineral platelets are as brittle as classroom chalk, the nanostructural combination of hard inclusions and soft matrix obviously leads to superior mechanical properties of the composite far better than the constituents. Might the nanometer length scale be the secret for such superior properties?

In related studies, it was established [**5-10**] that nature can produce very strong adhesion systems based on relatively weak van der Waals interactions. Using the same contact area as a human hand, geckos can stick strongly to a variety of chemically and mechanically different surfaces. Researchers discovered that in these systems, the size of the terminal adhesion elements is restricted to nanometer length scale. For instance, in geckos, the spatula has a typical diameter on the order of 200 nanometers [**7-10**]. Is restricting the length scale of adhesion elements to nanometer the key to explain such superior adhesion properties?

In recent studies [**1-4**], we have hypothesized that the design of nanoscale structural links is the key to understanding the properties of bulk and surface (e.g., adhesion systems) biological materials. In bulk materials, the critical structural links are the mineral platelets of the protein-mineral composite (Figure 1, left; for further details on the load transfer path, see discussions in [**1-4**]). In surface systems, the critical structural links are, for example, the spatulae of Gecko (Figure 1, right) [**5-10**]. Previously, we have used continuum mechanics concepts to establish the principle of flaw tolerance by size reduction of critical structural links. In the present paper we verify this principle by a series of atomistic simulations.

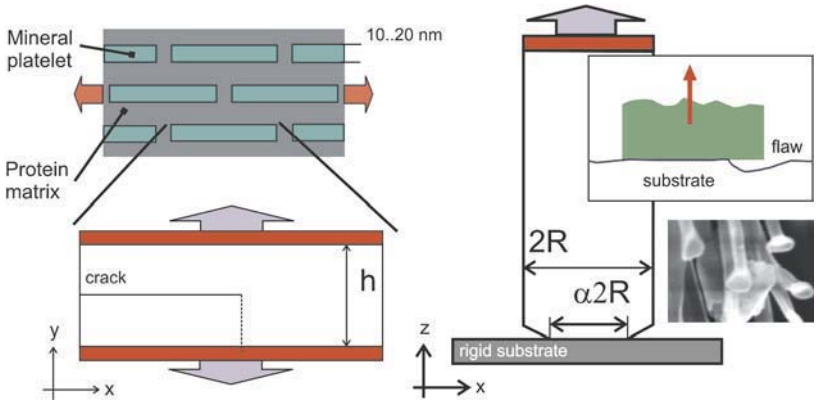

Figure 1. Left: Microstructure of bone-like biological materials. Such materials typically consist of brittle mineral platelets embedded in a protein matrix as soft as human skin. The combination of the hard inclusions and soft matrix results in superior materials properties. In our studies we focus on the fracture properties of mineral platelets. A schematic blowup shows the geometry and dimensions of a cracked platelet used in our study. Right: The schematic of our study of small scale adhesion. The model represents a cylindrical Gecko spatula attached to a rigid surface (inlay shows experimental picture by S. Gorb, MPI-MF). A circumferential crack represents adhesion flaws such as those due to surface roughness, which is depicted schematically in the inlay.

This paper is divided into two parts. We start with a discussion on the flaw tolerant property of nanoscale mineral platelets, where we consider a crack embedded in a brittle plate. We illustrate via atomistic simulations that if the width of the platelet is larger than the critical scale for flaw tolerant design, failure of the material is governed by the Griffith condition [**11**]. In contrast, if the width of the plate is below a critical size, the solid can sustain loads up to the theoretical strength, irregardless of the crack [**12**]. In the second part, we discuss robust design of biological contact elements. Considering a cylinder with radius R in contact with a rigid substrate, we show that for large radii R, the fracture condition can well be approximated

by the Griffith argument. However, when the radius of the cylinder approaches a critical length scale, the adhesion strength approaches the theoretical limit of the interface [**1-3, 9, 13**].

2. FLAW TOLERANCE OF A NANOSCALE BRITTLE MATERIAL

From classical fracture mechanics, the critical stress for crack nucleation is given by the Griffith condition $G = 2\gamma$, where γ is the fracture surface energy and G is the energy release rate [**11**]. For the geometry shown in Figure 1 (left) with strip width h, the energy release rate can be expressed as

$$G = \frac{\sigma^2 h(1-\nu^2)}{2E}, \tag{1}$$

where E is Young's modulus, ν Poisson's ratio, and σ the stress associated with an applied strain. At the critical point of onset of crack motion, the energy released must equal the energy necessary to create new surfaces. Using the Griffith condition, equation (1) can be solved for the critical applied stress (stress far ahead of the crack tip)

$$\sigma = \sqrt{\frac{4\gamma E}{h(1-\nu^2)}} \tag{2}$$

for onset of failure. For decreasing layer width h, equation (2) predicts an increasing stress for crack initiation, approaching infinity as h goes to zero. This can not be accepted since stresses can not exceed the theoretical strength of the material, denoted by σ_{th}. Equating the Griffith prediction of eq. (2) to σ_{th} immediately yields a critical layer width h_{cr} below which fracture is no longer governed by the Griffith condition, but by the theoretical strength of the material. This critical length can be easily calculated as

$$h_{cr} = \frac{4\gamma E}{\sigma_{th}^2 (1-\nu^2)}. \tag{3}$$

2.1 Atomistic modeling

To demonstrate the concept of flaw tolerance at a critical length scale, we use atomistic simulations with system sizes from several thousand atoms to several million atoms for the largest systems. We employ the ITAP-IMD code modified to model the problem of a cracked solid [**14, 15**]. The geometry is depicted in Figure 1 (left). Atoms in the red region are displaced according to a prescribed displacement field, and are otherwise rigid. The initial crack extends through the half of the slab. The slab size in the x direction is a few times larger than in the other direction. We model an FCC crystal oriented in the cubical orientation with $x=[100]$, $y=[010]$ and $z=[001]$, and the crystal is periodic in the z-direction. We use an energy minimization scheme to relax the crystal after each increment of loading. Loading is increased in very small increments of strain $\Delta\varepsilon = 0.001$ every 3,000 integration steps. We make sure that the results do not depend on the loading rate so the crystal approaches equilibrium before the next loading increment is applied. To model a perfectly brittle solid, we assume harmonic interactions in the bulk, and introduce a weak fracture layer with Lennard-Jones interactions. This constrains crack propagation along the weak layer and yields a perfectly brittle solid. With spring constant k_0 and normalization constant a_0, the harmonic interactions are defined as

$$\phi(r) = a_0 + k_0 (r - r_0)^2, \tag{4}$$

and the 12:6 Lennard-Jones (LJ) potential is given by

$$\phi(r) = 4\varepsilon\left(\left(\frac{\sigma}{r}\right)^{12} - \left(\frac{\sigma}{r}\right)^{6}\right) \tag{5}$$

with $\varepsilon = \sigma = 1$. The nearest neighbor distance $r_0 = 2^{1/6}$ is fitted to the spacing given in the LJ potential. Atoms in the bulk only interact with their nearest neighbors, and interactions across the weak fracture layer are cut off at a critical distance $r_{cut} = 2.5$. In this model, E can be varied independently from the other variables in equation (3), allowing tuning h^{cr} to within a range easily accessible to the MD simulations and to check the scaling law suggested in equation (3). All quantities are given in reduced units. Energies are scaled by the depth of the LJ potential ε and length scales are given in reduced units of σ. The shear modulus can be shown to be [**15**]

$$\mu = \frac{r_0^2}{2} k_0 . \tag{6}$$

The Young's modulus for the crystal orientation considered is given by $E = 8\mu/3$, and Poisson's ratio is $\nu = 1/3$. The fracture surface energy can be expressed as

$$\gamma = N_b \rho_A \Delta\phi \tag{7}$$

where N_b is the bonds of each atom across the surface, ρ_A is the density of surface atoms and $\Delta\phi$ is the potential energy stored in each bond. For the (010) fracture surface, the density of surface atoms is $\rho_A = 1/r_0^2 \approx 0.794$, and $N_b = 4$. The potential energy difference per bond is given by $\Delta\phi \approx 1$. Further details on the procedure are published elsewhere [**4, 15**].

2.2 Simulation results

Figure 2a plots the critical stress normalized by the theoretical strength for initiation of failure. The plot reveals that for thick layers $h > h_{cr}$, the Griffith condition is the governing measure for initiation of failure. In contrast, for small thicknesses $h < h_{cr}$, the stress magnification in the material vanishes, and failure occurs when the applied stress equals the theoretical strength. We observe that the transition from the Griffith-behavior to the flaw-tolerant behavior occurs smoothly, unlike the prediction by the linear elastic continuum mechanics theory [**2**]. Similar observation was made in the nonlinear VIB calculations of the problem [**12**], and the deviation can be attributed to the nonlinear character of the potential across the interface.

Figure 2b plots the distribution of the stress field a slight distance ahead of the crack just before failure of the material occurs. As the width of the strip is decreased, the stress distribution becomes more and more homogeneous. If the layer width is well below the critical length scale given by equation (3), the stress distribution ahead of the crack is homogeneous and does not depend on the choice of h any more. These results are in agreement with the predictions by the continuum modeling [**1**].

We have performed similar calculations with a material where the atomic interactions are defined by LJ in the whole slab. Similar behavior as reported for the model featuring the weak layer is observed. However, for the LJ potential, the critical length scale is on the order of a few atomic spacings, which makes it difficult to observe the saturation in strength. To prove the concept of flaw tolerant design, the weak layer approach allowing

independent variation of the elastic properties of the bulk provides a reasonable way to show the concept of flaw tolerant material design. The atomic values of the stress are averaged over space to approach the continuum limit of the virial stress (see e.g., [**4, 15**]).

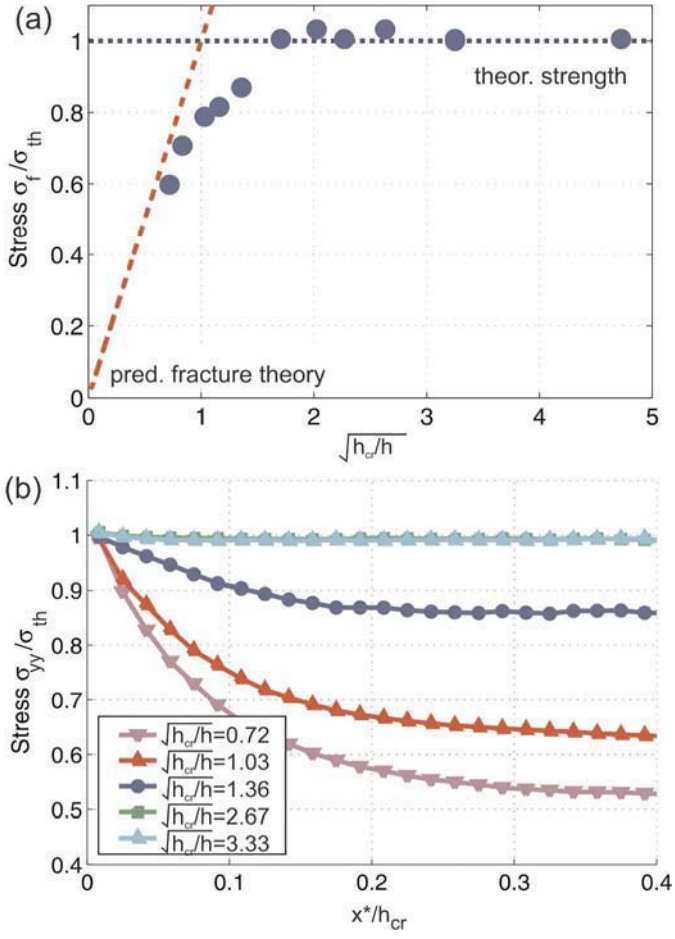

Figure 2. As the structural size reduces, a brittle material becomes flaw tolerant. This is identified by both a change in failure mechanism (subplot (a)) from Griffith failure to failure at the theoretical strength, and by the observation that the stress distribution ahead of the crack becomes increasingly homogeneous as the dimensions shrink (subplot (b)).

3. FLAW TOLERANT OF A NANOSCALE ADHESIVE JOINT

Here we perform atomistic simulations to investigate adhesion of a nanoscale spatula on a rigid substrate, similar to the studies reported in [**4,9,12**] based on continuum mechanics analyses. We consider a single spatula attached to a rigid substrate (Fig. 1, right). The spatula is modeled as a cylinder with radius R. Perfect contact between the substrate and the spatula is assumed only for $r < \alpha R$, and no contact is assumed for $\alpha R < r < R$, mimicking the existence of flaws. In our atomistic calculations we assume $\alpha = 0.7$ (corresponding to the case when the actual contact area is about 50 % of the total area available for contact). The outer region represents a flaw or regions with poor adhesion. For this particular geometry, according to the predictions by theory [**4,9,12**], the saturation in strength should occur at a critical radius R^{cr} similar to the length scale obtained for fracture of a nanoscale material. The main objective of the present study is to use atomistic simulations to show that (i) the stress distribution becomes more homogeneous as the radius of the spatula approaches the critical radius R^{cr}, and (ii) that the maximum strength of the interface is governed by the Griffith condition for $R > R^{cr}$, and approaches the theoretical strength for $R < R^{cr}$.

3.1 Atomistic modeling

Consider the geometry as depicted in Figure 1 (right). The spatula is in contact with a rigid substrate [**10, 13**]. Atoms in the red region are displaced according to a prescribed displacement field. As in the previous case, we assume an FCC crystal oriented in the cubical orientation, that is $x = [100]$, $y = [010]$ and $z = [001]$. The height in the z direction is several times the radius. Different choices of the height are used and no major difference in the behavior is observed. We use an energy minimization scheme to relax the structure after each increment of loading. Similarly as in Section 2.1, we select the loading rate slow enough such that elastic equilibrium is reached before the next loading increment is applied. As described above, we assume harmonic interactions (equation (4)) in the bulk, and introduce LJ interactions (equation (5)) to model adhesion between the spatula and the rigid substrate. The LJ potential serves as a model for weak vdW interaction across the interfaces, as suggested by recent experimental results of the interactions of spatula-substrate in Geckos [**5-9**]. As in the previous case, the Young's modulus of the spatula is adjusted such that the relevant length scales are accessible to MD simulations.

3.2 Simulation results

Figure 3 (a) plots the strength of the interface normalized by the theoretical interface strength over the inverse of the square root of the spatula radius. The plot reveals that for large radii $R > R_{cr}$, the Griffith condition is the governing measure for initiation of failure. In contrast, for small radii $R < R_{cr}$, the critical stress to initiate failure along the interface approaches the theoretical strength. We observe that the transition from the Griffith-behavior to the flaw-tolerant behavior occurs more smoothly than in the previous case (compare the curves in Fig. 2a).

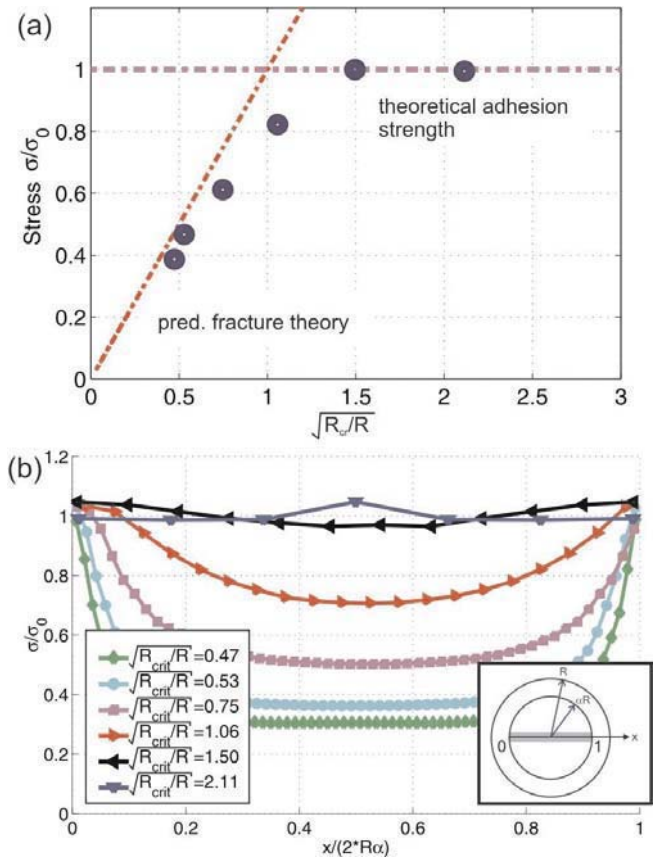

Figure 3. As the structural size reduces, the adhesive contact becomes more and more flaw tolerant. This is identified by both a change in failure mechanism (subplot (a)) from Griffith failure to failure at the theoretical adhesion strength, and by the observation that the contact stress distribution becomes increasingly homogeneous as the dimensions shrink (subplot (b)). Notably, the stress distribution is independent of the size of the contact element if the dimension is below the critical length scale.

Figure 3b plots the distribution of the contact stress σ_{zz} (virial average across a thin strip) in the cylinder. The radial direction is normalized by the radius associated with the contact area. As the radius is decreased, the stress distribution becomes more and more homogeneous. This observation is consistent with our expectations from a theoretical point of view [**4, 10, 12**]. The most important result of the analysis is that as the radius of the cylinder approaches the critical length scale, the contact stress distribution becomes more and more homogeneous. As a consequence, the strength of the interface increases and approaches a constant value independent of size.

4. DISCUSSION

We have been using continuum [**1, 4, 9, 12, 13**] and atomistic concepts [**4, 15**] to investigate the principle of flaw tolerance of nanoscale structural links in biological materials. The atomistic simulations reveal a smooth transition between Griffith mode of failure via crack propagation to uniform bond rupture at theoretical strength below a nanometer critical length, as shown in Figs. 2a and 3a. Below the critical length for flaw tolerance, the stress distribution becomes uniform near the crack tip, as clearly shown in Fig. 2b and 3b. The atomistic simulations thus fully support the previous hypothesis that materials become insensitive to flaws below a critical nanometer length scale [**1, 10, 11**].

At the beginning of this article, we asked if there is a common design principle for structural links in biological materials. The present studies show that the answer is very likely to be positive. The common design principle can be summarized in one sentence:

> *Nature selects nano-substructures to achieve robust, flaw-tolerance structural links*

This principle is found in different systems, including bulk and surface biological materials, and our investigations suggest not only "the smaller the stronger", but also a critical length scale to gauge the robustness of a structural link. This is underlined by the fact that such "robust design" has been developed in genetically independent species. The concept of robustness is found in completely different areas of biology as well: For instance, slight variations in genetic expressions do usually not lead to catastrophic consequences but rather help to improve the properties of its species. The adaptability of organisms to different environments is another example for successful, robust design of organisms. Robustness obviously has vast advantages for organisms to survive and thrive.

Finally, we remark that nature does not distinguish between different scientific disciplines, for instance materials and structures. It seems that mechanics (structure) and chemistry (material) are used by nature with equal importance to achieve optimized materials properties. Research on nanomechanics of biological systems such as that reported in this paper may help engineers design superior materials and structures in the future.

ACKNOWLEDGMENTS

MJB acknowledges the Institute for Theoretical and Applied Physics at the University of Stuttgart for providing their MD simulation code, and the Max Planck Society for a Postdoc fellowship.

REFERENCES

1. Gao H, Ji B, Jaeger IL, Arzt E, Fratzl P, "Materials become insensitive to flaws at nanoscale: lessons from nature", *Proc. Natl. Acad. Sci. USA*, **Vol. 100**, pp. 5597-5600, 2003.
2. Jaeger I and Fratzl P, "Mineralized collagen Mbrils: a mechanical model with a staggered arrangement of mineral particles", *J. Biophys.,* **Vol. 79**, pp. 1737–1746, 2000.
3. Okumura K, and de Gennes P.–G. "Why is nacre strong? Elastic theory and fracture mechanics for biocomposites with stratified structures", *Europ. Phys. J*., **Vol. E 4**, pp. 121-127, 2001.
4. Gao H, Ji B, Buehler, MJ, Yao, H, "Flaw tolerant bulk and surface nanostructures of biological systems", *Mechanics and Chemistry of Biosystems,* **Vol. 1**, pp. 5-12, 2004.
5. Scherge M, Gorb SN, *Biological Micro and Nano-Tribology*, Springer-Verlag, New York, 2001.
6. Autumn K, Sitti M, Liang YA, Peattie AM, Hansen WR, Sponberg S, Kenny TW, Fearing R, Israelachvili JN, and Full RJ, "Evidence for van der Walls adhesion in gecko setae", *Proc. Natl. Acad. Sci. USA*, **Vol. 99**, pp.12252-12256, 2002.
7. Arzt E, Enders S, and Gorb S, "Towards a micromechanical understanding of biological surface devices", *Z. Metallk*., **Vol. 93**, pp. 345-351, 2002.
8. Arzt E, Gorb S, Spolenak R, "From micro to nano contacts in biological attachment devices", *Proc. Natl. Acad. Sci. USA*, **Vol. 100**, pp. 10603-10606, 2003.
9. Persson BNJ, "On the mechanism of adhesion in biological systems", *J. Chem. Phys.,* **Vol. 118,** pp.7614-7621, 2003.
10. Gao, H. Yao, H. "Shape insensitive optimal adhesion of nanoscale fibrillar structures", *Proc. Natl. Acad. Sci. USA* **101** (2004), 7851–7856.
11. Griffith AA, "The phenomenon of rupture and flows in solids" *Phil. Trans. R. Soc. London A* **221** (1921), 163-198.
12. Gao H and Ji B, "Modeling Fracture in Nano-Materials via a Virtual Internal Bond Method", *Eng. Fract. Mech.*, **Vol. 70**, pp. 1777–1791, 2003.
13. Gao H, Wang X, Yao H, Gorb S and Arzt E, "Mechanics of hierarchical adhesion structure of gecko", *Mechanics of Materials*, in the press, 2004.

14. Roth J, Gähler F, and Trebin H-R, "A molecular dynamics run with 5.180.116.000 particles", *Int. J. Mod. Phys. C,* **Vol. 11**, pp. 317-22, 2000.
15. Buehler MJ, *Atomistic and continuum studies of deformation and failure in brittle solids and thin film systems*, PhD Thesis, University of Stuttgart, Germany, 2004

TOWARDS THE INTEGRATION OF NANO/MICRO DEVICES USING MEMS TECHNOLOGY

Weileun Fang, Jerwei Hsieh, and Hung-Yi Lin
Power Mechanical Engineering Dept, National Tsing Hua University, Hsinchu, Taiwan, phone:(886-3)574-2923, fax:(886-3)572-2840, email: fang@pme.nthu.edu.tw

Abstract: Technology platform is the key issue to accelerate the progress of N/MEMS. MUMPs is recognized as the first fabrication platform for MEMS. Many promising MEMS devices have been realized through the MUMPs platform. According the variety of MEMS devices, unique fabrication platform is unable to fulfill the requirements. Presently, other platforms such as SCREAM, SUMMIT, MPW, and CMOS-MEMS have been successfully explored or still under investigation. This presentation intends to introduce two fabrication platforms, named MOSBE and BELST, established in the Micro Devices laboratory of National Tsing Hua University. Moreover, various applications fabricated using these two platforms will also be presented.

Key words: Fabrication platform, MUMPs process, MOSBE process, BELST process.

1. INTRODUCTION

Technology platform is the key reason to accelerate the progress of MEMS. For instance, the MUMPs platform [**1**] enables the fast evolution of optical MEMS at late 90'. Due to the variety of MEMS devices, sole platform technology is not enough to fulfill the requirements. Presently, there are many platforms such as Sandia's SUMMIT [**2**], SensNor's MPW [**3**], and Cornell's SCREAM [**4**] have been developed. In addition, the well-known CMOS process has also been exploited to fabricate MEMS devices [**5**].

T. J. Chuang et al. (eds.), Nanomechanics of Materials and Structures, 151–159.
© 2006 *Springer. Printed in the Netherlands.*

In this study, I would like to present two fabrication platforms, named MOSBE [**6**] and BELST [**7**] processes, established in micro devices laboratory, National Tsing Hua University. The former platform is mainly used to fabricate thin film structures and devices. On the other hand, the later is employed to fabricate HARM (high aspect ratio micromachining) devices. Various MEMS devices are available in this study to demonstrate the potential applications of these two platforms.

2. MOSBE PLATFORM

The concept behind MOSBE process is shown in Fig. 1. Firstly, the DRIE is used to etch a depth around ~10 μm. Secondly, the standard surface micromachining process is exploited to fabricate structures around ~1μm thick. Finally, the bulk silicon etching is employed to provide a large free space under the structure.

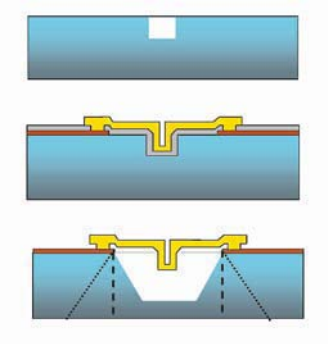

Figure 1. The schematic of MOSBE platform

According to MOSBE processes we can change the shape as well as the moment of inertia of the structure. Thus the stiffness of the microstructure can be significantly increased. However, the thickness of the structure remains the same. As shown in Fig. 2a, the measured tip deflection of the MOSBE beam was significantly reduced from 8 μm to less than 1 μm [**8**]. The MOSBE process can also be exploited to increase the flatness of the micro mirror [**9**]. As shown in Fig. 2b, the boundary of the mirror is changed from free to clamed condition after adding the reinforced frame. Therefore, the stiffness of the mirror is increased. The bending deformation of the mirror due to the static residual stress and the dynamic inertia force can be reduced.

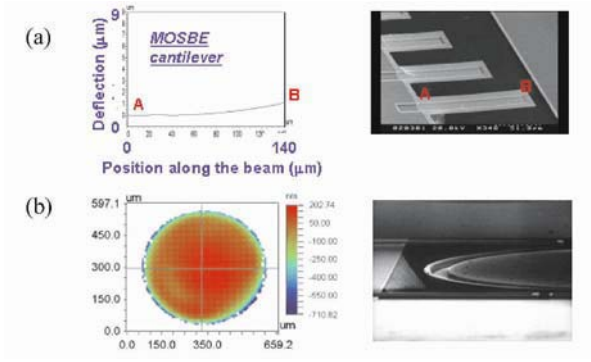

Figure 2. Passive MOSBE components, (a) rib reinforced cantilever, and (b) flat mirror.

In addition to the passive components, various actuators are also developed using the MOSBE process. Figure 3a shows an electrostatic actuator, named META engine [**10**]. When the electrostatic force applied through the electrode, the plate will rotate about the torsional spring. The MOSBE process provide a large cavity under the plate, thus the angular motion of the plate is increased. However, the space between the electrodes is still the same, so that the driving voltage remains unchanged. Figure 3b shows another electrostatic actuator, named EDLA Engine [**11**]. The EDLA engine is consisted of a parallel electrode and a lever. During operation, the electrode will be pull down by the electrostatic force, and the output displacement is significantly magnified by the lever. A large area gap-closing electrode is used to decrease the driving voltage to merely less than 25 volts. According to the lever mechanism, the output displacement can be greater than 15 μm.

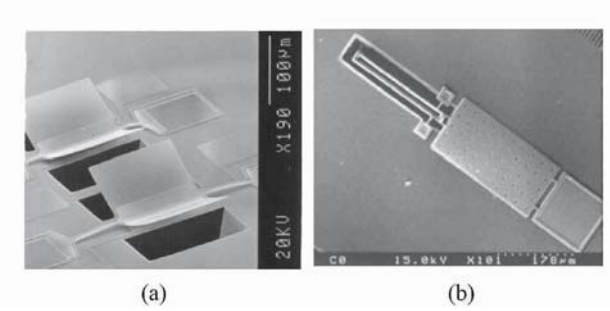

Figure 3. Active MOSBE components, (a) META engine, and (b) EDLA engine

After integrating the actuator and the passive components, various devices have been constructed. For instance, the scanner shown in Fig. 4 is consisted of a flat mirror, two couplers, and four EDLA engines [**12-13**]. According to the measurement results, it can reach a 17.7 kHz scanning rate. Figure 4 also shows the light spot scanning by the scanner. Other applications such as optical switch, and variable optical attenuator (VOA) are also available in Fig. 5 [**6**].

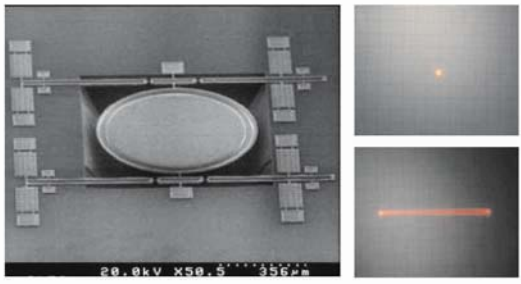

Figure 4. The MOSBE optical scanner.

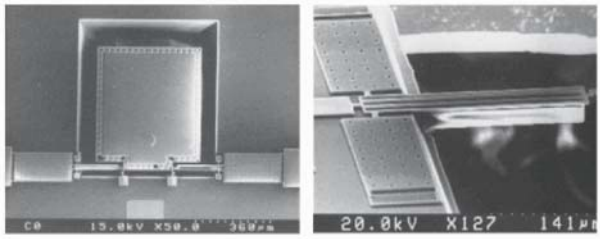

(a) (b)

Figure 5. Applications of the MOSBE devices, (a) Optical switch, and (b) VOA

3. BELST PLATFORM

The devices fabricated through MOSBE are thin film structures. In some cases, the thick or HARM structures are required to increase the stiffness, output force, or sensing signal. To meet these requirements, the second fabrication platform, named BELST processes, has also been established [**7**].

The concept behind BELST process is illustrated in Fig. 6. In BELST process, the DRIE is used to etch (111) silicon substrate. Then, the boron doped layer is used to form the electrode and the protection layer for etching.

After that the DRIE is used to define the gap between the moving structure and the substrate.

Finally, bulk Si etching is used to release the moving structure.

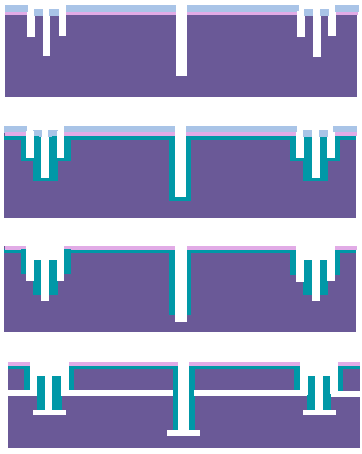

Figure 6. Concept of the BELST platform

There are many passive HARM components have been fabricated using the BELST platform, for instance, the rotor, spring, and beam shown in Fig. 7. As indicated on the SEM photo, the thickness of these components is near 50 μm. Active HARM components are also available. Figure 8a shows a liner actuator driven by the electrostatic force which came from the comb electrodes. Moreover, the electrostatic angular actuator is also available using the BELST process, as shown in Fig. 8b. This angular actuator is also driven by the comb electrodes. Both of the actuators in Fig. 8 are performing in-plane motion only.

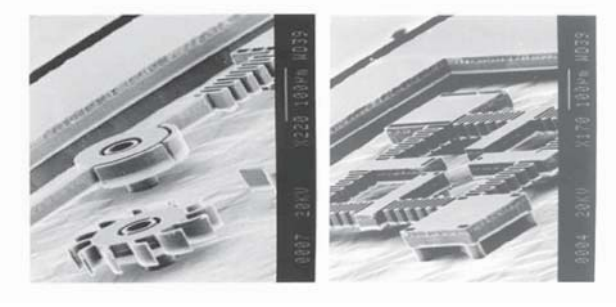

Figure 7. Passive components fabricated by MOSBE process

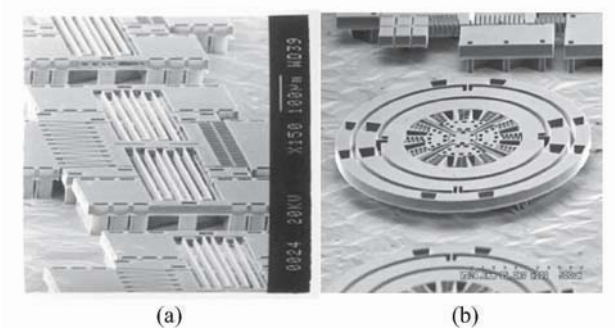

Figure 8. Actiive components fabricated by MOSBE process, (a) linear, and (b) angular in-plane motion actuators

The out-of-plane motion is crucial for various optical applications, for instance, the scanner and the switch. However, the devices fabricated using the BELST process have uniform thickness, and are difficult to perform out-of-plane motion. Accordingly, the BELST II process which containing more DRIE and film deposition than BELST is developed [**14**]. The BELST II process allows the HARM structures to have different thickness. Thus the vertical comb actuator (VCA) shown in Fig. 9a became available [**15**]. Three advantages for this VCA can be observed. Firstly, through some exquisite designs the fabrication process has no critical alignment and bonding problems. Secondly, the relative vertical position between the moving and the stationary fingers can be adjusted freely to optimize the performance of the VCA. Thirdly, both the large mirror structure and the trimmed torsional spring shown in Fig. 9b are available through this process. Thus improved performance regarding enlarged traveling distance with reduced driving voltage can be obtained. The angular motion actuator shown in Fig. 8b can be exploited as a gyroscope. Other potential applications of the BELST platform, including the optical scanner [**15**] and the VOA [**16**], are shown in Fig. 10.

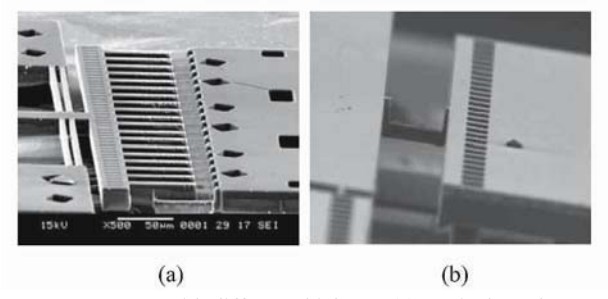

Figure 9. BELST structures with different thickness (a) vertical comb actuator, and (b) trimmed torsional suspension

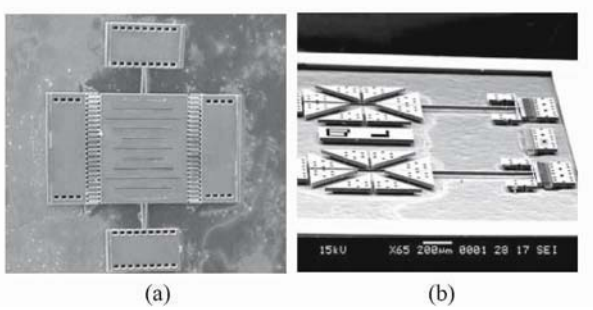

Figure 10. Applications of the BELST devices (a) optical scanner, and (b) VOA

4. DISCUSSION AND CONCLUSION

The fabrication processes of MEMS devices originated from the planar technology. Consequently, it is important to establish the fabrication platform to enhance the applications of MEMS. MUMPs has been demonstrated as a promising fabrication platform for MEMS. Many MEMS devices have been realized through the MUMPs platform. On the other hand, the mechanical behaviors are primary considerations while designing MEMS devices. The variety of the MEMS structures and devices are much larger than that of the IC. Thus, unique fabrication platform is unable to fulfill the requirements of MEMS devices. This study presents two fabrication platforms, named MOSBE and BELST, established in the Micro Devices laboratory of National Tsing Hua University. Moreover, various applications fabricated using these two platforms will also be presented.

The existing fabrication platform cannot meet with the requirements of all MEMS devices. It is possible to partially modify the fabrication processes to enhance the capability of the existing platform. For instance, based on the MUMPs platform, this study has established an improved fabrication process (MUMPs-like process) [**17**]. Through this process, the improved stress-induced self-assembly supporting mechanism has been realized. This supporting mechanism has been employed to lift up and assemble the 3-D optical switch shown in Fig. 11 [**17**]. According to the result of reliability test, stress relaxation is significantly reduced using the dielectric film instead of the metal film. Furthermore, a novel VOA as shown in Fig. 12 is also demonstrated using this MUMPs-like platform. In summary, with the improved stress-induced beam and stronger locking component, the robust and reliable stress-induced self-assembly supporting mechanism for optical devices becomes available.

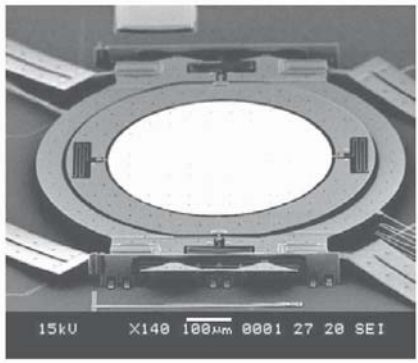

Figure 11. 3-D optical switch fabricated by MUMPs-like platform

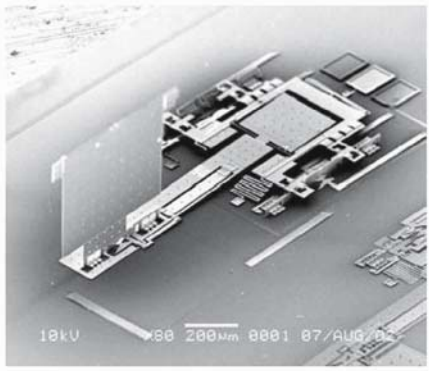

Figure 12. VOA fabricated by MUMPs-like platform

ACKNOWLEDGMENTS

This project was partially supported by NSC (NSC 93-3113-P-001-019). The authors also appreciate the NSC Central Regional MEMS Center of National Tsing Hua University, NSC Nano Device Laboratories, and Semiconductor Research Center of National Chiao Tung University in providing fabrication facilities.

REFERENCES

1. http://www.memsrus.com/cronos/svcsmumps.html.
2 http://www.sandia.gov/mstc/micromachine/overview.htm
3. http://www.sensonor.com/.
4. Z.L. Zhang and N.C. MacDonald, "An RIE Process for Submicron, Silicon Electromechanical Structures," *J. Micromech. Microeng*., **Vol. 2**, pp. 31-38, 1992.
5. http://www.ece.cmu.edu/~mems/projects/cmos-mems.s
6. H.-Y. Lin, M. Wu, M.-L. Tsai, and W. Fang, "Towards a Light Wave MEMS Platform Using MOSBE Process," *IEEE Optical MEMS*'01, Okinawa, Japan, Sept. 2001.
7. J. Hsieh, and W. Fang, "BELST Process for Improved High-aspect-ratio Silicon Micromachining and Its Applications," *J. Micromech. Microeng*, **Vol. 12**, pp. 574-581, 2002.
8. H.-Y. Lin, and W. Fang, " Rib-reinforced micromachined beam and it applications ," *J. Micromech. Microeng*, **Vol.10**, pp.93-99, 2000.
9. H.-Y. Lin, and W. Fang, "The Improvement of the Micro Torsional Mirror by a Reinforced Folded Frame," *ASME IMECE*, Orlando, FL, Nov. 2000.
10. J. Hsieh and W. Fang, "A Novel Microelectrostatic Torsional Actuator," *Sensors and Actuators A*, **Vol. 79**, pp. 64-70, 2000.
11. H.-Y. Lin, H.-H. Hu, W. Fang, and R.-S. Huang, "Electrostatically-driven-leverage actuator as an engine for out-of-plane motion," *Transducer*'01, Munich, Germany, 2001.
12. H.-Y. Lin, and W. Fang, "Torsional Mirror with an Electrostatically Driven Lever-Mechanism," *IEEE Optical MEMS* 2000 , Kauai, Hawaii, August 2000.
13. H.-Y. Lin and W. Fang, 2002, "A Reinforced Micro-torsional-mirror Driven by Electrostatic Torque Generators," *Sensors and Actuators A*, (accepted).
14. J. Hsieh, C.C. Chu, J.M. Tsai, and W. Fang, "Using Extended BELST Process in Fabricating Vertical Comb Actuator for Optical Applications," *IEEE/LEOS Optical MEMS*'02, Lugano, Switzerland, August 2002.
15. C.-C. Chu, J.-M. Tsai, J. Hsieh, and W. Fang, "A Novel Electrostatic Vertical Comb Actuator Fabricated on (111) Silicon Wafer," *IEEE MEMS*'03, Kyoto, Japan, Jan 2003.
16. J.-M. Tsai, C.-C. Chu, J. Hsieh, and W. Fang, "A Large Out-of-plane Motion Mechanism for Optical Applications," *IEEE/LEOS Optical MEMS'*02, Lugano, Switzerland, August 2002.
17. Y.-P. Ho, M. Wu, H.-Y. Lin, and W. Fang, "A Robust and Reliable Stress-induced Self-assembly Mechanism for Optical Devices," the *IEEE Optical MEMS* 2002, Lugano, Switzerland, August 2002

ATOMIC SCALE MECHANISMS OF STRESS PRODUCTION IN ELASTOMERS

A.F. Bower and J.H. Weiner
Division of Engineering, Brown University, Providence RI 02912,U.S.A.
Phone: (401)863-1493; Fax: (401)863-1157; Email: Allan_Bower@brown.edu, Jerome_Weiner@brown.edu

Abstract: We outline a series of molecular dynamics computations that reveal an intimate connection at the atomic scale between difference stress (which resists stretches) and pressure (which resists volume changes) in an idealized elastomer, in contrast to the classical theory of rubber elasticity. Our model predicts behavior that is in good agreement with experimental data of D.L. Quested, K.D. Pae, J.L. Sheinbein and B.A. Newman, J. Appl. Phys, 52, (10), 5977 (1981) for the influence of pressure on the difference stress induced by stretching solithane. Further studies along these lines offer opportunities to elucidate the atomic scale mechanisms that control the constitutive behavior of polymers, with the long-term goal of atomic scale materials design.

Key words: Rubber elasticity, molecular dynamics

1. INTRODUCTION

The mechanical response of polymers is a concern in many practical applications, including design of structural materials and composites; materials used for microelectronic packaging and dielectrics; and biological materials. By modifying their molecular structures, it is possible to design polymers with a wide range of mechanical properties. It is therefore of great interest to develop a fundamental understanding of the atomic scale processes that determine the elastic and visco-elastic properties of an elastomer or polymer melt. In this paper, we shall outline recent progress towards this goal, and suggest opportunities for further study. For brevity, we shall focus exclusively on a particular issue involving only one class of polymers. Specifically, our goal is to elucidate the atomic scale processes

T. J. Chuang et al. (eds.), Nanomechanics of Materials and Structures, 161–170.
© 2006 *Springer. Printed in the Netherlands.*

responsible for generating stress in rubbers, by means of simple molecular dynamic simulations.

It is well known that rubbers have several unique mechanical properties. They strongly resist volume changes, and have a shear modulus comparable to metals or covalently bonded solids. In contrast, they are highly compliant in shear, and typically have a shear modulus that is several orders of magnitude less than metals. The shear response is strongly dependent on temperature: at appropriate temperatures (above the glass transition) the shear modulus increases linearly with temperature, in sharp contrast to nearly all other materials. Finally, when rubber is stretched, it gives off heat.

This behavior is, of course, explained by the classical theory of rubber elasticity. In the classical theory, the response of rubber to volume changes and to volume-preserving (shear) deformations is treated separately. The volumetric response is attributed to liquid-like excluded volume interactions between mers on each chain, while the deviatoric (shear) response is attributed to the long chain molecules acting as entropic springs. In this picture, excluded volume interactions between mers play no role in generating deviatoric stress.

One example of a simple, and widely used, atomic scale theory of the deviatoric response of rubbers is the so called `affine network' model. In its simplest form, this model idealizes the solid as a set of long chain molecules, on which the mers interact through rigid bonds that permit rotation, but constrain the distance between neighboring mers. The end-to-end vectors of each chain are assumed to undergo the same affine deformation that characterizes the macroscopic deformation. In this model, the ends of each chain are intended to model junctions in a cross-linked polymer network. Therefore, junction fluctuations due to thermal motion are omitted from the model, as are any excluded volume interactions or entanglements. For the case of uniaxial, constant volume extension λ in the x_1 direction, the model predicts, for sufficiently small λ, the difference stress

$$t_{11} - t_{22} = \frac{N_c kT}{v}\left(\lambda^2 - \lambda^{-1}\right) \tag{1}$$

where t_{ij} denote the components of the Cauchy stress tensor, N_c is the number of identical chains in volume v, k is the Boltzmann constant, and T is temperature.

The classical models of rubber elasticity are widely accepted and predict shear response that is in good qualitative and quantitative agreement with experimental measurements under ambient pressure. Nevertheless, there is experimental evidence that suggests that the classical theory is, at best, incomplete. For example, the entropic spring model cannot account for the strong influence of pressure on uniaxial stress-v-stretch response observed experimentally by Pae and co-workers [**1**]. In this paper, we shall use simple

molecular dynamic simulations to show that, in contrast to the classical theory of rubber elasticity, pressure or mean stress (which resist volume changes) and deviatoric stress (which resists constant-volume shape changes) are intimately connected.

2. ATOMIC SCALE MODEL

Our simulations use the simplest model that captures the essential features of a rubbery material at the atomic scale. The solid is idealized as a collection of atoms which interact with two types of potentials: a bonding potential u_b, which models the covalent bonds that are responsible for the chains; and a potential u_{nb} that models the interaction between all nonbonded atoms; interchain and intrachain. The covalent bonds (u_b) are idealized as stiff linear springs, while nonbonded interactions (u_{nb}) are approximated using a truncated Lennard-Jones potential

$$u_b(r) = \frac{1}{2}\kappa(r-a)^2$$

$$u_{nb}(r) = \begin{cases} 4\in_{LJ}\left[\left(\frac{\sigma_{LJ}}{r}\right)^{12} - \left(\frac{\sigma_{LJ}}{r}\right)^{6}\right] & r \le R_c \\ u(R_c) & r > R_c \end{cases} \qquad (2)$$

where R_c denotes a convenient cutoff (equal to half the simulation cell size in our computations). A model rubber system with $N_c = 40$ chains and with $N_b = 19$ bonds per chain is formed by specifying those atoms of the system that interact pairwise through u_b. The system is illustrated schematically in Fig. 1. In all our simulations, the bond length a and the radius of the Lennard-Jones potential σ_{LJ} are taken to be equal. Values for remaining parameters in our computations are given in ref. [**2**].

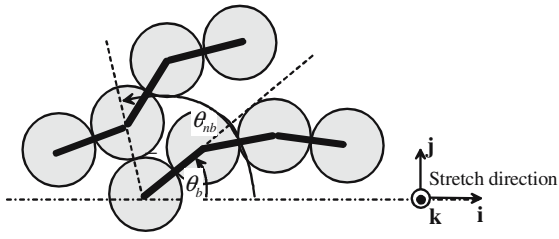

Figure 1. A schematic diagram illustrating the idealized model of the atomic structure of rubber used in molecular dynamic simulations.

The chain network is idealized using a simple extension of the classical 'affine network' model: it consists of a similar set of chains, which interact through both covalent and non-bonded interactions. All of the atoms are free to undergo thermal motion, but the end atoms on each chain are constrained to maintain a constant end-to-end vector as the chains move through the system. When the simulation cell is deformed, the chain vectors, as well as the boundaries of the simulation cell, are subjected to the same affine deformation.

A typical simulation begins by generating a cubic unit cell, with side length L, volume $v = L^3$, which contains N_c identical chains, each with N_b bonds. Periodic boundary conditions are imposed on all sides of the cell. The set of initial chain vectors $\mathbf{R}_0(n)$ with $n = 1,2,3\ldots N_c$ are generated by means of a random walk along each chain, and therefore have an approximately uniform orientation distribution and Gaussian distribution of lengths. The cell is then deformed (at constant temperature) by transforming the shape of the basic cell, and imposing the same affine deformation $\mathbf{R}_0(n) \mapsto \mathbf{R}(n)$ on all chain vectors. As a particular example, we focus on the response of the system to a volume-preserving uniaxial stretch λ parallel to the x_1 axis. The system is then annealed until it reaches equilibrium, and the time average of the Cauchy stress tensor is computed by means of the virial stress formula

$$vt_{ij} = -\rho v k T \delta_{ij} + \sum_{\alpha} \left\langle f_i^{\alpha} r_j^{\alpha} \right\rangle \tag{3}$$

$\rho = N / L^3$ is the number of atoms per unit volume, r_j^{α} are the components of the vector $\mathbf{r}_{\alpha}$ connecting the αth pair of atoms, and f_i^{α} is the bond force. The sum over α is taken over all atom pairs in the system, and the brackets denote long-time averages.

This procedure is repeated for an ensemble of 250 basic unit cells, and the ensemble average of the stress is determined. The normalized mean stress $\Pi = vt_{kk} / 3kT$ (which does work through volume changes) and difference stress $\sigma = v(t_{11} - t_{22}) / kT$ (which does work through volume-preserving deformations) are of particular interest. In particular, we shall compute these stress components as a function of stretch λ, temperature, and reduced density

$$\rho^* = N\sigma_{LJ}^3 / L^3 \tag{4}$$

where $N = (N_b + 1)N_c$ denotes the number of atoms in the unit cell, and σ_{LJ} denotes the radius of the Lennard-Jones potential.

3. RESULTS AND DISCUSSION

Fig 2(a) shows the normalized difference stress as a function of stretch λ for the system, while Fig. 2(b) shows the mean stress predicted by our numerical simulations as a function of reduced density ρ^* for several values of normalized temperature. For comparison, the chain line in Fig 2(a) shows the results of a simulation in which the nonbonded interactions were not included. As a partial check on the accuracy of our simulations, the predictions of this computation may be compared to the analytical solution for ideal Gaussian chains, Eqn. 1, which is shown as a dashed line. The response predicted by molecular dynamic simulations is broadly in agreement with the classical theory; we do observe, however, an influence of reduced density on difference stress that is not predicted directly by classical models.

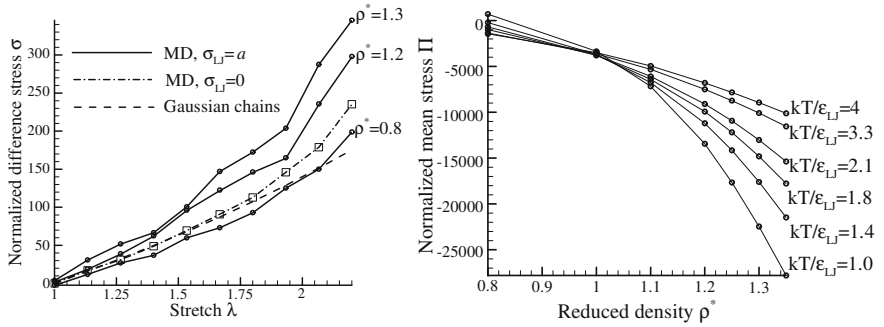

(a) *(b)*

Figure 2. (a) Normalized difference stress as a function of stretch, for temperature $kT/\in_{LJ}=3.5$; (b) Mean stress as a function of reduced density, for stretch $\lambda=1.6$.

The variation of difference stress with temperature, shown in Fig. 3, also shows a marked departure from the classical theory. Results are shown for two different stretches and for several values of reduced density. For $\rho^*=0.8$ the stresses vary linearly with temperature over the full range covered in our simulations, as predicted by the entropic spring model. For higher values of reduced density, this linear variation is observed only at high temperatures. For low temperatures, the stress begins to rise as temperature is reduced, and this effect becomes more pronounced as ρ^* is increased. We have some preliminary evidence [**2**] that the rise in stress at low temperatures and high reduced density is associated with a glass transition, but further study is required to fully elucidate the behavior of the system in this regime.

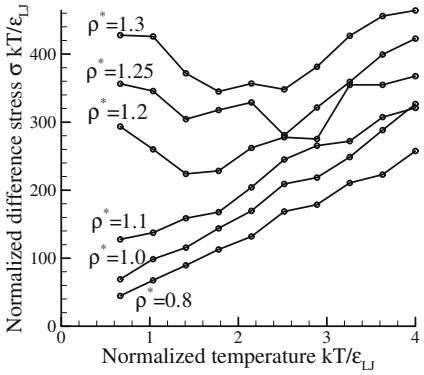

Figure 3. The variation of difference stress with temperature and reduced density, for $\lambda = 1.6$. The stress has been re-normalized to show temperature dependence clearly.

We turn next to examine in more detail the atomic-scale processes that give rise to the macroscopic stress-stretch behavior. In both the classical theory, as well as in our molecular dynamic simulations, the difference stress is closely related to deformation-induced anisotropy in the orientation of the covalent bonds. One may define a scalar measure of bond anisotropy as $\langle P_2(\theta_b)\rangle = \left\langle\left\langle (3\cos^2\theta_\alpha - 1)/2 \right\rangle\right\rangle$, where θ_α is the angle between a representative covalent bond and the x_1 direction, (Fig. 1), and the double carats denote averages over all bonds, over all members of the ensemble, and over time. In the affine network model, bond anisotropy is related to stretch by the well known Kuhn and Grun relation $\langle P_2(\theta_b)\rangle = (\lambda^2 - \lambda^{-1})/5N_b$. We observe a similar relation of the form $\langle P_2(\theta_b)\rangle = F(\rho)(\lambda^2 - \lambda^{-1})/5N_b$ in our simulations, but $F(\rho)$ exceeds unity and varies slightly with reduced density, as illustrated in Fig. 4(a).

Evidence for the role of bond anisotropy in generating difference stresses is provided by a relationship between the difference stress and the bond orientation measure of the form $\bar{\sigma} = C\langle P_2(\theta_b)\rangle$ where C is related to the stress-optical coefficient, and $\bar{\sigma} = \sigma / N = \sigma_{LJ}^3 \sigma / v\rho^*$ is the contribution to the stress from one atom in the simulation cell. The value of *C* is plotted in Fig 4(b) as a function of stretch for several values of ρ^*.

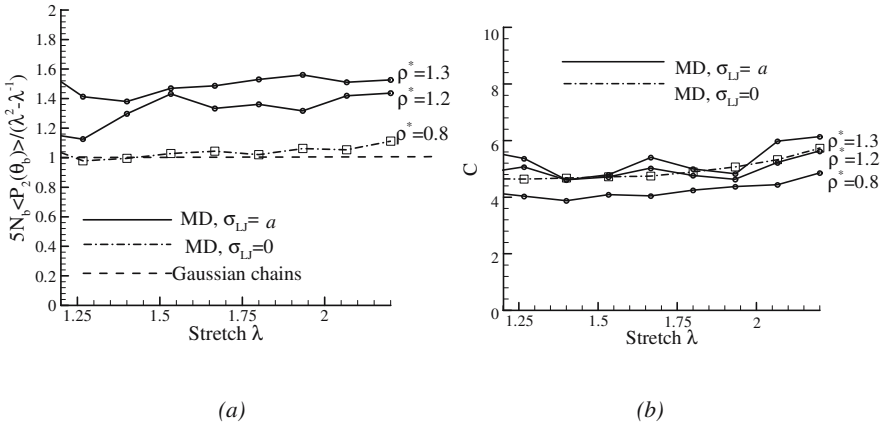

(a) *(b)*

Figure 4. (a) Normalized bond anisotropy as a function of stretch, for $kT/\in_{LJ}=3.5$; (b) The ratio C of difference per atom to a bond anisotropy as a function of stretch, for $kT/\in_{LJ}=3.5$.

We obtain further insight into the atomic-scale nature of stress by examining the relative contributions to the deviatoric stress and pressure from covalent bonds and from nonbonded interactions. To this end, we rearrange the virial stress formula (Eqn. 4) as $vt_{ij}=v(t_{ij}^{k}+t_{ij}^{b}+t_{ij}^{nba}+t_{ij}^{nbr})$, where $t_{ij}^{k}=-\rho vkT\delta_{ij}$ is the kinetic contribution to the stress, while

$$t_{ij}^{b}=\sum_{\alpha\in b}f_i r_j \qquad t_{ij}^{nba}=\sum_{\alpha\in nba}f_i r_j \qquad t_{ij}^{nbr}=\sum_{\alpha\in nbr}f_i r_j \tag{5}$$

denote, respectively, (i) the contribution to the stress from the covalent bonds (with sum $\alpha\in b$ taken over covalent bonds), (ii) the contribution to the stress from attractive nonbonded interactions (with sum $\alpha\in nba$ taken over tensile noncovalent interactions) and (iii) the contribution to the stress from repulsive nonbonded interactions (with sum $\alpha\in nbr$ taken over compressive noncovalent interactions. We then compute the contribution to the normalized difference stress and mean stress from covalent bonds as $\sigma_b=v[t_{11}^{b}-t_{22}^{b}]/kT$, $\Pi_b=vt_{kk}^{b}/3kT$, respectively, with similar definitions for stresses generated by attractive and repulsive nonbonded interactions. Fig 5 shows these various contributions to the difference stress and mean stress. Results are shown for a stretch of $\lambda=1.6$, and several values of temperature.

Several features of this result are worthy of comment. Firstly, the dominant contribution to the total difference stress is σ_{nbr} , arising from repulsive nonbonded interactions. The attractive portion of the Lennard-Jones potential contributes a negligible fraction of the difference stress, particularly at high values of ρ^{*} . The covalent bonds provide a *negative* contribution to the difference stress, except at low values of ρ^{*} and high

temperatures. Secondly, both σ_{nbr} and σ_b are strongly dependent on reduced density. The relative insensitivity of the total stress to ρ^* that is observed in the entropic regime arises because σ_{nbr} and σ_b have opposite signs, and their sum is only weakly dependent on reduced density. The dominant contribution to the mean stress arises from the repulsive portion of the Lennard-Jones interactions, which is balanced by the long-range attractive forces. This situation resembles the van-der-Waals picture of a liquid.

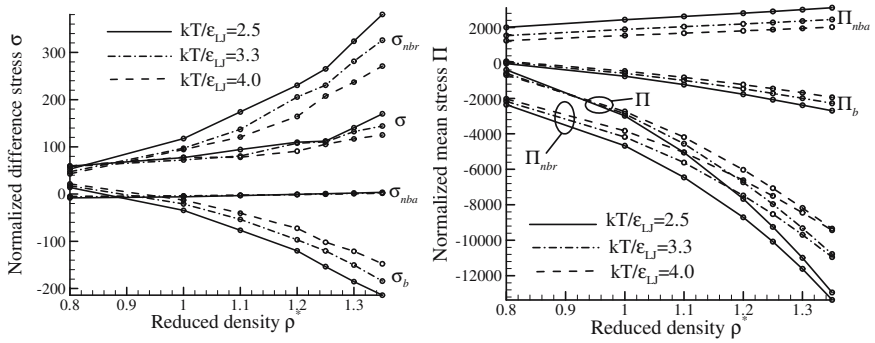

Figure 5. Contributions to the stress from: covalent bonds (*b*), repulsive (*nbr*) and attractive (*nba*) nonbonded interactions, for $\lambda = 1.6$. (a) Difference stress; (b) Mean stress

We proceed to examine the connections between mean stress and difference stress in more detail. We focus first on the nonbonded interactions. In light of the connection between difference stress and bond anisotropy, one might expect to observe a correlation between the nonbonded contribution to stress and the anisotropy of *nonbonded* interactions. An appropriate measure of this anisotropy is $\langle P_2(\theta_{nb})\rangle = \left\langle\left\langle (3\cos^2\theta_\alpha - 1)/2 \right\rangle\right\rangle$, where θ_α is the angle between a representative interaction and the x_1 direction, (Fig. 1), and the double carats denote averages over repulsive nonbonded interactions, over all members of the ensemble, and over time. A detailed analysis of the nonbonded contribution to stress in a hard-sphere model is given in ref [**2**]. The details are too lengthy to reproduce here, but the result is simple, and shows that $\sigma_{nbr} = A\Pi_{nbr}\langle P_2(\theta_{nb})\rangle$ where $A = 3$. We find a similar result in our simulations. This relationship is illustrated in Fig. 6(a), which shows the

ratio $\sigma_{nb}/\Pi_{nbr}\left\langle P_2(\theta_{nb})\right\rangle$ as a function of stretch for several values of reduced density. For $\rho^* \approx 1.2$, our simulations show $A = 3.5$.

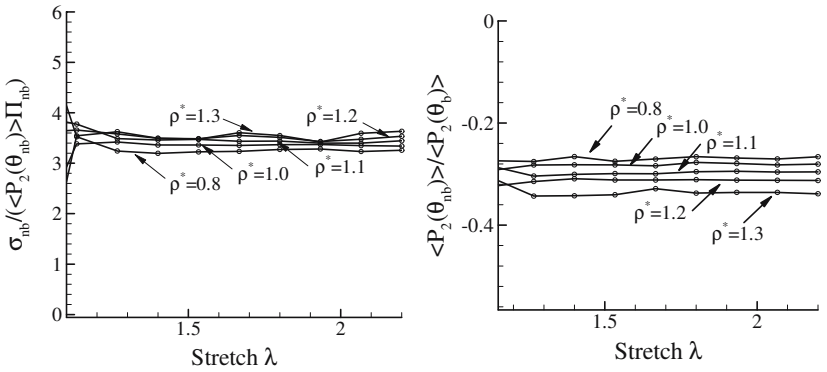

(a) *(b)*

Figure 6. (a) The relationship between nonbonded stress and anisotropy of nonbonded interactions; (b) The relationship between orientation of bonds and nonbonded interactions.

We showed earlier that the total difference stress is proportional to the anisotropy of covalent bonds (characterized by $\left\langle P_2(\theta_b)\right\rangle$). The stress due to excluded volume interactions is proportional to the anisotropy of *nonbonded* interactions. It is natural, therefore, to look for a relationship between the anisotropy of covalent bonds to that of nonbonded interactions. Fig. 6(b) shows the ratio $\left\langle P_2(\theta_{nb})\right\rangle / \left\langle P_2(\theta_b)\right\rangle$ as a function of stretch, for several values of reduced density. The anisotropy of nonbonded interactions and covalent bonds are evidently closely related – physically, this occurs because covalent bonds tend to align along the stretch direction, which forces nonbonded interactions to orient transverse to the stretch direction.

Finally, analytical calculations [**2**] show a similar connection between the contribution to mean stress and difference stress from covalent bonds. In this case, analytical considerations suggest $\sigma_b = D\Pi_b \left\langle P_2(\theta_b)\right\rangle$, where the coefficient $D = 3$. Our simulations confirm that this expression provides a reasonable approximation to the bonded contribution to difference stress. To demonstrate this, we have plotted the ratio $\sigma_b / \Pi_b \left\langle P_2(\theta_b)\right\rangle$ as a function of stretch for several ρ^* in Fig 7(a). Using $D \approx 2.5$ appears to give a good fit to the numerical simulations for $\rho^* > 1.1$.

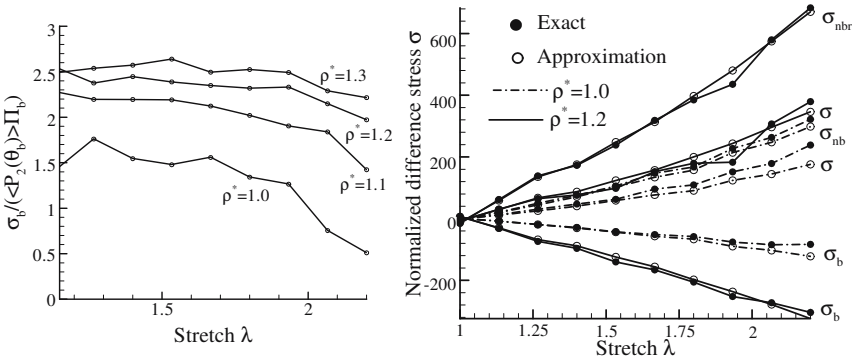

(a) *(b)*

Figure 7. (a) The relationship between stress due to covalent bonds and bond anisotropy; (b) comparison of the analytical expression for difference stress in Eqn. 6 with simulation data.

4. CONCLUSIONS

Combining our results gives a simple, approximate relationship between pressure (or mean stress) and difference stress

$$\sigma \approx \sigma_b + \sigma_{nbr} = F\left(D\Pi_b - AB\Pi_{nbr}\right)(\lambda^2 - \lambda^{-1})/5N_b \qquad (6)$$

For realistic values of reduced density ($\rho^* \approx 1.2$) we find that $A \approx 3.5$ and $B \approx 0.3$, $D \approx 2.5$, and $F \approx 1.3$. Fig. 7(b) compares the predictions of Eqn. 6 with our simulations. We conclude that difference stress and mean stress are intimately related at the atomic scale, in contrast to the classical viewpoint.

There are several promising directions for further study, including (i) modeling the dilatation of rubber during stretching; (ii) Detailed study of the glass transition; (iii) It appears that Π_b and Π_{nb} must be related, since the difference stress predicted by Eqn. 6 must have the entropic character observed in simulations – this requires further study; (iv) More detailed studies of the role of cross links, junctions and entanglements, and finally (v) studies of stress relaxation mechanisms under transient loading conditions.

REFERENCES

1. D.L. Quested, K.D. Pae, J.L. Sheinbein and B.A. Newman, "Viscoplastic behavior of a glass at high pressures", *J. Appl. Phys*, **52**, pp.5977-5982, 1981.
2. A.F. Bower and J.H. Weiner, "The role of pressure in rubber elasticity", *J. Chem. Phys*. **120**, pp. 11948-11964, 2004.

DYNAMIC INDENTATION OF POLYMERS USING THE ATOMIC FORCE MICROSCOPE

H. Y. Hou[1], N. K. Chang[1], S. H. Chang[1,2,*]
[1]*Department of Mechanical Engineering, National Taiwan University, Taipei, Taiwan*
[2]*National Taiwan University Nano-Electro-Mechanical-Systems Research Center*
**Email: shchang@ntu.edu.tw*

Abstract: The applications of Atomic Force Microscope (AFM) on study of surface property of polymeric materials have been demonstrated. The surface microstructure of the material was characterized by the so called dynamic indentation technique. Being penetrated by the AFM tip, the sample surface was simultaneously undergoing an oscillation at smaller amplitude (3-5 nm) by a piezoelectric actuator. The merit of the developed dynamic indentation technique is to characterize the material's modulus as a function of indentation depth using one cycle of the depth sensing indentation force data. The results have shown that the technique is a powerful method for polymer characterization with nanometer spatial resolution. The obtained photo-detector signals from AFM were numerically processed by Fourier series to analyze the storage modulus of the sample. The PDMS polymer materials were tested and results were compared with MTS Nano Indenter data. It is believed that the technique can be readily applied for indentation study of thin film, coating materials and nano-structures.

Key words: Nanoindentation, AFM, polymer, dynamic indentation.

1. INTRODUCTION

Nanoindentation technique with depth sensing has been popularly used for measurement of mechanical properties of materials for thin films,

T. J. Chuang et al. (eds.), Nanomechanics of Materials and Structures, 171–180.

coating, magnetic recording medium and nano-structures [1]. The instrument with indentation tip of radius on the order of 200 nm and force of up to mN is able to penetrate material surface and characterize the mechanical properties, such as hardness, modulus, fatigue, visco-elasticity, etc. However, the soft modulus of polymeric materials creates difficulty for accurate measurement using indentation testing. This difficulty is due to the force resolution, typically on the order of 100 nN [2].

Atomic force microscopy (AFM) has been used to study polymeric materials with nanometer spatial resolution [3]. The AFM uses a sharp tip with radius on the order of 20 nm to penetrate the material surface. The sharp tip is located at one end of the cantilever. Therefore, the bending mode of the cantilever was applied for indentation. The indentation force depends on the stiffness of the AFM cantilever and can be varied from nN to micron N. The indentation depth can be in nanometer spatial resolution. The recorded indentation force and depth curve can be used using Oliver and Pharr theory [4] to calculate the mechanical properties, such as hardness and storage modulus, etc.

Due to the specific demand of nanoindentation measurement, commercial nano-indentation systems were developed as special instrument to achieve the continuous stiffness measurement [5]. It is capable to obtain a series of modulus data with increasing the depth into the surface within one set of measurement. However, the indentation using AFM system is limited for solving single modulus in one set of test.

In this paper, we describe the design of a dynamic indentation mechanism to achieve the continuous stiffness measurement. We superpose the oscillation of the sample on the depth sensing indentation of AFM tip. The sample oscillates at a smaller amplitude compared with the indentation depth is provided by an additional piezoelectric actuator. With the process of Fourier series to analyze the recorded depth-force curve, polymer material PDMS was tested for demonstration of the technique.

2. DESIGN

In indentation test, the modulus of material is solved by measuring the value of contact stiffness S, through Canonical Sneddon stiffness eqn. [4]:

$$S = \beta \frac{2}{\sqrt{\pi}} E_r \sqrt{A} \tag{1}$$

Where E_r is the reduced modulus that accounts for the fact that elastic deformation occurs in both the sample and the indenter. Parameter β is a constant that depends on the geometry of the indenter, for example β=1.034 for Berkovich indenter. A is the projected contact area.

In this paper, the proposed dynamic indentation technique with its set up is shown in Fig. 1. The dynamic indentation is achieved using a piezoelectric actuator in combination with an AFM. Under the AFM probe tip, a piezoelectric actuator (PZT) is installed to hold the sample and provides the oscillation during the AFM indentation process.

In the indentation process, the AFM probe tip was controlled to move and penetrate into the surface of the sample at the specified force, displacement and speed. The sharp tip normally with the radius of 20-30 nm was fabricated at one end of the AFM cantilever beam. Here, we refer it the dc displacement of the AFM tip which is compared to the sample's oscillation at a higher frequency and smaller amplitude. While the AFM tip penetrates the sample surface, the PZT actuator was controlled to oscillate at a specified frequency and is referred as the ac displacement. With respect to the dc displacement of the AFM probe tip, the ac displacement of several nm was provided by the electrical controlled piezoelectric actuator. The bending of the AFM cantilever beam during the indentation process was measured by the laser and photo-detector. The quantities of both cantilever bending and indentation depth were simultaneously recorded by the laser signals and AFM scanner.

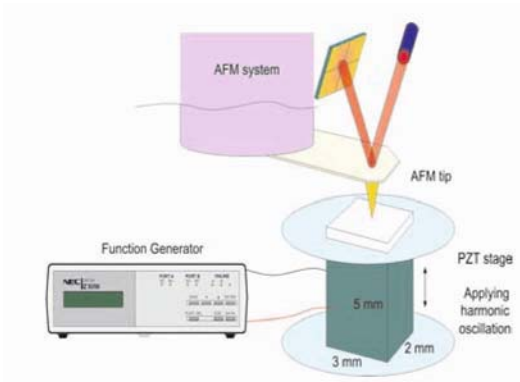

Figure 1. Experimental set-up for dynamic indentation.

The dynamic indentation technique provides the ac indentation during the quasi-static dc indentation process and is illustrated in Fig. 2. It shows an ordinary smooth loading curve superposed by a relative smaller amplitude, higher frequency oscillation signals which can be written as load $F(t)=F_0 e^{i\omega t}$ or displacement $z(t)=z_0 e^{i\omega t}$, where ω is the controlled frequency and F_0 is the maximal oscillatory force and z_0 is the maximal oscillatory displacement.

The typical recorded force-depth curve in Fig. 2 can be resolved for the depth dependent storage modulus. The merit of the technique is that the storage modulus as a function of the indentation depth can be found from one cycle of the indentation experiment, instead of numerous indentation experiments.

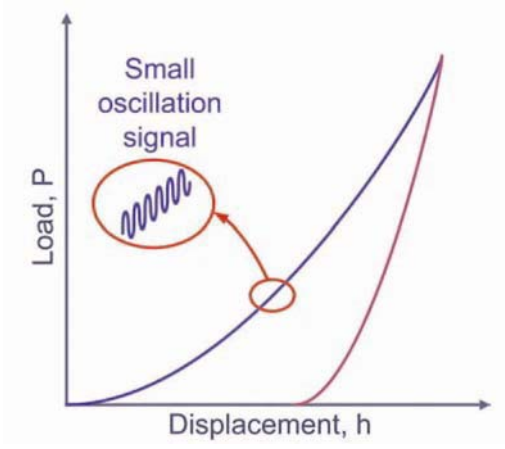

Figure 2. Illustration of dynamic indentation technique.

In this case, the dynamic system can be simplified as a lump mass-spring model as shown in Fig.3. The model includes two springs in series, i.e., the stiffness of the AFM cantilever and the stiffness of the contact between the AFM tip and the tested sample, with the boundary condition of the oscillating contact point. The material's modulus, such as the storage modulus，E' and the Loss modulus, E'' [5] can be found as following:

$$E' = \frac{\sqrt{\pi} \cdot S}{2\sqrt{A}} \tag{2}$$

$$E'' = \frac{\sqrt{\pi} \cdot C_s \omega}{2\sqrt{A}} \tag{3}$$

where C_s is the damping parameter.

The simplified model in Fig. 3 includes quantity Z as the oscillation displacement of PZT. K_c is the spring constant of AFM cantilever and S is the contact stiffness. The maximum amplitude of the displacement of the sample, Z_0, can be adjusted by the PZT controller. The deformation of AFM tip, Z_c, is detected by the AFM photo-detector. Thus the penetration depth, Z_s caused by AFM tip is:

$$Z_s = Z_o - Z_c \tag{4}$$

Due to the serial structure, the relation between displacement and spring constant appear inversely proportional. The contact stiffness is:

$$S = \frac{Z_c}{Z_s} \cdot K_c \tag{5}$$

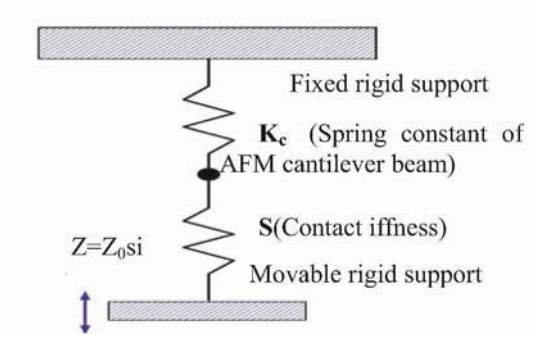

Figure 3. The simplified model of dynamic indentation mechanism.

3. EXPERIMENTS AND RESULTS

The performance of the PZT actuator was evaluated first. A function generator was used to supply electrical voltage at specified frequency to drive the PZT and a Laser interferometer with sub-nanometer displacement resolution was used to measure the displacement responses. The relationship of the displacement sensitivity of the PZT as function of the electric voltage was measured. A typical PZT displacement measurement in response to the electrical excitation is shown in Fig. 4. The displacement of +3.5 nm to -3.5 nm in response of 300 mV electrical excitation is found. The signal noise of less than 1 nm is acceptable in this study. The various oscillation frequencies were tested for best dynamic indentation experiments.

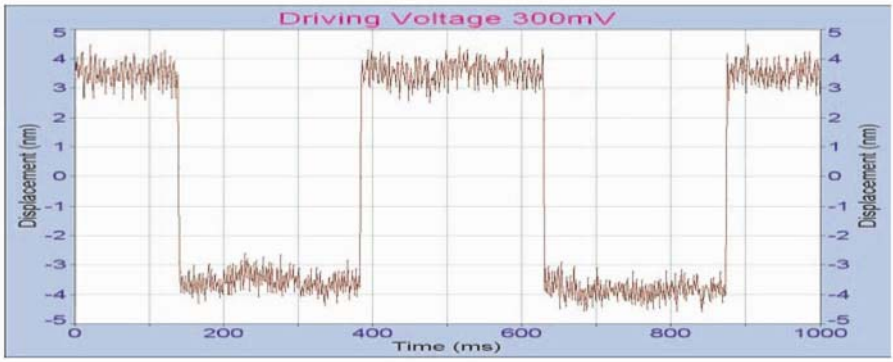

Figure 4. Square wave displacement of the PZT actuator in response to an electrical input of 300mV.

The bulk PDMS (poly-dimethyl-siloxane) samples made by the Down Corning Corporation were used in this study. Its Si-O backbone structure offers high elasticity and mobility of the macro molecular structure of PDMS. In addition, its property of homogeneous visco-elastic material and low storage modulus is suitable for AFM indentation with low stiffness. The average roughness of the surface of this specimen measured by AFM is 15 nm. Therefore, the effect of roughness upon the results of the nano-indentation can be neglected in this case for the indentation depth is several hundred times of the roughness.

A typical measured cantilever bending versus indentation depth curve is shown in Fig. 5. The small oscillation displacement can be barely observed in the figure. The x axis denotes the displacement of AFM tip along the penetration direction detected by the AFM PZT scanner. The y axis represents the deformation of AFM cantilever detected by the AFM photo-detector with units of nano ampere. It can then be converted into displacement quantity in nm. In this case, the experiment was carried out at the indentation rate, oscillation frequency of PZT, driving voltage, of 0.05 μm/s, 500 mHz and 500 mV, respectively.

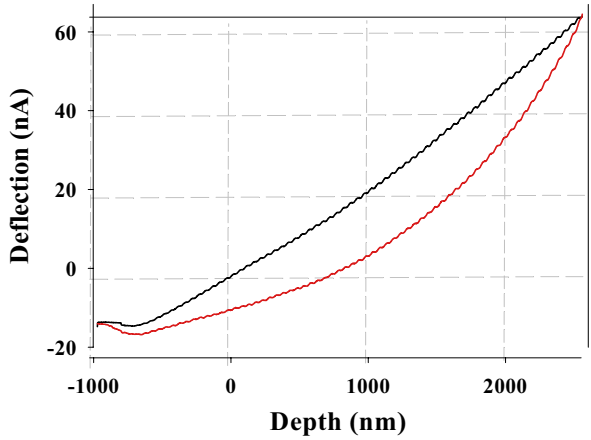

Figure 5. The typical recorded indentation curve using AFM probe to indent PDMS.

The contact area usually is too complex to accurately find and was evaluated here for calculation of the modulus. The contact area of the AFM probe tip as a function of the indentation depth was calibrated using the PMMA materials. The indentation experiments were carried out using both MTS indenter and the AFM probe. The calibration polynomial formula was derived. While the AFM tip is approaching the sample surface, it will be pulled toward the sample surface when the attractive force between the tip and sample exceeds the cantilever stiffness. Hence the starting contact point can be defined from the force-depth curve. The penetration depth and loading force during the indentation process can then be calculated from any arbitrary point in the force-depth curve by taking account of the oscillation of PZT and the bending of the cantilever.

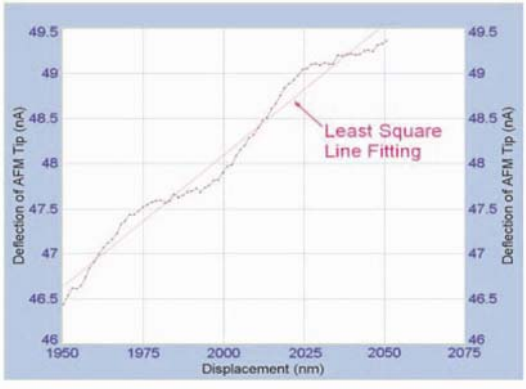

Figure 6. The result of indentation curve and the least square for numerical processing.

Next, the harmonic amplitude of the small signals on the force-depth curve will be calculated. The least square line fitting the force-depth curve as shown in Fig. 6 is used to filter the harmonic signals. At this stage, the numerical process of Fourier series was applied to decompose the frequency contents. We omit the detail procedure of the numerical process here. Finally the contact stiffness for each period of the oscillation signal in the indentation cycle was calculated using equ. (5).

Both data obtained from the AFM indentation and MTS Nano-indenter is plotted in Fig. 7. The AFM was operated at 0.05 μm/s and PZT actuator was operated at 0.5 Hz and 500 mV, respectively. The AFM data indicated that the modulus decreases as the depth increases. The modulus is also smaller compared with MTS data. It's possibly due to the complexity of the AFM tip shape and the contact area calculation.

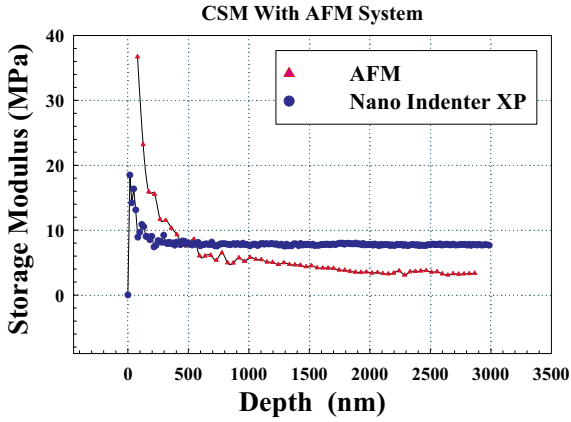

Figure 7: The storage modulus of PDMS measured by AFM dynamic indentation technique and MTS Nano Indenter.

Further comparison of the AFM indentation data, at various loading condition with results obtained using commercial instruments, MTS Nano Indenter XP and Rheometrics Solids Analyzer (RSA) II was shown in Fig. 8. The other two measurements were conducted at the NIST, Gaithersburg, MD, USA and details will be described else where. The operating condition in Nano Indenter XP, such as strain rate and oscillated frequency were at 0.01 1/s and 20 Hz, respectively. Due to limitation of each instrument, it is not possible to conduct experiments at the same operation range. As shown in the figure, the results of the AFM technique were found relatively close to that obtained by RSA.

Operating at 0.01 mm/s and 0.05 mm/s indentation speed, the AFM data does not span over the wide frequency range, compared with data of Nano Indenter and RSA. It is due to the limitation of operated frequency in AFM system. Theoretically AFM results should be closer to results of MTS Nano Indenter due to similar indentation mechanism.

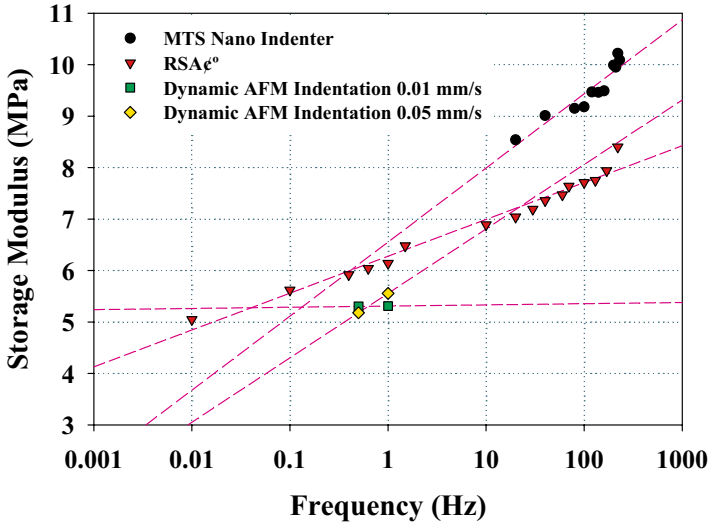

Figure 8: Comparison of the different measurement results.

With regard to the numerical deviation of data, the error source mainly comes from the contact area in the AFM indentation. Here, it is presumed AFM has a perfect pyramid tip. The size of the predicted contact area will be larger than real size of the contact area and leads to smaller modulus. The lateral force in AFM cantilever may also lead to numerical deviations during penetration process. However, the dynamic indentation of using AFM probe tip is demonstrated and results of same order of magnitude compared with other techniques were found.

4. SUMMARY

Using PDMS polymer materials, we demonstrate a dynamic nano-indentation technique using the AFM probe tip with an additional piezoelectric actuator. The advantage of the dynamic indentation provides the depth dependent modulus information obtained from one cycle of the experiment. The further purpose of using AFM probe tip is to take advantage of the indenter with radius on the order of 20 nm which is much favorable

compared with the micron size of the indenter in the commercial instruments. The bending mode of the AFM cantilever causes complexity of the data processing. The technique can be readily applied to the indentation study of the thin flim, nano-structures and nano-wires.

ACKNOWLEDGMENTS

The authors gratefully acknowledge Drs. M. R. VanLandingham, C.C. White, L. Sung, T. Nguyen and J. W. Martin, of the National Institute of Standards and Technology (NIST), USA for their technical assistance and NSC of Taiwan for their financial support under contract No.NSC90-2212-E002-198.

REFERENCES

1. Saha and W. D. Nix, “Effects of the Substrate on the Indentation of Thin Film Mechanical Properties by Nanoindentation,” Acta Materials, 50, 22-38, 2002.
2. M.R. VanLandingham, J.S. Villarrubia, W.F. Guthrie, and G.F. Meyers, **“**Nanoindentation of Polymers: An Overview,” Recent Advances in Scanning Probe Microscopy. Proceedings. 220th American Chemical Society National Meeting, August 2000, Washington, DC. Macromolecular Symposia, Wiley-VCH Verlag GmbH, Tsukruk, V. V. and Spencer, N. D., Editors, 15-43, 2001.
3. P. M. McGuiggan, D. J. Yarusso, “Measurement of the Loss Tangent of a Thin Polymeric Film Using the Atomic Force Microscope,” *Journal of Material Research.*, 19(1), 387-395, 2004.
4. G. M. Pharr, W. C. Oliver and F. R. Brotzen, "On the Generality of the Relationship Among Contact Stiffness, Contact Area, and Elastic Modulus During Indentation," *J. Mater. Res.*, 7(3), 613–617 1992.
5. B. N. Lucas, W. C. Oliver and A. C. Ramamurthy, "Spatially Resolved Mechanical Properties of a TPO Using a Frequency Specific Depth–sensing Indentation Technique," *SPE ANTEC’97*, 1997.

FABRICATION AND SIMULATION OF NANOSTRUCTURES ON SILICON BY LASER ASSISTED DIRECT IMPRINT TECHNIQUE

Fei-Bin Hsiao[1*], Yung-Chun Lee[2], Chuan-Pu Liu[3], Cheng-Hsin Chuang[4], Chun-Ping Jen[1], Di-Bao Wang[1], Chun-Yi Lin[1]

[1] *Department of Aeronautics and Astronautics,* [2] *Department of Mechanical Engineering*

[3] *Department of Materials Science and Engineering*

National Cheng Kung University, Tainan, 70101 TAIWAN

[4] *Electronics Research & Service Organization/Industrial Technology Research Institute, Hsinchu, 300 TAIWAN*

* *Phone:886-6-237-8874; Fax: 886-6-276-6549; Email: fbhsiao@mail.ncku.edu.tw*

Abstract: In this paper a newly proposed nano-patterning technology, namely laser assisted direct imprinting (LADI), is adopted with fabrication and numerical simulation for nano-scaled structures. We focused on the target material as silicon and utilized a single KrF excimer laser pulse (248nm wavelength and 30ns pulse duration) as heating source. We also demonstrated the fabrication of a positive quartz mold within micro-level and nano-level trenches by combination of conventional photolithography and novel focused ion beam (FIB) system. The influence of laser fluence and imprinting pressure on resulting nanostructure is evaluated by varying the laser fluence (0.6~1.2 J/cm^2) and imprint pressure (370~1120 MPa). The results show that the magnitude of imprinting pressure and the laser characteristics can affect the thickness of the melted layer on the substrate surface and the morphology of the resulting nanostructures. In the other aspect, an analytical modeling of laser induced melting and solidification during LADI process was also established for the comparison between experimental results and numerical simulation. The transient temperature profiles inside the substrate, melt depth and melting duration after the irradiation of a laser pulse were evaluated by various fabrication parameters; such as materials of the substrate (silicon and copper were investigated) and the characteristics of the laser pulse (including wavelength, fluence and pulsed duration). Generally speaking, the nanostructures fabricated by LADI are quite consistent with the results of numerical simulation.

Key words: LADI, Excimer Laser, Nanostructures, FIB, Nanoimprinting

T. J. Chuang et al. (eds.), Nanomechanics of Materials and Structures, 181–189.
© 2006 *Springer. Printed in the Netherlands.*

1. INTRODUCTION

Nano-imprinting lithography (NIL) has been developed over a decade [**1-5**] and is now a promising method for nano-patterning and nano-fabrication. Figure 1 illustrates the basic concepts of conventional nano-imprinting, which includes a mold, an etching resist layer and a sample substrate. The mold has some nano-scale features on the surface fabricated by either E-beam lithography (EBL) or focus ion bean (FIB) techniques. The resist layer is usually thermo-plastic polymer such as poly-methylmethacrylate (PMMA). By heating up the resist layer above its glass transition temperature (T_g), the mold can imprint into the resist layer and form a pattern. Following by reaction ion etching (RIE or ICP), the nano-pattern is transformed to the resist layer and the substrate. It is then followed by standard lithography processes to achieve nano-structures on the substrate surface. However, the heating mechanism of conventional nanoimprinting is slow and usually causes misalignment due to the different thermal expansion between the mold and substrate. Recently, laser assisted direct imprinting (LADI) method was proposed by Chou *et. al*. [**6**]. This new imprinting method shares some similar concepts of the NIL but with a much more straightforward approach for nano-pattern transformation. As depicted schematically in Figure 2, LADI process utilizes a laser pulse to radiate on the sample surface which is in contact with and is pre-loaded by a mold (fused quartz) with pre-fabricated nano-scale features on its contact side. Upon radiating the laser pulse on the sample surface, the near-surface materials melt and a laser-induced molten layer is formed, which allows the mold to imprint into the sample directly. Subsequent cooling and solidification of the molten layer will then complete the transformation of the nano-patterns from the mold to the sample. This LADI method has several obvious advantages over the nano-imprinting technique in terms of simplicity and efficiency, and therefore shows a great potential for future nano-patterning and fabrication of nano-structures. However, this newly proposed method raises a number of issues such as the basic mechanism underlies the LADI processing, the key parameters and variables for a successful LADI processing, the influence of material properties, etc. To investigate these crucial and fundamental problem, we initiate a three-year national project, “A Theoretical and Experimental Study on Laser Assisted Direct Nano-Imprinting Technology”, funded by National Science Council in Tainan. This project includes three parts: I Theoretical Analysis and Numerical Modeling of LADI; II Experimental Setup and Parameters Testing of LADI; III Characterization of LADI Induced Variation in Microstructure and Material Properties. In this study, a platform of LADI processing and its preliminary results of experimental tests have been

established to evaluate the effects of laser fluence (J/cm^2) and imprinting pressure (MPa) on the resulting patterns and the thickness of molten layer. In addition, an analytical modeling of laser induced melting and solidification during LADI processing is performed to predict the melting of silicon substrate.

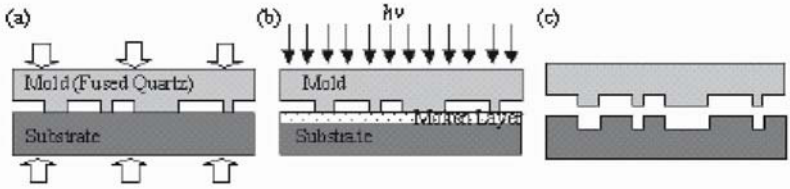

Figure 1. Nano-Imprinting Lithography (NIL) processing

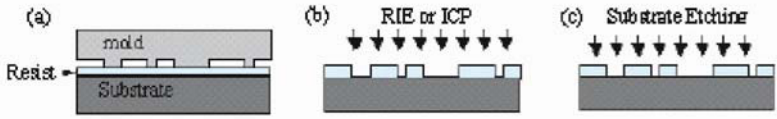

Figure 2. Laser Assisted Direct Imprinting (LADI) processing

2. EXPERIMENTAL SETUP

As in the reference [**6**] by S. Y. Chou, the LADI processing is performed by a single XeCl excimer laser pulse (308 nm wavelength and 20ns pulse duration) with laser fluence, 1.6 J/cm^2. They found that there is a range of laser fluence between 0.8 ~ 2.0 J/cm^2 in order to melt the silicon surface and to avoid laser ablation of silicon, but without any additional illustration. Also, the other important parameter, imprinting pressure, is derived in an indirect way, thus, the actual pre-load pressure acting on the substrate still unclear. In the present study, for a quantitative examination of these two processing parameters, laser fluence and imprinting pressure, a novel design for LADI is shown in Figure 3(a) and 3(b), including a optical system and a loading mechanism. The laser source of optical system is a KrF excimer laser (248 nm wavelength and 30ns pulse duration) and the laser fluence can be controlled by using an attenuator. The sample holder integrated with a loading fixture and pressure measurement device is shown in Figure 3(b). To be able to fit in the laser laminate area, the size of the mold is dicied as 2x2 mm^2, which will be the entire imprinting area. Another fused quartz blank plate on top of the mold will press the mold

against the substrate when the linear actuator is activated. A load cell will then output the total force and thus the pressure by divined by contact surface area. The mold, sample, load cell, and linear actuator should be aligned along the central line of the fixture to avoid sample tilting and measurement errors.

The experimental details are described as follow. First, the mold is made of fused quartz 3 mm thick and has 5μm linewidth trench-type array on the quartz surface that is fabricated by photolithography and CF4 reactive ion etching. A series of tests is performed to investigate the dependence of laser fluence and imprinting pressure on LADI processing. The laser fluence and imprinting pressure are varied from 0.6 to 1.2 J/cm^2 and from 370 to 1120 MPa, respectively, as Table 1.

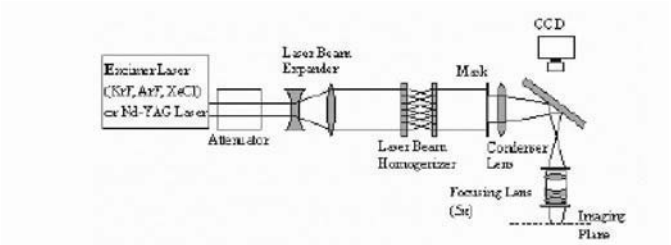

Figure 3(a) The pulse laser optical system for LADI processing

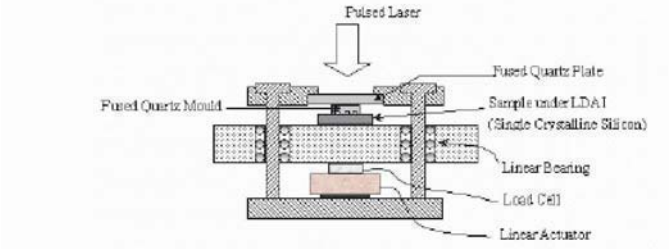

Figure 3(b) The sample holder and loading mechanism for LADI processing

Table 1. The experimental parameters for LADI processing

Fluence (J/cm^2)	Pressure (MPa)
0.6	370
0.8	620
1.0	870
1.2	1120

3. THEORETICAL MODELING

Laser-material interaction between a pulse laser and a solid substrate is the key element for laser-assisted nanoimprinting. During the heating process of the substrate by the pulsed laser, one-dimensional transient heat-diffusion equation can be employed herein. The source term of heat-generation originating from the energy absorption of a laser pulse can be described as: $S(x,t) = (1-R)\beta \exp(-\beta x) I(t)$, where x and t are the spatial variable and time, respectively. R is the reflectance, β is the optical absorption coefficient and I(t) is the power density function of the incident laser pulse (power per unit area). According to the concept of the super position procedure, the medium which is heated by the heat-generation sources, $S(x,t)$, the time-dependent temperature profile is solved analytically and expressed as:

$$\theta(x,t) = \int_0^{t_p} \int_{-\infty}^{\infty} \frac{S(\xi,\tau)}{2\rho C[\pi\alpha(t-\tau)]^{1/2}} \exp\left[-\frac{(x-\xi)^2}{4\alpha(t-\tau)}\right] d\xi\, d\tau \qquad (1)$$

where $\theta(x,t) = T(x,t) - T_i$ is the excess temperature relative to the initial (far-field) temperature of the domain (T_i). t_p is the irradiating time of a laser pulse. Thus, the temperature inside the substrate is rewritten as following:

$$T(x,t) = \int_0^{t_p} \int_{-\infty}^{\infty} \frac{S(\xi,\tau)}{2\rho C[\pi\alpha(t-\tau)]^{1/2}} \exp\left[-\frac{(x-\xi)^2}{4\alpha(t-\tau)}\right] d\xi\, d\tau + T_i$$

$$\text{for } x \geq 0,\ t \geq 0 \qquad (2)$$

The calculated domain has been extended to an infinite medium; hence, the virtual heat sources have to impose in the negative region of the medium to conserve the total energy absorbed in the substrate. The source term S(ξ,τ) should be written as:

$$S(\xi,\tau) = (1-R)\beta \exp(-\beta|\xi|) I(\tau) \qquad \text{for } -\infty < \xi < \infty \qquad (3)$$

When the surface temperature of the substrate reaches the melting point T_m, the boundary between the solid and liquid phase begins to move from the surface into the depth of the substrate. The equilibrium model (i.e. the isothermal one-dimensional Stefan problem [**7**]) is considered in this work. The temperature at the solid/liquid interface ($x = h(t)$) is constant and equal to the melting temperature T_m. However, the moving boundary can be treated as a moving heat sink inside the substrate [**8**]. The temperature induced by the heat sink is approximated as a constant value of $T_q = q/C$, where q is the latent heat of fusion. Therefore, the resultant temperature in the substrate can be superposed after the onset of melting:

$$T(x,t) = \int_0^{t_p} \int_{-\infty}^{\infty} \frac{S(\xi,\tau)}{2\rho C[\pi\alpha(t-\tau)]^{1/2}} \exp\left[-\frac{(x-\xi)^2}{4\alpha(t-\tau)}\right] d\xi\, d\tau + T_i - T_q \quad (4)$$

The analytical solutions of the temperature distribution above can be integrated using Gauss-Legendre quadrature. The calculation of the melt depth and melting duration can be performed by tracking the position of the moving boundary numerically. It should be notice that non-equilibrium between electrons and phonons is not speculated due to that the time scale of pulses investigated herein is nanosecond that is still much longer than the time scale (i.e. picosecond) in which the non-equilibrium occurs. Moreover, the non-equilibrium process of amorphization [**9-11**] is not taken into consideration in this study. Meanwhile, the vaporization of the substrate is not considered herein.

4. RESULTS AND DISCUSSION

The molten depth of the silicon substrate with time under 30ns pulse durations of a KrF pulsed laser (248 nm) is analytically evaluated and shown in Figure 4. The molten depth increases during the laser heating, after the heating of a laser pulse, the molten depth decreases to zero due to solidification of the substrate. When the laser fluence is larger, the absorbed energy increases and the molten zone enlarges. By using other pulse duration parameter, the time of starting to melt is postponed while the duration is longer under the same laser fluence. The energy deposited in the substrate under longer duration becomes slower and the energy dissipates gradually, therefore, the molten depth decreases. These results of other time durations are not shown in present paper.

From the experimental results, the SEM pictures of samples imprinted by differ pressure under the same laser fluence, 1.2 J/cm^2, are show in Figure 5. It is found that the imprinted depth depends on applied pressure, which cannot be explained by simple theory of mechanics as proposed in earlier studies. Instead, a more sophisticated theory based on elastic deformation and wave dynamics is needed to quantitatively reveal the underlying mechanism between the applied pressure and the imprinted results of LADI, but the theoretical analysis will be demonstrated in later paper not here. On the other aspect, the results of the samples radiated by differ laser fluences under the same pressure are shown in Figure 6. It is obviously that the imprinted depth is deeper for a larger laser fluence, which means the thickness of molten layer on the silicon surface is thicker while the laser fluence is larger. This trend is similar with the results of numerical simulation. In addition, the actual depth of molten layer can be verified by

SEM cross-sectional picture due to the laser-induced oxidation layer on the surface and its results also consistent with the simulation results shown in the Figure 4.

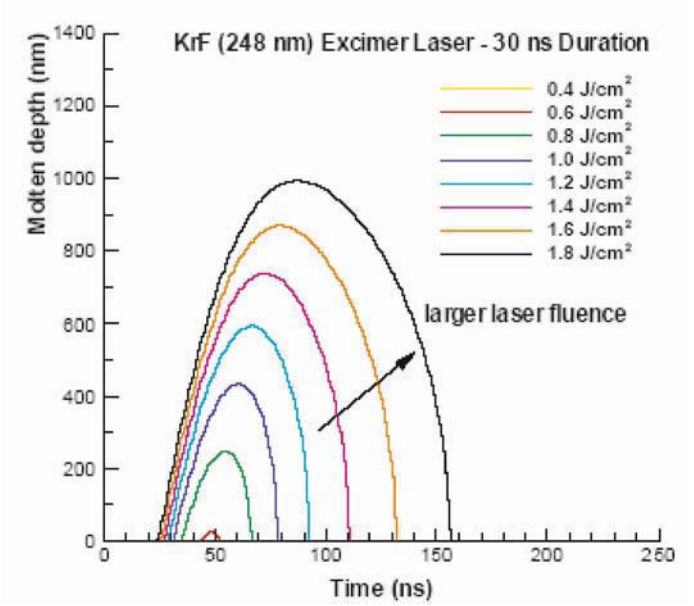

Figure 4. The molten depth of the silicon substrate with 30 ns pulse durations of a KrF pulsed laser (248 nm).

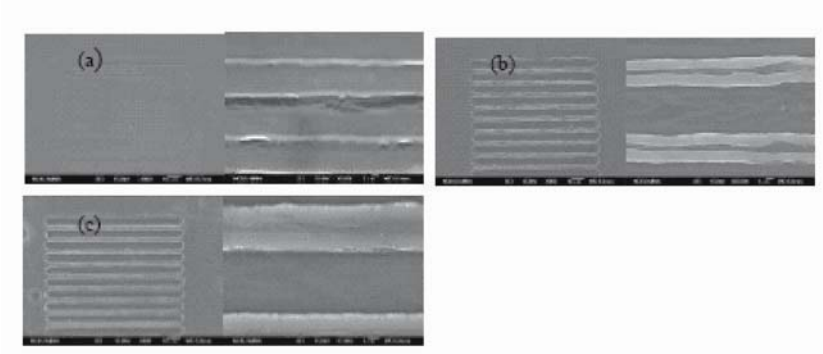

Figure 5. The SEM pictures of silicon substrates imprinted by 5μm linewidth trench-type mold with differ imprinting pressure under the same laser fluence, 1.2 J/cm^2 : (a) Pressure = 620 MPa; (b) Pressure = 870 MPa; (c) Pressure = 1120 MPa

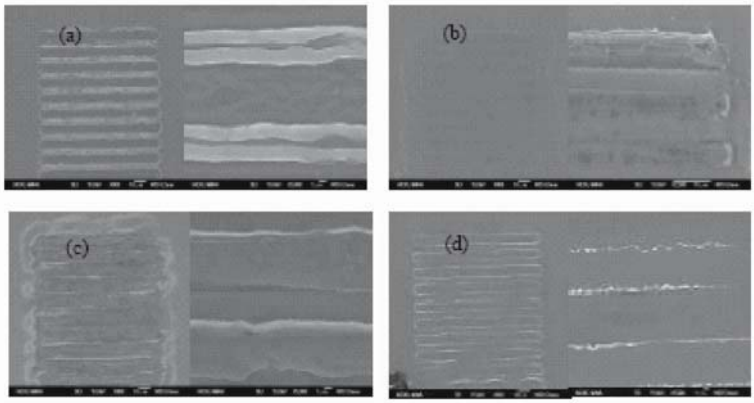

Figure 6. The SEM pictures of silicon substrates imprinted by 5μm linewidth trench-type mold with differ laser fluence under the same imprinting pressure, 870 MPa: (a) Fluence = 1.2 J/cm^2; (b) Fluence = 1.0 J/cm^2; (c) Fluence = 0.8 J/cm^2; (d) Fluence = 0.6 J/cm^2

5. CONCLUSION

A theoretical model for simulation of LADI processing is established, and it could predict the melting depth and temperature history for silicon material. From the experimental results, imprinted area on silicon is as large as the laser-radiated area, which means LADI is potentially as a large-area patterning technology depending on the spot size of laser. The transferred patterns are affected by laser fluence and imprinting pressure. The phenomenon of fluid can be obviously discovered in the SEM pictures, which is approved the three steps in LADI, melting, compressing and solidification. This laser assisted direct imprinting method has several obvious advantages over the nano-imprinting technique in terms of simplicity and efficiency, and therefore shows a great potential for future nano-patterning and fabrication of nano-structures.

REFERENCES

1. S.-Y. Chou, P.R. Krauss, and P.J., "Imprint lithography with 25-nanometer resolution", Renstrom, *Science*, **272**(5258), pp.85-87 (1996).
2. L. Guo, P.R. Krauss, and S.-Y. Chou, "Nanoscale silicon field effect transistors fabricated using imprint lithography", *Applied Physics Letters*, **71**(13), pp.1881-1883 (1997)
3. S.-Y. Chou and P.R. Krauss, "Imprint lithography with sub-10 nm feature size and high throughput", *Microelectronic Engineering*, **35**(1-4), pp.237-240 (1997).

4. W. Zhang and S.-Y. Chou, "Fabrication of 60-nm transistors on 4-in. wafer using nanoimprint at all lithography levels", *Applied Physics Letters*, **83**(8), pp.1632-1634 (2003).
5. W. Wu, , J. Gu, H. Ge, C. Keimel, S.-Y. Chou, "Room-temperature si single-electron memory fabricated by nanoimprint lithography", *Applied Physics Letters*, **83**(11), pp. 2268-2270 (2003).
6. S.-Y. Chou, C. Keimei, and J. Gu, *Nature*, **417**, pp.835-837 (2002).
7. L. I. Rubenstein, *The Stefan problem*, **Vol. 27**. of *AMS Translations of Mathematical Monographs* (American Mathematical Society, Providence, R.I., 1971)
8. V. N. Tokarev and A. F. H. Kaplan, "An analytical modeling of time dependent pulsed laser melting", *J. Appl. Phys.,* **86**(5), 2836-2846 (1999)
9. R. Tsu, R. T. Hodgson, T. Y. Tan and J. E. Baglin, "Order-Disorder Transition in Single-Crystal Silicon Induced by Pulsed uv Laser Irradiation", *Phys. Rev. Lett.*, **42**(20), 1356-1358 (1979).
10. A. G. Cullis, H. C. Webber, N. G. Chew, J. M. Poate and P. Baeri, "Transitions to Defective Crystal and the Amorphous State Induced in Elemental Si by Laser Quenching", *Phys. Rev. Lett.*, **49**(3), 219-222 (1982).
11. R. Cerny, V. Chab, P. Prikryl, "Non-equilibrium model of laser-induced phase change processes in amorphous silicon thin films", *Phys. Rev. B*, **57**(1), 194-202 (1998).

STRUCTURE AND STRESS EVOLUTION DUE TO MEDIUM ENERGY ION BOMBARDMENT OF SILICON

N. Kalyanasundaram[1], M. C. Moore[1], J. B. Freund[2] , and H. T. Johnson[1, a]
[1]*Department of Mechanical and Industrial Engineering, University of Illinois at Urbana-Champaign, Urbana, IL 61801*
[2]*Department of Theoretical and Applied Mechanics, University of Illinois at Urbana-Champaign, Urbana, IL 61801*
[a]*Corresponding author: H. T. Johnson, 140, Mechanical Engineering Building, 1206 W Green Street, Urbana, IL 61801. USA. Tel.: +1-217-265-5468 Email: htj@uiuc.edu*

Abstract: Sputtering, stress evolution and surface evolution due to ion bombardment of silicon are studied in this work. Impacts due to argon ions at normal incidence with beam energies of 500eV and 700eV are simulated using Molecular Dynamics (MD). Impacts on (001) silicon surface are simulated on a silicon crystal that is initially undamaged and is 5.43nm x 5.43nm x 5.43nm in dimension. The (001) silicon surface is tiled in order to impose periodic boundary conditions during the MD simulation. Converged statistical description of observables is obtained by performing multiple randomized simulations, with each randomized simulation involving more than 100 ion impacts. A planar radial distribution function and a structure factor-like crystallinity measure are used to study the structure and damage evolution. Stresses are calculated using a force balance method and approach 1.7GPa and 1.3GPa in the 700eV and 500eV cases respectively after about 125 impacts. Continuum descriptions of the damaged surface are obtained from atomistic coordinate data using a silicon probe atom method.

Key words: Molecular dynamics calculations, Ion sputtering, Structure, Stress evolution, Surfaces

T. J. Chuang et al. (eds.), Nanomechanics of Materials and Structures, 191–198.
© 2006 *Springer. Printed in the Netherlands.*

1. INTRODUCTION

Ion bombardment at beam energies in the range of 500eV to 700eV is used to fabricate surface nanostructures [**1 - 2**] and in chemically neutral ion beam machining of silicon [**3**]. Comprehending different aspects of material rearrangement and stress evolution is critical to understanding the evolution of surface nanostructures and the changes in curvature due to ion bombardment in free standing thin film microelectromechanical systems (MEMS). This study uses MD simulations to study sputtering, stress and structure evolution due to argon ion bombardment. Stillinger-Weber [**4**] and Molière potentials [**5 - 6**] are used to model silicon-silicon interactions and argon-silicon or argon-argon interactions respectively. Simulations are performed on a 5.43nm × 5.43nm × 5.43nm initially undamaged silicon crystal. Lateral periodic boundary conditions are applied to the (001) target surface. The effects of the periodic boundary conditions are indiscernible with the transverse box size chosen in this work. The velocity-Verlet algorithm [**7 - 8**] used in the MD simulation uses a time step of 0.25fs for most parts of the simulation and 0.1fs during the initial stages of ion impact. Details of the MD simulation are reported by the authors in [**9**]. At least five simulations of more than 100 ions impacts are performed at both 500eV and 700eV ion energies.

2. RESULTS AND DISCUSSION

2.1 Sputtering and structure analysis

Bombardment by argon atoms leads to sputtering of some near-surface atoms. Fig. 1 shows the sputtering and implantation data for ion fluences up to 4.0×10^{14} ions/cm^2 for both 500eV and 700eV cases. It is observed that for the 500eV case 80% of the incident argon is implanted in to the target material. The rate of implantation is slightly higher in the 700eV case than in the 500eV case. The sputter yields, defined as the number of silicon or argon atoms sputtered per impact, for the 500eV and 700eV cases are 0.49 and 0.67 respectively. Sputter yields during the initial transient period, when ion bombardment occurs on a predominantly crystalline surface, are up to 20% higher than the steady state values observed.

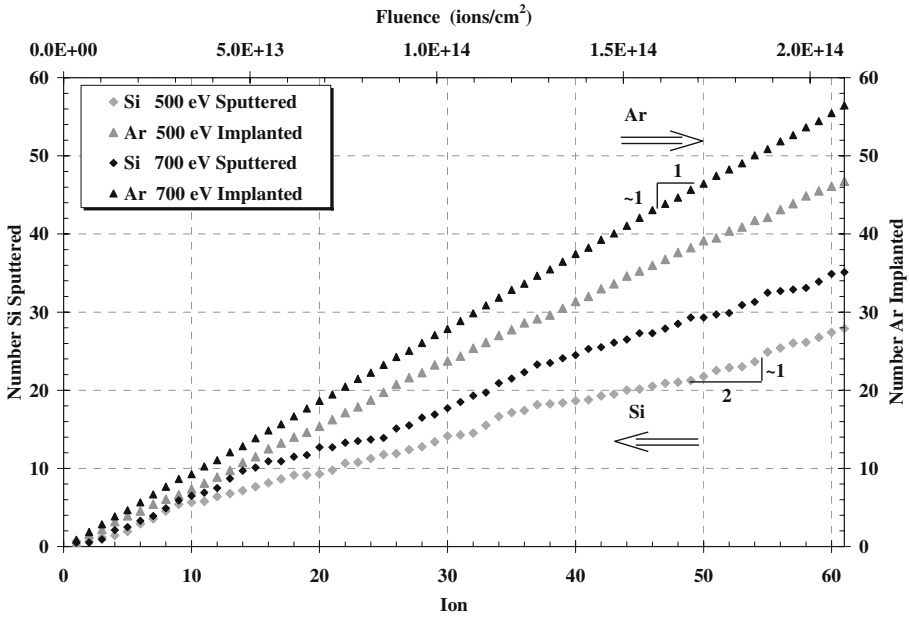

Figure 1. Sputtering rates of silicon and argon averaged over 8 randomized cases for 500eV incident energy and 5 randomized cases for 700eV incident energy.

Structural and damage evolution is quantified using a planar radial distribution function and a structure factor-like measure of crystallinity [**9**]. The crystallinity measure is a dimensionless quantity defined such that it varies between zero and one, with the upper limit corresponding to a perfectly crystalline, undamaged material and the lower limit corresponding to an amorphous material. Fig. 2 shows the plot of variation of degree of crystallinity for the 500eV case and the damaged region is seen to extend to 2.2nm into the material after about 61 impacts (2.07×10^{14}ions/cm^2 fluence). An almost amorphous near-surface layer is observed at fluences as small as 1.0×10^{14}ions/cm^2. The 500eV damage evolution pattern is similar to the 700eV case except for the depth of damage from the surface, which is deeper (about 3nm instead of 2.2nm) in the 700eV case. The material is, for the most part, crystalline and damage-free below these depths.

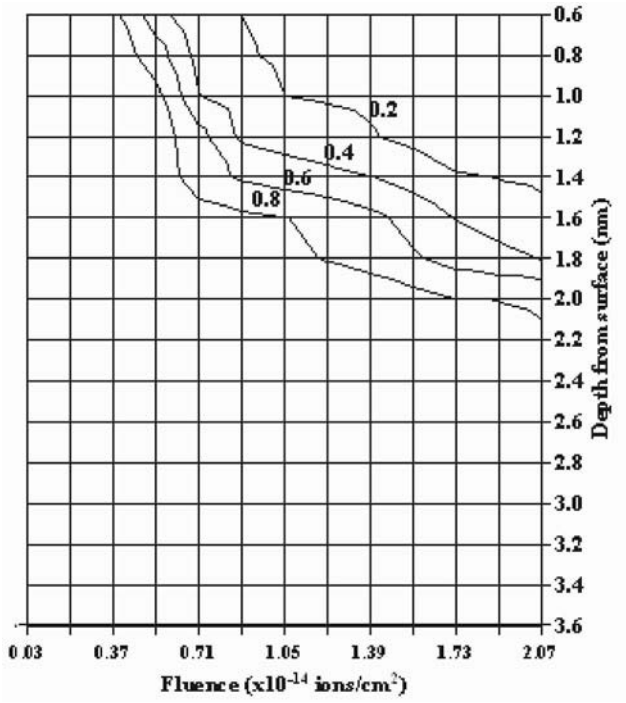

Figure 2. Plot of variation of crystallinity with depth and fluence for the 500eV ion energy case. Data presented here is averaged over 8 randomized cases.

2.2 Stress analysis

Traction after every impact is computed using the interplanar mechanical stress method described in [**10**]. Fig. 3 shows the variation of stress after each impact for the 500eV and 700eV cases. The ion incidence directions and the reference axes are shown in the inset in Fig. 3. The stress component σ_{xx} is calculated using the two body and three body forces acting across a planar area. Tractions in the simulation cell are averaged by calculating tractions in smaller local regions. For the data presented here the local regions are located at seven planar areas aligned parallel to the *y-z* plane, at ten different depths in the ion incidence direction at each plane of interest. Stresses are seen to approach a value of 1.3GPa and 1.7GPa for the 500eV and 700eV cases respectively after a fluence of 4×10^{14}ions/cm^2.

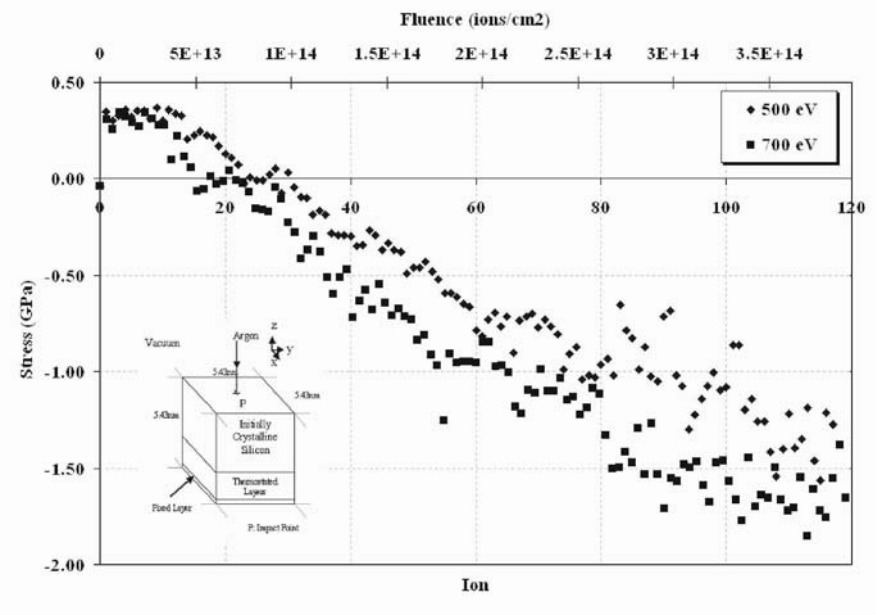

Figure 3. Stress evolution during ion bombardment at 500eV and 700eV ion energies. Data presented here is averaged over 7 randomized cases until the 100th ion and 3 randomized cases beyond the 100th ion for 500eV ion energy. Stress data is averaged over 5 randomized cases until the 78th ion, three randomized cases from 79th ion to 114th ion and only one randomized case is presented beyond 114th ion for 700eV ion energy. Inset shows the reference coordinate axes.

2.3 Mapping atomic positions to surface equations

In an ion bombardment process used to fabricate nanostructures, the surface changes shape due to two processes that occur at disparate length and time scales. The first process is the rearrangement of atoms due to the effects of incident ions. The spatial surface roughness changes due to slope and position dependent sputtering due to ion bombardment. The second process involves rearrangement of atoms at the surface in order to minimize the surface free energy and is believed to cause atoms to diffuse from regions of high chemical potential to low chemical potential. The combination of surface diffusion and the effects of the incident ions on sputtering and mass rearrangement lead to the development of nanostructures like semiconductor quantum dots, under certain conditions, with linear length scales in the range 1nm - 10nm. An atomistic simulation of such dimensions could involve tens of thousands of atoms and a fully

atomistic simulation of such systems is not feasible for more than nanosecond time scales. One strategy is to treat the short timescale ion effects separately from the large timescale chemical potential effects. Continuum description of ion bombarded surface is required to perform such analyses of the growth of nanostructures. A silicon probe atom method is used here to map the atomic positions calculated during the MD simulation to a continuum surface description in terms of surface height coordinates and equations. In this method, a silicon atom is brought far away from the material at a particular (x, y) position along a line parallel to the z-axis. Then as the probe atom approaches the surface, the z-position at which the potential energy, calculated using Stillinger-Weber or Molière potential, attains a minimum is used to define the surface coordinates. Piecewise bicubic interpolation of surface coordinate data yields surface equations of the form $z = f(x, y)$. Fig. 4 shows the atomic positions near the surface after 100 impacts (3.39×10^{14} ions/cm^2 fluence) for the 500eV case and Fig. 5 shows the corresponding surface obtained using the probe atom method.

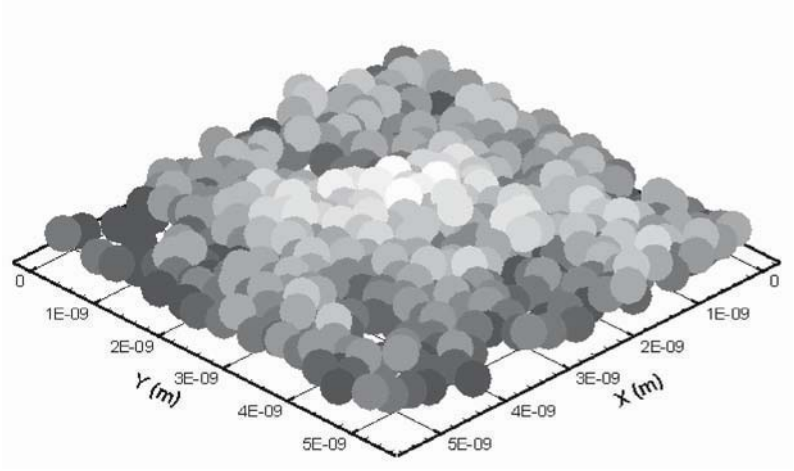

Figure 4. Positions of silicon and argon atoms near the surface after 100 impacts at 500eV ion energy. Color indicates height measured from the highest point of undamaged crystal - with white color indicating 0.2nm above the reference height and black color indicating 0.4nm below the reference height.

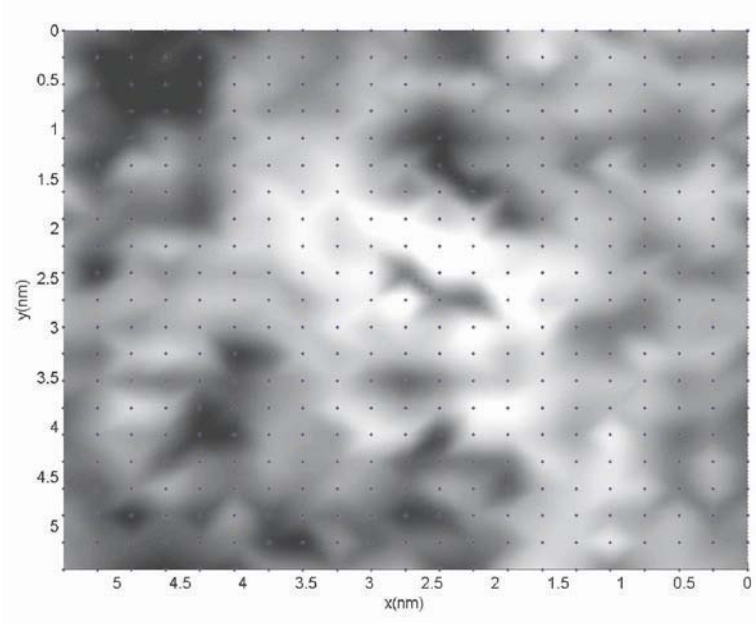

Figure 5. Surface calculated using the silicon probe atom method. Surface coordinates and surface equations mapped from discrete atomic positions using the probe atom method. Color indicates height measured from the highest point of undamaged crystal - with white color indicating 0.2nm above the reference height and black color indicating 0.4nm below the reference height. The black dots represent (*x*,*y*) points at which silicon probe atom method is used to calculate height. Data between points represented by blue dots is calculated by bicubic interpolation.

ACKNOWLEDGMENTS

NSF grant DMI 02-23821 supported this work. The authors express gratitude to Prof. T. G. Bifano of Boston University for many inputs.

REFERENCES

1. T. Bobek, S. Fackso, H. Kurz. "Temporal evolution of dot patterns during ion sputtering", *Phys. Rev. B*, **68**, 085324, 2003.
2. C. Hofer, S. Abermann, C. Teichert, T. Bobek, H. Kurz, K. Lyutovich, E. Kasper. "Ion bombardment induced morphology modifications on self-organized semiconductor surfaces", *Nucl. Instr. and Meth. B*, **216**, pp.178-184, 2003.

3. T. G. Bifano, H. T. Johnson, P. Bierden, R. Mali. "Elimination of stress-induced curvature in thin-film structures", *J. MEMS*, **11**, pp. 592-597, 2002.
4. F. Stillinger, T. Weber. "Computer simulation of local order in condensed phases of silicon", *Phys. Rev. B*, **31**, pp. 5262-5271, 1985.
5. V.G. Molière. "Theorie der Streuung schneller geladener Teilchen I: Einzelstreuung am abgeschirmten Coulomb-Field", *Z. Naturforschg.*, **2 A**, pp. 133-145, 1947.
6. I. M. Torrens. *Interatomic Potentials*, Academic Press, New York, 1972.
7. M. P. Allen, D.T. Tildesley. *Computer Simulations of Liquids*, Claredon Press, Oxford, 1987.
8. D. Frenkel, B. Smit. U*nderstanding Molecular Simulation from Algorithms to Applications, 2nd ed.*, Academic Press, NY, 2002.
9. M. C. Moore, N. Kalyanasundaram, J. B. Freund, H. T. Johnson. "Structural and sputtering effects of medium energy ion bombardment of silicon", *Nucl. Instr. and Meth. B*, **225** pp. 241-255, 2004.
10. K. S. Cheung, S. Yip. "Atomic-level stress in an inhomogeneous system", *J. Appl. Phys.*, **70**, pp. 5688-5690, 1991.

MECHANICS OF NANOSTRUCTURES

R. Ruoff[1] and N. Pugno[2]
[1]*Department of Mechanical Engineering, Northwestern University, Evanston, IL 60208-3111, USA, E-mail: r-ruoff@northwestern.edu, n-pugno@northwestern.edu.*

[2]*Department of Structural Engineering, Politecnico di Torino, Corso Duca degli Abruzzi 24, 10129, Italy, Email: nicola.pugno@polito.it.*

Abstract: Quantized fracture mechanics is applied for studying the mechanics of nanostructures. An application for predicting the strength of defective nanotubes, compared with atomistic simulations and experiments, clearly shows that materials are sensitive to flaws (also) at nanoscale.

Key words: nanomechanics, nanostructures, nanotubes, quatized fracture mechanics, quantized strength

1. INTRODUCTION

The energy release rate is defined as $G = \frac{K_I^2}{E'} + \frac{K_{II}^2}{E'} + \frac{1+\nu}{E} K_{III}^2$, where $K_{I,II,III}$ are the stress-intensity factors for modes I, II, III of crack propagation, with $E' = E$ (for plane stress) or $E' = E/\left(1-\nu^2\right)$ (for plane strain), where E is the Young's modulus and ν is the Poisson's ratio of the material. According to classical Fracture Mechanics the crack propagation will arise for [**1**]:

$$G \equiv -\mathrm{d}W/\mathrm{d}A = G_C \text{ or } K_{I,II,III} = K_{I,II,IIIC} \quad (1)$$

T. J. Chuang et al. (eds.), Nanomechanics of Materials and Structures, 199–203.
© 2006 *Springer. Printed in the Netherlands.*

where W is the total potential energy and the subscript C denotes a critical condition for the crack propagation (G_C and $K_{I,II,IIIC}$ are the fracture energy and toughness of the material). On the other hand, according to Quantized Fracture Mechanics (QFM) the crack propagation will arise for [**2**]:

$$G^* \equiv -\Delta W/\Delta A = G_C \text{ or } K^*_{I,II,III} \equiv \sqrt{\left\langle K^2_{I,II,III} \right\rangle_A^{A+\Delta A}} = K_{I,II,IIIC} \tag{2}$$

where $\left\langle \cdot \right\rangle_A^{A+\Delta A} \equiv \dfrac{1}{\Delta A} \int_A^{A+\Delta A} \cdot \, \mathrm{d}A$. QFM assumes "dissipation energy" in quanta $G_C \Delta A$ where ΔA is the fracture quantum. Values for the stress intensity factors $K_{I,II,III}$ are available for the most interesting cases [**3**]; thus QFM can be applied in a very simple way. In contrast to classical fracture mechanics, that can treat only "large" (with respect to the fracture quantum) and sharp (vanishing tip radius) cracks, QFM has not restriction in treating defects with any size and shape. Thus, QFM can be applied also at nanoscale, where classical fracture mechanics does not work [**4**].

2. MATERIALS ARE SENSITIVE TO FLAWS AT NANOSCALE

Consider a linear elastic infinite plate in tension, of uniform thickness t, with a blunt crack of length $2l$ and tip radius ρ orthogonal to the applied far field σ (crack opening mode I). The material is described by the fracture toughness K_{IC} and by the fracture quantum at the considered size-scale $\Delta A = at$. Applying QFM the failure strength is predicted as:

$$\sigma_f(l,\rho) = K_{IC}\sqrt{\frac{1+\rho/2a}{\pi(l+a/2)}} = \sigma_C\sqrt{\frac{1+\rho/2a}{1+2l/a}} \tag{3}$$

where σ_C is the strength of the plain structure; accordingly the fracture quantum is estimated as $a \approx 2K_{IC}^2/\left(\pi\sigma_C^2\right)$. Eq. (3) shows that for $l << a$ ("short" cracks) the structure becomes insensitive to flaws, whereas for $l >> a$ (and $\rho = 0$) QFM recovers classical fracture mechanics, that is not able to predict such "short crack behaviour". Thus materials with a large value of a present a significant zone in which they become insensitive to

flaws (e.g., bio-nanocomposites [**4**]). On the other hand at nanoscale such parameter can be also as smaller as the interatomic spacing, as observed for nanotubes (see next section). Thus, in contrast to what reported in the title of ref. [**4**], "materials become insensitive to flaws at nanoscale" is in general not correct, as demonstrated in the next section.

2.1 The example of carbon nanotubes

A pioneer experimental work on strength and fracture of nanotubes is reported in [**5**]. The tensile strengths of individual multiwalled carbon nanotubes (MWCNTs) were measured with a *nanostressing stage* composed of two opposing atomic force microscope (AFM) tips, Fig. 1a,b, and located within a scanning electron microscope (SEM). The tensile experiment was prepared and observed entirely within the microscope and was recorded on video until fracture. The sum of the fragment lengths, Fig. 1c, far exceeded the original nanotube length. This apparent discrepancy was explained by a *sword-in-sheath* type fracture mechanism, similar to that observed in carbon fibers, i.e., the MWCNTs broke in the outermost layer. The tensile and fracture strength of this layer ranged from 11 to 63 GPa for the set of 19 MWCNTs that were loaded (in particular, values of 63, 43, 39, 37, 37, 35, 34, 28, 26, 24, 24, 21, 20, 20, 19, 18, 18, 12, 11 GPa were measured). Analysis of the stress-strain curves for individual MWCNTs indicated that the Young's modulus E of the outermost layer varied from 270 to 950 GPa. Transmission electron microscopic (TEM) examination of the broken nanotube fragments revealed a variety of structures, such as a nanotube ribbon, a wave pattern, and partial radial collapse, Fig. 1d,e.

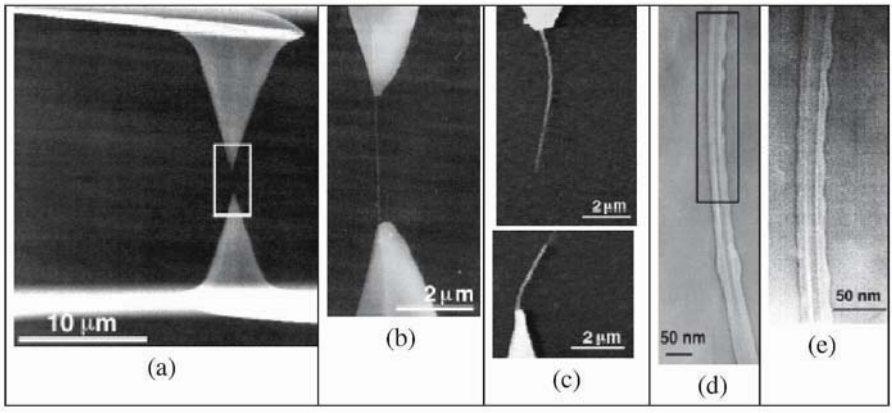

Figure 1. Experiments on fracture strength of nanotubes [5].

The experimental results on nanotubes [**5**] show distinct clusters about a series of decreasing values of strength, with the maximum 63GPa, and the other values "quantized" at 43, 36-37, 25-26, 19-20 and 11-12GPa. The measured strength of 63GPa is not in agreement with the ideal tensile strength of nanotubes (around 100GPa). The observed strength quantization could be related to the quantization in the size of the defects. We apply QFM assuming the fracture quantum identical to the distance between two adjacent broken chemical bonds, i.e., $a \approx \sqrt{3} r_0$, with $r_0 \approx 1.42 \,\text{Å}$ interatomic length. For example, consider defects like n adjacent vacancies $2l = na$ in eq. (3). This case was treated by molecular mechanics (MM) atomistic simulations in [**6**]. The comparison between these MM simulations and the predictions of eq. (3) (we thus neglect here boundary effects) is summarized in Table 1; the MM-calculated strengths clearly follow the $(1+n)^{-1/2}$ dependence predicted by QFM with a fit of $\sigma_C \sqrt{1+\rho/2a} = 111\,\text{GPa}$. For the value of the ideal strength calculated in [**6**], $\sigma_C = 93.5\,\text{GPa}$, it gives the reasonable value of $\rho \approx 0.8a \approx 2.0\,\text{Å}$. In Table 1 between brackets are reported the measured strengths. The first three values are well fitted assuming nano-flaws having length of n=2,4,8 (in units of fracture quanta). Thus, it is clear that nano-flaws affect the strength of nanotubes. For a more detailed investigations, including also nano-hole defects, see the QFM paper [**2**].

Strength [GPa]	n=2 (63)	n=4 (...)	n=6 (43)	n=8 (39)	
MM - (80,0)	64.1	50.3	42.1	36.9	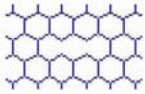
QFM	64.1	49.6	42.0	37.0	

Table 1. MM [6] and QFM [2] comparison on fracture strength of nanotubes with n adjacent vacancies (the graph reports the example of n=2, the applied load is vertical). In brackets the observed strengths [5].

3. CONCLUSIONS

The analysis clearly demonstrates that, in contrast to [4], materials are (in general) sensitive to flaws (also) at nanoscale.

ACKNOWLEDGMENTS

We gratefully acknowledge the grant support from the NSF grant "*Mechanics of Nanoropes*" (NSF #0200797, Ken Chong and Oscar Dillon, program managers), and the NSF grants *NIRT: Electrical and Mechanical Properties of Boron and Metal and Nanoscale Devices Built from them* (NSF #0210120) and *NIRT: Synthesis, Characterization and Modeling of Aligned Nanotube Arrays for Nanoscale Devices and Composites* (NSF #030450); and from the Office of Naval Research *"Mechanics of Nanostructures"* grant under award No. N000140210870 and the NASA University Research, Engineering and Technology Institute on *Bio Inspired Materials (BIMat)* under award No. NCC-1-02037(Jeff Jordan, program manager).

REFERENCES

1. Griffith A.A., "The phenomenon of rupture and flow in solids", *Phil.Trans. Roy. Soc.* **A221**, pp. 163-198, 1921.
2. Pugno N., Ruoff R., "Quantized Fracture Mechanics", *Philosophical Magazine* **84/**27, pp. 2829-2845, 2004.
3. Murakami H., *Stress intensity factors handbook*, Oxford (UK), Publ. Pergamon, 1986.
4. Gao H., Ji B., Jaeger I.L., Arzt E. and Fratzl P., "Materials become insensitive to flaws at nanoscale: lesson from Nature", *Proceedings of the National Academy of Sciences of USA*, **100**, pp. 5597-5600, 2003.
5. Yu M-F, Lourie O., Dyer M.J., Moloni K., Kelly T.F., Ruoff R.S., "Strength and breaking mechanism of multiwalled carbon nanotubes under tensile load", *Science* **287**, pp. 637-640, 2000.
6. Belytschko T., Xiao S.P., Ruoff R., "Effects of defects on strength of nanotubes: experimental-computational comparison", *Los Alamos National Laboratory, Preprint Archive*, *Physics* 1-6, 2002.

RESIDUAL STRESSES IN NANO-FILM/SUBSTRATE SYSTEMS

Sanboh Lee
Department of Materials Science and Engineering National Tsing Hua University, Hsinchu, Taiwan Phone:886-3-574-2624, Fax:886-3-572-2366, Email:sblee@mse.nthu.edu.tw

Abstract: Residual stresses in elastic multi-layer film/elastic substrate systems were derived in closed-form solutions. There are always three unknowns to be solved and three equilibrium conditions to be satisfied. The special case of an elastic single nano-film deposited on an elastic substrate was demonstrated to analyze the viscoelastic stress relaxation. Two models of Maxwell and Kelvin were described the viscoelastic body. Two cases of viscoelastic film/elastic substrate and elastic film/viscoelastic substrate are considered. The stress in the elastic body in the space coordinates has the same form as the stress in the viscoelastic body in the Laplace transform coordinates. According to this analogy, we solve the residual stress in nano-film/substrate system. For the case of viscous flow in the film, both models show that the stress relaxation rate increases with decreasing film thickness. However, both models for the case of viscous flow in the substrate exhibit the opposite trend to those for the case of viscous flow in the film. The Maxwell model has full stress relaxation, but the Kelvin has not.

Key words: Film, substrate, Kelvin, Maxwell, bending

1. INTRODUCTION

Thin film deposition on a substrate has been applied to many fields, such as semi-conductor, optical electronics and structural devices, etc. During the deposition process, residual stresses are built up because of thermal mismatch, lattice mismatch, phase transformation and other factors etc. Residual stresses influences not only on the mechanical properties but also on the electric and optical properties. The residual stresses are often

T. J. Chuang et al. (eds.), Nanomechanics of Materials and Structures, 205–215.
© 2006 *Springer. Printed in the Netherlands.*

analyzed by using the linear elasticity [**1**]. At temperature near glass transition point of polymeric materials or above one-third of melting point of inorganic materials, viscoelastic flow must be considered. The viscoelasticity was described by both Maxwell and Kelvin models [**2**]. The governing equations of elasticity in the space coordinate system have a similar form to those of viscoelasticity in Laplace transform coordinate system [**3**]. The purpose of this study is to develop an analytical model to analyze the elastic multi-layer film/substrate systems and viscoelastic single-layer film/substrate systems.

2. ELASTIC SOLUTION

Consider n layers of films with individual thickness t_i deposited on a substrate with t_s at high temperatures as shown in Fig. 1(a). The subscript i denotes the layer number for the film from 1 to n. The coordinate system is also shown in Fig. 1(a). The relation between h_i and t_i is written as

$$h_i = \sum_{j=1}^{i} t_j \quad (i = 1 \text{ to } n) \tag{1}$$

The system is cooled to room temperature. The stresses in the system solved as followings. First, the system experiences unconstrained differential strains, $\Delta\varepsilon_s$ and $\Delta\varepsilon_i$ (see Fig. 1(b)), existing in the substrate and film layers, respectively. These differential strains arise from the thermal expansion mismatch, lattice expansion mismatch, phase transformation, etc. Second, a uniform strain c in the multi-layer is applied and total force on the system remains zero (Fig. 1(c)). Third, bending occurs to behave balance the bending moment induced by asymmetric stresses in the system (Fig. 1(d)).

The total strain in the system is decomposed into a uniform strain and a bending component,

$$\varepsilon = c + (z - t_b)/r \tag{2}$$

where r is the radius of curvature and t_b is the location of bending axis.

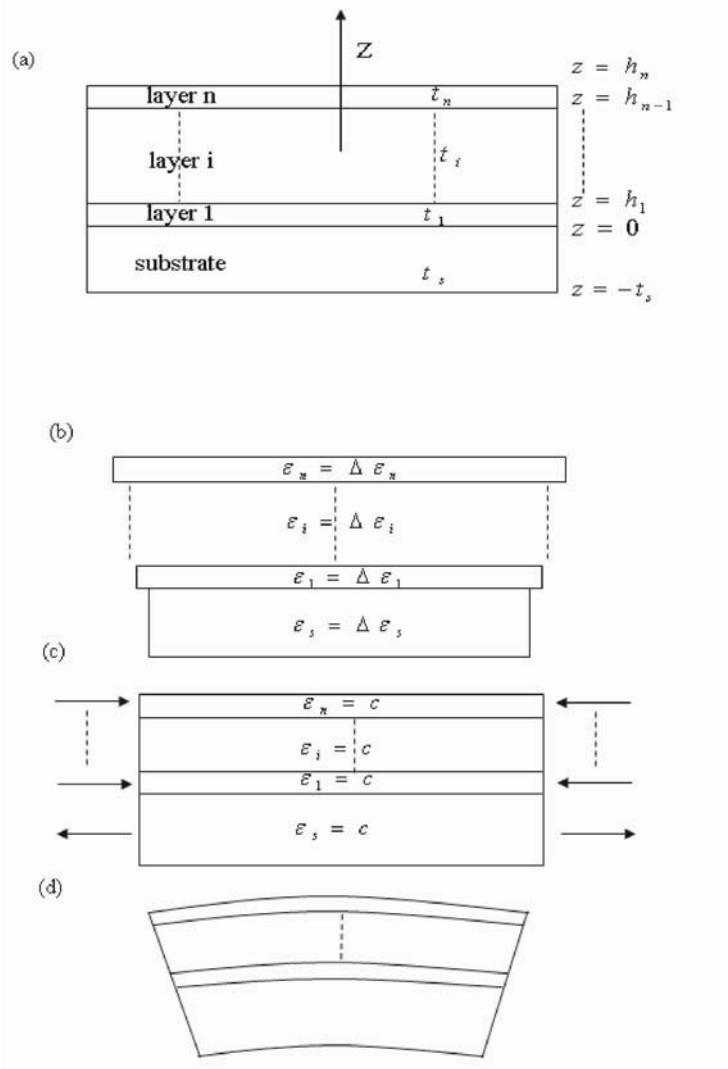

Figure 1. Schematics showing bending of a multi-layer films deposited on a substrate. (a) stress-free condition, (b) unconstrained strain due to residual strain, (c) constrained strain to maintain displacement compatibility and (d) bending induced by asymmetric stresses.

The strain-stress relation in the system is

$$\sigma_s = B_s\left(\varepsilon - \Delta\varepsilon_s\right) \quad \text{for } -t_s \le z \le 0 \tag{3a}$$

$$\sigma_i = B_i(\varepsilon - \Delta\varepsilon_i) \qquad \text{for } 0 \le i \le n \tag{3b}$$

where B_s and B_i are the biaxial moduli of substrate and layer i of film. Three parameters c, r and t_b can be determined from the following three equilibrium conditions. First, the resultant force due to uniform strain is zero. Second, the resultant force due to the bending strain is zero. Third, the bending moment is zero. The solutions are

$$c = (B_s t_s \Delta\varepsilon_s + \sum_{i=1}^{n} B_i t_i \Delta\varepsilon_i) \Big/ (B_s t_s + \sum_{i=1}^{n} B_i t_i) \tag{4a}$$

$$t_b = \left[- B_s t_s^2 + \sum_{i=1}^{n} B_i t_i (2h_{i-1} + t_i) \right] \Big/ 2(B_s t_s + \sum_{i=1}^{n} B_i t_i) \tag{4b}$$

$$\frac{1}{r} = \frac{3\left[B_s (c - \Delta\varepsilon_i) t_s^2 - \sum_{i=1}^{n} B_i t_i (c - \Delta\varepsilon_i)(2h_{i-1} + t_i) \right]}{B_s t_s^2 (2t_s + 3t_b) + \sum_{i=1}^{n} B_i t_i \left[6h_{i-1}^2 + 6h_{i-1} t_c + 2t_i^2 - 3t_b (2h_{i-1} + t_i) \right]} \tag{4c}$$

where $i = 1$, $h_{i-1} = h_0$ is defined as zero in Eq. 4(b) and Eq. 4(c). The position of bending axis is independent of residual strain and both c and $1/r$ are linearly proportional to the residual strain.

Now consider n=1, i.e. one layer of film deposited on a substrate. Assuming that $\Delta\varepsilon_s = 0$ and $\Delta\varepsilon_1 = \Delta\varepsilon$, Eqs. (4) are reduced to

$$c = B_1 h_1 \Delta\varepsilon / (B_1 h_1 + B_s h_s) \tag{5a}$$

$$t_b = (B_1 h_1^2 - B_s h_s^2) / 2(B_1 h_1 + B_s h_s) \tag{5b}$$

$$\frac{1}{r} = \frac{6 B_1 B_s h_1 h_s (h_1 + h_s) \Delta\varepsilon}{B_1^2 h_1^4 + B_s^2 h_s^2 + 2 B_1 B_s h_1 h_s (2h_1^2 + 2h_s^2 + 3h_1 h_s)} \tag{5c}$$

When film thickness is nano-size, the film stress is obtained from Eqs. 3(b), (2) and (5), and the first-order approximation is

$$\sigma_1 = -B_1 B_s h_s \Delta\varepsilon / (4B_1 h_1 + B_s h_s) \tag{6}$$

When a zero-order approximation is considered, Eq. (6) is reduced to

$$\sigma_1 = -B_1 \Delta\varepsilon \tag{7}$$

Eq. (7) corresponds to the well-known Stoney's equation with different sign because of the different conventions to define curvature.

3. ELASTIC SOLUTION

While the stress in the elastic body is time independence, the stress in a viscous material is a function of time. Two types of Kelvin and Maxwell models are popular to describe the rheological behavior of material. It was proved that the governing equation of elasticity and the Laplace transform with respect to time of the viscoelastic governing equation are analogous in form. It was found that the biaxial moduli in the elastic medium have the following transforms in formulating the Laplace transform of stress in the corresponding viscoelastic system.

$$B \to 18KG\eta s / \left[3K(G + \eta s) + 4G\eta s\right] \tag{8}$$

for Maxwell model and

$$B \to 18K(G + \eta s) / \left[3K + 4(G + \eta s)\right] \tag{9}$$

for Kelvin model. K and G are the bulk modulus and shear modulus, respectively, and η is the Newtonian shear viscosity.

3.1 Maxwell model

Two cases of viscoelastic film/elastic substrate and elastic film/viscoelastic substrate systems are studied. The residual differential strain occurs at the initial time, $\Delta\varepsilon_0$ for both cases.

3.1.1 Viscoelastic film/elastic substrate

Replacing B_1, in Eq. (6) by Eq. (8) and Laplace transform of $\Delta\varepsilon_0$, we get the viscoelastic stress in the film in the Laplace transform coordinate. Then inversing the Laplace transform yields

$$\sigma_1(t) = -\frac{B_1 B_s h_s}{4B_1 h_1 + B_s h_s}\left\{\Delta\varepsilon_0 \exp\left[\frac{-B_1 B_s h_s t}{6(4B_1 h_1 + B_s h_s)\eta_1}\right]\right\} \tag{10}$$

The effect of viscous flow in the film on the relaxation of film is studied using Eq. (10). The film stress, σ_1, is normalized by its initial stress σ_1(t=0), and plotted as a function of normalized time, $B_1 t/\eta_1$. Using B_1/B_s =0.5, the stress relaxation is shown in Fig.2 for different relative thicknesses. The rate of stress relaxation decreases with increasing relative thickness. The stress relaxes completely for all relative thicknesses. The stress relaxation in the film is accompanied by stress relaxation in the substrate. Because no force is applied in the system, the stresses in the film and substrate satisfy the equilibrium condition:

$$\sigma_1 h_1 + \overline{\sigma_s} h_s = 0 \tag{11}$$

Because h_1 is nano-size, which is very small compared with h_s, stress in the film is expected to be uniform. Here, the average stress in the substrate σ_s becomes relaxation as film relaxes.

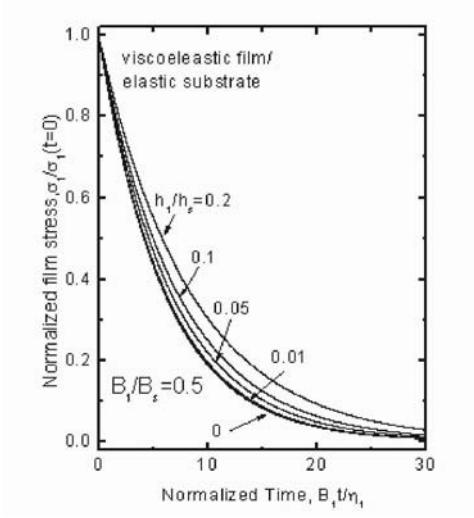

Figure 2. Film stress as a function of time at different relative thicknesses for viscoelastic film/elastic substrate system using Maxwell model.

3.1.2 Elastic film/viscoelastic substrate

Replacing B_s in Eq. (6) by Eq. (8) and Laplace transform of $\Delta\varepsilon_0$, we get the viscoelastic stress in the film in the Laplace transform coordinate. Then inversing the Laplace transform yields

$$\sigma_1(t) = \frac{-B_1 B_s h_s}{4B_1 h_1 + B_s h_s}\left\{\Delta\varepsilon_0 \exp\left[\frac{-2B_1 B_s h_1 t}{3(4B_1 h_1 + B_s h_s)}\right]\right\} \tag{12}$$

Using B_1 / B_s=0.8 and Eq. (12), the stress relaxation is shown in Fig.3 for different relative thicknesses. The rate of stress relaxation increases with increasing relative thickness. When h_1 / h_s=0, the stress in the film can not be relaxed at all. Compare to Fig.2, Fig.3 reveals slower stress relaxation.

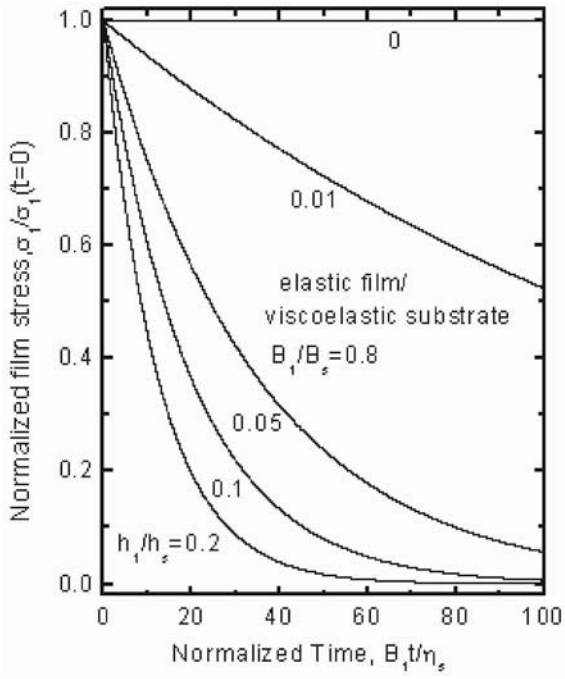

Figure 3. Film stress as a function of time at different relative thicknesses for elastic film/viscoelastic substrate system using Maxwell model.

3.2 Kelvin model

Two cases of viscoelastic film/elastic substrate and elastic film/viscoelastic substrate systems are investigated. The residual differential strain is assumed to maintain constant at all times, $\Delta\varepsilon(t) = \Delta\varepsilon_0$

3.2.1 Viscoelastic film/elastic substrate

Replacing B_1 in Eq. (6) by Eq. (9) and changing $\Delta\varepsilon_0$ by $\Delta\varepsilon_0 / s$ where s is the Laplace transform coordinate, we get the stress in the viscoelastic film in the Laplace transform coordinate. Then inversing the Laplace transform yields

$$\sigma_1(t) = \frac{-B_1\Delta\varepsilon_0}{1+\dfrac{4B_1h_1}{B_sh_s}}\left\{1+\frac{\dfrac{1+\nu_1}{1-\nu_1}}{2\left(\dfrac{1-2\nu_1}{1-\nu_1}+\dfrac{6B_1h_1}{B_sh_s}\right)}\exp\left[\frac{-\dfrac{1-\nu_1}{1+\nu_1}\left(1+\dfrac{4B_1h_1}{B_sh_s}\right)B_1t}{4\left(\dfrac{1-2\nu_1}{3(1-\nu_1)}+\dfrac{2B_1h_1}{B_sh_s}\right)\eta_1}\right]\right\} \quad (13)$$

The effect of viscous flow in the film on the stress relaxation is investigated using Eq. (13). Assuming that B_1 / B_s =0.5, the stress in the viscoelastic film normalized by σ_1 (t=0) is plotted as a function of normalized time B_1t / η_1 with different relative thicknesses where ν_1 =0.3. Note that the stresses at the initial time and infinite time are

$$\sigma_1(t=0) = -3B_1\Delta\varepsilon_0 \Big/ 2\left[\frac{1-2\nu_1}{1-\nu_1}+\frac{6B_1h_1}{B_sh_s}\right] \quad (14)$$

$$\sigma_1(t=\infty) = -B_1B_sh_s\Delta\varepsilon_0 / (4B_1h_1 + B_sh_s) \quad (15)$$

respectively. It can be seen from Fig.4 that the stress decreases monotonically with increasing time until it reaches steady state. The stress relaxation rate is faster for a smaller relative thickness, which is similar to that of Maxwell model.

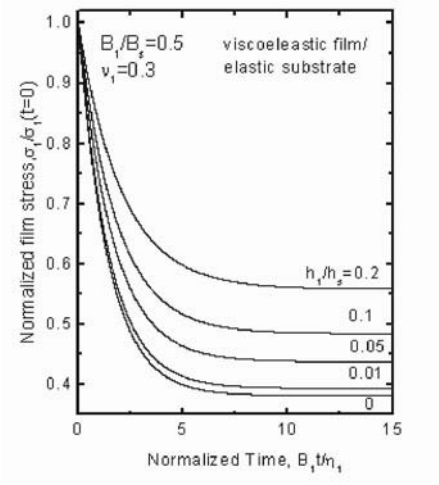

Figure 4. Film stress as a function of time at different relative thicknesses for viscoelastic film/elastic substrate system using Kelvin model.

3.2.2 Elastic film/viscoelastic substrate

Replacing B_s in Eq. (6) by Eq. (9) and changing $\Delta\varepsilon$ by $\Delta\varepsilon / s$ where s is the Laplace transform coordinate, we get the stress in the nano-film in the Laplace transform coordinate. Then inversing the Laplace transform yields

$$\sigma_1(t) = \frac{-B_1\Delta\varepsilon_0}{1+\dfrac{4B_1h_1}{B_sh_s}}\left\{1+\frac{\dfrac{1+\nu_1}{1-\nu_1}}{2\left(\dfrac{1-2\nu_s}{1-\nu_s}+\dfrac{3B_sh_s}{8B_1h_1}\right)}\exp\left[\frac{-\dfrac{1-\nu_s}{1+\nu_s}\left(4+\dfrac{B_sh_s}{B_1h_1}\right)B_st}{2\left(\dfrac{8(1-2\nu_s)}{3(1-\nu_s)}+\dfrac{B_sh_s}{B_1h_1}\right)\eta_s}\right]\right\} \tag{16}$$

Using Eq. (16) and B_1 / B_s =0.8, the stress in the elastic film as function of normalized time B_1t/η_s is shown in Fig.5 where ν_s =0.3. The stress in the elastic film at the initial time and infinite time are

$$\sigma_1(t=0) = -B_1\Delta\varepsilon_0 \Big/ \left[1+\frac{8}{3}\frac{(1-2\nu_s)B_1h_1}{(1-\nu_s)B_sh_s}\right] \tag{17}$$

$$\sigma_1(t=\infty) = -B_1B_sh_s\Delta\varepsilon_0 / (4B_1h_1 + B_sh_s) \tag{18}$$

It can be seen from Fig.5 that the stress relaxation rate increases with increasing relative thickness, which is the same as that of Maxwell model. Eq. (18) is equal to the stress in the elastic film at the initial time for Maxwell model.

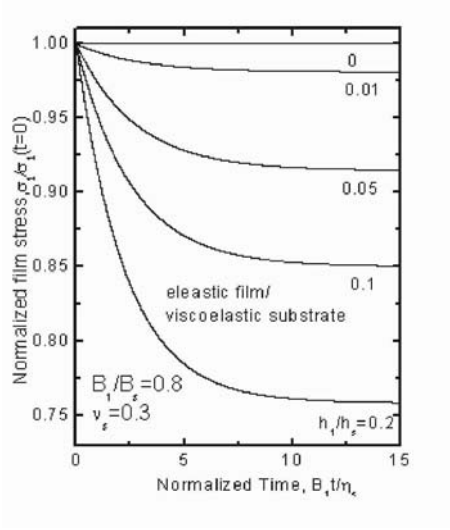

Figure 5. Film stress as a function of time at different relative thicknesses for elastic film/viscoelastic substrate system using Kelvin model.

4. SUMMARY

1. Bending axis is utilized to solve the bending problem and its position is independent of residual stresses.
2. For a multi-layer system, there are always three unknown and three equilibrium conditions to be solved.
3. For the case of viscous flow in the film, the stress relaxation rate in nano-film decreases with increasing relative thickness for both Maxwell and Kelvin models.
4. The stress relaxation rate in nano-film for the case of viscous flow in the substrate has the opposite trend to that for the case of viscous flow in nano-film for both viscoelastic models.
5. The nano-film stress at the infinite time for Kelvin model is the same as that at initial time for Maxwell model.
6. The Maxwell model has full stress relaxation, but Kelvin model has not.

ACKNOWLEDGMENTS

This work was supported by the National Science Council, Taiwan, Republic of China.

REFERENCES

1. C. H. Hsueh, *J. Am. Ceram. Soc*. **74**, 646 (1991).
2. W.Nowacki, *Thermoelasticity, 2nd ed*. (Pergamon, Oxford, 1986), P.476.
3. G. E. Mase, Schaum's Outline Series: *Theory and Problems of Continuum Mechanics* (Mc Graw-Hill, New York 1970), P.196.

NANOMECHANICS OF CRACK FRONT MOBILITY

Ting Zhu[1], Ju Li[2] and Sidney Yip[3]
[1]*Department of Mechanical Engineering,*
Massachusetts Institute of Technology, Cambridge, MA 02139, USA
[2]*Department of Materials Science and Engineering,*
Ohio State University, Columbus, OH 43210, USA
[3]*Departments of Nuclear Engineering and Materials Science and Engineering,*
Massachusetts Institute of Technology, Cambridge, MA 02139, USA (syip@mit.edu)

Abstract: Minimum energy paths for unit advancement of a crack front are determined by reaction pathway sampling, thus providing the reaction coordinates for the analysis of crack tip mechanics in ductile and brittle materials. We compare results on activation energy barrier and atomic displacement distributions for a atomically sharp crack in Cu, where one observes the emission of a partial dislocation loop, and in Si, where crack front extension evolves in a kink-like fashion.

Key words: Minimum energy path, crack front, dislocation loop nucleation, double kink formation and migration, atomic displacement.

1. INTRODUCTION

Is it possible to study how a sharp crack evolves in a crystal lattice without actually driving the system to the point of instability? By this we mean determining the pathways of crack front motion while the lattice resistance against such displacement is still finite. Despite a large number of molecular dynamics (MD) simulations on crack tip propagation (e.g., see [**1**]), this particular issue has not been examined. Most studies to-date have been carried out in an essentially 2D setting, with periodic boundary

T. J. Chuang et al. (eds.), Nanomechanics of Materials and Structures, 217–223.
© 2006 *Springer. Printed in the Netherlands.*

condition imposed along the direction of the crack front (see Fig. 1). In such simulations the crack tip is sufficiently constrained that the natural response of the crack front cannot be investigated. Besides the size constraint on the crack front, there is also the problem that in direct MD simulation one frequently drives the system to instability, resulting in abrupt crack-tip displacements which make it very difficult to characterize the deformation.

We have developed an approach capable of probing crack front evolution without subjecting the system to critical loading. This involves using reaction pathway sampling to probe the minimum-energy path (MEP) [**2**] for the crack front to advance by one atomic lattice spacing, while the imposed load on the system is below the critical threshold. We have applied this method to characterize the atomistic configurations and energetics of crack extension in a metal (Cu) [**3**] and a semiconductor (Si) [**4**]. In this report we will compare the results of these two studies to show how ductility or brittleness of the crystal lattice can manifest in the mechanics of crack-front deformation at the nanoscale.

Consider a 3D atomically sharp crack front which is initially straight, as shown in Fig. 1(a). Suppose we begin to apply a mode-I load in incremental steps. Initially the crack would not move spontaneously because the driving force is not sufficient to overcome the intrinsic lattice resistance. What does this mean? Imagine a final configuration, a replica of the initial configuration with the crack front translated by an atomic lattice spacing in the direction of crack advancement. At low loads, e.g. K'_{I} as shown in Fig.1(b), the initial configuration (open circle) has a lower energy than the final configuration (closed circle). They are separated by an energy barrier which represents the intrinsic resistance of the lattice. As the loading increases, the crack will be driven toward the final configuration, one can regard the overall energy landscape as being tilted toward the final configuration with a corresponding reduction in the activation barrier, see Fig. 1(b). As the load increases further the biasing becomes stronger. So long as the barrier remains finite the crack will not move out of its initial configuration without additional activation, such as from thermal fluctuations. When the loading reaches the point where the lattice-resistance barrier disappears altogether, the crack is then unstable at the initial configuration; it will move without any thermal activation. This is the athermal load threshold, denoted by K_{Iath} in Fig. 1(b). In our simulation, we study the situation where the applied load is below this threshold, thereby avoiding the problem of a fast moving crack that is usually over-driven.

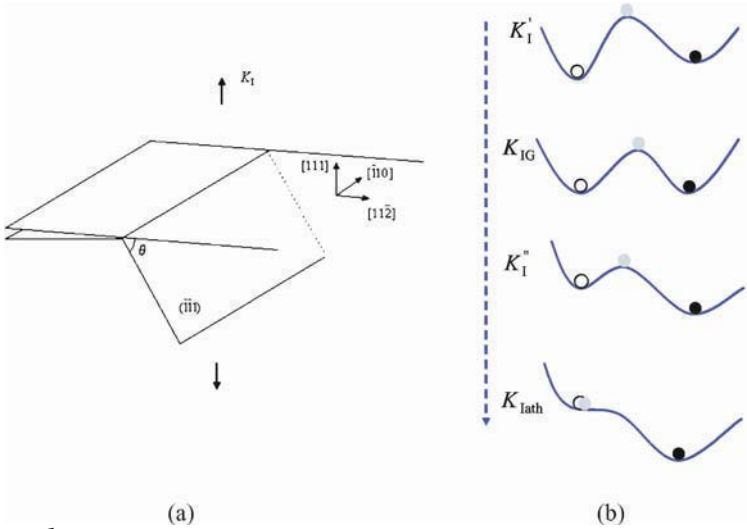

Figure 1.(a) Schematics of a 3D atomically sharp crack front under a mode-I load K_I ; (b) energy landscape of the crack system at different loads ($K'_I < K_{IG} < K''_I < K_{Iath}$). Open circle represents the initial state of a straight crack front under an applied load K_I, closed circle is the final state after the crack front uniformly advances by one atomic spacing (under the same load K_I as the initial state), and shaded circle corresponds to the saddle-point state in between.

2. PATHWAYS OF CRACK FRONT MOTION FOR CU AND SI

The cracks in Cu and Si that we will compare are both semi-infinite cracks in a single crystal, with the crack front lying on a (111) plane and running along the $[1\bar{1}0]$ direction. The simulation cells consist of a cracked cylinder cut from the crack tip, with a radius of 80Å. The atoms located within 5Å of the outer surface are fixed according to a prescribed boundary condition, while all the remaining atoms are free to move. To probe the detailed deformation of the crack front, the simulation cell along the cylinder is taken to be as long as computationally feasible, 24 (Cu) and 20 (Si) unit cells. Periodic boundary condition is imposed along this direction. For interatomic potentials we use a many-body potential of the embedded atom method type for Cu [**5**], and a well-known three-body potential model proposed by Stillinger and Weber (SW) for Si [**6**].

Next, we compare studies of Cu [**3**] and Si [**4**] in terms of MEP profiles and atomic displacement distributions. Fig. 2(a) shows the MEP for the nucleation of a dislocation loop from the crack front in Cu, loaded at $K_I = 0.87K_{Iath}$. Notice that at this loading the final state is strongly favored over the initial state. Fig. 2(a) shows clearly the presence of a lattice-resistance barrier at this particular loading. To visualize the atomic configurations

along the MEP, we turn to displacement distributions along the crack front. Fig. 3(a) is a contour plot of the *shear* displacement distribution. One can see clearly the shape of a dislocation loop bowing out. It is evident that the distribution represents the development of an embryonic dislocation loop; the profile of $b/2$ shear displacement is a reasonable representation of the locus of dislocation core. Also this is an indication that the enclosed portion of the crack front has been swept by a fully formed dislocation. Besides shear displacement, normal, or *opening* displacement, in the direction along x_3, $[\bar{1}\,\bar{1}\,1]$, is also of interest. The corresponding distribution is shown in Fig. 3(b). One sees that large displacements are not at the center of the crack front. In Figs. 3(a) and 3(b) we have a detailed visualization of the crack front evolution in three dimensions. The largest displacements are indeed along the crack front but they are not of the same character; the atoms move in a shear mode in the central region and in an opening mode on the two sides.

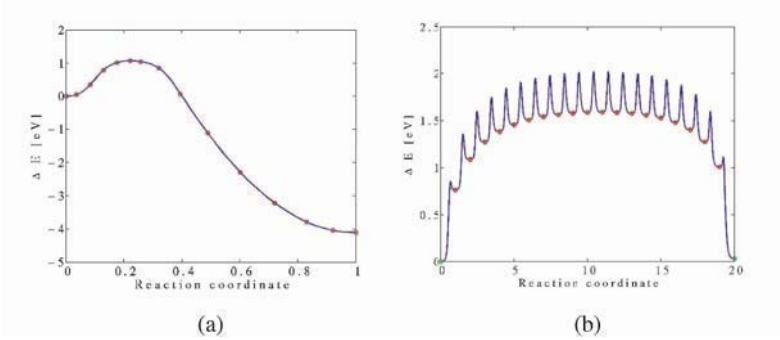

Figure 2.(a) MEP of dislocation loop emission in Cu at a load of $K_I = 0.87K_{Iath}$ [**3**]; (b) MEP of crack extension in Si at the Griffith load K_{IG} [**4**].

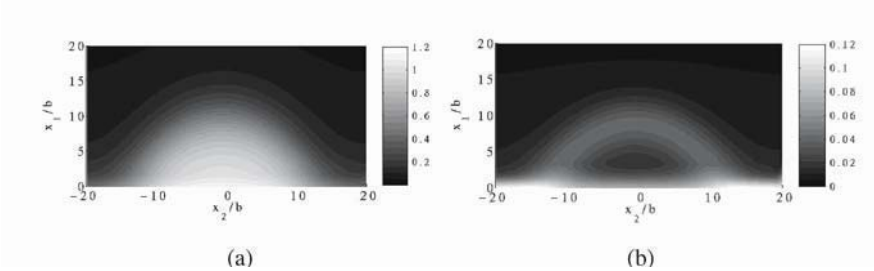

Figure 3. Contour of (a) shear displacement (normalized by b=1.476A) and (b) opening displacement (normalized by the interplanar-spacing h=2.087A) across the slip plane at the saddle-point state [**3**].

Turning to Si, We find that the most energetically favored pathway for

the front to advance by one atomic spacing is the breaking of the 20 bonds *sequentially*. At a load equal to the Griffith value $K_{IG} = 0.646\text{MPa}\sqrt{\text{m}}$, the MEP we obtain is shown in Fig. 2(b). A slightly different reaction coordinate is used in this case, with integer *s* labeling a locally equilibrated state with *s* broken bonds on the crack front. One sees the energy variation is a series of barrier, each one corresponding to the rupture of a bond along the crack front. The reason Figs. 2(a) and (b) have distinctly different appearance is that the two MEP correspond to *different* deformation modes, bond rupture in Fig. 2(a) and bond shearing/switching in Fig. 2(b).

Figure 4 shows the opening displacement distribution in Si at the Griffith load K_{IG}. We see a new feature in the outline of displacements of intermediate magnitude (dark-gray line). In the region ahead of the crack front the distribution of these displacements has the shape of a rectangular wedge protruding in the direction of crack front advancement. The presence of a wedge shape suggests a kink mechanism of crack advancement, namely, nucleation of a local kink distortion followed by spreading across the entire crack front. It is significant that this behavior is not seen in Fig. 3(b). Taking Cu to be a prototypical ductile material, we see that while the crack opening still occurs at the front, the large normal displacements lie outside the central region enclosed by the emerging dislocation loop. We attribute this feature to a mode-switching, or shear-tension coupling, process. The initially large opening displacements in the region swept by the emerging loop are relaxed by giving way to large shear displacements, which are then carried away by the emitted dislocation loop.

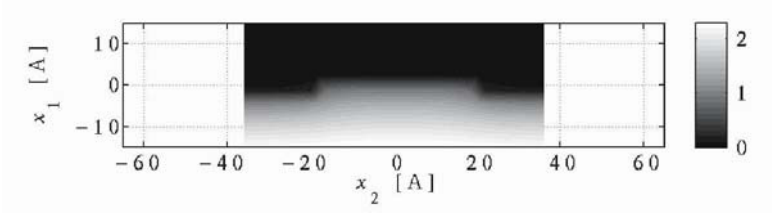

Figure 4. Contour of opening displacement distribution (normalized by the interplanar spacing h=2.35 Å) at the Griffith load K_{IG} [**4**].

It is relevant to interpret the behavior of atomic displacements at the transition state in Cu and Si on the basis of the nature of interatomic bonding in these two materials. One expects that the crack front response in Cu should reflect delocalized metallic bonding while that in Si should correspond to directional, localized covalent bonding. In terms of characteristic features of the energy landscape along the reaction path, we see in Cu a rather smooth MEP with a single major nucleation barrier, indicating that crack advancement involves a concerted motion of atoms to

overcome this barrier by thermal activation. In contrast MEP in Si reveals the existence of significant secondary barrier (cusps in Fig. 2(b)) which should be a general feature of covalently bonded crystals. In this case crack extension proceeds via individual bond breakings, a series of thermally activated events of kink-pair formation and lateral kink migration along the front. It is of interest to point out the crack front mobility is not only controlled by kinks at the atomic scale as demonstrated in this work, acoustic emission and fractographic measurements have indicated the crack advancement at the mesoscopic scale is also governed by the kink mechanism which involves a process of unzipping along the crack front (W. W. Gerberich, private communication; [**7**]).

The fact that kink mechanism appears to play a central role in crack front mobility raises an interesting question of the implications of structural similarity between the crack front, acting as the core of a sharp crack, and the core of a dislocation, both being "*line defects*" in a crystal lattice. It is rather well known that dislocation mobility in a directionally bonded crystal like Si is governed by thermal activation of nucleation and migration of kink pairs [**8**]. The present results showing that a similar mechanism also operates in crack front advancement reinforces the notion that mobility fundamentally depends on crystal structure and chemical bonding. From this perspective the appearance of kink-like structure in Fig. 4 is perhaps to be expected. Since dislocation mobility and crack-tip extension are both active topics for modeling and simulation, recognition of their underlying connections could lead to a broader appreciation of the role of structure and bonding [**9**] in controlling both phenomena.

ACKNOWLEDGMENTS

We thank A. S. Argon and W. W. Gerberich for stimulating discussions. TZ and SY acknowledge support by NSF, Honda R&D, DARPA-ONR, and the Lawrence Livermore National Laboratory. JL acknowledges support by Honda R&D, and the OSU Transportation Endowment Program.

REFERENCES

1. Buehler MJ, Abraham FF, Gao H, "Hyperelasticity governs dynamic fracture at a critical length scale", *Nature*, **426**, pp. 141-146, 2003.
2. Jonsson H, Mills G, Jacobsen KW, "Nudged elastic band method for finding minimum energy paths of transitions", in *Classical and Quantum Dynamics in Condensed Phase Simulations*, Ed., Berne BJ, Ciccotti G, Coker DF, 1998, pp.385-404.
3. Zhu T, Li J, Yip S, "Atomistic study of dislocation loop emission from a crack tip", *Phys. Rev. Lett.*, **93**, 020503, 2004.

4. Zhu T, Li J, Yip S, "Atomic configurations and energetics of crack extension in silicon", *Phys. Rev. Lett.*, 2004, in press.
5. Mishin Y, et al., "Structural stability and lattice defects in copper: Ab initio, tight-binding, and embedded-atom calculations", *Phys. Rev.* B, **63**, 224106, 2001.
6. Stillinger FH, Weber TA, "Computer simulation of local order in condensed phases of silicon", *Phys. Rev.* B, **31** , pp. 5262-5271, 1985.
7. Lii MJ, Chen XF, Katz, Y, Gerberich WW, "Dislocation modeling and acoustic-mission observation of alternating ductile/brittle events in Fe-3wt% Si crystals", *Acta. Metall. Mater*., pp. 2435, 1990.
8. Cai W, Bulatov VV, Chang J, Li J, Yip S, *Dislocation Core Effects on Mobility*, Dislocations in Solids, Nabarro FRN and Hirth JP (eds), Elsevier, Amsterdam, 2004, vol. 12, chap 64, pp. 1-80.
9. Ogata S, Li J, Hirosaki N, Shibutani Y, Yip S, "Ideal shear strain of metals and ceramics", *Phys. Rev.* B **70**, 104104, 2004.

FINITE TEMPERATURE COUPLED ATOMISTIC/CONTINUUM DISCRETE DISLOCATION DYNAMICS SIMULATION OF NANOINDENTATION

Behrouz Shiari and Ronald E. Miller
Department of Mechanical and Aerospace Engineering, Carleton University, 1125 Colonel By Dr., Ottawa, On., Canada, K1S 5B6; Tel: +1- 613- 520- 2600/5703; Fax:+1-613-520-571; E-mail: bshiari@mae.carleton.ca, rmiller@mae.carleton.ca

Abstract: Simulations of nanoindentation in a hexagonal aluminum single crystal are performed using a finite temperature coupled atomistic/continuum discrete dislocation (CADD) method. The method captures, at the same time, the atomistic mechanisms and the long-range effects without the computational cost of full atomistic simulations. The effects of several process variables are investigated, including system temperature. We discuss the results and the deformation mechanisms that occur during a series of indentation simulations.

Key words: Multiscale modeling, discrete dislocations, nanoindentation, finite temperature.

1. INTRODUCTION

The vast applications of thin film structures and the miniaturization of devices and components are challenging the existing micro-scale approaches of measuring elastic and plastic properties. Among the apparatus developed for this purpose, nanoindentation stands out as a capable technique for probing the mechanical properties of small volumes of materials. From the load-displacement data, many mechanical properties such as hardness and elastic modulus can be determined without imaging the indentations. However, nanoindentation experiments are difficult to interpret at a

T. J. Chuang et al. (eds.), Nanomechanics of Materials and Structures, 225–234.
© 2006 *Springer. Printed in the Netherlands.*

fundamental level because of the involvement of multiple length scales. The classical theory of plasticity is not an appropriate approach to be used in the analysis of nanoindentation tests because the inelastic processes under the indenter involve a small number of dislocations, which form a population too small to obey the rules of continuum theory. Under these conditions, the effect of dislocation nucleation on the load-displacement curve becomes dominant [**1**]. Attempts to more accurately model this situation have involved atomistic simulations of the indentation process [**2-4**]. Molecular dynamics (MD) simulations can successfully handle the early stages of the indentation process and reveal dislocation nucleation events. Although dislocation nucleation continues at the later times during indentation, the mechanism that controls the process becomes dislocation interaction. For these mainly elastic interactions, the discrete nature of dislocations becomes more important [**5**]. Due to computing power limitations, most of MD simulations have been restricted to small volumes and have been performed at strain rates many orders of magnitude higher than those used in actual tests. Thus, multiscale methods are excellent techniques to model the nanoindentaion process because of the length scales involved. There are many examples in the literature of numerical modeling techniques whereby an atomistic region is directly coupled to a continuum region by finite elements [**6-9**]. A recent review [**10**] has discussed, in detail, many of their challenges and advantages. Of specific interest here is multiscale modeling of nanoindention in single crystals, where the primary deformation mode will be the nucleation and long-range motion of discrete dislocations. The coupled atomistics and discrete dislocation (CADD) method described in [**11-13**] is one such method.

In this work, we employ the CADD model to investigate the mechanisms of homogeneous (subsurface) and heterogeneous (surface) defect nucleation in an initially defected-free single aluminum crystal with an atomically smooth surface which is subjected to normal nanoindentation by a rigid cylindrical tip. Despite limitations arising from its two-dimensional geometry, this model enables the demonstration of different atomic-level dislocation processes that cannot be easily observed otherwise by either experiment or pure 3D MD simulations. This multiscale model is found to be an effective system for both visualization and quantification of dislocation nucleation and motion beneath the indenter, including the evolution of surface deformation resulting from defect nucleation. The results reported here provide direct and fundamental mechanistic insights into the processes associated with contact deformation and quantitative predictions about discrete plasticity events that are consistent with experimental observations of nanoindentaion in single crystals [**14**]. An important extension of the CADD model made here is the use of a finite temperature, dynamic

formulation, in contrast to the original zero temperature approach. One of the main objectives of this publication is to examine the significance of the temperature on the deformation response in light of previously published zero temperature single-cycle nanoindention results.

2. MODEL SYSTEM AND SIMULATION METHOD

The details of the CADD approach have been published previously [**11-13**]. Thus, in this paper we provide only a brief description of the main ideas and some new improvements of the method for finite temperature application. The CADD method contains three main elements: a scheme to mechanically couple an atomistic region with a continuum region containing discrete dislocations, an algorithm to detect dislocations near the atomistic/continuum interface, and an algorithm to pass dislocations from the atomistic region to the continuum region, or vice versa. In the CADD method, a distinction is made between regions of the model experiencing a slowly varying deformation on the atomic scale and those subject to deformation with highly varying deformation. Atomic resolution is required only in regions of high gradients, while in all other regions, a continuum treatment is a good approximation and there is no need to consider all degrees of freedom of the real solid. This observation allows for a significant reduction in the size of the problem. In regions of high gradients, all atoms are retained in the model and all forces upon them are computed considering their whole neighborhood, as in regular MD simulations. The remaining regions are discretized in finite elements. A lumped-mass scheme is applied for dynamic simulations of the finite element region.

The material properties of the model are determined from the underlying atomistic model employed. Here we use the ‘‘embedded atom method’’ (EAM) [**15**] interatomic potentials, although any model providing atomic forces can be used. The atomistic region is thus a fully nonlinear, non-local atomistic model that reduces exactly to molecular dynamics when no continuum region is appended. The continuum region requires the anisotropic elastic moduli, computed a priori from the atomistic model for an appropriately oriented crystal of the material. The fields in the continuum region can be treated using the standard discrete dislocation (DD) method [**5**]. The continuum region is divided into two complementary problems. First, a problem consists of dislocations in an infinite elastic continuum and is solved by superposition of the analytical elastic fields due to individual dislocations at known positions, yielding a total field denoted as the ~ field. The tractions and displacements due to these fields along a physical boundary of the model are also found. A second problem consists of a linear

elastic continuum with no dislocations but subjected to corrective tractions and displacements along the physical boundary of the model. These fields, denoted as ^ fields, are smooth and obtained numerically by the finite element method. The total fields in the continuum are superposition of the fields from first and second problem.

To assure that real atoms at and near the interface are properly coordinated, we use a pad of atoms (as shown in Fig. 1) as an intermediary between the local continuum and the non-local, discrete atomistics, essentially overlapping the continuum and atomistic regions along the interface.

Once the fields in the dislocated solid are known, the second ingredient is to determine the instantaneous change of the dislocation structure. The important point to note first is that the key quantity involved in constitutive rules for dislocation evolution is the so-called Peach-Koehler force. It can be shown that in the approach outlined above, the component of the Peach-Koehler force on dislocation k in the slip plane can be expressed as [**5**]:

$$f^{(k)} = n_i^{(k)}(\hat{\sigma}_{ij} + \sum_{l \neq k} \tilde{\sigma}_{ij}^{(l)})b_j^{(k)} \tag{1}$$

where $n_i^{(k)}$ is the slip plane normal and the Burgers vector b_i^k of dislocation k. $\hat{\sigma}_{ij}$ is the stress arising from the corrective solution, and $\tilde{\sigma}_{ij}$ is the stress due to another dislocation, l. The expression highlights the long-range contribution of all other dislocations, through the second term in parentheses.

For two-dimensional simulations, involving only edge dislocations, the glide component of the Peach-Koehler force reduces to $f^{(k)} = \tau^{(k)}b^{(k)}$ where, $\tau^{(k)}$ is the resolved shear stress on the slip plane. Glide of a dislocation is accompanied by drag forces due to interactions with electrons and phonons. The simplest models of this lead to drag forces that can be expressed as $Bv^{(k)}$ where B is the drag coefficient. Thus, we assume that, the magnitude of the glide velocity $v^{(k)}$ of dislocation k is linearly related to the Peach-Koehler force through [**16**]:

$$f^{(k)} = Bv^{(k)} \tag{2}$$

A straightforward discretization of this expression in the time domain yields,

$$u^{(k)}(t + \Delta t) = u^{(k)}(t) + Bf^{(k)}\Delta t \tag{3}$$

where $u^{(k)}$ is the displacement in the glide direction of dislocation k.

Detection and moving dislocation between different regions, is a unique feature of the CADD method. Dislocations nucleated in atomistic region during the loading period may experience driving forces to move from the atomistic region into the continuum region, or to move from continuum region to the atomistic region during the unloading process. Detection of these defects and the passing of them between the region is an automatic feature built into the CADD methodology, and has been described in detail in [**11-13**].

The model of the indentation problem along with the boundary conditions and the mesh used in the computations are shown in Fig. 1. A rigid cylindrical indenter is driven into a block of hexagonal aluminum with c-axis normal to the in-plane deformation. The region close to the indentation site is simulated with atomic resolution, while the remaining regions are simulated in a continuum sense, by finite elements. This allows for consideration of a large specimen without significant increase in the size of the problem. Hence, the boundary of the model can be remote enough from the process region (indentation site) such that the boundary conditions do not influence the results and at the same time support long-range effects. The application of the CADD technique for modeling the given sample shown in Fig. 1, permits the modeling of more than 100,000 atoms using only 2800 atoms and 200 nodes. Periodic boundary conditions are used in the out-of-plane direction. The rigid indenter is modeled as a repulsive potential of the form:

$$\Phi = \begin{cases} C(r-R)^2 & for \quad r < R \\ 0 & for \quad r \geq R \end{cases} \tag{4}$$

Where $C = 10 \ \ eV / \text{Å}^2$ is chosen empirically and $R = 100$ Å is chosen in this study as the indenter radius. This form is adequate to repel the atoms and force them to remain outside the 100 Å radius of the indenter. Further, the indenter remains circular and frictionless throughout the simulation. This can be approximately achieved in experiments by an indenter tip which is coated with passivating layer.

The indented material studied is hexagonal aluminum which is unstable in out-of-plane shear, but such deformation is not permitted in the 2D calculations performed here. The hexagonal crystal provides a simplified model, but one with sufficient slip systems that some qualitative comparison to real crystals can be made. Specifically, the hexagonal crystal will contain only edge dislocations on the three slip systems at 0°, 60° and -60°. The dislocation cores do not split into partials and can readily dissociated from one system onto the other two, a 2D analog of 3D cross-slip.

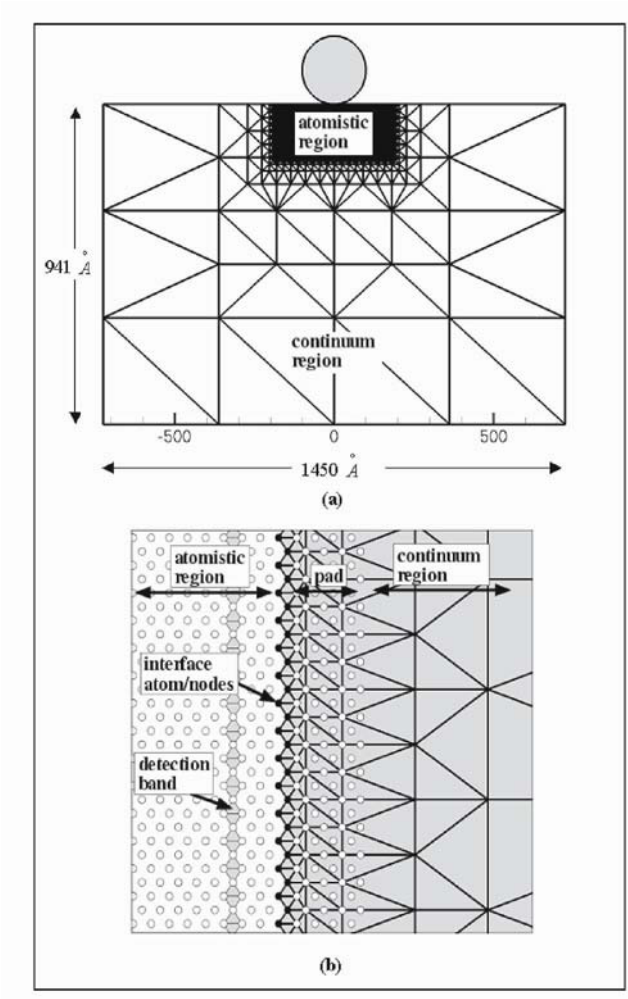

Figure 1. (a) Model geometries for the nanoindentation simulations (b) Close-up of the atomistic/continuum interface.

The equations of motion are integrated using the Velocity-Verlet algorithm for atoms and nodes with time step of $0.001p\,\mathrm{sec}$. We find it efficient to move the atoms and nodes for 1000 time steps while holding the dislocations fixed in the crystal. The dislocations are then moved once, using Eqn. 3, with $0.1p\,\mathrm{sec}$. We determine the effective temperature of the system from kinetic energy of atoms inside the atomistic region. The atoms inside the atomistic region are thermostated with the Nose-Hoover thermostat in order to dissipate any heat produced by the indentation process. Many authors [**17-18**] have noted the challenges of spurious wave reflections from the atomistic/continuum interface. We have found that for our purpose, the

Nose-Hoover thermostat, as implemented, adequately dissipates the reflected waves. Whether or not this approach is adequate for more severe loading situations is a subject of continued study.

3. RESULTS AND DISCUSSION

In this section, we present some results of the nonoindentaion simulations at finite temperature. We performed a series of nanoindentaion simulations for temperatures ranging from $10^{\circ}K$ to $400^{\circ}K$. The indentation and unloading rates were $0.05A^{\circ}/p\sec$. Three typical loading curves are plotted in Fig. 2. The load acting on the rigid indenter is obtained by summing the resultant forces contributed by the surrounding aluminum atoms on the indentation direction. The thermal noise was suppressed by averaging the force over a period of $0.5p\sec$. As is seen in the figure, the onset of plasticity or dislocation nucleation is affected by the temperature. Increasing temperature makes the nucleation of dislocation happen earlier. This phenomenon was recently pointed out by Dupuy et al. [**19**] using the finite temperature quasicontinuum method.

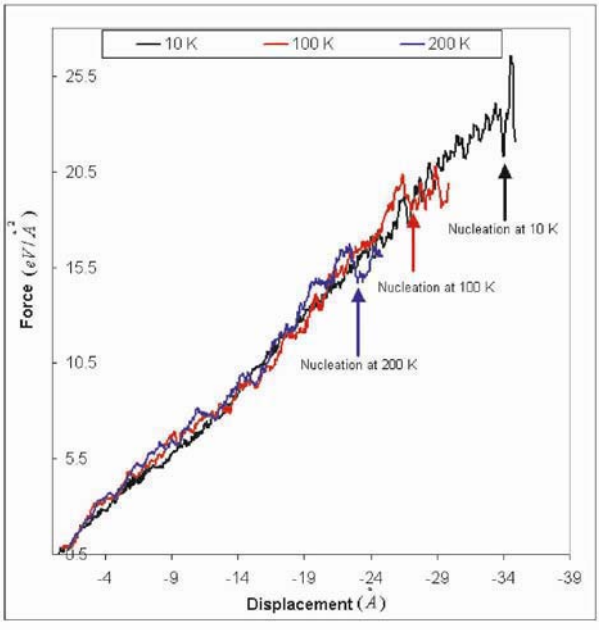

Figure 2. Load-displacement curves for three different temperatures.

The load-displacement curve is essentially reversible as long as the indentation depth is less than the critical value (corresponding to the first dislocation nucleation) that is indicated in Fig. 2. The variation of this critical value versus temperature is plotted in Fig. 3. The simulations at finite temperature show the same dislocation nucleation processes that has been observed at zero temperature by Miller et al. [**12**]. The only difference is the first homogeneous nucleation event does not occur along the loading axis at the depth which is reported in [**12**] at finite temperature above $100^{\circ}K$. Fig. 4 shows the load-displacement curve for one complete loading/unloading cycle at two different finite temperatures. As the figure shows, there is less plastic recovery at higher temperature. Fig. 4 also indicates, for the maximum depth of indentation, the load of indentation decreases as the temperature increases. In other words, the sample material softens at higher temperature. The state of deformation at the peak load ($40A^{\circ}$ indentation at $100^{\circ}K$) and after unloading are shown in Fig. 5(a) and Fig. 5(b). The discrete dislocations are plotted as circles. The figures show that a number of dislocations have moved out of the bottom of the atomistic region into continuum region. Upon unloading from the peak load, the continuum dislocations glide back toward the indenter. Configurations of the atomistic region at maximum load and after full unloading are presented in Fig. 5(b) and Fig. 5(d). After unloading, there is clearly a permanent deformation and flow of material. As Fig. 5(d) shows, slip steps are formed on the indented surface because of migration of internally nucleated dipole pairs [**16**] to the free surface and their reflection back after hitting the surface. Simulations at different temperatures show that as the temperature increases, there is greater debris pile-up along the dimple fringe [**4**].

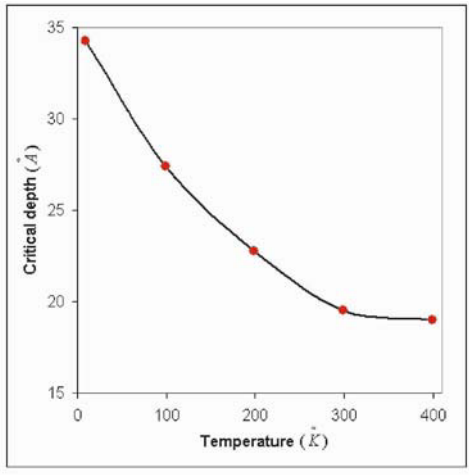

Figure 3. Variation of critical depth for dislocation nucleation with increasing temperature.

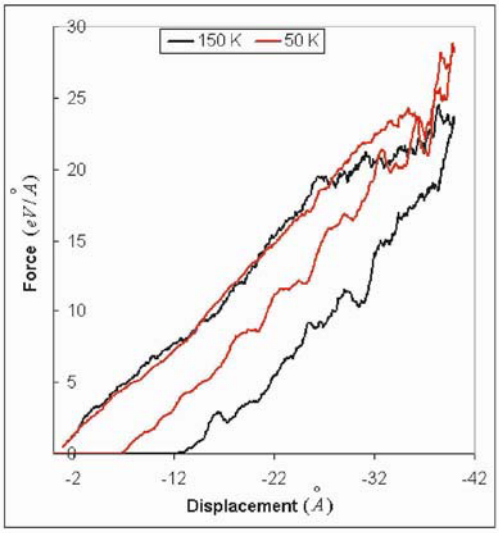

Figure 4. Load-displacement curves for two different temperatures.

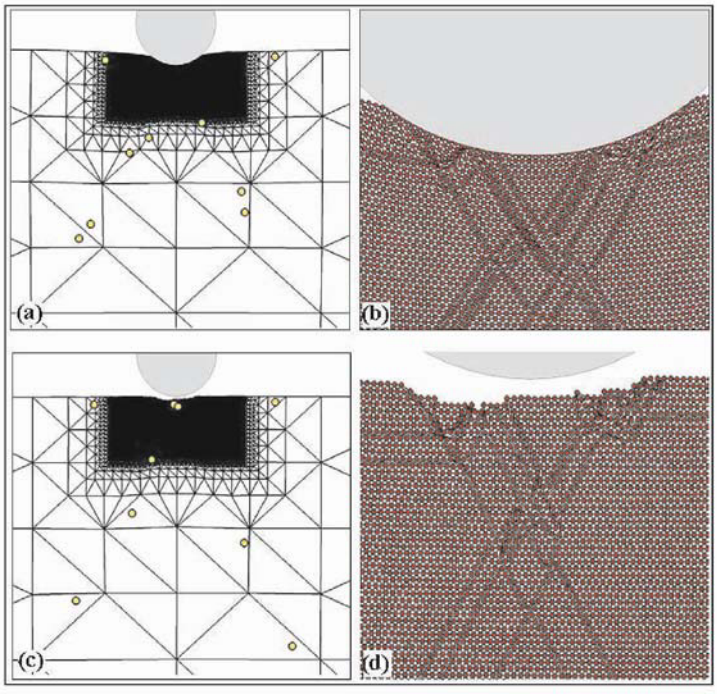

Figure 5. Configuration of positions of the discrete dislocations and the atomic region at maximum load ((a), (b)) and after unloading ((c), (d)).

ACKNOWLEDGMENTS

This research was funded by the US Air Force Office of Scientific Research, Grant #F49620-99-1-0272, and NSERC of Canada.

REFERENCES

1. Picu RC. "Atomistic-continuum simulation of nano-indentation in molybdenum", *J. of Computer-Aided Materials Design*, **7**, pp. 77-87, 2000.
2. Kelchner CL, Plimpton S, Hamilton JC. "Dislocation nucleation and defect structure during surface indentation", *Phys. Rev. B*, **58**, pp. 11058-11088, 1998.
3. Zimmerman JA, Kelchner CL, Klein PA, Hamilton JC, Foiles SM. "Surface step effects on nanoindention", *Phys. Rev. Lett.*, **87**, pp. 165507, 2001.
4. Fang TH, Weng CI, Chang JG. "Molecular dynamics analysis of temperature effects on nanoindentation measurement", *Mater. Sci. Eng.*, **A357**, pp. 7-12, 2003.
5. Van der Giessen E, Needleman A. "Discrete dislocation plasticity: a simple planar model", *Simul. Mater. Sci. Eng.*, **3**, pp. 688-691, 1995.
6. Abraham FF, Broughton JQ, Bernstein N, Kaxiras E. "Spanning the length scales in dynamic simulation", *Comput. Phys.*, **12**, pp. 538, 1998.
7. Kohlhoff S, Gumbsch P, Fischmeister HF. "Crack propagation in bcc crystals studied with a combined finite-element and atomistic model", *Philos. Mag. A*, **64**, pp. 851-878, 1991.
8. Rudd RE, Broughton JQ. "Concurrent coupling of length scales in solid state systems", *Phys. Stat. Sol. B*, **217**, pp. 251-291, 2000.
9. Miller RE, Ortiz M, Phillips R, Shenoy V, Tadmor EB. "Quasicontinuum models of fracture and plasticity", *Eng. Fract. Mech.*, **61**, pp. 427-444, 1998.
10. Curtin WA, Miller RE. "Atomistic/continuum coupling in computational materials science", *Modeling Simul. Mater. Sci. Eng.*, **11**, pp. R33-R68, 2003.
11. Shilkrot LE, Miller RE, Curtin WA. "Coupled atomistic and discrete dislocation plasticity", *Phys. Rev. Lett.*, **89**, pp. 025501-1-0255501-4, 2002.
12. Miller RE, Shilkrot LE, Curtin WA. "A Coupled atomistic and discrete dislocation plasticity simulation of nanoindentation into single crystal thin films", *Acta Materialia*, **52**, pp. 271-284, 2004.
13. Shilkrot LE, Miller RE, Curtin WA. "Multiscale plasticity modeling: Coupled atomistic and discrete dislocation mechanics", *J. Mech. Phys. Solids*, **52**, pp. 755-787, 2004.
14. Van Vliet KJ, Suresh S. "Simulations of cyclic normal indentation of crystal surfaces using the bubble-raft model", *Philos. Mag. A*, **82**, pp. 1993-2001, 2002.
15. Daw MS, Baskes MI. "Embedded-atom method: derivation and application to impurities, surface, and other defects in metals", *Phys. Rev. B*, **29**, pp. 6443-6453, 1984.
16. Cleveringa HHM, Van der Giessen E, Needleman A. "A discrete dislocation analysis of bending", *Inter. J. of Plasticity*, **15**, pp. 837-868, 1999.
17. Cai W, Koning M, Bulatov V, Yip S. "Minimizing boundary reflections in coupled-domain simulations", *Phys. Rev. Lett.*, **85**, pp. 3213-3216, 2000.
18. E W, Huang Z. "Matching conditions in atomistic-continuum modeling of materials", *Phys. Rev. Lett.*, **87**, pp. 135501, 2001.
19. Dupuy L, Miller RE, Phillips R. "A finite temperature quasicontinuum", *Bulletin of APS March Meeting*, Montreal, Quebec, Canada, March. 22-26, 2004, pp. 1420.

STATIC ATOMISTIC SIMULATIONS OF NANOINDENTATION AND DETERMINATION OF NANOHARDNESS

Yeau-Ren Jeng and Chung-Ming Tan
Department of Mechanical Engineering,National Chung Cheng University, Chia-Yi, Taiwan
Tel: 886-5-242-8189; E-mail: imeyrj@ccu.edu.tw

Abstract: This paper develops a nonlinear finite element formulation to analyze nanoindentation using an atomistic approach, which is conducive to observing the deformation mechanisms associated with the nanoindentation cycle. The simulation results of the current modified finite element formulation indicate that the microscopic plastic deformations of the thin film are caused by instabilities of the crystalline structure, and that the commonly used procedure for estimating the contact area in nanoindentation testing is invalid when the indentation size falls in the nanometer regime.

Key words: Nanoindentation, Finite Element Formulation, deformation mechanism, Hardness.

1. INTRODUCTION

Nanoindentation has evolved into a valuable means of determining the mechanical properties of thin films and surfaces in nanometer regimes [**1-4**]. In conventional hardness tests, "hardness" is defined as the maximum load divided by the area of the residual impression. The prevailing definition of "nanohardness" during nanoindentation is the maximum load divided by the contact area at that load, which is calculated from an analysis of the load-depth curve based on Hertzian continuum mechanics contact theory.

T. J. Chuang et al. (eds.), Nanomechanics of Materials and Structures, 235–243.
© 2006 *Springer. Printed in the Netherlands.*

Previous studies mainly adopted a Molecular Dynamics approach to investigate the dislocation activities induced by the incipient plasticity of single perfect crystals during nanoindentation. However, MD simulation is very time-consuming since it involves time resolutions of a pico-second or less. Furthermore, nanoindentation experiments are performed under quasi-static conditions in order to avoid dynamic effects such as heating and creep and to provide a clearer view of the deformation mechanisms of the substrate. However, MD simulation of quasi-static conditions incurs significant computational costs.

Hence, this present study utilizes an alternative approach which resembles FEM methodology and is referred to hereafter as the modified FEM approach [**5-6**]. Since atoms oscillate thermodynamically around their minimum-energy positions, the proposed approach simply calculates the incremental changes in the minimum-energy positions during the indentation process. In this way, the indentation process becomes quasi-static, thereby reducing the computational task. This study employs the modified FEM approach to simulate elastic-plastic deformations in a copper substrate during a complete nanoindentation cycle. Furthermore, the relative influences of indenter geometry and indentation depth upon the nanohardness are explored and discussed.

2. METHODOLOGY

As shown in Figures 1(a) and 1(b), the simulated system configurations include a perfect three-dimensional crystalline slab of copper atoms with a (001) surface, and two indenters of different geometries The first indenter is in the form of a sphere whose outer surface atoms form many facets due to a crystalline structure. Meanwhile, the second indenter has a triangular pyramidal form. In the simulation, it is assumed that the hardness of the indenter's diamond tip far exceeds that of the thin copper film, and hence indenter deformation may be neglected during the indentation process. The simulation assumes boundary conditions in which the atoms located at the four sides and base of the simulated film are fully constrained.

The interatomic potential of the copper substrate is modeled using the Sutton-Chen potential [**7**], which has the same functional form as an EAM potential, i.e.:

$$U = \sum_i U_i \tag{1}$$

$$U_i = \frac{1}{2}\sum_{j\neq i}\phi(r_{ij}) + F(\rho_i) = \varepsilon\left(\frac{1}{2}\sum_{j\neq i}\left(\frac{a}{r_{ij}}\right)^n - c\sqrt{\rho_i}\right) \qquad (2)$$

where ρ_i is an electron density-like term for atom *i*, which is defined as:

$$\rho_i = \sum_{j\neq i} f(r_{ij}) = \sum_{j\neq i}\left(\frac{a}{r_{ij}}\right)^m \qquad (3)$$

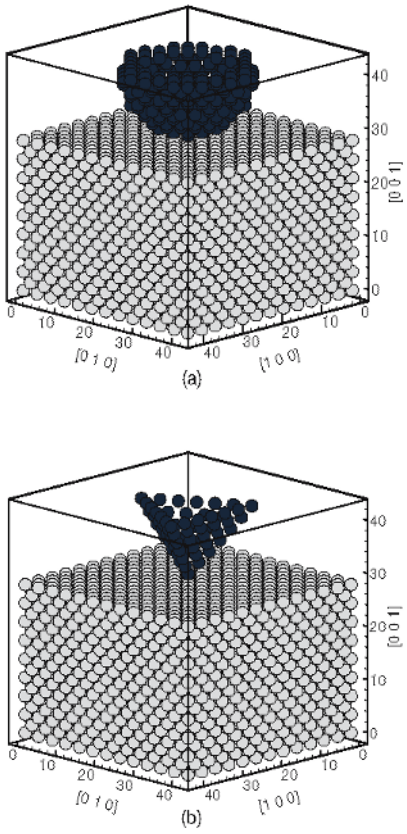

Figure 1. Atomistic model used in nanoindentation simulations. (Units: angstrom).

where r_{ij} is the distance between atoms *i* and *j*. The copper constants ε, a, c, m, and n have values of 1.238×10^{-2}, 3.6, 39.432, 6, and 9, respectively. The potential between the carbon and copper atoms is simulated using the Born-Mayer potential [**8**], which produces an impulsive force only. This potential has the following form:

$$\phi(r_{ij}) = A \exp[-2\alpha(r_{ij} - r_0)] \tag{4}$$

where r_{ij} is the distance between carbon atom *i* and copper atom *j*, and the carbon/copper constants A, a, and r_o have values of 0.3579, 0.9545, and 2.5, respectively.

Taking any two arbitrary atoms *i* and *j* as two nodes, and their potential as one element, this study develops a computationally efficient approach based on the nonlinear finite element formulation. Interested readers are invited to refer to the detailed derivation of this approach presented previously by the current authors [**5-6**].

3. RESULTS AND DISCUSSIONS

Figure 2(a) presents the variation in load (i.e. force experienced by the indenter) with indentation depth for spherical indenter nanoindentation cycles performed to maximum indentation depths of 0.4 nm, 0.7 nm, and 1 nm. Meanwhile, Figure 2(b) shows the equivalent load-depth curves for pyramidal indenter nanoindentation cycles. It is clear that each of the indentation cycles in Figure 2 represents a hysteretic loop, which indicates that plastic deformations take place during the loading process. In the present study, the stability of a crystalline structure is correlated to, and can be monitored by, the positiveness of the modified FEM tangent stiffness matrix. The irreversible plastic deformations observed in the simulation can be attributed to changes of the crystalline structure caused by instabilities induced by high localized stress. This perspective of the plastic deformation mechanism bears witness in the work of Li *et al.*[**10**], but the precise prediction of the onset of incipient plasticity falls beyond the scope of the present study. Figure 2 reveals that compared to pyramidal indentation, spherical indentation leads to an enhanced yielding phenomenon, which resembles that observed in the uniaxial compression testing of ductile metals. Comparing the hysteresis loops of Figures 2(a) and 2(b), it is clear that the enclosed areas are greater in the case of spherical indenter indentation. This indicates that more plastic work is dissipated in indentation cycles performed with this particular indenter geometry.

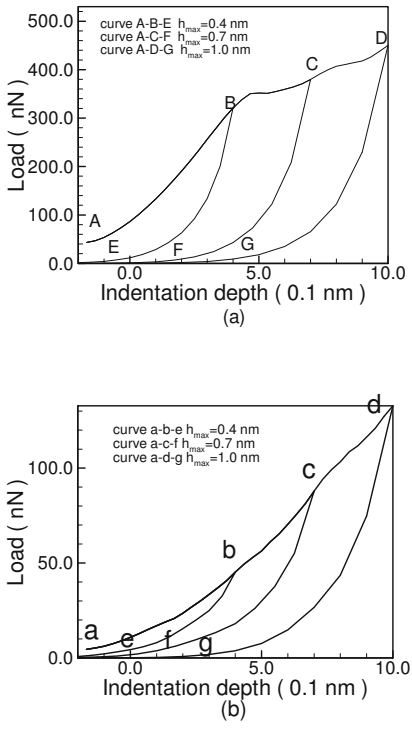

Figure 2. Load-depth curves for maximum indentation depths of 0.4 nm, 0.7 nm, and 1 nm: (a) spherical indenter, and (b) pyramidal indenter.

The high stresses induced as the indenter impresses the substrate cause structural instability of the crystal, which causes some of the atoms to slip. Therefore, a correlation must exist between the stresses at the atomic sites and the atom slippage. The stress tensor is calculated at each atomic site of the copper crystal for indentation to a depth of 0.4 nm using the spherical indenter. Figures 3 (a)~(b) show the distributions of von Mises shear stress exceeding 4.5 GPa in the [111], [001] directions, respectively. Meanwhile, Figures 3 (c)~(d) present the distributions of the norm of the slip vector in the [111], [001] directions, respectively. A comparison of the subplots in the upper and lower rows of Figure 3 indicates that the von Mises shear stress is a qualitatively good indicator of the plastic deformation induced in the simulated nanoindentation.

The principal goal of nanoindentation testing is to determine the elastic modulus and nanohardness of the specimen material from experimental measurements of indenter load and penetration depth. These readings

provide an indirect measure of the contact area at full load, from which the mean contact pressure, and hence the hardness, may then be estimated.

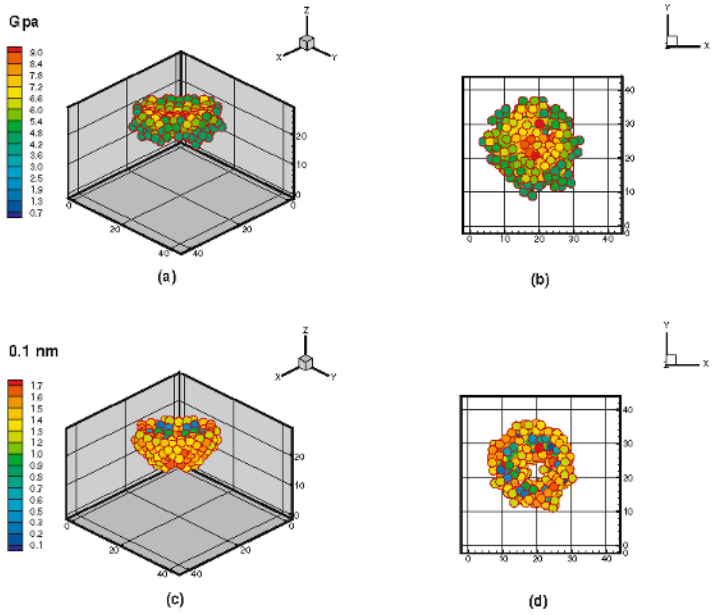

Figure 3. von Mises shear stress and slip vector distributions for indentation to a depth of 4 Å using a spherical indenter. Figures 3 (a)~(b): distributions of von Mises shear stress viewed in the [111] and [001] directions, respectively. Figures 3 (c)~(d): distributions of the norm of the slip vector viewed in the [111] and [001] directions, respectively.

Therefore, the validity of the nanohardness and elastic modulus results depends largely upon the analytical procedure employed to process the raw data. The present simulations utilize the hydrostatic stress to identify the true contact area at full load. Figures 4(a) and 4(b) present flooded contour diagrams of the contact pressure distributions on the copper surface for spherical and pyramidal indentations, respectively. The bold contour lines represent the boundaries of the contact areas at which the contact pressure vanishes. Once the true contact area has been determined, the nanohardness can be computed by dividing the load by the projected area of contact at that load. Table 1 presents the nanohardness magnitudes calculated using this method for spherical and pyramidal indentations with maximum indentation depths of 0.4 nm, 0.7 nm, and 1 nm.

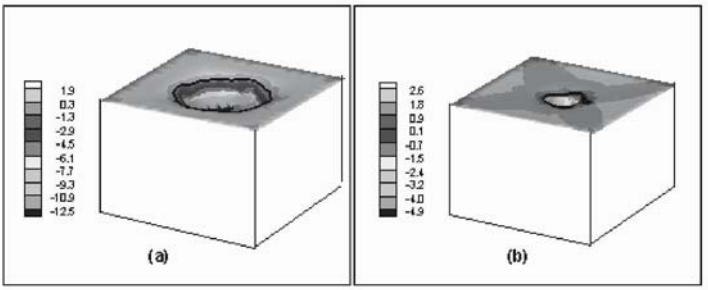

Figure 4 Flooded contour diagrams of contact pressure distributions on the copper surface. Figure 4(a): spherical indenter. Figure 4(b): pyramidal indenter. The two bold contour lines represent the boundaries of the contact areas where contact pressure vanishes. (Stress units: GPa).

In nanoindentation tests, analysis of the load-depth curve based on continuum mechanics contact theory gives an indirect measure of the contact area. The contact depth (h_c) is estimated from the total indentation depth (h_t) via:

$$h_c = h_t - \varepsilon P_{\max} / S_{\max} \tag{5}$$

whereε=0.72 for the pyramidal indenter, ε=0.75 for the spherical indenter, and S_{max} is the stiffness, which is equal to the slope of the unloading curve (dp/dh) at the maximum load (P_{max}).

The projected contact area is obtained by the projected contact area-to-contact depth relationship for the indenter geometry. The nanohardness is then determined by dividing the maximum load by the projected contact area. Table 1 presents the results when this procedure is applied to the simulated load-depth curves to determine the corresponding nanohardness values.

Table 1 shows that the nanohardness values calculated using Equation (5) are far higher than those calculated using the true contact area identified by the contact pressure. Hence, Equation (5) significantly underestimates the contact depth in all of the simulation cases. The results also reveal that the nanohardness varies with the indentation depth and the indenter geometry. Therefore, it can be concluded that the indentation size effect is significant in the nanoscale indentations simulated in this present study.

It can also be seen that the nanohardness obtained using the pyramidal indenter is higher than that obtained using the spherical indenter when the contact area is measured via the contact pressure. In contrast, if the contact area is obtained from Equation (5), the pyramidal indenter indentation yields a higher nanohardness. Figure 2 has demonstrated that the spherical indenter

Table 1. Nanohardness values calculated using two methods for two different indenter geometries and three indentation depths.

Geometry of indenter	Indentation depth h_t ($\mathring{A}$)	Nano-hardness calculated using the true contact area (GPa)	Nano-hardness calculated using equation (5) (GPa)
pyramidal	4	5.1	15.7
pyramidal	7	4.9	11.8
pyramidal	10	4.7	9.5
spherical	4	7.6	8.1
spherical	7	6.2	7.3
spherical	10	6.3	7.8

indentation consumes greater plastic work. This observation is consistent with the result that the nanohardness calculated by direct measurement of the contact area is higher. Therefore, it can be concluded that the commonly used procedure for estimating the contact area in nanoindentation testing is invalid when the indentation size falls in the nanometer regime.

4. CONCLUSION

In conclusion, this paper has presented a more efficient approach than conventional MD simulation for the investigation of the elastic-plastic deformations which occur during nanoscale indentations of a thin film. The proposed approach utilizes the minimum energy principle via nonlinear finite element formulation to reduce the indentation process to a quasi-static problem. The simulation results of the current modified finite element formulation indicate that the microscopic plastic deformations of the thin film are caused by instabilities of the crystalline structure. It has been shown that the analytical procedure commonly adopted in nanoindentation testing significantly overestimates the nanohardness. The simulation results have confirmed that both the indentation depth and the indenter geometry influence the nanohardness results.

ACKNOWLEDGMENTS

The authors gratefully acknowledge the financial support provided to this study by the National Science Council of Taiwan, under Grant No. NSC 91-2218-E-274-001, and the U.S. Air Force Office of Scientific Research, under Contract No. F62562-03-P-0378.

REFERENCES

1. Lucas, B. N., Oliver, W. C., Swindeman,J. E., 1998, The Dynamics of Frequency-Specific, Depth-Sensing Indentation Test, *Mat. Res. Soc. Symp. Proc.* **522**, pp. 3-14.
2. Hay, J. C., Pharr, G. M., 1998, Experiment Investigation of the Sneddon Solution and an Improved Solution for the Analysis of Nanoindentation Data, *Mat. Res. Soc. Symp. Proc.* **522**, pp. 39-44.
3. Hay, J. L., O'Hern, M. E., Oliver, W. C., 1998, The Importance of Contact Radius for Substrate-Independent Property Measurement of Thin Film, *Mat. Res. Soc. Symp. Proc.* **522**, pp. 27-32.
4. Lu, W., Komvopoulos, K., 2001, Nanotribological and Nanomechanical Properties of Ultrathin Amorphous Carbon Films Synthesized by Radio Frequency Sputtering, *J. Tribo.* **123**, pp. 641-650
5. Jeng, Y. R., Tan, C. M., 2002. Computer Simulation of Tension Experiments of a Thin Film Using an Atomic Model. *Phys. Rev. B* **65,** 174107.
6. Jeng, Y. R., Tan, C. M., 2004. Theoretical Study of Dislocation Emission around a Nanoindentation Using a Static Atomistic Model. *Phys. Rev. B* **69,** 104109.
7. Rafii-Tabar, H., 2000, Modelling the Nano-Scale Phenomena in Condensed Matter Physics via Computer-Based Numerical Simulations, *Physics Report* **325**, pp. 239-310.
8. Inamura, T., Suzuki, H., Takezawa, N., 1991, Cutting Experiments in a Computer Using Atomic Models of a Copper Crystal and a Diamond Tool, *Int. J. Japn Soc. Prec. Eng.* **25** pp. 259-266.
9. Horstemeyer, M. F., Baskes, M. I., Godfrey, A., Hughes, D. A., 2002, A Large Deformation Atomistic Study Examining Crystal Orientation Effects on the Stress-Strain Relationship, *Int. J. Plast.***18**, pp. 203-229.
10. Li, J., Vliet, K. J. V., Zhu, T., Yip, S., Suresh, S., 2002, Atomistic Mechanisms Governing Elastic Limit and Incipient Plasticity in Crystals, *Nature* **418**, pp. 307-310.

ELECTRIC FIELD-DIRECTED PATTERNING OF MOLECULES ON A SOLID SURFACE

W. Hong and Z. Suo*
Division of Engineering and Applied Sciences, Harvard University, Cambridge, MA 02138
**Tel: 617-495-3789 Fax: 617-496-0601 Email: Suo@deas.harvard.edu*

Abstract: Adsorbed on a solid surface, a molecule can migrate and carry an electric dipole moment. A nonuniform electric field can direct the motion of the molecule. A collection of the same molecules may aggregate into a monolayer island on the solid surface. Place such molecules on a dielectric substrate surface, beneath which an array of electrodes is buried. By varying the voltages of the electrodes individually, it is possible to program molecular patterning, direct an island to move in a desired trajectory, or merge several islands into a larger one. This article develops a phase field model to simulate the molecular motion and patterning under the combined actions of dipole moments, intermolecular forces, entropy, and electrodes.

Key words: self-assembly, diffusion, adsorbate, electric dipole

1. INTRODUCTION

When a molecule from liquid or vacuum attaches to a solid surface, the total energy of the system reduces by an amount. Provided the energy reduction is much larger than the thermal fluctuation, the molecule will stay adsorbed on the surface. In the absent of external interference, the molecule adsorbed performs a random walk. Such motion is thermally activated, its rate depending on the ratio of the migration barrier energy to the thermal energy [**1**].

Most asymmetric molecules intrinsically carry electric dipole moments. Even if the molecule is symmetric and nonpolar when isolated, the adsorption breaks the symmetry. The resulting asymmetric in charge distribution gives rise to a dipole moment. It is also possible to increase the

T. J. Chuang et al. (eds.), Nanomechanics of Materials and Structures, 245–254.
© 2006 *Springer. Printed in the Netherlands.*

dipole moment greatly by implanting a specific functional group [**2**]. The competition between the dipole-dipole repulsion and the intermolecular attraction aggregates the adsorbates into islands or stripes [**3**]. As the solid surface is isotropic, the pattern formed is randomly distributed and lack of long range order. Surface curvature could help to form better arranged pattern [**4**], but it's still far from the non-periodic pattern needed for micro-fabrication.

The motion of the adsorbates can be directed by a non-uniform electric field. Such motion has been demonstrated experimentally for cesium atoms on a doped GaAs substrate [**5**]. Other experiments of electric field directed motion are adatoms on metal surfaces [**6**] and lipids on air/water interface [**7**]. The scanning tunneling microscope tip servers as a strong tool in searching for better adsorbate-substrate pairs and studying the migration processes, but the lack of parallel ability and versatility limits its practical usage. A mask with topographic profile could guide a more complex pattern [**8**], but the pattern could never be changed once formed, and the alignment of the mask within a small distance to the substrate has technical difficulties. An array of electrodes, on which voltage could be set individually, forms a perfect candidate for the guide of the molecular assembly.

Fig. 1 shows the design. This design requires electrodes in nano-scale. Integrated circuits today contain feature size below 100 nm. Methods to fabricate complex structures of nanometer sizes are under intensive development. This article assumes that the technique for nano-scale electrode array will be available, simulates the use of such electrodes to guide the molecular motion, and discusses the potential of reconfigurable patterns and molecular cars.

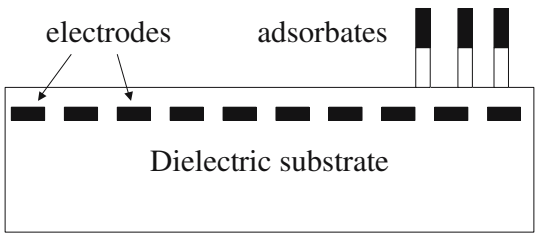

Figure 1. A dielectric substrate, with adsorbates migrating on its surface, and electrodes buried beneath the surface. The adsorbates carry electric dipole moments. Vary the voltage of the electrodes individually, one can program the motion and assembly of the adsorbates.

2. MODELING

The space above the substrate can be vacuum or a dielectric fluid. We will refer to the top space as fluid, and the dielectric substrate as solid. Let (x_1, x_2, x_3) be the spatial coordinates, and the plane (x_3 = 0) be the solid surface on which molecules are adsorbed. Let C be the adsorbate coverage, restricted in the interval $0 < C < 1$. Represent the adsorbate distribution by the time-dependent field $C(x_1, x_2, t)$. During the time of interest, we assume that the solid surface no longer exchange molecules with the environment, so that the average coverage, C_0, is invariant.

The adsorbates may form a single phase or separate into two phases, depending on the magnitude of the inter-adsorbate attraction relative to the thermal energy. We describe the binary mixture of the occupied and the vacant surface sites as a regular solution. The free energy of mixing per unit surface area is

$$g(C) = \Lambda k_B T\left[C\ln C + (1-C)\ln(1-C) + \Omega C(1-C)\right], \tag{1}$$

where Λ is the number of surface sites per unit area, k_B Boltzmann's constant, T the absolute temperature, and Ω the dimensionless parameter that measures the interadsorbate attraction relative to the thermal energy. The first two terms in the bracket come from the entropy of mixing, and the third term from the enthalpy of mixing. When $\Omega < 2$, the thermal energy prevails, the function $g(C)$ has a single well, and the binary mixture forms a solution. When $\Omega > 2$, the inter-adsorbate attraction prevails, the function $g(C)$ has double wells, and the binary mixture separates into two phases. While the regular solution model is one of many that can be invoked, it does have the ingredients essential to the phenomenon.

To incorporate the dipole-dipole and dipole-electrode interactions, we need to solve the electric field in both the fluid and the solid. The adsorbate mobility is low compared to the charge mobility in the electrodes. At a certain time, given a distribution of the adsorbates, the electric field is governed by electrostatic equations. Let $\Psi(x_1, x_2, x_3, t)$ be the electric potential field. Assuming that no excess charge exists inside the dielectric fluid and solid, Ψ obeys the Laplace equation. The electrode array underneath the dielectric, at a depth H, forms a boundary condition. A pre-programmed electric potential field is applied:

$$\Psi(x_1, x_2, -H, t) = Us(x_1, x_2, t), \tag{2}$$

where U represents the voltage magnitude, and s the time-dependent electrode voltage pattern, taking to be a spatially continuous function.

The electric dipoles of the adsorbates cause a change in the surface potential, which can be measured experimentally using the Kelvin method [**7**]. We assume that the surface potential is linear in the adsorbate coverage. That is, at the fluid/solid interface, $x_3 = 0$, there's a potential jump:

$$\Psi\left(x_1, x_2, 0^+, t\right) - \Psi\left(x_1, x_2, 0^-, t\right) = \zeta C\left(x_1, x_2, t\right). \tag{3}$$

The slope ζ is a material constant. This boundary condition couples the electrostatic field to the adsorbate distribution. Assuming the adsorbates to be electrically neutral, the electric displacement component normal to the interface, D_3, is continuous across the interface:

$$-\varepsilon_f \left.\frac{\partial \Psi}{\partial x_3}\right|_{x_3=0^+} = -\varepsilon_s \left.\frac{\partial \Psi}{\partial x_3}\right|_{x_3=0^-} = D_3, \tag{4}$$

where ε_f and ε_s are the permittivity of the fluid and the solid. The Laplace equation, together with the boundary conditions, determines the electric potential field.

The driving force on an adsorbate, **f**, is the reduction of the free energy of the system associated with the adsorbate moving a unit distance. Following the procedure in [**8**], we obtain that

$$\mathbf{f} = -\frac{1}{\Lambda}\nabla\left(\frac{\partial g}{\partial C} - 2h\nabla^2 C - \zeta D_3\right). \tag{5}$$

The first term comes from the free energy of mixing, which accounts for the thermal energy and the inter-adsorbate interaction. The second term represents the Cahn-Hilliard gradient energy [**10**], where h is a constant. The third term accounts for the dipole-dipole and dipole-electrode interactions. Assume that the adsorbate flux is linearly proportional to the driving force, $\mathbf{J} = M\mathbf{f}$, where M is the adsorbate mobility. The conservation of the adsorbates requires that $\Lambda \partial C / \partial t = -\nabla \cdot \mathbf{J}$. These considerations, together with Eqn. 5, lead to the diffusion equation:

$$\frac{\partial C}{\partial t} = \frac{M}{\Lambda^2}\nabla^2\left(\frac{\partial g}{\partial C} - 2h\nabla^2 C - \zeta D_3\right). \tag{6}$$

The third term in the bracket couples the evolution of the adsorbate distribution to the electrostatic field.

3. SIMULATION

A comparison between the first two terms the parenthesis of Eqn. 6 defines a length scale:

$$b = \left(\frac{h}{\Lambda k_B T} \right)^{1/2}, \tag{7}$$

which scales the width of the phase boundary. To resolve events occurring over this length scale, we introduce a time scale, $\tau = b^2 / D$, where D is the diffusivity, scaling as $D \sim Mk_BT / \Lambda$. Disregarding a dimensionless factor, we have the time scale

$$\tau = \frac{h}{M(k_B T)^2}. \tag{8}$$

In calculation, we normalize the spatial coordinates by b and time by τ. A dimensionless number, representing the relative magnitude of the dipole moment to the intermolecular attraction, appears in the normalized equation:

$$W = \frac{\varepsilon_f \zeta^2}{\sqrt{h\Lambda k_B T}}. \tag{9}$$

W determines the equilibrium island size.

To evolve Eqn. 6, one needs to solve the electrostatic boundary value problem in every time step. Fortunately in the current system, the boundary value problem could be solved analytically in Fourier space. Take the Fourier transform of a field variable with respect to the two lateral coordinates x_1 and x_2, and let k_1 and k_2 be the corresponding coordinates in the Fourier space. The Laplace equation becomes an ordinary differential equation $d^2\hat{\Psi} / dx_3^2 = k^2\hat{\Psi}$, where $k = \sqrt{k_1^2 + k_2^2}$. The solution takes the form $\hat{\Psi} = A\exp(kx_3) + B\exp(-kx_3)$, with constants A and B determined by the boundary conditions. The solution gives the electric displacement at the fluid/solid interface:

$$\hat{D}_3 = \frac{Uk\hat{s} + \zeta\hat{C}k\cosh kH}{\frac{\cosh kH}{\varepsilon_f} + \frac{\sinh kH}{\varepsilon_s}}. \tag{10}$$

Applying the solution to the diffusion Eqn. 6, we have the evolving equation in the Fourier space:

$$\frac{\partial \hat{C}}{\partial t} = -k^2 \hat{P} - 2k^4 \hat{C} + Wk^3 \frac{(U/\zeta)\hat{s} + \cosh kH\hat{C}}{\cosh kH + \varepsilon_f / \varepsilon_s \sinh kH}. \quad (11)$$

Here both k and H are normalized by b, and $\hat{P}(k_1, k_2)$ is the Fourier transform of the function

$$P(x_1, x_2) = \ln\left(\frac{C}{1-C}\right) + \Omega(1-2C). \quad (12)$$

A commonly used numerical scheme is adopted here. The computational cell is divided into 256×256 grids, and subject to a periodical boundary condition at all edges. We evolve the values of the C-field at all the grid points. At a given time, the C-values are known in both the real and the Fourier spaces. Calculate the nonlinear function P at all the grid points in the real space according to Eqn. 12, and transform them into the Fourier space. Update $\hat{C}$ at all grid points in the Fourier space according to Eqn. 11, and perform the inverse Fourier transform to obtain C-values in the real space. Repeat this procedure for many time steps. The results are plotted as a gray scale contour of C-values in the real space.

4. RESULTS

The model has many dimensionless numbers: Ω, W, $\varepsilon_f / \varepsilon_s$, H/b, U/ζ and the average coverage C_0. In addition, the initial adsorbate distribution field is spatial dependent, and the electrode voltage pattern is spatial and time dependent. A survey of the full parameter space is beyond the scope of this paper. In the following numerical examples, unless otherwise noted, we set $\Omega = 2.2$, $W = 2$, $\varepsilon_f / \varepsilon_s = 1$, $H/b = 10$. For the value $\Omega = 2.2$, the free energy of mixing, $g(C)$, has two wells at the coverage $C = 0.25$ and $C = 0.75$. To illustrate several considerations, we will vary U/ζ, the initial adsorbate distribution, and the electrode voltage pattern.

4.1 Electric field-directed assembly

When the adsorbates separate into two phases, the phase boundary energy drives the phases to coarsen. The molecular dipole moments are aligned in the same direction: they repel one another. Consequently, the

dipole-dipole interactions drive the phases to refine. In equilibrium, the phases will reach equilibrium sizes, typically ranging from nanometers to micrometers [**11**-**13**]. Because of the symmetry of the system, the patterns assembled don't have a long-range order. Here we use the electrode voltage pattern to direct the assembly processes.

Fig. 2 shows two time sequences, guided by different electrode voltage patterns, the top row by an array of stripes, and the bottom row by a lattice of dots. At $t = 0$, adsorbates distribute uniformly, with coverage $C_0 = 0.5$. A small magnitude of the electrode voltage, $U / \zeta = 0.02$, is prescribed. In the absence of the electrode voltage pattern, the adsorbates at the average coverage $C_0 = 0.5$ self-assemble into a pattern of randomly oriented noodles (e.g., **11**). As illustrated in Fig. 2, the small-magnitude electrode voltage patterns can guide the adsorbates to form straight stripes and other patterns.

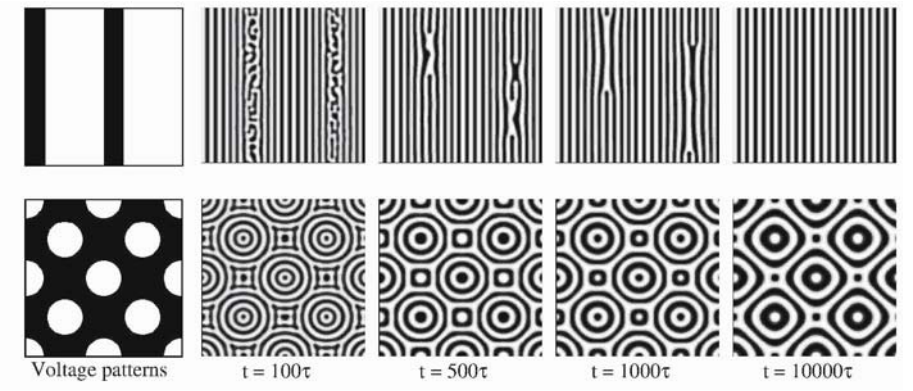

Figure 2. Electric field-guided self-assembly. In the top row, the electrode voltage pattern is an array of widely spaced stripes, and the adsorbates assemble into an array of finely spaced stripes. In the bottom row, the electrode voltage pattern is an array of large dots, which guide the assembly of the adsorbate pattern. In both cases, the electrode voltage is small, so that adsorbates still retain the natural pattern of fine stripes, and the electrode voltage only affects the overall layout.

One can change the electrode voltage pattern at any time, so that the adsorbate pattern is reconfigurable. Fig. 3 shows a time sequence. The initial adsorbate distribution is uniform, with coverage $C_0 = 0.35$. Prescribe the electrode array with a voltage pattern of the letter P using a relative high voltage, $U / \zeta = 1$. Under the guidance of the electrode voltage pattern, the adsorbates form a pattern of the letter P. In the background, the remaining adsorbates self-assemble into islands. We then change the electrode voltage pattern into the letter H. The adsorbates reassemble to form the letter H. The newly assembled pattern bears no resemblance to the old one.

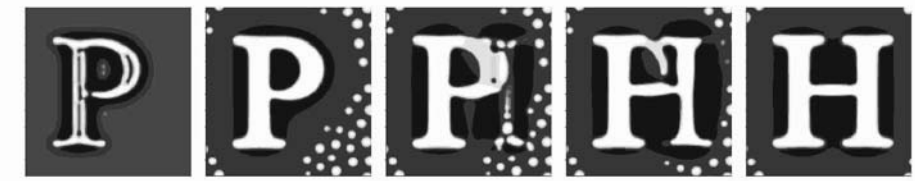

Figure 3. Reconfigurable assembly. Initially, the electrode voltage pattern is the letter P, and the adsorbates assemble accordingly. Then switch the electrode voltage pattern to the letter H, and the adsorbates re-assemble. The electrode voltage is high, so that the electrode voltage pattern overwhelms the natural pattern of the adsorbates.

The above examples demonstrate that a static electrode voltage pattern can either guide the self-assembly of the adsorbates, or impose a desired pattern. The main difference in the two operations is the relative magnitude of the electrode voltage to the surface potential, U / ζ. A small-amplitude electrode voltage pattern guides the overall layout of the stripes. The natural pattern such as the stripes is more or less preserved. A large-amplitude electrode voltage pattern overwhelms the natural pattern, and the adsorbate pattern is nearly a replica of the electrode voltage pattern.

4.2 Programmable motion

When the electrode voltage pattern is time-dependent, the adsorbates will move around. For example, consider a single island of aggregated adsorbates. If one applies voltage on the electrodes sequentially, the island can be propelled to move in a desired direction. Fig. 4 shows two time sequences, using parameters $U / \zeta = 1$, $C_0 = 0.2$. At such a low coverage, no phase separation takes place in the absence of the external electric field. We apply a circular shaped voltage pattern at the center to assemble the adsorbates. Subsequently, we program the electrode voltage pattern into a traveling wave. Fig. 4 shows snap shots for islands driven at two electrode voltage wave velocities. When the voltage wave moves slowly ($v = 0.02b/\tau$), the island distorts somewhat, but follows the motion. When the voltage wave moves too fast ($v = 0.05b/\tau$), the island ruptures.

Fig. 5 shows that the electrode voltage can be programmed to split an island. The parameters used are the same as those for Fig. 4. Again, we apply a circular shaped voltage pattern at the center. After a time of 2000τ, an island of the size similar to the electrode voltage pattern assembles. We then divide the voltage pattern into two halves, and move them apart with a constant velocity of $v = 0.025b/\tau$. The island also splits into two halves, which follow the two electrode voltage waves. By reversing the process, we could also combine two islands into one.

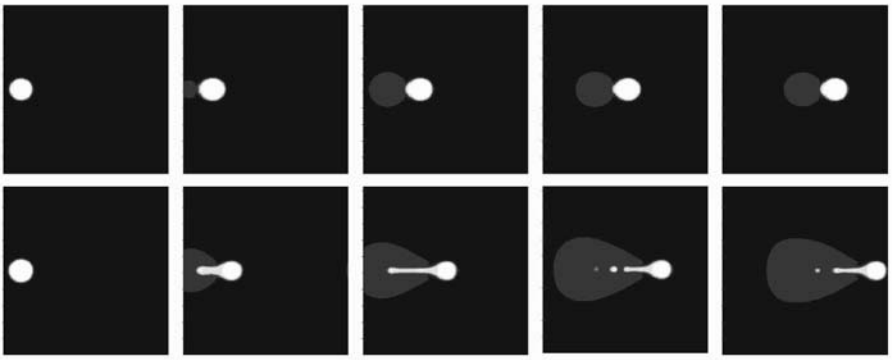

Figure 4. Top row: an adsorbate island driven by a slow electrode voltage wave at a low velocity. Bottom row: an adsorbate island driven by a fast electrode voltage wave.

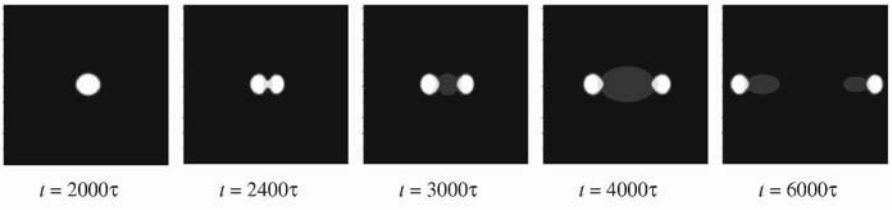

Figure 5. Splitting an island. The initial electrode voltage pattern is a single circular dot. The voltage pattern is then divided into two halves, and move in the opposite directions. The adsorbate island is split into two smaller islands.

5. CONCLUSION

Adsorbed on a solid surface, a molecule carries an electric dipole moment, and moves on the surface by a thermally-activated process. A patterned electrode array can direct the motion of the molecules. When a collection of the molecule partially covers the solid surface, their motion is influenced by the entropy, the intermolecular attraction, the dipole-dipole interaction, as well as the dipole-electrode interaction. We develop a phase field model to evolve adsorbate distribution field under the multiple thermodynamic forces. An array of electrodes can be programmed to guide the assembly of the adsorbates, or move the adsorbates in desired ways. Our numerical simulation illustrates the potential of the reconfigurable assembly and the programmable adsorbate motion. Technological implications of this model are explored in [**14**].

ACKNOWLEDGMENTS

This project was initiated under the support of the National Science Foundation through the Materials Research Science and Engineering Center (MRSEC) at Princeton University. Our work in this area has been supported by the Department of Energy through Grant DE-FG02-03ER46091, and by the Division of Engineering and Applied Sciences at Harvard University.

REFERENCES

1. Barth JV. "Transport of adsorbates at metal surfaces: From thermal migration to hot precursors". *Surf. Sci. Rep.* **40,** 75-149, 2000.
2. Evans SD, Urankar E, Ulman A, Ferris N. "Self-assembled monolayers of alkanethiols containing a polar aromatic group-effects of the dipole position on molecular packing, orientation, and surface wetting properties". *J. Am. Chem. Soc.* **113,** 4121-4131, 1991.
3. Suo Z, Gao YF, Scoles G, "Nanoscale domain stability in organic monolayers on metals". *Journal of Applied Mechanics*. **71**, 24-31, 2004.
4. Hong W, Suo Z, "Molecular assembly on cylindrical surfaces". *International Journal of Solids and Structures*. In press.
5. Whitman LJ, Stroscio JA, Dragoset RA, Gelotta RJ. "Manipulation of adsorbed atoms and creation of new structures on room-temperature surfaces with a scanning tunneling microscope". *Science* **251,** 1206-1210, 1991.
6. Tsong TT, Kellogg G. "Direct observation of direct walk of single adatoms and adatom polarizability". *Phys. Rev. B* **12,** 1343-1353, 1975.
7. Lee KYC, Klingler JF, McConnell HM. "Electric-field-induced concentration gradients in lipid monolayers". *Science* **263,** 655–658, 1994.
8. Gao YF, Suo Z. "Guided self-assembly of molecular dipoles on a substrate surface". *J. Appl. Phys.* **93,** 4276-4282, 2003.
9. Sessler GM. *Electrets*, Berlin, Springer-Verlag, 1987.
10. Cahn JW, Hilliard J E. "Free energy of a nonuniform system: 1. Interfacial free energy". *J. Chem. Phys*. **28**, 258-267, 1958.
11. Lu W, Suo Z. "Dynamics of nanoscale pattern formation of an epitaxial monolayer". *J. Mech. Phys. Solids* **49**, 1937-1950, 2001.
12. Seul M, Andelman D. "Domain shapes and patterns – The phenomenology of modulated phases". *Science* **267**, 476-483, 1995.
13. Ng K-O, Vanderbilt D. "Stability of periodic domain-structures in a 2-dimensional dipolar model". *Phys. Rev.* B **52**, 2177-2183, 1995.
14. Suo Z, Hong W, "Programmable motion and assembly of molecules on solid surfaces". *Proc. Nat, Acad. Sci.* **101**, 7874-7879, 2004.

DYNAMICS OF DISLOCATIONS IN THIN COLLOIDAL CRYSTALS

Peter Schall, Itai Cohen, David A. Weitz and Frans Spaepen
Division of Engineering and Applied Sciences, Harvard University, Cambridge MA 02138, Phone:(617)495-3760, Fax:(617)495-983, Email: spaepen@deas.harvard.edu

Abstract: Suspensions of μm-size colloidal particles form structures similar to those formed by atoms (vapor, liquid, glass, crystal). Since they can be observed optically in real time on the particle scale, colloids can be used to study the dynamics of these structures. Large single crystals of hard-sphere-like colloidal particles can be grown in the f.c.c. structure on a (100) template. They contain vacancies, stacking faults and dislocations. The stacking faults are extended because of their negligible energy and are bounded by Shockley partial dislocations. Dislocations are introduced by lattice mismatch at the template or by deformation (e.g., indentation). Their strain fields are imaged by laser diffraction microscopy (geometrically similar to electron microscopy) and their cores by confocal optical microscopy. The critical thickness of the epitaxial crystal, the rate of introduction of the interfacial dislocations and their offset from the template are accurately predicted by continuum dislocation theory.

Key words: Colloidal crystal, dislocation, stacking fault, epitaxy, critical thickness

1. COLLOIDAL SUSPENSIONS

Colloids are small solid particles, with diameter on the order of a μm, that are suspended in a solvent. They can be neutral or charged and interact as hard spheres or as screened charges. With increasing volume fraction they form dilute (gas), liquid or crystalline phases, similar to those formed by atoms as the temperature is decreased. This similarity arises because both systems are held together by central interparticle potentials. In the dense hard sphere colloids, the interparticle spacing is set by the osmotic pressure;

T. J. Chuang et al. (eds.), Nanomechanics of Materials and Structures, 255–261.
© 2006 *Springer. Printed in the Netherlands.*

in the atomic systems, it is set by shape of the electronic potential. The modulus of a condensed phase can be estimated by a dimensional argument as ε/Ω, where ε is the cohesive energy and Ω the particle volume. For an atomic system this gives $1eV/1Å^3$~100 GPa; for a hard-sphere colloidal system this becomes $kT/1\mu m^3$~1 Pa. Dense colloidal systems are therefore a type of "soft matter" (or, more fundamentally: "compliant matter").

Because of the size of their constitutive particles, colloidal systems can be studied by optical microscopy. In particular, confocal microscopy makes it possible to track the particles in three dimensions and in time. This makes colloidal systems unique models for studying the dynamics of condensed matter on the atomic scale. It can be considered an *analog computer* for such studies, which, because of its vast parallel processing capability, allows modeling of phenomena of a size and scale that are difficult to achieve by digital computation. Examples of such studies include crystal nucleation [**1**] and structural relaxation in liquids and glasses [**2**].

2. COLLOIDAL CRYSTALS

Hard-sphere-like colloids at high volume fraction form close-packed crystals, with a maximum volume fraction of $\pi/3\sqrt{2}=0.7405$. The particles form hexagonally close-packed two-dimensional layers. Since the next-nearest neighbor interactions are negligible, these layers are stacked randomly in the A,B and C positions of the hexagonal plane, unless special geometrical constraints are imposed. Randomly nucleated crystals or crystals formed by sedimentation on a flat surface are randomly stacked. One can consider these as face-centered cubic (fcc) or hexagonal close packed (hcp) crystals that are heavily faulted on, respectively, a (111) or the (0001) basal plane. Nevertheless, since these crystals are still periodic in one dimension, they show diffraction effects. Natural opals are of this type.

It is possible to create nearly perfect fcc crystals by sedimenting the particles onto a template that contains holes that determine their positions in a (100) plane [**3,4**]. In that case, the stacking deposition alternates between *two* sets of positions, and an fcc single crystal forms.

Because the stacking faults in hard-sphere crystals have negligible energy, they form easily and extend far. Their edges are Shockley partial dislocations with Burgers vector 1/6<112>, which repel over large distances. Figure 1 shows an example of a stacking fault observed by confocal microscopy in one crystal. Most of the stacking faults extend all the way through the sample. Identification of the Burgers vector on the edge of stacking fault confirmed it to be a Shockley partial. Because these partials are independent, they become the elementary dislocations that govern plastic flow in these crystals. This is different in the more familiar crystals with

long-range interparticle potentials, where the partials are kept together by the energy cost of the stacking fault between them, and where the elementary dislocation has a net Burgers vector 1/2<110>, the shortest lattice translation distance.

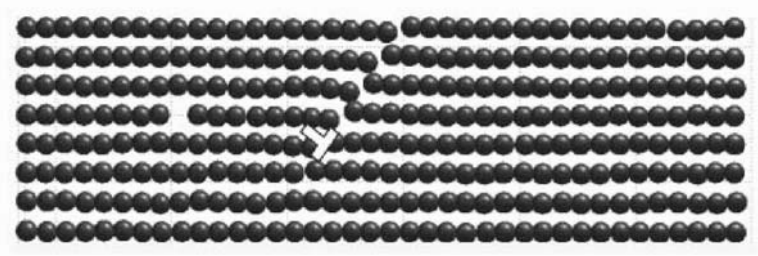

Figure 1. Confocal microscopy image of a section of a colloidal crystal parallel to the (110) plane. The image shows a stacking fault on the $(1\bar{1}1)$ plane that ends in an edge dislocation. The latter is a Shockley partial with Burgers vector $b=1/6[\bar{1}12]$ The dislocation core is offset from the template (below the crystal, not shown) by three atom layers. The equilibrium interparticle diameter is 1.63 μm. After Schall, *et al.* [**4**]

3. OBSERVATION OF DISLOCATIONS

The data from the confocal microscope can be used to identify dislocation cores and to trace Burgers circuits. The strain field of the dislocation can be imaged in the same way that it is imaged by the electron microscope in atomic-scale crystals. The strain locally changes the lattice plane orientation and thereby the Bragg condition for diffraction. As a result, dislocations are revealed by changes in contrast in bright or dark field images. Since the lattice parameter of the colloidal crystals is on the order of a μm, these effects can be obtained by optical diffraction and imaging [**4**], as illustrated in the laser diffraction microscope of Figure 2A.

The images in Fig. 2B and 2C are of the dislocation array formed near the template when its interparticle spacing is slightly (1.5%) greater than the equilibrium spacing of the crystal plane. The reversal of the contrast when the diffraction vector **q** is made to deviate from a reciprocal lattice vector **g** (excitation error **s=q-g**≠0) demonstrates that the contrast does indeed arise from Bragg diffraction.

The interface dislocations shown in Fig. 2 are edge dislocations whose Burgers vector **b**=1/6<112> is inclined to the plane of the template by an angle α=arc cos(1/√3), as illustrated in Fig. 1. There is a second set of edge dislocations, along the y-direction, which is not visible, because their Burgers vectors satisfy the extinction condition **g.b**=0.

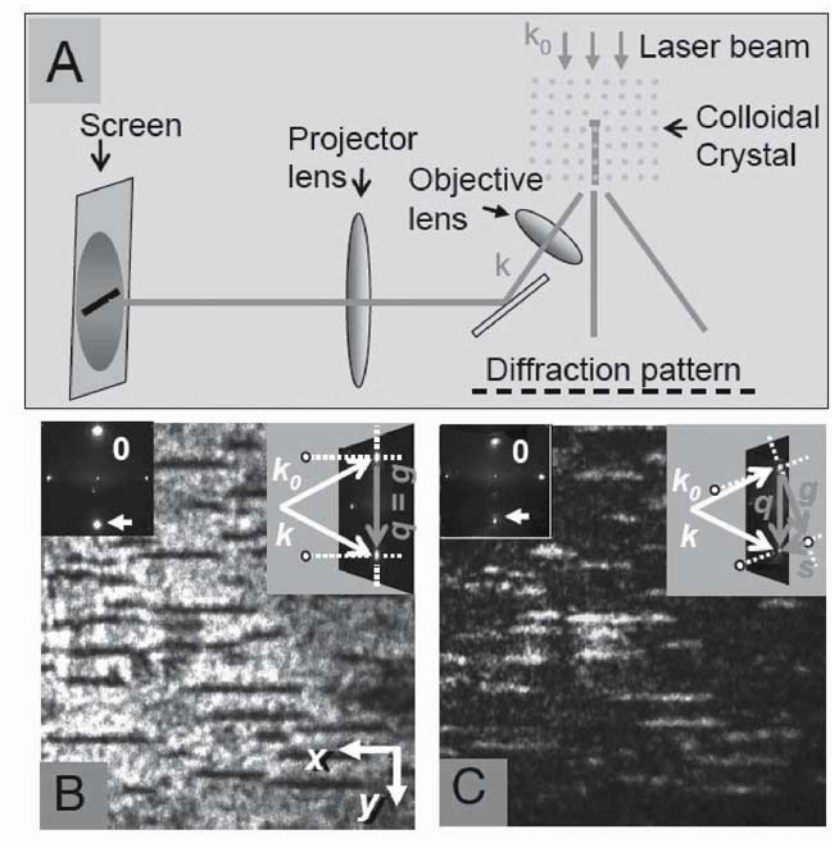

Figure 2. A: Schematic diagram of the laser diffraction microscope used to image the strain field of dislocations. B and C: images of one set of edge dislocations formed at the interface between a colloidal crystal and a template with 1.5% greater lattice spacing. The upper left insets are the diffraction patterns (0: transmitted beam; arrow: (220) diffracted beam used for imaging). The upper right insets are diagrams that show the relation between the scattering vector **q** and the reciprocal lattice vector **g**. The contrast of C is inverted because of the excitation error **s**. A perpendicular set of edge dislocations is present but are not imaged because their Burgers vectors are subject to the condition **g.b**=0. After Schall, *et al*. [**4**].

The laser diffraction microscopy made it possible to monitor the formation and lengthening of the interface dislocations as a function of time. As with epitaxial growth of atomic crystals, there is critical thickness, h_c, below which the interfacial dislocations do not nucleate. We found that for the conditions of the crystal of Fig. 2, we found the first dislocations at a

thickness of 31 μm. Once nucleated, the dislocation length, L, increased according to:

$$L = L_{\text{inf}}\left[1 - \exp\left(-\frac{t}{\tau}\right)\right] \tag{1}$$

where L_{inf} is the length after full relaxation and τ is a time constant, measured to be 130±40 s.

4. COMPARISON WITH CONTINUUM THEORY

Three observations are compared to the predictions of continuum dislocation theory, and remarkable agreement is found. In the first two cases (the critical thickness and the core offset), this is not surprising, since the quantities depend on Poisson's ratio, which in these crystals is close to the canonical value of 1/3 [**5**]. The lengthening rate of the dislocations, however, is a more interesting test. Here, we give only the results of the analysis. The details can be found in our original paper [**4**].

4.1 Critical thickness

The classical isotropic elastic analysis by Frank and van der Merwe [**6**] and by Matthews and Blakeslee [**7**], in which the sum of the strain energy in the film and the line tension of the interfacial dislocations is minimized, gives the following expression for the critical thickness:

$$h_c = \frac{b}{8\pi(1-\nu^2)\ \cos\alpha\ \varepsilon_0}\ln\left(\frac{4h_c}{b}\right) \tag{2}$$

where ν is Poisson's ratio and ε_0 is the strain of the lattice with respect to the template. For this crystal, the lattice parameter is 2.31 μm, and hence b=0.94 μm. For ν=1/3 and ε_0=0.015, Eqn. 2 gives h_c=22 μm, in agreement with the observations.

4.2 Offset from the interface

The offset of the dislocation from the rigid template is determined by two forces: a force toward the interface that tends to relieve the strain in the layers below the dislocations and a repulsive image force as a result of the rigid boundary condition. The two forces balance at a distance:

$$z_0 = \frac{(b\ \cos\alpha)^2}{4\pi(1-\nu^2)\Lambda\varepsilon_0^2} \tag{3}$$

where Λ is the average distance between the dislocations. In these experiments Λ=53 μm, so that z_0=2.2 μm, in reasonable agreement with the observation of Fig. 1.

4.3 Lengthening rate

The lengthening of the interfacial dislocations after nucleation is determined by the resultant of three forces [**8**]: a Peach-Koehler force on the threading screw segment at the end of the dislocation, the line tension of the edge dislocation being generated, and a drag force on the screw segment. The latter is characteristic for colloidal crystals, in that it is proportional to the dislocation velocity and to the viscosity of the solvent [**9**]. The latter can be understood since the motion of the particles past each other in the solvent is a hydrodynamic phenomenon. The analysis results in an exponentially decaying lengthening rate, as in Eqn. 1, with a time constant:

$$\tau = \frac{(1-\nu)\eta}{Eb^2\rho_{screw}\cos^2\alpha\ \sin\alpha} \tag{4}$$

where E is Young's modulus, η is approximately equal to the shear viscosity of the solvent and ρ_{screw} is the density of threading screw dislocations. The latter quantity was measured to be 3 x 10^{-4}μm^{-2}. If η is given a value of 4x10^{-3} Pa.·s, the shear viscosity of the solvent, the observed relaxation time of 130 s implies a Young's modulus E=0.3 Pa, which is the right order of magnitude for these crystals [**5**].

5. CONCLUSIONS

These experiments on colloidal crystals show that colloidal systems are useful "analog computers" in the study of the structure and dynamics of condensed matter. Other phenomena we have investigated include the indentation of colloidal crystals and the shear of colloidal glasses [**10**]. In the area of nanomechanics, these types of experiments allow a unique look, at both the particle-level and the intermediate length scale, at phenomena such as the behavior of dislocation nodes and the interaction of dislocation with custom-prepared grain boundaries.

ACKNOWLEDGMENTS

This work has been supported by the National Science Foundation through the Harvard MRSEC (DMR-0213805) and by contract number DMR-0243715. PS acknowledges partial support by a Lynen Fellowship from the Alexander von Humboldt Stiftung.

REFERENCES

1. Gasser U, Weeks ER, Schofield, A, Pusey PN, Weitz DA. "Real Space Imaging of Nucleation and Growth in Colloidal Crystallization", *Science*, **292**, pp. 258-262, 2001.
2. Weeks ER, Crocker JC, Levitt AC, Schofield A, Weitz DA. "Three-Dimensional Direct Imaging of Structural Relaxation near the Colloidal Glass Transition", *Science,* **287**, pp. 627-631, 2000.
3. Van Blaaderen A, Ruel R, Wiltzius P. "Template-directed Colloidal Crystallization", *Nature,* **385**, pp. 321-324, 1997.
4. Schall P, Cohen I, Weitz DA, Spaepen F. "Visualization of Dislocation Dynamics in Colloidal Crystals", *Science*, in press, 2004.
5. Frenkel D, Ladd AJC. "Elastic Constants of Hard-Sphere Crystals", *Phys. Rev. Lett.*, **59**, pp. 1169-70, 1987.
6. Frank FC, van der Merwe JH. "One-Dimensional Dislocations. I. Static Theory", *Proc. Roy. Soc. (London) A*, **198**, pp. 205-225, 1949.
7. Matthews JW, Blakeslee AE. "Defects in Epitaxial Multilayers. I. Misfit Dislocations", *J. Cryst. Growth*, **27**, pp. 118-125, 1974.
8. Matthews JW, Mader S, Light TB. " Accommodation of Misfit across the Interface between Crystals of Semiconducting Elements or Compounds", *J. Appl. Phys.*, **41**, pp. 3800-3804, 1970.
9. Jorand M, Rothen F, Pieranski P. "Dislocation Motion in Colloidal Crystals", *J. de Phys. Coll.*, **46**, pp. 245-255, 1985.
10. Schall P., Cohen I. Unpublished results.

MESOSCOPIC LENGTH SCALES FOR DEFORMED NANOSTRUCTURES

W.M. Mook,[1] M.D. Chambers,[1] C.R. Perrey,[1] C.B.Carter,[1] R.E. Miller,[2] W.A. Curtin[3] and W.W. Gerberich[1]*

*[1]Chemical Engineering and Materials Science, University of Minnesota, 421 Washington Ave. S.E., Minneapolis, MN 55455, *Phone:612-625-8548,Fax: 612-626-7246, Email: wgerb@umn.edu; [2]Mechanical and Aerospace Engineering, Carleton University, 1125 Colonel By Dr., Ottawa, Ont., Canada, K1S 5B6; [3]Division of Engineering, Brown University, Providence, RI 02912*

Abstract: Defining mesoscopic length scales for deformed nanostructures requires a close coupling of theory and experiment. One approach to this is to mechanically probe single crystal nanospheres of the same size that can be evaluated computationally. This involves analyzing dislocation nucleation and its corresponding yield instability represented by either a displacement excursion or load drop. We propose that the external work necessary to create the instability can be accounted for by idealized prismatic loop punching when the associated surface work, dislocation work and stored elastic energy of the loop are accounted for. This is shown both for experimentally compressed silicon nanospheres and theoretically simulated nanoindentation of silver (from work of Christopher, *et al*., 2001). For relatively large cumulative strains in a freestanding aluminum nanostructure, it is shown that Taylor hardening can predict flow stress behavior consistent to first order with atomistic simulations.

Key words: Length scales, nanoindentation, discretized dislocations

1. INTRODUCTION

To define a length scale controlling deformation in structures less than 100 nm in size is a daunting task. Numerous approaches to this have been recently taken including attempts employing strain gradient plasticity [**1-2**],

T. J. Chuang et al. (eds.), Nanomechanics of Materials and Structures, 263–275.
© 2006 *Springer. Printed in the Netherlands.*

volume to surface area (V/S) ratios [**3-4**], geometric constraint [**5-6**], free energy elastic stability [**7**] and energy balance criteria [**8**]. Much of this has been experimentally based and has guided researchers in analyzing challenging issues associated with the indentation size effect (ISE) [**2,9**] and dislocation nucleation [**10-11**]. Still, computational materials science which is free from experimental complexities has probably made the most advances in solving the multiscale modeling problem [**12-14**] because simulations at the nanometer scale can be quite accurate and provide an appropriate bottom–up format from tight–binding to finite element solutions with coupled boundary value approaches.

With the advent of scanning tunneling and atomic force microscopies (STM and AFM) and transmission electron microscopes (TEM) equipped with *in situ* nanoindenters, it is becoming increasingly possible to conduct experiments and simulations with similar volumes of material and matched boundary conditions. A good example of this from a dislocation plasticity standpoint is the study of Rodriguez de la Fuente, *et al*. [**15**] in which partial dislocations were induced and imaged in a gold film with STM; the results of which agreed with the predictions of the atomistic simulations. Although the goal of accurately defining a controlling length scale is still ill–defined, progress towards this end has been substantial. The following describes our initial attempts in resolving the energy balance in the first stages of deformation and progress in applying this to a simulation where a coupled atomistics and discrete dislocation (CADD) model can be used.

2. ENERGY BALANCE OF YIELD EXCURSIONS

A series of recent papers has shown that single–crystal nanospheres of silicon and titanium exhibit strengths greater than their bulk counterparts. Although these were reported in terms of being superhard, at the suggestion of Veprek and Argon [**16**], it is more appropriate to call these superstrong. The "hardness" reported was a reflection of the Hertzian type contact pressures that the spheres were subjected to. However, it is clear that the side constraint of a penetrating spherical indentation into a surface is missing for a compressed nanosphere resulting in a vastly different state of stress. This, however, makes these "superstrong" mean contact pressures even more interesting when comparing them to mean contact pressures of nanoindenters into bulk single crystals.

The nanospheres were hypersonically accelerated out of a high–pressure plasma [**17**]. Previous compression tests of these relatively ideal single crystal samples as seen in Fig. 1 demonstrated that silicon had higher than normal strength, produced yield discontinuities at relatively low loads, and work–hardened substantially under larger displacements [**18**]. As they also

exhibited reversed plasticity [**19**], it was thought that dislocations were the main, if not the only source of plasticity. There were a number of factors that led to this conclusion. First a phase transformation, e.g. β–Sn, was rejected as a source since pop–out was not detected upon unloading. Second, the steps in the load–displacement curve in Fig. 1(b) sum to the total residual displacement. Third, there are a number of examples of dislocation plasticity in Si with and without superimposed confining pressures. Rabier, *et al*. [**20**] has shown with a multi–anvil apparatus that Si deforms via dislocations at room temperature under confining pressures of 5 GPa. Additionally small volume TEM *in–situ* indentation experiments into wedge shaped silicon samples demonstrated dislocation loops and no evident phase transformations [**21**]. This is in agreement with our recent unpublished finding on freestanding silicon nanostructures which were of a similar size to the tested nanospheres. Here the plastically deformed structures imaged with TEM also provided evidence of dislocation activity without phase transformations.

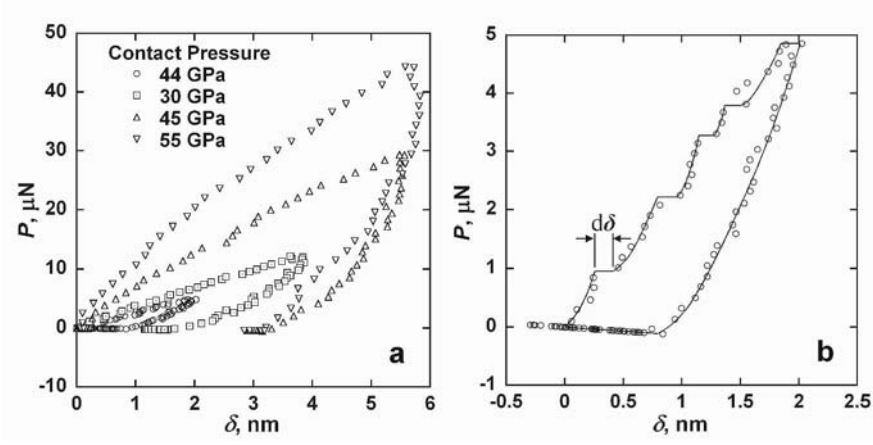

Figure 1. Compressions of a 39 nm diameter single crystal silicon nanosphere showing (a) consecutive compressions to increasing loads and (b) magnification of the first compression exhibiting displacement excursions that add up to the residual displacement upon unloading.

The intriguing aspect of the multiple steps seen in Fig. 1(b) described here and elsewhere [**19**] is that each excursion is on the order of 0.2 nm, slightly less than a Burgers vector in silicon. We have taken this as evidence of dislocation emission. As stored elastic energy was released when each of the yield excursions occurred, it was first necessary to speculate on where the energy was absorbed. An obvious choice was plastic work associated with moving a dislocation. To solve this problem one needs to know where the dislocations nucleate, of what character they are and where they end up

inside the nanosphere. For a single loop inside a sphere a solution by Willis [**22**] exists but it was desirable to have this for all of the steps shown.

The situation was idealized to sequential prismatic loops of the same size as the contact radius, a, as shown in Ref. [**18**]. Emitting the first dislocation at the edge of the contact requires a force needed to exceed an image force combined with a resisting Peierls barrier. When it exceeds this the dislocation glides to a new equilibrium position. There are three caveats here, the first is the loop would have to be slightly outside the contact to experience a free surface which is probably not unrealistic. The second caveat is that a vacuum is used to represent the image force condition implying that the oxide film is broken. As this might act as the nucleation site, this is also possible and even if not, the modulus of SiO_2 is substantially less than Si (70 GPa < 160 GPa). The third caveat is that only prismatic loops are considered, while shear loops might be just as likely if not more so. Given those caveats, we utilized a Hertzian stress distribution for a given spherical contact as given by Johnson [**23**]. This was further coupled to a dislocation model for crack tip shielding of a plastically polarizable material by Zhou and Thomson [**24**]. By substituting the spherical contact stress field for the crack–tip stress field one finds

$$\sigma_f = \frac{p_o}{2}\left[\frac{1+\nu}{1-\frac{z_i}{a}\tan^{-1}\left(\frac{a}{z_i}\right)+\frac{1}{2}\left(1+\frac{z_i^2}{a^2}\right)}-\frac{a^2}{a^2+z_i^2}\right] - \frac{\mu b_i}{4\pi(1-\nu)z_i}+\sum_{\substack{j\\ j\neq i}}\frac{\mu b_j}{2\pi(1-\nu)(z_i-z_j)} \tag{1}$$

where p_o is the maximum pressure, z_i is the distance of the i^{th} dislocation below the contact, a is the contact radius, ν is the Poisons ratio, μ is the shear modulus and b_i and b_j are the Burgers vectors of the i^{th} and j^{th} dislocations which in this case are assumed to be the same. Additionally, σ_f is the friction stress to be either exceeded by the driving force minus any back force or to govern final arrest. The maximum pressure for a spherical contact is $3P/2\pi a^2$ where P is the external load. The first term is the external driving force, the second term is the image force and the third concerns the dislocation-dislocation interaction force from any previously injected dislocations. Applying this to the first four displacement excursions in Fig. 1(b) is accomplished using μ = 66 GPa, ν = 0.218 and b = 0.236 nm for the 39 nm diameter silicon sphere. The resulting stress on the assumed

prismatic loop at distances z below the surface are shown in Fig. 2(a) for the force associated with each excursion. The first excursion at $P = 0.92$ μN, the dislocation sees an initial negative stress as the loop starts to form and gradually goes positive as it proceeds further from the surface. When the positive stress becomes sufficiently large to exceed the friction stress, here assumed to be a Peierls stress of 4 GPa, the dislocation can freely glide to a distance about 8 nm below the surface where it arrests.

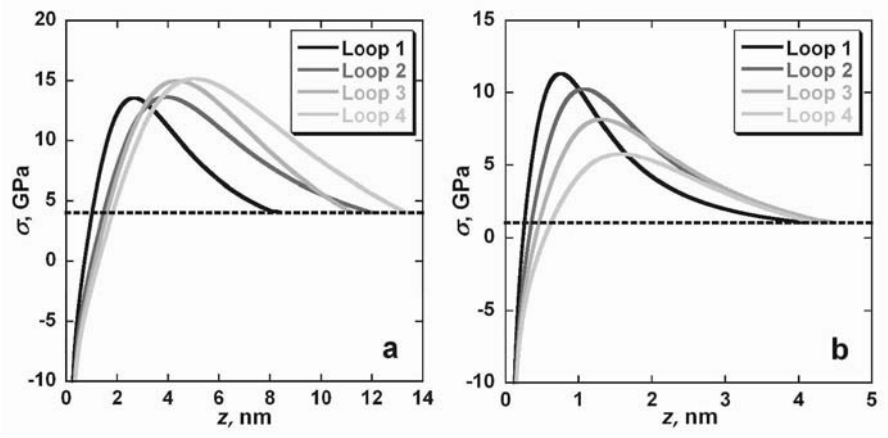

Figure 2. The resulting stress from Eqn. 1 at distances z below the surface on prismatic dislocation loops which are assumed to form during yield excursions from (a) the compression of 39 nm diameter Si nanosphere and (b) the simulated nanoindentation of Ag {100} crystal.

The real work associated with this is the force on the dislocation per unit length, τb, multiplied by both the loop length, $2\pi a$, and z, the distance the dislocation moves before it can glide freely to its equilibrium position. In this case $z = 1.02$ nm which is where the stress exceeds 4 GPa. Therefore the plastic work for this excursion is

$$\delta W_{\mathrm{p}} = \tau \; b \cdot 2\pi a \cdot z \,. \tag{2}$$

Energy can also be absorbed by new surface creation. Here we take the contact area before and after the excursion, giving

$$\delta S = \gamma_{\mathrm{s}} A\big|_{\mathrm{after}} - \gamma_{\mathrm{s}} A\big|_{\mathrm{before}} \tag{3}$$

and use a geometric contact with $\gamma_{\mathrm{s}} = 1.56$ J/m^2 for Si. Also, using this description requires an area of $2\pi a^2$ since there is a contact both at the top

and bottom of the sphere. In addition to this energy absorbed, elastic energy remains within the created loop, given as

$$\delta U_\ell = \pi a \left[1 + \frac{1}{1-\nu} \right] \left[\frac{\mu b^2}{4\pi} \ln\left(\frac{ae^2}{b} \right) \right] \tag{4}$$

where the first term in brackets is for a dislocation of half screw and half edge character, and the second term is the energy per unit length for a screw dislocation which includes a continuum description of the core energy contribution. The total energy that is absorbed or remaining is balanced by the external work such that

$$Pd\delta_{\text{exc}} = \delta W_{\text{p}} + \delta S + \delta U_\ell \tag{5}$$

where the external work is $Pd\delta_{\text{exc}}$. As shown in Table 1, 93 ± 20% of the work is accounted for by these three terms.

Table 1. External work and energy balance in Si experiments and Ag simulations of Christopher, *et al*. [**25**] (Units multiplied by 10^{18} for J).

	P μN	$d\delta_{\text{exc.}}$ nm	$W_{\text{ext.}}$ J	δA nm^2	δW_{s} J	z^* nm	δW_{p} J	U_ℓ J	$W_{\text{int.}}$ J
Silicon Experiment	0.92	0.155	*143*	18.7	29.1	1.01	104	27	*160*
	2.2	0.19	*418*	22.8	35.6	1.46	238	46	*320*
	3.2	0.16	*512*	18.3	28.5	1.60	322	53	*404*
	4.4	0.12	*528*	14.2	22.1	1.82	438	62	*522*
Silver Simulation	0.055	0.265	*14.7*	1.03	1.17	0.26	8.93	7.35	*17.4*
	0.107	0.179	*19.1*	1.10	1.25	0.36	16.4	11.6	*29.3*
	0.135	0.217	*29.2*	1.64	1.87	0.46	21.5	15.0	*38.4*
	0.152	0.291	*44.4*	2.64	3.01	0.62	27.1	18.9	*49.0*

To examine whether the critical distances, z, below the indenter from Eqn. 1 and used in Eqn. 2 were realistic, an atomistic simulation that was conducted using a sharp indenter penetrating an ideally perfect Ag {100} crystal [**25**] was used for comparison. This atomistic modeling of nanoindentation used a 90º pyramid indenting a 40,960 atom array using an atomistic potential developed by Ackland [**26**]. While this is non-ideal from a Hertzian stress field standpoint it was rationalized that the mean pressure represented by the given force and contact area would nucleate dislocations in a similar manner. Furthermore, the hillocks they observed on their FCC silver were similar to those later observed both experimentally and

theoretically in Au by STM [**15**]. The latter hillocks were identified as partial dislocations coalescing into stair–rod configurations. The useful aspect of the theoretical Ag study was that load–depth curves were provided and the forces were scaled to loads, e.g. 125 eV/Å was 200 nN at a maximum depth of 1.75 nm. Four yield excursions similar to those in Fig. 1(b) were found with each displacement excursion and were about equal to the Burgers vector of silver. The total of 0.9 nm displacement represented by these excursions was the majority of the 1.3 nm residual displacement found upon unloading. The only difficulty in analyzing this data with Eqn. 1 was to define a contact radius. This was accomplished by taking a perfect cube corner geometry and allowing the contact area represented by an equilateral triangle with side, a_Δ, to be equal to the contact area represented by a circle of πa^2 where a is the spherical contact radius. For this it was found that

$$a^2 = \frac{2}{\sqrt{3}\pi}\delta^2. \tag{6}$$

It was reasoned that a consistent mean pressure would give first order conditions for dislocation nucleation recognizing that the local stresses would deviate. Using this representation of a, the resulting stress distance plot for the Ag {100} simulation is shown in Fig. 2(b). It is seen to be similar to that for the Si nanosphere in Fig. 2(a), the main difference being that the displacements for releasing the dislocation into a freely gliding situation are about a factor of three smaller. This is partly due to the larger friction stress of 4 GPa used for Si compared to 1 GPa for Ag. With the critical distances of Fig. 2(b), Eqns. 2–4 are applied to determine if the energy balance represented by Eqn. 5 is realistic. Everything is known except for the dislocation line length, originally $2\pi a$ for the nanosphere, now becomes $3a_\Delta$ in Eqn. 4 to describe the cube corner contact. With μ_{Ag} = 33.8 GPa, b_{Ag} = 0.288 nm, ν_{Ag} = 0.354 and γ_s^{Ag} = 1.14 J/m^2, the values of Eqns. 2–4 were determined as shown in Table 1. The external work ranging from 14 to 41x10^{-18} J could be accounted for 121 ± 20% of the time. If one can describe these early stages of deformation quite accurately and carry these to longer range dislocation structures, this should allow for prediction of the early stages of linear hardening. For such cases the governing energy balance and the coupled length scales are addressed in a forthcoming publication [**8**].

3. DISPLACEMENT CONTROLLED NANOSCALE DEFORMATION

At somewhat larger strains we compare the mechanical response of an experimental compression of a freestanding aluminum nanostructure to an atomistic simulation of nanoindentation into aluminum fully described in Ref. [**14**]. While this is not a direct comparison since the simulation considers only two dimensions, both the experiment and simulation were run under displacement control, probe similar volumes of material and demonstrate consistent mechanical response.

The coupled atomistic discrete dislocation (CADD) simulation shown in Fig. 3 involved a 50 nm diamond tip indenting a 94.1 nm thick aluminum film modeled with an embedded atom potential [**27**]. The nucleation process in Fig. 3(a) took place during the load drop from point I to point II in Fig. 3(b) [**14**]. This response captured by the simulation is strikingly similar to the load drops seen in the experimental compression of the freestanding aluminum nanostructure in Fig. 4.

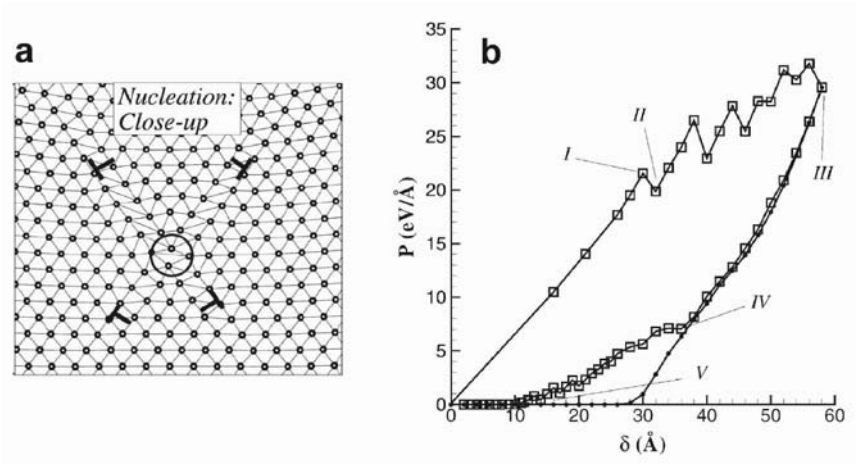

Figure 3. Coupled atomistics and discrete dislocation model of a displacement controlled indentation into a 94.1 nm thick Al film with (a) the nucleation of the dislocation representing the load drop from point I to point II in (b).

To create the nanostructures, a 400 nm thick film of poly(methyl methacrylate) (PMMA) was spin–coated onto a Si (100) substrate following standard photolithographic procedures. The PMMA was patterned via e–beam lithography and the aluminum was deposited by e–beam evaporation at 2 Å/s. The Al structure was characterized first by AFM and found to be 46 nm high. It was then centered under the 5 μm radius diamond tip in the nanoindenter (Hysitron TriboIndenter®). This was accomplished by

scanning the surface with the diamond tip using a normal load of approximately 200 nN. While this load was necessary to maintain contact between the tip and substrate, it did deform the Al nanostructure during scanning to the point that its measured height was 21 nm before the compression in Fig. 4. After the compression, the structure was measured by both the nanoindenter and AFM to be 12 nm high. The compression was run using displacement control with a loading and unloading rate of 2 nm/s and a hold time at maximum displacement of 5 s. After about 6 nm of displacement, a series of three distinct load drops of about 1 μN occurred. This is seen more clearly in the load versus time graph in Fig. 4(b). Smaller load drops occurred at larger displacements.

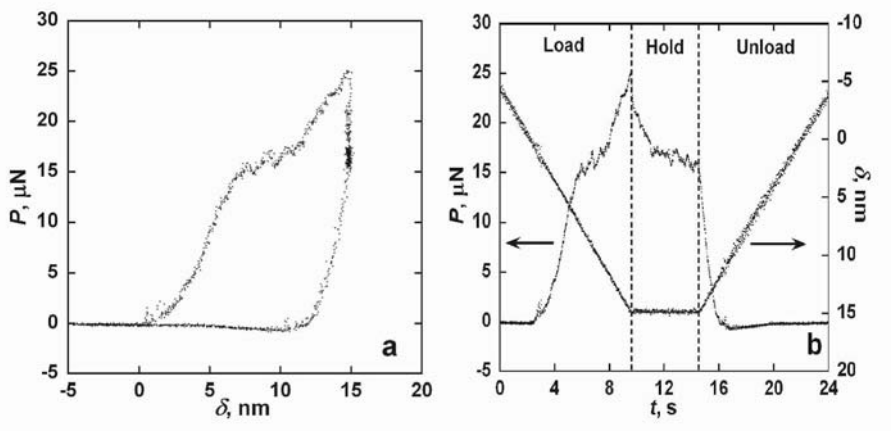

Figure 4. Compression of a freestanding aluminum nanostructure with a 5 um radius diamond tip. The structure had an initial height of 46 nm as measured with AFM. The height before compression was 21 nm compared to 12 nm after the test. The test was run under displacement control at a loading and unloading rate of 2 nm/s with a 5 s hold at maximum displacement.

In order to compare the experimental results to the simulation, a stress–strain curve was generated (Fig. 5) from the load–displacement data in Fig. 3, Fig. 4 and a simulation of a 7.85 nm thick Al film (data from Fig. 12 Ref. [**14**]). The stress–strain curve was generated by scaling forces per unit area to the elastic modulus of aluminum and defining strain as δ/t, the displacement normalized on film or nanostructure thickness. The interesting feature of Fig. 5 is that the stress drops at similar strain levels for the simulations of the 7.85 nm and 94.1 nm thickness films bracketed the stress drop magnitudes from the experiment.

A final set of comments addresses the original goal of this investigation which was to establish a length scale approach for deformation of nanostructures. This current study and four previous ones [**4,5,8,28**]

demonstrate how difficult this task will be. In three recent papers [**4,5,8**] we had sequentially proposed a volume to surface ratio, a linear hardening inverse pile–up approach and a geometric approach to length scales for deformation of small volumes. All of these can be defended on the grounds they apply to slightly different length scale regimes and different hardening mechanisms [**5**].

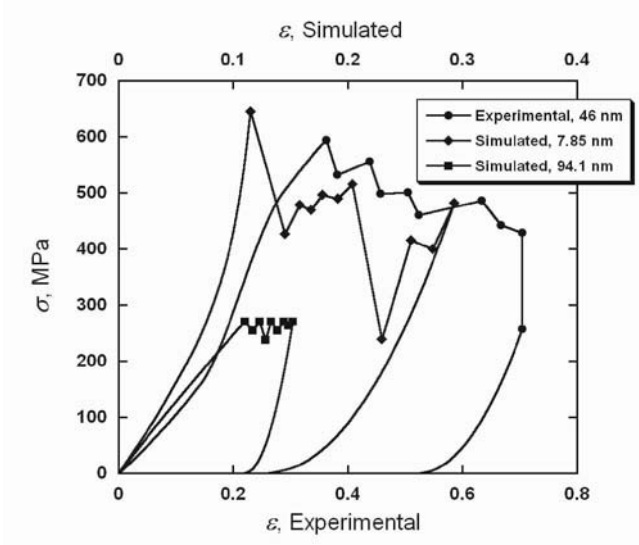

Figure 5. Stress–strain relationship generated from the load–displacement data of the displacement controlled experiment and simulation into Al.

For the relatively large strains shown in Fig. 5 we consider that forest dislocation hardening is most likely for the freestanding nanostructure. This type of flow stress behavior of the structure is compared to a length scale determined for the nanosphere given elsewhere [**5**] as

$$\ell_s = \left[\frac{8b}{3\delta}\right]^{1/2} r_o \tag{7}$$

where b is the Burgers vector, δ is the cumulative displacement and r_o is the sphere radius. From Eqn. 7 we obtaine a very small length scale of 3.94 nm representing a dislocation density of 6.4×10^{16} m^{-2}. This length scale seemed too small probably due to the assumption that the average loop radius was the particle radius divided by four. Applying this to Taylor hardening and using the observed flow stress of 600 MPa allows one to back out the Taylor coefficient, α_T, from

$$\sigma_{\text{flow}} = 2\alpha_{\text{T}}\mu b\sqrt{\rho} \tag{8}$$

with the dislocation density of $\rho = 6.4\text{x}10^{16}$ m^{-2}, the shear modulus of $\mu_{\text{Al}} =$ 26.3 GPa and a Burgers vector of $b_{\text{Al}} = 0.286$ nm. The observed 600 MPa flow stress would require $\alpha_{\text{T}} = 0.158$ which is on the low side of the expectation.

A more realistic approach for these heavily deformed nanostructures is to assume that their original volume of $3.61\text{x}10^{-22}$ m^3 remains constant and that the dislocations created to first order do not annihilate. If the further assumption is that the average distance between dislocations is the average loop radius, $r_\ell = \ell$, then the two common definitions of dislocation density lead to a more appropriate length scale. The first definition of line length per unit volume is represented by the number of dislocations (δ_{cum}/b) times the average length ($2\pi r_\ell$) per unit volume or

$$\rho = \frac{2\pi r_\ell \delta_{\text{cum}}}{bV_{\text{o}}}. \tag{9}$$

Meanwhile the second dislocation density definition is

$$\rho = \frac{1}{\ell^2} = \frac{1}{r_\ell^2}. \tag{10}$$

Eliminating ρ results in

$$r_\ell^3 = \frac{V_{\text{o}} b}{2\pi\delta_{\text{cum}}}. \tag{11}$$

For the above volume and Burgers vector with a cumulative displacement of 30 nm, Eqn. 11 results in a loop radius of 8.3 nm and a dislocation density of $1.45\text{x}10^{16}$ m^{-2}. This seems more realistic and coupled with the Taylor hardening of Eqn. 8, gives a more realistic Taylor coefficient of $\alpha_{\text{T}} = 0.33$.

4. SUMMARY

We have seen that the earliest stages of dislocation nucleation of a relatively few dislocations can be modeled by bottom–up atomistic simulations and top–down discrete dislocation formulations based on continuum descriptions of dislocation and contact mechanic stress fields. At

larger deformation, although much more tenuous, there is promise that coupled atomistic discretized dislocation approaches will be able to produce the yield instabilities experienced by small volumes.

ACKNOWLEDGMENTS

The authors would like to thank Michael Lund and Chris Leighton for the aluminum deposition and the Hypersonic Plasma Particle Deposition (HPPD) group for Si and Ti nanoparticles. Additionally we would like to acknowledge discussions with Stan Veprek, Eric Stach, Alan Needleman and Sid Yip. Support from an NSF-IGERT through grant DGE-0114372, a NIRT through grant DMI0103169 and a current NSF grant CMS-0322436 are gratefully acknowledged.

REFERENCES

1. Fleck NA, Muller GM, Ashby MR, Hutchinson JW. “Strain gradient plasticity: theory and experiment”, *Acta Metall. Mater.*, **vol. 42 no. 2**, pp. 475-487, 1994.
2. Gao H, Huang K, Nix WD, Hutchinson JW. “Mechanism-based strain gradient plasticity. I. Theory “, *J. Mech. Phys. Solids*, **47. 6**, pp. 1239-1263, 1999.
3. Horstemeyer MF, Baskes MI. “Atomistic finite deformation simulations: a discussion on length scale effects in relation to mechanical stresses”, *ASME J. Engin. Mater. Technol.*, **121. 2**, pp. 114-119, 1999.
4. Gerberich WW, Tymiak NI, Grunlan JC, Horstemeyer MF, Baskes MI. “Interpretations of indentation size effects”, *J. Appl. Mech*., **v 69 n 4**, pp. 433-442, 2002.
5. Mook WM, Jungk JM, Cordill MJ, Moody NR, Sun Y, Xia Y, Gerberich WW. “Geometry and surface state effects on the mechanical response of Au nanostructures”, *Z. Metallkd*., **v 95 n 6**, pp. 416-424, 2004.
6. Jungk JM, Mook WM, Cordill MJ, Bahr DF, Hoehn J, Chambers M, Gerberich WW. *J. Mater. Research*, accepted, 2004.
7. Van Vliet KJ, Li J,Zhu T, Yip S, Suresh S. “Quantifying the early stages of plasticity through nanoscale experiments and simulations”, *Phys. Rev. B*, **v 67 n 10**, pp. 104105-1-15, 2003.
8. Gerberich WW, Cordill MJ, Mook WM, Moody NR, Perrey CR, Carter CB, Mukherjee R, Girshick SL. “A boundary constraint energy balance criterion for small volume deformation”, *Acta mater*., submitted, 2004.
9. Shu JY, Fleck NA. “The prediction of a size effect in micro-indentation”, *Int. J. Solids Struct*., **v 35 n 13**, pp. 1363-1383, 1998.
10. Kiely JD, Houston JE. “Nanomechanical properties of Au (111), (001), and (110) surfaces”, *Phys. Rev. B*, **v 57 n 19**, pp. 12588-12594, 1998.
11. Gerberich WW, Nelson JC, Lilleodden ET, Anderson P, Wyrobek JT. “Indentation induced dislocation nucleation: the initial yield point”, *Acta mater.*, **v 44 n 9**, pp. 3585-3598, 1996.
12. Rudd RE, Broughton JQ. “Concurrent coupling of length scales in solid state systems”, *Phys. Stat. Sol. B*, **v 217 n 1**, pp. 251-91, 2000.

13. Ortiz M, Cuitino AM, Knap J, Koslowski M. "Mixed atomistic-continuum models of material behavior: the art of transcending atomistics and informing continua", *MRS Bull*., **v 26 n 3**, pp. 216-221, 2001.
14. Miller RE, Shilkrot LE, Curtin WA. "A coupled atomistics and discrete dislocation plasticity simulation of nanoindentation into single crystal thin films", *Acta Mater*., **v 52 n 2**, pp. 271-284, 2004.
15. Rodriguez de la Fuente O, Zimmerman JA, Gonzalez MA, de la Figuera J, Hamilton JC, Pai WW, Rojo JM. "Dislocation emission around nanoindentations on a (001) fcc metal surface studied by scanning tunneling microscopy and atomistic simulations", *Phys. Rev. Lett*., **v 88 n 3**, pp. 036101/1-4, 2002.
16. Veprek S, Argon A. private communication, 2004.
17. Di Fonzo F, Gidwani A, Fan MH, Neumann D, Iordanoglou DI, Heberlein JVR, McMurry PH, Girshick SL, Tymiak N, Gerberich WW, Rao NP. "Focused nanoparticle-beam deposition of patterned microstructures", *Appl. Phys. Lett*., **v 77 n 6**, pp. 910-912, 2000.
18. Gerberich WW, Mook WM, Perrey CR, Carter CB, Baskes MI, Mukherjee R, Gidwani A, Heberlein J, McMurry PH, Girshick SL. "Superhard silicon nanospheres", *J. Mech. Phys. Solids*, v 51 n 6, pp. 979-992, 2003.
19. Gerberich WW, Mook WM, Cordill MJ, Carter CB, Perrey CR, Heberlein J, Girshick SL. "Reverse plasticity in single crystal nanospheres", *Intern. J. Plasticity*, accepted, 2004.
20. Rabier J, Cordier P, Demenet JL, Garem H. "Plastic deformation of Si at low temperature under high confining pressure", *Mater. Science and Engin. A*., **v 309–310**, pp. 74–77, 2001.
21. Minor AM, Lilleodden ET, Jin M, Stach EA, Chizan DC, Morris Jr. SW. *Philos. Mag. A*, submitted, 2004.
22. Willis JR, Bullough R, Stoneham AM. "The effect of dislocation loops on the lattice parameter determined by x-ray diffraction", *Phil. Mag. A*, **v 48**, pp. 95-107, 1983.
23. Johnson KL. Contact Mechanics, Cambridge University Press, Cambridge, MA, 1985.
24. Zhou SJ, Thomson R. "Shielding of cracks in a plastically polarizable material", *J. Mater. Res*., **v 6 n 8**, pp. 1763-1772, 1991.
25. Christopher D, Smith R, Richter A. "Atomistic modelling of nanoindentation in iron and silver", *Nanotechnology*, **v 12 n 3**, pp. 372-383, 2001.
26. Ackland GJ, Tichy G, Vitek V, Finnis MF. "Simple N-body potentials for the noble metals and nickel", *Phil. Mag. A*, **v 56 n 6**, pp. 735-756, 1987.
27. Daw MS, Baskes MI. "Embedded-atom method: derivation and application to impurities, surfaces, and other defects in metals", *Phys. Rev. B*, **v 29 n 12**, pp. 6443-6453, 1984.
28. Gerberich WW, Jungk JM, Li M, Volinsky AA, Hoehn JW, Yoder K. "Length scales for the fracture of nanostructures", *Int. J. of Fracture*, **v 119/120**, pp. 387-405, 2003.

ROUGH SURFACE PLASTICITY AND ADHESION ACROSS LENGTH SCALES

Yan-Fei Gao and Allan F. Bower
Divsison of Engineering, Brown University, Providence, RI 02912, USA, Tel: +1-401-863-2864; Fax: +1-401-863-9009; Email: Yanfei_Gao@brown.edu

Abstract: The study of interacting rough surfaces, especially at mesoscale and nanoscale, has been playing a central role in a broad spectrum of novel applications, e.g. nanostructure fabrication and reliability. The multiscale nature of surface roughness, the structure- and size-sensitive material deformation behavior, and the importance of surface forces and other physical interactions give rise to very complex surface phenomena at mesoscale and nanoscale. In this work, we present a contact mechanics model based on the power spectral density function of the surface roughness. This is more relevant to large-scale rough surface contact with the use of classic plasticity theory. If using phenomenological strain-gradient plasticity theory, we can show that one can only flatten asperities in a certain frequency interval of the roughness spectrum. We also present a new scheme of modeling rough surface adhesion by using the Dugdale model and the self-affine fractal surface, which leads to a discussion of gecko adhesion. We also present some of our perspectives about the interaction between adhesion and micro-plasticity for, e.g., nano-imprinting and nano-welding applications.

Key words: Multiscale roughness, roughness evolution, size-dependent plasticity, rough surface adhesion, micromechanics of surface plasticity.

1. INTRODUCTION

Solid-solid interactions of rough surfaces, especially at mesoscale and nanoscale, govern many important mechanical and physical properties for a number of novel applications, including nanostructure fabrication and reliability (e.g. nano-imprinting, nano-welding, chemical mechanical planarization, MEMS stiction), soft material adhesion, nanostructured

T. J. Chuang et al. (eds.), Nanomechanics of Materials and Structures, 277–287.
© 2006 *Springer. Printed in the Netherlands.*

coating design, friction and wear, among many others [**1-2**]. The classic work of rough surface contact is the Greenwood-Williamson (GW) model [**3**], which models the surface roughness as a collection of uniform asperities with a Gaussian height variation and gives a statistical way to deduce multi-asperity contact from single-asperity contact. Certainly this model has its advantages in the study of many engineering surfaces, but not appropriate for the small scale rough surface mechanics for the following three reasons.

(1) Surface roughness typically has a multiscale nature, i.e. the existence of roughness details at many length scales [**4-5**]. Statistical parameters defined in the GW model depend on the measurement window size and instrument resolution, so that cannot describe surface roughness uniquely. It should also be noted that the fractal description is only one example of multiscale roughness.

(2) Deformation mechanisms at small scale are very complicated. There have been a lot of experimental evidences that plastic deformation is size-dependent [**6**]. In addition, rough surfaces could also be sources and sinks of dislocations, leading to so-called surface plasticity. We can use phenomenological strain-gradient plasticity theories based on Taylor hardening rule at microscale [**6-7**], or study the cooperative behaviors of defects and the interaction with rough surfaces at nanoscale [**8-9**].

(3) Surface forces and adhesion play an important role for small scale structural integrity [**10**], for example, in MEMS stiction problem. It's more interesting to study the coupling behavior between adhesion and surface plasticity. Physical forces from less familiar origins (e.g. surface stress) may also be pronounced when the feature size is reduced.

The above three aspects and their interactions contribute to the complex surface phenomena at mesoscale and nanoscale. The theme objective of this paper is to examine scaling relations and scale effects for multiscale modeling of rough surface plasticity and adhesion. Future emphasis will be placed on how to link atomic and mesoscale contacts.

2. LARGE-SCALE ROUGH SURFACE CONTACT

The GW model describes a rough surface by the rms height σ, rms slope σ' and rms curvature σ'' [**3,11-12**]. Unfortunately, because of the fractal nature of surface roughness, those statistical parameters depend on the measurement window size and instrument resolution. As a consequence, we shall characterize the surface roughness by the power spectral density function (PSDF), which is the Fourier transform of the autocorrelation function [**4-5,11**]. Figure 1 shows a typical rough surface topography and the corresponding PSDF. For an ideally self-affine fractal surface, the PSDF is a

straight line with respect to ω, and the slope tells the fractal dimension. In reality, there is a low-frequency cutoff due to component size, surface inhomogeniety or grain size. The high-frequency cutoff is usually due to the measurement resolution, though the ideal fractal roughness is not expected to extend to nanoscale. It should be noted that our following contact analysis is not restricted to fractal description of surface roughness.

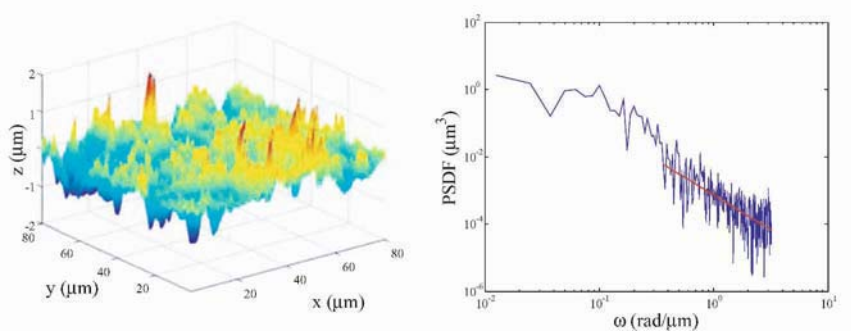

Figure 1. (a) AFM topography of single crystal Cu. (b) Fractal properties can be deduced from the power spectral density function, using the line information at y~20μm in (a). The straight line is by least squares fitting, giving rise to fractal dimension D~1.5.

The self-affine fractal rough surface can be idealized by using a Weierstrass function of the form

$$z(x) = A_0 \sum_{n=0}^{\infty} \gamma^{(D-2)n} \cos\left(2\pi\gamma^n x/\lambda_0\right) \tag{1}$$

where A_0 and λ_0 are amplitude and wavelength of the zero-th scale, and γ, D ($1<D<2$) are scale-independent, dimensionless parameters that characterize the fractal properties. We can approximate the PSDF of Eqn. 1 by a continuous one, which is proportional to ω^{2D-5} [**4**].

Rough surface contact analyses can be categorized into three types. (1) The GW model is based on the height distribution of isolated asperities. Although it gives a neat statistical means of deducing multi-asperity contact from single-asperity contact, the roughness description is not appropriate, as discussed in previous section. We have to introduce an artificial cutoff high-frequency in order to obtain meaningful statistical parameters for the GW model. (2) Direct numerical simulations are usually difficult to cover the whole spectrum of asperities, because asperity feature sizes range over many length scales and much smaller than the component size. Some hybrid schemes inherit drawbacks of GW-type statistical models. The calculation is usually limited by the cutoff size of mesh and asperity measurement

resolution. While refining the mesh size and measurement resolution, we would observe endless contact details. However, a microstructurally relevant length-scale might give a meaningful cutoff if we are concerned with certain failure analysis. (3) Many fractal-based contact models [**4,13**], out of thin air, give the contact size distribution directly from the "bearing-area" relation, and sum up all possible isolated asperity contacts. Actually, the true contact size distribution by our following contact analysis is radically different.

The contact mechanics based on self-affine fractal roughness, however, remains a challenge [**14-17**]. We recently establish an elastic-plastic contact analysis based on Archard's method and Weierstrass series [**17**]. Refer to Fig. 1 again. Idealizing a self-affine fractal rough surface by the Weierstrass function, we bridge two successive scales in the roughness spectrum by the assumption that the nominal pressure at the fine scale is equal to the true pressure at the coarse scale. Of course, this is justified if asperities at successive scales have large difference in contact compliance (usually true if successive wavelengths are far apart). If two successive scales are quite close, clearly we cannot decouple the roughness scales, and the contribution to the contact compliance from the fine scales must be included.

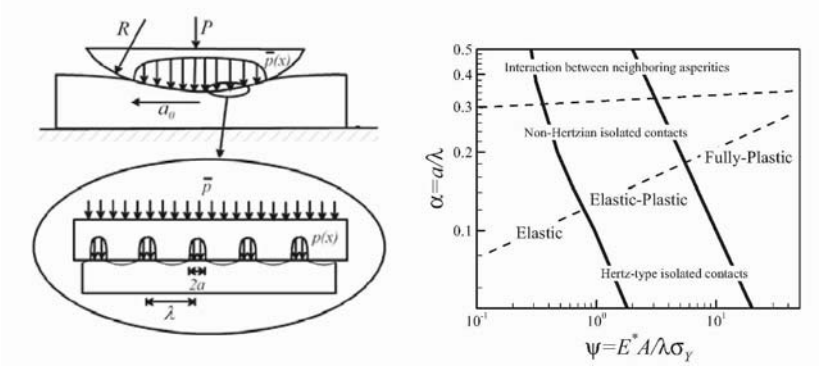

Figure 2. (a) Schematic of rough surface contact in Archard's manner. (b) Indentation map illustrating the deformation characteristics of sinusoidal surface.

As shown by the schematic in Fig. 2(a), we can compute the contact properties of the scale n from the scale $n-1$. Fig. 2(b) gives the indentation map of sinusoidal contact, which can be characterized by two parameters: $\alpha = a/\lambda$ and $\psi = E^* A/\lambda\sigma_Y$, where a is the contact half-width, A is the amplitude and λ is the period of the sinusoidal surface, E^* is the effective modulus and σ_Y is the yield stress of the elastic-perfectly plastic solid. Most importantly, when $2\alpha \to 1$, we have significant interaction between neighboring asperities. For a sufficiently large ψ, as the contact fraction

increases, the contact pressure first reaches the material hardness $H \sim 3\sigma_Y$, and then rises up to a value $H^* \sim 6\sigma_Y$. It should also be noted that this transitional behavior is weakly dependent on the asperity shape as long as it is wedge-like.

For elastic multiscale contact, the analysis is rather complicated. *Assuming the asperity pressure distribution be uniform*, we can easily derive the scaling relations for the contact fraction and the contact pressure when the roughness scale is sufficiently large. The asymptotic solution for the contact fraction is $2\alpha_{n\to\infty} = \gamma^{1-D}$, and the total contact area is

$$L_n / \lambda_0 \approx 0.4\gamma^{-(D-1)(n-1)}\tilde{p} \tag{2}$$

with $\tilde{p} = F/\pi E^* A_0$. The contact is supported by infinite number of zero-size contact spots, each of which has infinite contact pressure. Such an understanding is also evident by the FEM calculation. If we refine mesh size and include more asperities at smaller scales, the pressure distribution will evolve from rather smooth to quite spike-like [**17-18**]. Of course, fine scale contact cannot be elastic. Plasticity or others may change this conclusion.

The critical wavelength of plastic-yield can be easily computed, using $2\alpha_{n\to\infty} = \gamma^{1-D}$. The calculation gives $\lambda_{cr} \approx \lambda_0 \psi_0^{1/(D-1)}$. The plastic deformation therefore is confined to a thin layer near the surface, with the width comparable to λ_{cr}. The above result is only valid when ψ_0 is small. Our latest work [**17**] gives a complete analysis.

Now consider rigid-plastic contact of self-affine fractal surface (i.e., very large ψ). If the contact pressure is limited by material hardness, with a given load F, the total contact area is $L_n \equiv F/H$. Because of the pressure rise-up feature in Fig. 2(b), and the fact that nominal pressure at fine scale is limited by true pressure at coarse scale, the fine-scale contact can never reache complete contact, namely, asperity persistence at every roughness scale. The contact area as $n \to \infty$ is $L_{n\to\infty} = F/H^*$.

An important conclusion from the above analysis is that a perfectly fractal description of surface roughness ($1 < D < 2$) appears to lead to unphysical predictions of the true contact size and number of contact spots, for both elastic and elastic-plastic solids. It is anticipated that either non-fractal roughness (but possibly multiscale), or micro-plasticity, or adhesion might resolve this open question.

3. ROUGHNESS EVOLUTION AND MICROMECHANICS OF SURFACE PLASTICITY

Experimentally, we can measure the change of PSDF before and after contact loading, a potential link between contact analysis of surface failure mechanisms. Load-displacement curves, e.g. [**19**], wouldn't contain enough information about surface deformation. Because of self-affine fractal roughness, smaller asperities are rougher and large frequencies deform mainly plastically. The critical wavelength of elastic-plastic transition approximately happens at $\lambda_0 \psi_0^{1/(D-1)}$, also drawn schematically in Fig. 3(a).

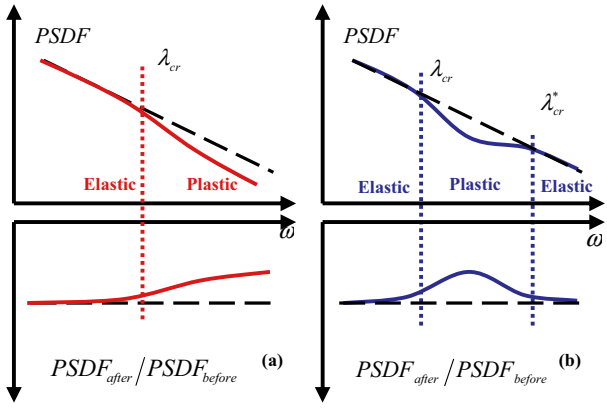

Figure 3. Schematics of the evolution of power spectral density function.

We also conjecture that at very high frequency, plastic deformation is difficult to realize because of small size. Thus there would be another critical scale beyond which asperities deform elastically, and only an intermediate range of frequencies can be plastically crushed and likely smoothened. This can be proved by using the phenomenological strain-gradient plasticity theory by Nix and Gao [**6**], which is a statistical description of dislocation interaction based on Taylor hardening rule. The material hardness H is given by $H/H_0 = \sqrt{1+\hat{l}\chi}$, where H_0 can be explained as bulk hardness, $\hat{l}$ is a material length scale, and χ is the strain gradient. Approximately $\chi \sim$ asperity slope/contact size. The Weierstrass surface roughness in Eqn. 1 tells us that asperity slope increases rapidly with respect to roughness scale n. Our calculations shows that the plastic-elastic transition occurs at the critical wavelength $\lambda^*_{cr} \approx \lambda_0 \left(A_0/\hat{l}\right)^{-1/(1-D/2)}$, as shown in Fig. 3(b).

However, we should be very careful about this result, because the Nix-Gao theory is based on bulk defects. The size effects of nanoindentation also depend on surface roughness. Even though roughness is confined into a very thin layer, the resulted plastic deformation can extend to a very far depth.

We need to clarify the contribution to the size effects from bulk contact and surface roughness. The usefulness of strain gradient plasticity may be very limited. It's more reasonable to carry out a micromechanics analysis of defects. We need to consider the plastic deformation due to the novel surface property and surface geometry, and the interaction with surface and bulk defect structures. This can be denoted as micromechanics of surface plasticity.

The work in [**9**] considers the indentation of a stepped surface. The surface ledge can be regarded as an existing pileup dislocation. Dislocations can emit from this ledge and may or may not pile up underneath. Because of adhesion and long-range dislocation interaction, we also need to model the lateral interaction between neighboring ledges. It is anticipated that dislocation mechanics study can bridge the scale gap between AFM-based nanotribology and mesoscale phenomena such as nano-imprinting.

4. EFFECTS OF ROUGHNESS ON ADHESION

When studying the effect of roughness on adhesion, we need to proceed from the finest scale, in contrast to the top-down manner in the rough surface contact analysis. Consider the schematic in Fig. 4, in which the two-scale rough surface obeys Eqn. 1. Assume asperity contact at scale 1 is JKR-like [**10,20-22**], i.e. $\delta_1 \to 0$ while w_1 remains finite. For isolated, spherical asperity contact, the pull-off force is $F_c \sim w_1 R_1$ with corresponding separation $\delta_c \sim \left(w_1^2 R_1 / E^{*2}\right)^{1/3}$. The equivalent cohesive zone in Figure 4(b), with strength σ_0 and characteristic bridging-length δ_0, has the following properties: $\sigma_0 \sim F_c / \lambda_1^2$ and $\delta_0 \sim \delta_c$, where $1/\lambda_1^2$ is the asperity density at scale 1. Consequently, the apparent work of adhesion at scale 0 is

$$w_0 = \sigma_0 \delta_0 \sim \frac{w_1 R_1}{\lambda_1^2}\left[\frac{w_1^2 R_1}{E^{*2}}\right]^{1/3} \sim w_1\left[\frac{w_1 \lambda_1}{E^* A_1^2}\right]^{2/3}, \text{ or } \frac{w_0}{w_1} \sim \frac{1}{\alpha_1^2} \tag{4}$$

where $\alpha_1 = \left(E^* A_1^2 / w_1 \lambda_1\right)^{1/3}$ determines whether the contact at fine scale 1 is adhesive or elastic. Thus the apparent work of adhesion at coarse scale depends on the contact characteristics of the fine scale. If fine scale contact is adhesive, $\alpha_1 << 1$, then $w_0 / w_1 > 1$. If fine scale contact is elastic, $\alpha_1 >> 1$, then $w_0 / w_1 < 1$.

The above simple analysis [**23**] shows the importance of morphology on adhesion. It should be noted that the adhesion strength depends on the apparent work of adhesion as well as the contact area, which is determined

by the contact analysis from the long wavelength. Thus, whether a rough surface is "adhesive" depends on the morphology and the loading history.

In addition, adhesive contact of isolated asperity is not appropriate for a self-affine fractal rough surface. For non-isolated contact, consider a sinusoidal surface with amplitude A and period λ. Define two dimensionless parameters $\alpha = \left(E^* A^2 / w\lambda\right)^{1/3}$ and $\beta = \sigma_0 \left(\lambda^2 / wE^{*2} A\right)^{1/3}$. Small α gives rise to adhesive contact, and large α elastic contact. Small β gives rise to large scale bridging (LSB), and *cohesive zone may spread to the whole period.* Large β gives small scale bridging (SSB). With varying α and β, we can have a variety of contact behaviors. We may have a critical roughness scale beyond which the roughness does not contribute to the adhesion.

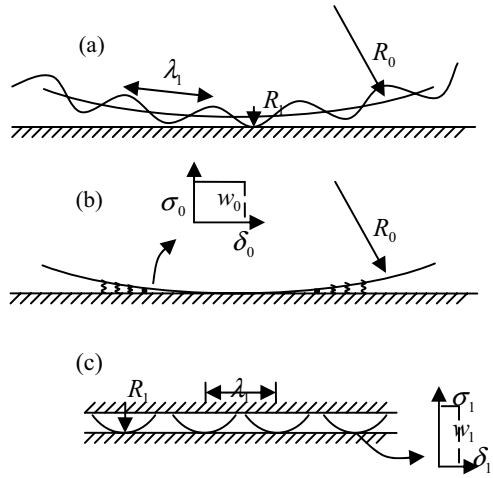

Figure 4. (a) A two-scale adhesive contact with superposition of spheres. Cohesive zone properties in coarse-scale contact in (b) are deduced from fine-scale contact in (c).

By the GW model, roughness only attenuates the adhesion. With the consideration of self-affine fractal roughness and non-isolated adhesive contact, we can get the opposite conclusion under certain conditions. Strong adhesion can be attained by obtaining a large true contact area (since roughness can also increase the contact compliance), and keeping the large-scale-bridging feature (to increase the fracture strength), at every roughness scale. For gecko adhesion, those are attained by the hierarchical structure of gecko foot, which can also accommodate a wide range of roughness

frequencies. From the computational point of view, we can simulate the adhesion of rough surfaces by using either cohesive zone model [**24**] or molecular simulation [**25-26**], and interpret the results as in Fig. 4.

5. COUPLING OF ADHESION AND PLASTICITY

For MEMS stiction and many new nanofabrication methods [**27**], the strong adhesion between rough surfaces is critically affected by the surface plasticity. The plastic deformation during asperity separation can dramatically increase the apparent work of adhesion. A fundamental understanding of coupling adhesion and surface plasticity is eagerly needed.

Johnson's approximate analysis [**10**] shows that small contact size and low hardness promotes the ductile separation, which therefore is often observed in nanoscale molecular simulations and large-scale contact of extremely soft metal (indium, for example). However, the contact behavior at mesoscale is still poorly understood. Though plastic deformation can increase the work of adhesion, surface roughness can do the opposite. Also the size-dependent surface plasticity is less studied along this line.

Rough surface plasticity and adhesion at the mesoscale would be the link between atomic and macroscopic contacts. It is anticipated that mesoscale adhesive contact could be promoted or weakened, depending on the coupling between adhesion and micromechanics of surface plasticity. Therefore, we have a large degree of freedom to either bond, imprint and/or peel two rough surfaces at nano- and meso-scale.

6. SUMMARY

In this work, we first present a contact mechanics model based on the power spectral density function of the surface roughness, and give the elastic-plastic contact analysis. Size-dependent plasticity shows that one can only flatten asperities in a certain frequency interval of the roughness spectrum. But the most important topic is micro-mechanics of surface plasticity, which studies the dislocation nucleation and interaction with the rough surface. We also present a new scheme of modeling rough surface adhesion by using the Dugdale model and self-affine fractal surface, which leads to a morphology- and history-dependent cohesive zone law.

ACKNOWLEDGMENTS

This work is supported by the Brown/General Motors Collaborative Research Lab at Brown University. We are very grateful to discussions with Prof. K.-S. Kim (Brown) and Drs. Y.-T. Cheng, L. Lev and Y. Qi (GM).

REFERENCES

1. Singer IL, Pollock HM. *Fundamentals of friction: macroscopic and microscopic processes*, Kluwer Academic, Boston, 1992.
2. Bhushan B. *Handbook of micro/nanotribology*, CRC Press, 1999.
3. Greenwood JA, Williamson JBP. "Contact of nominally flat surfaces", *Proc. R. Soc. Lond. A,* **vol. 295**, pp. 300-319, 1966.
4. Majumdar A, Bhushan B. "Fractal model of elastic-plastic contact between rough surfaces", *ASME J. Tribol,.* **vol. 113**, pp. 1-11, 1991.
5. Greenwood JA, Wu JJ. "Surface roughness and contact: an apology", *Meccanica,* **vol. 36**, pp. 617-630, 2001.
6. Nix WD, Gao H. "Indentation size effects in crystalline materials: a law for strain gradient plasticity", *J. Mech. Phys. Solids,* **vol. 46**, pp. 411-425, 1998.
7. Bhushan B, Nosonosky M. "Scale effects in friction using strain gradient plasticity and dislocation-assisted sliding (microslip)", *Acta Mater.*, **vol. 51**, pp. 4331-4345, 2003.
8. Hurtado JA, Kim K-S. "Scale effects in friction of single-asperity contacts. I. From concurrent slip to single-dislocation-assisted slip", *Proc. R. Soc. Lond. A*, **vol. 455**, pp. 3363-3384, 1999. "II. Multiple-dislocation-cooperated slip", *ibid*, pp. 3385-3400.
9. Yu HH, Shrotriya P, Wang J, Kim K-S. 2004, "Dislocation nucleation and segregation in nano-scale contact of stepped surfaces", *Mat. Res. Soc. Symp. Proc.*, **vol. 795**, 7.9, 2004.
10. Johnson KL. "Mechanics of adhesion", *Tribo. Int.,* **vol. 31**, pp. 413-418, 1998.
11. Greenwood JA. "A unified theory of surface roughness", *Proc. Roy. Sco. Lond. A*, **vol.** 393, pp. 133-157, 1984.
12. McCool JI. "Comparison of models for the contact of rough surface", *Wear*, **vol.** 107, pp. 37-60, 1986.
13. Yan W, Komvopoulos K. "Contact analysis of elastic-plastic fractal surfaces", *J. Appl. Phys.*, **vol. 84**, pp. 3617-3624, 1998.
14. Archard JF. "Elastic deformation and the laws of friction", *Proc. R. Soc. Lond. A*, **vol. 243**, pp. 190-205, 1957.
15. Ciavarella M, Demelio G, Barber JR, Jang YH. "Linear elastic contact of the Weierstrass profile", *Proc. R. Soc. Lond. A*, **vol. 456**, pp. 387-405, 2000.
16. Persson BNJ. "Elastoplastic contact between randomly rough surfaces", *Phys. Rev. Lett.*, **vol. 87**, art no. 116101, 2001.
17. Gao YF, Bower AF. Submitted for publication, 2004.
18. Borri-Brunetto M, Carpinteri A, Chiaia B. "Scaling phenomena due to fractal contact in concrete and rock fractures", *Int. J. Fract.*, **vol. 95**, pp. 221-238, 1999.
19. Buzio R, Boragno C, Biscarini F, de Mongeot FB, Valbusa U. "The contact mechanics of fractal surfaces", *Nature Mater.*, **vol. 2**, pp. 233-236, 2003.
20. Johnson KL, Kendall K, Roberts AD. "Surface energy and the contact of elastic solids", *Proc. R. Soc. Lond. A*, **vol. 324**, pp. 301-313, 1971.

21. Derjaguin BV, Muller VM, Toporov YP. "Effect of contact deformations on the adhesion of particles", *J. Coll. Interface Sci.*, **vol. 53**, pp. 314-326, 1975.
22. Maugis D. "Adhesion of spheres: the JKR-DMT transition using a Dugdale model", *J. Coll. Interface Sci.*, **vol. 150**, pp. 243-269, 1992.
23. Gao YF, Bower AF. Unpublished work, 2004.
24. Gao YF, Bower AF. "A simple technique for avoiding convergence problems in finite element simulations of crack nucleation and growth on cohesive interfaces", *Modelling Simul. Mater. Sci. Eng.*, **vol. 12**, pp. 453-463, 2004.
25. Qi Y, Cheng Y-T, Cagin T, Goddard III WA. "Friction anisotropy at Ni(100)/(100) interfaces: molecular dynamics studies", *Phys. Rev. B*, **vol. 66**, art no. 085420, 2002.
26. Cha P-R, Srolovitz DJ, Vanderlick TK. "Molecular dynamics simulation of single asperity contact", *Acta Mater.*, **vol. 52**, pp. 3983-3996, 2004.
27. Forrest SR. "The path to ubiquitous and low-cost organic electronic appliances on plastic", *Nature*, **vol. 428**, pp. 911-918, 2004.

MODELING THE EFFECT OF TEXTURE ON THE DEFORMATION MECHANISMS OF NANOCRYSTALLINE MATERIALS AT THE ATOMISTIC SCALE

M.-J. Caturla*, T. G. Nieh**

* Departament de Fisica Aplicada, Facultat de Ciencies. Fase II, Universitat d'Alacant, E-03690 Alacant, Spain

*** Department of Metrials Science and Engineering, The University of Tennessee, 422 Dougherty Engineering Building, Knoxville, TN 37996-2200*

Abstract: Molecular dynamics simulations show significant differences in the deformation behavior of nanocrystalline nickel with low and high angle grain boundaries. At a grain size of 12nm, low angle boundary sample show enhanced dislocation activity and reduced strength with respect to high angle boundary sample. However, at a smaller grain size of 4nm, low angle boundary sample shows a higher strength, revealing a change in deformation behavior. At this grain size, regardless the type of grain boundary, no dislocation activity negligible.

Key words: texture, nanocrystalline materials, molecular simulation, grain boundary, yield strength.

1. INTRODUCTION

At small grain sizes (a few tens of nanometers), the classical Hall-Petch relationship breaks down [**1**]. Grain boundary processes such as grain boundary sliding or diffusional creep are some of the mechanisms that could control deformation at these small grain sizes. Molecular dynamics simulations have shown that grain boundary sliding is the dominant process for sizes below 8 to 12nm, depending upon material [**2, 3**], and softening with decreasing grain size occurs at these sizes. However, synthesizing bulk materials with nanometer scale grains and both high purity and high density is difficult. In fact, the experimentally observed effects as grain size

T. J. Chuang et al. (eds.), Nanomechanics of Materials and Structures, 289–297.
© 2006 *Springer. Printed in the Netherlands.*

approaches about 20nm or less have been in many cases associated with flaws in the samples and not due to a simple reduction in grain size [**4**].

Nanocrystalline materials produced by electrodeposition can result in high-density materials and eliminate some of the microstructural uncertainties. Recent experiments with electrodeposited nanocrystalline (nc) Ni have shown an increase in hardening as grain size decreases down to 14 nm grains, but a softening between 14 and 12nm [**5**]. Experiments by Lu et al [**6**] on electrodeposited nanocrystalline copper samples have also shown that large elongations, up to 30% can be obtained. In contrast, other fabrication methods produce nanocrystals that fail at a negligible elongation [**7**]. One important characteristic of these electrodeposited samples is the abundance of low angle grain boundaries [**6, 8**]. The mechanical response of these samples is, therefore expected to be affected by the nature of their grain boundaries. However, due to the small scale, experimental characterization of the deformation mechanisms is extremely challenging.

Molecular dynamics simulations allow for an atomistic view of the processes occurring both within grains and at grain boundaries. However, most of the atomic-scale simulations of deformation of nanocrystalline materials have been conducted using high-angle grain boundaries, and only a limited number with low-angle grain boundaries. Creep simulations [**9**] indicate significant dislocation activity in sample with low-angle grain boundaries with partial dislocations observed in grains as small as 5nm.

In the present paper, the influence of texture on the macroscopic deformation of nanocrystalline materials is presented. Studies were conducted with nanocrystalline Ni with 4 and 12 nm grain sizes, containing either high or low angle boundaries. The methodology used in this study is explained in section II of this paper, followed by a description of the results and conclusions.

2. SIMULATION METHODOLOGY

Molecular dynamics simulations are used to study the atomistic processes occurring during the deformation of nanocrystalline materials. The average sizes of the nanocrystal grains in these models are between 4nm and 12nm, and a total of 20 grains are included in each simulation. A Voronoi construction is used to generate the initial configurations [**10**]. A model to build nanocrystalline samples with any given misorientation (disorientation) between the different grains is developed. This model is based on the quaternion formalism [**11**] taking into account the symmetry of the crystal to select a unique rotation among all equivalent ones [**12**]. Using this approach, grains with misorientation angles within some limits can be constructed, therefore going from low-angle to high-angle grain boundaries. For the case of low-angle grain boundaries misorientations between grains that are no larger than 17° are selected, while for high-angle grain boundaries no

restriction in the misorientation angle is imposed. The average number of neighbors for each grain or, equivalently, the average number of faces of each grain, is 13.7 for a configuration of 4 nm average grain size, close to the expected value of 13.5.

The interatomic potential used in these calculations is the one derived from a second moment tight-binding model [**13**]. Tensile tests are simulated using an approach similar to that described by Schiøtz et al [**3**]. In the present simulations, a uniaxial tension and a concurrent biaxial compression are applied, keeping the values of ε_0 and β constant, (10^{-6} and 0.4 respectively).

$$\varepsilon_{app} = \varepsilon_0 \left\{ \begin{pmatrix} 0 & 0 & 0 \\ 0 & 0 & 0 \\ 0 & 0 & 1 \end{pmatrix} + \beta \begin{pmatrix} -1 & 0 & 0 \\ 0 & -1 & 0 \\ 0 & 0 & 0 \end{pmatrix} \right\}$$

Before applying a deformation the nanocrystalline structure was equilibrated at 300K and fixed volume. To remove possible internal stresses due to the generation of the nanocrystals, the system is further relaxed using Parinello-Rahman [**14**] boundary conditions until zero pressure is recovered and volume is equilibrated.

3. RESULTS

Using the starting configurations described above the stress vs. strain response for the case of low angle and high angle misorientation between grains and two different average grain sizes (12nm and 4nm) were examined. As in any molecular dynamics simulation the strain rate applied is very high, in the present case, it is 5×10^8 s^{-1}. Nevertheless these simulations are able to extract information about the effect of grain boundary misorientation, provided all other parameters are kept fixed. All simulations are for 300K.

The stress vs. strain curve obtained from the MD simulations for the case of Ni with a 12 nm average grain size is shown in Fig. 1(a). The high-angle sample results in a Young's modulus in good agreement with experimental values for polycrystalline Ni (204 GPa from simulations vs. 207 GPa from experiments [**15**]). For low misorientation angle the Young's modulus is close to that for <100> orientation (112 GPa from simulations vs. 137 GPa measured along <100>) since the texture selected in this simulation is along <100>. Variations in crystallographic texture clearly affect the stress-strain response. To affirm the potential influence of texture on the simulation results, we applied Taylor and Sachs type analysis to provide a rough estimate of texture effect.

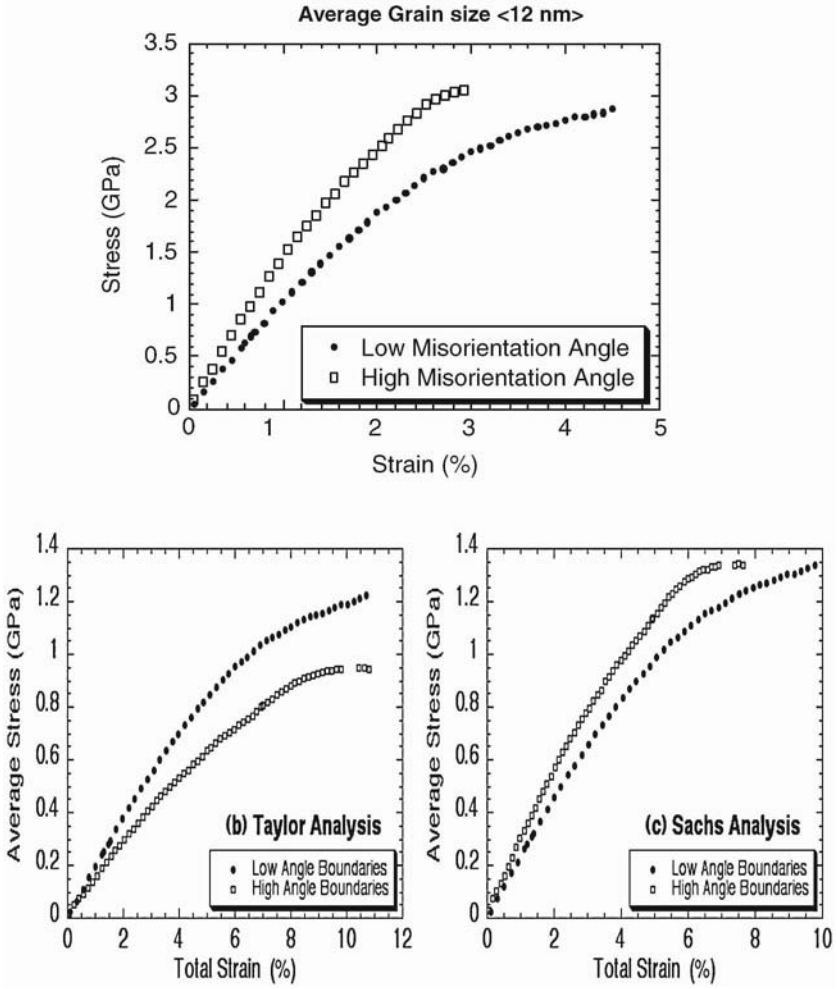

Figure 1. (a) Stress vs Strain curves for Ni with a 12nm average grain sizes and for low-angle and high-angle misorientations obtained from MD simulations and (b) Taylor analysis and (c) Sachs analysis.

effects. Although the Taylor analysis is a rigorous upper-bound, the Sachs model is only a true lower-bound for uniaxial tension with all grain boundaries parallel to the stress axis; however, for the present purpose, this model shall be sufficient. Application of the Taylor and Sachs analysis to the data results in an estimate for crystallographic shear stress-strain response at the slip system level via an effective "Taylor Factor". If the differences in the overall stress-strain response were entirely due to texture effects, then the two curves of crystallographic shear stress-strain response would superpose. As shown in Figures 1(b) and (c) for the Taylor and Sachs models

respectively they do not coincide. The Taylor analysis actually reverses the relative ordering of the stress response, indicating that this analysis overestimates the influence of texture. The Sachs analysis does bring the two curves closer together, however, it does not quite bring the stress-strain curve into coincidence. This type of result is typical in macroscopic plasticity, suggesting that a "relaxed constraints" model may be more appropriate; the exact number of slip systems active is between the one active slip-system assumed by the Sachs model and the five active slip-systems mandated by the Taylor Model. This is in fact consistent with the observations of the MD simulations.

To understand the atomistic processes that govern plasticity in these molecular dynamics simulations we study the micro-structural evolution as a function of strain. The common neighbor analysis method [**16**] is used to identify atoms belonging to grain boundaries, as well as atoms associated with partial dislocations and stacking faults. This method samples the local atomic environment of each atom. Three types of atoms are classified: fcc (not shown in the pictures), hcp (shown in gray) and not perfect fcc atoms (shown in black), as did in previous works [**2, 3, 17**]. Most of the atoms at grain boundaries are not in a perfect fcc environment, and are easily identified with this method. Stacking faults appear as parallel <111> hcp planes while twin boundaries are single <111> planes of hcp atoms. Figure 2 are snapshots for different values of strain for a sample with high angle and 12 nm average grain sizes. In the figures shown here we present cuts through the center of the sample 8 atomic layers thick. Nucleation of partial dislocations at triple junctions (gray) appears to occur even at the lowest strain presented here (2.0%), however, these partial dislocations do not travel across grains until much higher strains are achieved (~ 2.8%).

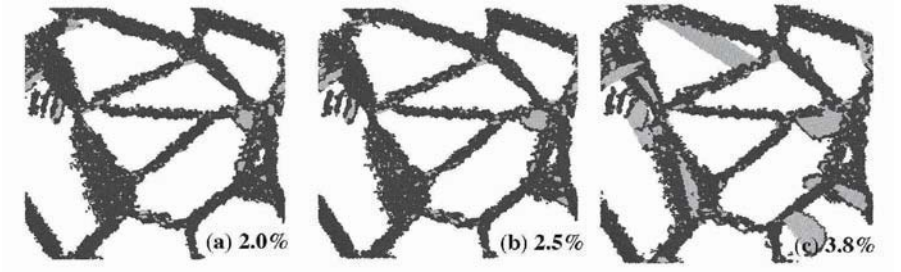

Figure 2. High-angle boundaries, 12nm grains, atoms that are not perfect fcc (black) and atoms that are hcp (gray). Cut through the center of the sample, for different strains (a) 2.0%, (b) 2.5 %, (c) 3.8 %. The 3-D cell is 32nm in side length.

For the case of low misorientation angle, the initial grain boundary structures show a large number of atoms in an hcp type of environment, as shown in Figure 3(a). Low angle grain boundaries are essentially formed by dislocations, therefore, the stacking faults between dislocations at these grain boundaries are identified by this analysis method. As the strain increases, partial dislocations begin to emit from grain boundaries, as in the case of

high misorientation angle. However, in the low angle boundary case, the number of partial dislocations emitted is greater. Figure 4 shows the number of hcp atoms as a function of strain (normalized to the initial number of hcp atoms). Notice that the number of hcp atoms is larger than in the case of high misorientation angle boundary. The number of hcp atoms increases exponentially with the applied strain. This exponential behavior indicates that the emission of partial dislocations is activated by the stress applied once it is sufficiently high.

The large number of partial dislocations emitted in the case of low angle grain boundaries is also revealed in Figure 3. For a 2.5% strain (Figure 3(b)) the number of partial dislocations crossing grains is much greater than in the case of the 2.5% strain shown in Figure 2(b) for high angle grain boundaries. As the strain increases (Figure 4(c), 3.8% strain) the transmission of partial dislocations across grain boundaries is observed in low angle grain boundaries, as well as the reflection of some of the partial dislocations at the grain boundaries. In the case of high angle grain boundaries partial dislocations travel across grains but do not cross grain boundaries, even at the highest strain level used in these simulations. This is attributable to the fact that low-angle boundaries are generally not effective barriers for dislocation motion. It is also interesting to point out that the amount of dislocation activity varies in each grain in a given sample, probably depends upon its specific orientation with respect to stress axis. Even in the case of low angle boundaries, there is a distinct grain where no dislocation activity is observed, as indicated in Figure 3(c)**.**

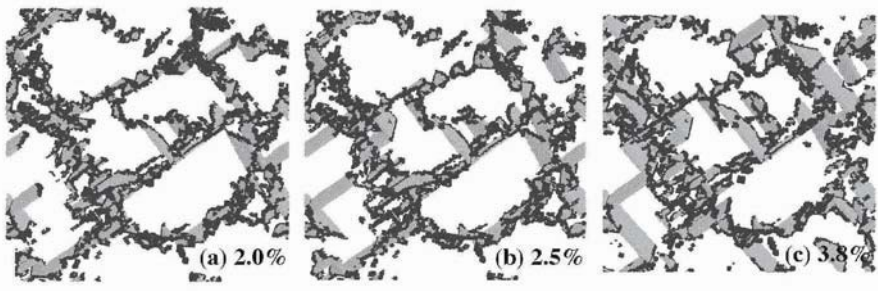

Figure 3. Low-angle boundaries, 12nm, atoms that are not perfect fcc (black) and atoms that are hcp (gray). Cut through the center of the sample, for different strains (a) 2.0 %, (b) 2.5 %, (c) 3.8%. In figure (c) the arrow points to a grain where very small dislocation activity occurs. The 3-D cell is 32nm in side length.

To understand the effect of grain size on the deformation behavior of these nanocrystalline materials, we have performed the same type of simulations for grains with average grain size of 4nm. In the case of these small grains (4nm) the Young's modulus is greatly reduced (137 GPa) for the case of high angle grain boundaries with respect to the values at 12nm grain size. No significant differences are observed for the case of low angle boundaries when reducing the grain size. The reduction in the Young's

modulus for random (high-angle) grain boundaries is in agreement with previous simulations [**2**] where a reduction of 25% was observed between 10 and 3.4 nm average grain sizes. This is a result of the fact that in the case of random grain boundaries a 4 nm grain size sample contains about 50% volume fraction of grain boundary region. The presence of a large volume fraction of grain boundary region in the high-angle boundary sample results in a lower yield strength as compared to the sample with low-angle grain boundaries, as shown in Fig. 5. The result of Fig. 5 is reproduced even when we have imposed a strain rate 10 times faster than the one used in Figure 5, suggesting the behavior is independent of strain rate.

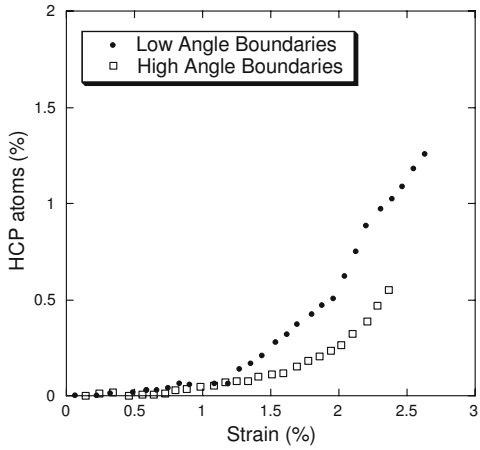

Figure 4. Number of hcp atoms for low and high angle boundaries as a function of strain for Ni with a 12nm grain sizes

From a plasticity point of view, at a small grain size of ~ 4nm plasticity must be accommodated by grain boundary sliding and grain rotations, as noted by previous MD simulations [**18**] since all dislocation activity is suppressed. Low-angle grain boundaries are believed to be more resistant to sliding than high angle grain boundaries, as revealed experimentally [**19**] and by simulations [**20**]. Previous MD simulations have demonstrated that sliding is proportional to grain boundary energy [**20**], with lower energy boundaries offering more resistance to sliding. This difference in grain boundary sliding may also explain the different behavior between high-angle and low-angle boundaries at this small scale.

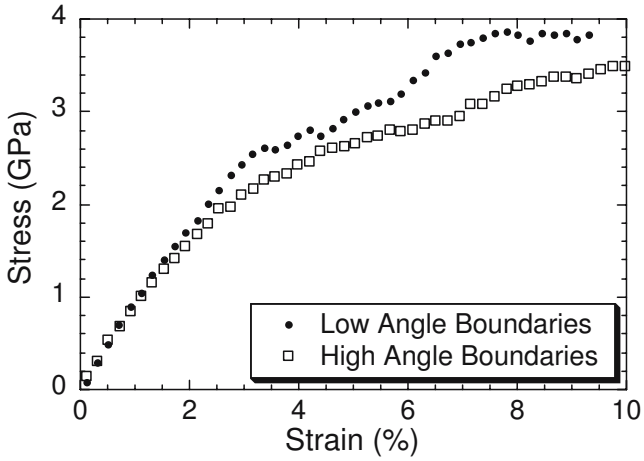

Figure 5: Stress vs. strain for Ni with a 4nm average grain size, and consists of either low or high misorientation angle boundaries.

4. CONCLUSION

The deformation behavior of nanocrystalline Ni is different, depending on the type of grain boundary. The present study reveals that for the average grain size of 12nm both low- and high-angle grain boundaries emit partial dislocations upon straining, however, dislocation activity is greater for the case of low-angle grain boundaries, and shows the transmission and reflection of dislocations across grains. For the case of small rotations of grains along <100> direction, higher yield strength is observed for high misorientation than that for low misorientation. For smaller grains (<4nm>), however, this situation is reversed, low-angle grain boundaries show higher yield strength than high-angle ones. Two factors could contribute to this behavioral difference: reduction in the Young's modulus caused by the presence of a large volume fraction of grain boundary region as the grain size decreases, and a higher sliding resistance for low-angle grain boundaries.

ACKNOWLEDGMENTS

This work was performed under the auspices of the Division of Materials Sciences and Engineering, Office of Basic Energy Sciences, US Department of Energy under contract DE-AC05-00OR-22725 with UT-Battelle. The authors want to thank Dr. J.S. Stolken for his Taylor and Sachs analyses. Special appreciation to H. Van Swygenhoven, P. Derlet and M. Bartelt for very useful discussions and help with the simulation set up.

REFERENCES

1. Nieh, T. G., Wadsworth, J., Scripta Met. et Mat. **25**, 955, 1991.
2. Van Swygenhoven H., Spaczer M., Caro A., Farkas D., Phys. Rev. B, **60**, 22, 1999.
3. Schiøtz J., Vegge T., Di Tolla F., Jacobsen K. W., Phys. Rev. B, **60**, 11971, 1999.
4. Koch, C. C. Narayan, J, Mater. Res. Soc., **634**, 306, 2001.
5. Schuh, C., Nieh T. G., Yamasaki, T., Scripta Mater., **46**, 735, 2002.
6. Lu L., Wang L. B., Ding B. Z., Lu K., J. Mater. Res., **15**, 270, 2000.
7. Koch C.C., Morris D. G., Lu K., Inoue A.,Mat. Res. Soc. Bulletin, **24**, 54, 1999.
8. L. Lu, M. L. Sui, K. Lu, Science, **287**, 1463, 2000
9. Van Swygenhoven H., Spaczer M., Farkas D., Caro A., Nanostructured Materials, **12**, 323 and 629, 1999.
10. Okabe A., Boots B., Sugihara K., Spatial Tesselations: Concepts and Applications of Voronoi Diagrams, Wiley, Chichester, 1992
11. Morawiec A., Pospiech J., *Textures and Micros*. **10**, 211, 1989.
12. Grimmer H.,Acta. Cryst. A, **30**, 685, 1974.
13. Cleri F., Rosato V., Phys. Rev. B, **48**, 22, 1993.
14. Parinello M., Rahman A., J. Appl.Phys., **52**, 7182, 1981.
15. Hirth,J.P.,Lothe,J., Theory of Dislocations Ed.J. Wiley & Sons, NY 1982
16. Jonsson H., Andersen H. C., Phys. Rev. Lett, **60**, 2295, 1988.
17. Yamakov V., Wolf D., Salazar M., Phillpot S. R., Gleiter H., Acta. Mater., **49**, 2713, 2001.
18. Van Swygenhoven H., Derlet P., Phys. Rev. B, **64**, 224105, 2001.
19. Wadsworth J. and Pelton A.R., Scripta Metall., **18**, 387, 1984.
20. Chandra N., Dang P., J. of Mat. Sci.,**34**, 65, 1999.

MODELING THE TRIBOCHEMICAL ASPECTS OF FRICTION AND GRADUAL WEAR OF DLC FILMS

Feodor M. Borodich, Chad S. Korach, and Leon M. Keer
School of Engineering, Cardiff University, P.O. Box 925, Queens Buildings, Cardiff CF24 3AT, UK; Department of Mechanical Engineering, Northwestern University, Evanston, IL 60208

Abstract: Problems in nanomechanics often need to combine mechanical approaches together with methods of physics and chemistry that are outside of the traditional mechanics scope. Recent experimental studies of dry sliding between two hydrogenated DLC (diamond-like carbon) coated counterparts in low oxygen environment showed that adsorbates have considerable influence on friction and the friction coefficient increases with the increasing of the time interval between contacts. The observed friction phenomena are assumed caused by a reaction between the adsorbate and carbon atoms of the coatings, and when the slider passes a point on the track, it removes mechanically some adsorbate from the surface. The mechanical action leads to re-exposure of the surface to gases in the environment. This paper focuses on physical and tribochemical processes that occur in sliding contact between the DLC coated slider and the counterpart. We develop further our recently presented model of the process and assume that there is a transient short-life high temperature field at the vicinities of contacting protuberances that may cause various transformations of the surface. The model helps to explain how microscopic processes, such as the breaking and forming of interatomic bonds, may affect macroscopic phenomena, such as friction and wear.

Key words: friction, wear, adsorption, oxidation, DLC films

T. J. Chuang et al. (eds.), Nanomechanics of Materials and Structures, 299–308.
© 2006 *Springer. Printed in the Netherlands.*

1. INTRODUCTION

This paper deals with the modeling of dry sliding between two DLC (diamond-like carbon) coated counterparts in a low oxygen environment. It is known that understanding the physical and tribochemical processes that occur in a sliding contact is a question of particular interest for tribology [**1**]. The applicability of the Elovich (Roginsky-Zeldovich)[**2**] equation for modeling the gas adsorption process when environmental molecules form bonds to the surface, and the modeling of friction and gradual wear when some part of the adsorbate is removed due to rubbing the surface by a slider are examined.

1.1 Amorphous carbon films

Amorphous carbon (*a*-C) films are widely used as protective overcoats in various industries. Because *a*-C has no exact geometric configuration, the following characteristics of *a*-C samples are commonly used: (i) the density of a sample; (ii) the sp^3/sp^2 ratio; and (iii) the hydrogen concentration. Amorphous hydrogenated carbon coatings are denoted as *a*-C:H. If the density and sp^3/sp^2 ratio are high, and the hydrogen concentration is low (up to 30%) then *a*-C:H coatings are called hydrogenated diamond-like carbon (DLC:H) coatings. Friction coefficients for various DLC films span a range from 0.001 to more than 0.6 [**2**].

1.2 Friction forces

Friction occurs when two bodies rub each other and such studies can be traced back to Leonardo da Vinci. Theoretical studies of the molecular friction began with G.A. Tomlinson [**3**], whose model involves a lattice oscillation mechanism. Currently, it is common to present the total friction force (F_f) as the sum of mechanical $(F_{f,mech})$ and molecular friction $(F_{f,mol})$ (see e.g. [**4**])

$$F_f = F_{f,mech} + F_{f,mol} \tag{1}$$

Thus, there are various explanations of the friction phenomenon; in particular, molecular adhesion of contacting protuberances and other mechanisms. When two bodies are in sliding contact, various

mechanical, physical, chemical and physio-chemical processes can take place at the interface [**1, 2, 5-8**]. Following Derjaguin's idea of generalization of the Coulomb law, the measured friction coefficient may be represented as

$$\mu = \mu_{mech} + \mu_{mol,1} + \mu_{mol,2} \tag{2}$$

where $\mu_{mol,1}$ is the part of the friction coefficient caused by the breaking of interatomic bonds between the adsorbate and a surface, $\mu_{mol,2}$ is the part caused by all other molecular effects, in particular by the lattice oscillation mechanism, and μ_{mech} is the part caused by mechanical effects. In this paper we concentrate on modeling that part of the friction coefficient caused by breaking of interatomic bonds between the adsorbate and a surface, $\mu_{mol,1}$.

1.3 Environmental effects on the friction of DLC:H films

Dry sliding interaction between a slider and a coated surface leads to various chemical and physical transformations in DLC coatings. It is known that surfaces exposed to ambient air possess adsorbed layers of hydrocarbons and other small molecules or atoms [**9**]. The substance that adsorbs and desorbs is referred to as the adsorbate and the substance to which the adsorbate adsorbs is called the substrate. It was established that the friction and wear properties of carbon based coatings are dependent on the atmospheric conditions, the structure of the films, and surface chemistry [**2, 10-14**].

Our studies are mainly concentrated on the friction of hydrogenated DLC films, and our models will be compared with some recent experimental results obtained by Heimberg et al. [**13**] that studied the friction of DLC:H films. A simplified modeling, in an earlier paper [**16**], is now refined by addition of an explicit analysis of the gas adsorption and desorption at points averaged along the cycle.

2. MODELING FRICTION OF DLC:H FILMS

2.1 Tribochemistry of hydrogen free and hydrogenated DLC films

Molecules or atoms adsorbed on surfaces of materials are currently viewed as a collection of point masses coupled to the surface by harmonic springs, so that they can oscillate about the adsorption bonds [**17**]. During sliding, protuberances of surfaces interact with each other and generate oscillations of the adsorbates. The local increase of temperature may also activate the dissociation of physically adsorbed molecular oxygen into atomic oxygen. The oxygen molecule O_2 first becomes physically adsorbed and then undergoes dissociation into two oxygen atoms due to activation by the sliding interface. This leads chemisorbed O atoms to the active sites of the surface. The scenario agrees with a previous discussion of a similar process [**15**].

The process is different for a hydrogenated DLC surface. Hydrogen entrapment in the DLC during deposition will change the film structure. Hence, a surface C atom in hydrogenated DLC films may be bonded not to its immediate C neighbors but to H atoms. There is a greater probability that the hydrogen will be removed due to mechanical action of the slider. Once hydrogen is removed from the DLC surface, unoccupied surface sites will be present and gas components from the atmosphere may absorb to these sites. This mechanism will increase the overall friction between the surfaces.

2.2 Kinetics of adsorption

One of the main characteristics of the adsorption process is the fractional coverage of adsorbate θ, which can be defined as $\theta = N_c/N$ where N_c is the number of surface sites occupied by adsorbate, N is the total number of active substrate adsorption sites, and $0 \le \theta \le 1$. One of the most cited equations is an empirical one, introduced by Roginsky and Zeldovich (the Elovich equation) [**2**], to describe the process of chemical reactions involving chemical adsorption of gases on solid surfaces without the desorption of products:

$$\frac{d\theta}{dt} = Be^{-\alpha\theta} \tag{3}$$

Here α and B are constants during any one experiment, and θ is the fractional part of solute adsorbed at time t. To describe the kinetics of gas adsorption, Zaïdi *et al.* [11] considered a particular integral of (3) when the initial time $t_0 = 0$ and $\theta(0) = 0$; i.e. $\theta(t_p) = \frac{1}{\alpha}\ln(1 + B\alpha\, t_p)$, where t_p is the period of the cycle. This formula gives the value of θ after one period with no adsorbate at the beginning of the cycle. Integrating the Elovich equation (3), one has

$$\theta(t) = \frac{1}{\alpha}\ln\left[e^{\alpha\theta(t_0)} + B\alpha(t - t_0)\right] \tag{4}$$

where t_0 and $\theta(t_o)$ are the initial instant and initial relative amount of adsorbate, respectively.

The Elovich equation (3) is an empirical equation, where indirect estimations can be used for the constants. Experiments by Valenzuela-Calahorro et al. [**19**] showed that the adsorption specific rate constant k_1 varies from 5.29 x 10^{-4} $s^{-1}$to 44.85 x10^{-4} s^{-1}. Hence, we can expect that B that has the same order as k_1, which is of order 10^{-4} s^{-1}. If $\theta(0) = 0$, then for a small interval Δt, $\theta = B\Delta t$. Taking B=2 x 10^{-4} s^{-1} and Δt =10 s, gives $\theta = 2\cdot 10^{-3}$. From the definition of coverage with N=2x10^5 the number of surface sites occupied by adsorbates is N_c = 400. A constant value is used for $\mu_{mech} + \mu_{mol,2}$. Since the track length, L, is taken as 5mm, then the slider speed should be less then 0.5 mm/s for a noticeable change in the friction coefficient. This value corresponds with the experiments of Heimberg et al. [**13**], where a speed of 533μm/s showed little change in friction.

3. COMPARISON WITH EXPERIMENTS

An excellent data set on friction between two DLC:H coated counterparts was presented by Heimberg et al. [**13**]. An attempt to describe the experiments was recently presented by Borodich & Keer [**16**], which assumed a circular track on a fixed disk. The current refined model is employed to describe the experiments better. In the experiments, the DLC coatings were deposited to a 1 mm thickness on H13 steel flats and either 6.35 mm sapphire balls or 12.7 mm diameter steels balls. Reciprocating pin-on-disk tests were performed in a nominally dry nitrogen environment with

an oxygen level of 0.7%. The track length, L, was 5 mm. Each track was initially run-in for 1000 cycles at high sliding speeds (1-5 mm/s). Then, a series of "speed-dependent" and "time-delay" tests were performed: (i) Each speed-dependent test began with 100 cycles at high speed (1-5 mm/s) followed by 20 cycles at a lower speed; (ii) Each time-delay test was performed at a constant high sliding speed (≥1 mm/s). The tests began with 100 cycles without stops, followed by 20 cycles with fixed delays at the endpoints of the track. At slow stages, the speed of the ball (v_0) was 513.0, 303.0, 100.0, 75.0, 50.0, 30.0, and 10 μm/s.

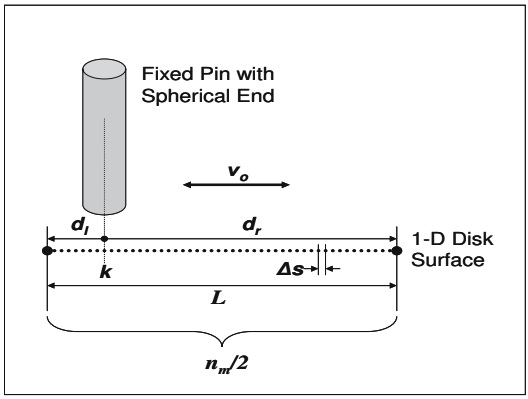

Figure 1. Diagram of experimental setup

The increase of the adsorbate surface coverage depends on the time $\Delta t(k,i)$ between passes. If the Elovich equation (3) is employed, then from (4)

$$\theta(k,i)\big|_{t+\Delta t(k,i)+0+} = \ln\left[\exp\left(\alpha\left(\theta(k,i)\big|_{t+0-} - \left[\theta(k,i)\right]^{\pm}\right)\right) + \alpha B \Delta t(k,i)\right]\Big/\alpha \quad (5)$$

where $t+0-$ and $t+\Delta t(k,i)+0+$ are the moments just before and after the successive passing of the k-th point. It is assumed that the jump in the coverage $[\theta(k,i)\,]^{\pm}$ is proportional to $\theta(k,i)\big|_{t+0-}$ and to the probability p ($0 \le p \le 1$) of the mechanical breaking of interacting bonds. Hence, one can write,

$$\left[\theta(k,i)\right]^{\pm} = p\,\theta(k,i) \quad (6)$$

Substituting (6) into (5), we obtain

$$\theta(k,i)\big|_{t+\Delta t(k,i)+0+} = \ln\left[\exp\left(\alpha\theta(k,i)(1-p)\right) + \alpha B \Delta t(k,i)\right]\Big/\alpha \quad (7)$$

It is assumed for a particular sample that p is constant during an experiment and that the molecular friction is proportional to the number of interacting bonds that were mechanically broken when the slider passes a point on the track. Hence, $\mu_{mol,1}$ is proportional to $[\theta(k,i)]^{\pm}$ and the average friction coefficient measured on the ith cycle ($\mu(i)$) is

$$\mu(i) = \mu_c + \frac{1}{n_m}\sum_{k=1}^{n_m}\mu_{mol,1}(i,k) = \mu_c + \frac{c}{n_m}\sum_{k=1}^{n_m}\left[\theta(k,i)\right]^{\pm} \tag{8}$$

where $\mu_c = \mu_{mech} + \mu_{mol,2}$ and c are assumed constant

In our numerical simulations of the speed dependent test, the speed of the ball is taken as 1053 μm/s during the high speed cycles. If $B = 4.1\cdot 10^{-4}\ \mathrm{s}^{-1}$, $\mu_c = 0.0065$, $\alpha = 0.6$, $p = 0.14$, $t_p = L / v_0$, $c = 0.81$, $t_0 = 0$ and $\theta(0) = 0.001$, and employing equations (6), (7), and (8), one can obtain figure 2. Figure 3 presents graphs of the relation between friction coefficient and the cycle number at slow stages of the experiment.

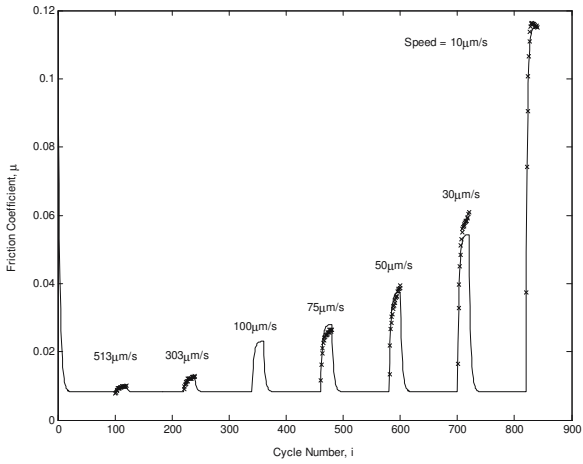

Figure 2. Friction coefficient vs. Cycle numbers

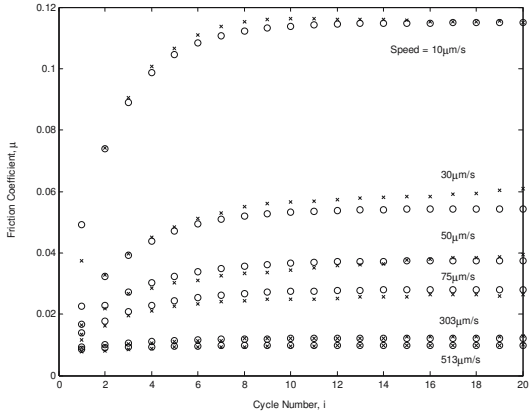

Figure 3. Friction coefficient vs. Cycle numbers at slow stages of the experiment

In the time-delay test, the durations of the stops (t_d) at the endpoints of the track were 5.0, 12.0, 45.0, 95.0 and 162s respectively. It was assumed in the numerical simulations of the time-delay test that the fixed speed v_0 was 1053μm/s. The time $\Delta t(k,i)$ between passes by the slider of the k-th point is $\Delta t(k,i) = 2d_l / v_0 + t_d$ for the first part of the cycle and $\Delta t(k,i) = 2d_r / v_0 + t_d$ for the second part. Taking $\mu_c = 0.003$, $B = 2.3 \cdot 10^{-4}$ s^{-1}, $\alpha = 0.6$, $t_p = L / v_0 + t_d$, $p = 0.3$, and $c = 0.81$, and employing equations (6), (7), and (8), one can obtain figure 4.

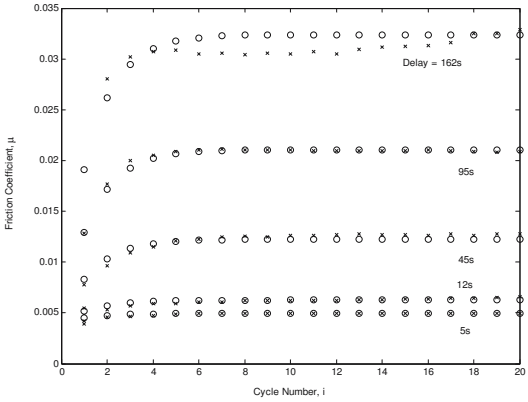

Figure 4. Friction coefficient vs. Cycle numbers in time-delay test

4. DISCUSSION AND CONCLUSIONS

The results of the numerical model based on the Elovich equation have been compared with the experimental results from Heimberg et al. [**13**] and show that the application of the Elovich [**18, 20**] equation agrees well with the results. Adsorbate removal is assumed proportional to the number of broken bonds and the jump in coverage The addition of a desorption feature in the model differs from previous models by Zaïdi et al. [**11**] and Heimberg et al. [**13**].

The numerical analyses of the friction coefficient were compared with experimental DLC friction results in Figures 2-4 and showed that for a wide range of pin speeds (10-513μm/s) the model compares well with experiments. As the speed of the pin relative to the disk surface decreases the time for the pin to return to a previous point increases, which allows a larger number of active sites to be satisfied by gaseous 'sticky' species in turn increasing the friction coefficient. Gradual wear of hydrogenated DLC films is approached with the idea of removal of CO and CO_2 from the surface of the film and is an oxidational wear approach.

ACKNOWLEDGMENTS

The authors are grateful for support of this research from the National Science Foundation and by the NSF Center for Surface Engineering and Tribology at Northwestern University and the NSF IGERT program. Thanks are extended to Professor Y.-W. Chung for his valuable comments.

REFERENCES

1. Krim, J., 2002, "Friction at Macroscopic and Microscopic Length Scales," *Am. J. Phys.*, **70**, pp. 890-897.
2. Erdemir, A., 2001, "The Role of Hydrogen in Tribological Properties of Diamond-Like Carbon Films," *Surface & Coatings Technology*, **146**, pp. 292-297.
3. Tomlinson, G.A., 1929, "A Molecular Theory of Friction," *Phil. Mag. Ser. 7*, **7**, pp. 905-939.
4. Mikhin, N. M., 1978, "Calculation of Coefficients of External Friction and Preliminary Displacement," Friction, Wear and Lubrication, I.V. Kragelsky and V.V. Alisin, eds., Mir Publishers, Moscow, 1, pp. 54-101.
5. Heinicke, G., 1984, Tribochemistry, Academie-Verlag, Berlin.
6. Quinn, T.F.J., 1991, *Physical Analysis for Tribology*, Cambridge University Press, Cambridge.

7. Goryacheva, I.G., 1998, *Contact Mechanics in Tribology*, Kluwer Academic Publishers, Dordrecht.
8. Chung, Y.-W. (2001) *Practical guide to surface science and spectroscopy*. Academic Press, San Diego.
9. He, G., Müser, MH., and Robbins, M.O., 1999, "Adsorbed Layers and the Origin of Static Friction," *Science*, **284**, pp. 1650-1652.
10. Marchon, B., Heiman, N. and Khan, M.R., 1990, "Evidence for Tribochemical Wear of Amorphous Carbon Thin Films," *IEEE Trans. Magnetics*, **26**, pp. 168-170.
11. Zaïdi, H., Paulmier, D. & Lepage, J., 1990, "The Influence of the Environment on the Friction and Wear of Graphitic Carbons. II. Gas Coverage of Wear Debris," *J. Appl.Surf. Sci.*, **44**, pp. 221- 233.
12. Dugger, M.T., Wahl, K.J., Chung, Y.-W., Bhushan, B., and Rothschild, W., 1991, "An Investigation of Environmental Effects on the Wear and Surface Composition of Thin Film Magnetic Discs," *STLE SP***31**, pp. 43-53.
13. Heimberg, J.A., Wahl, K.J., Singer, I.L., and Erdemir, A., 2001, "Superlow Friction Behavior of Diamond-Like Carbon Coatings: Time and Speed Effects," *Appl. Phys. Letters*, **78**, pp. 2449-2451.
14. McGuiggan, P.M., Hsu, S.M., Fong, W., Bogy, D. and Bhatia, C.S., 2002, "Friction Measurements of Ultra-thin Carbon Overcoats in Air," *J. Tribology*, **124**, pp. 239-244.
15. Adamson, A.W., 1990, Physical Chemistry of Surfaces, Wiley, New York.
16. Borodich, F.M., and Keer, L.M., 2004, "Modeling Effects of Gas Adsorption and Removal on Friction During Sliding Along Diamond-Like Carbon Films," *Thin Solid Films*, (Accepted).
17. Pykhtin, M.V., Lewis, S.P., Mele, E.J., and Rappe, A.M., 1998, "Collective Motion and Structural Order in Adsorbate Vibrational Dynamics," *Phys. Rev. Lett.*, **81**, pp. 5940-5943.
18. Roginsky, S.Z., 1949, Adsorption and Catalysis on Heterogeneous Surfaces, Akademia Nauk USSR, Moscow.
19. Valenzuela-Calahorro, C., Navarrete-Guijosa, A., Stitou, M., and Cuerda-Correa, E.M., 2003, "Retention of Progesterone by Four Carbonaceous Materials: Study of the Adsorption Kinetics," *Colloids and Surfaces A*: Physicochemical and Engineering Aspects, **224**, pp. 135-147.
20. Elovich, S.Y., and Zhabrova, G.M., 1939, Zh. Fiz. Khim, **13**, pp. 1775-1786. (English Abstract, 1941, Chem. Abs. **35**, pp. 373).

SUBJECT INDEX

-A-

ab initio 4, 6, 19, 23-24, 32, 67-68, 75, 78, 223

Adhesion 5, 6, 9, 11, 69, 128, 130-131, 139-142, 146-147, 149, 277-279, 281, 283-287, 300

AFM 4, 8, 11-12, 16-17, 46-49, 51-52, 121-122, 127-132, 135-136, 171-180, 201, 264, 270-271, 279, 283

Asperity 45-46, 51, 134, 278-283, 285-287

-B-

BELST 151-152, 154-157, 159

Biomineralization 99, 107-108

-C-

Calcite 99-108

Cantilever 16, 21, 47-48, 122, 127-128, 130, 132, 135, 153, 172-177, 179-180

Carbon nanotube 10, 55-56, 58-61, 64-65, 79-80, 82, 136

Cartesian frame 92

Comb actuator 156, 159

Continuum analysis 79-80, 88

Coupled atomistic discrete dislocation 270

Crack front 217-223

-D-

Deformation 2, 6, 8, 17, 24, 56, 61, 64, 69, 80-82, 84-85, 107, 115, 128-133, 150, 152, 162, 164, 166, 172, 174, 176, 186, 218-219, 221, 225-227, 229, 232, 235-236, 238-239, 243, 255, 263-264, 269-272, 274-275, 277-278, 280-282, 285-286, 289-291, 293-297

Discrete dislocation 8, 9, 225, 226, 227, 234, 264, 270, 273, 275

Dislocation loop nucleation 217

DLC films 299-303, 305, 307

-E-

Elastic substrate 205, 209-210, 212, 213

Electric dipole 245, 246, 253

Elovich equation 302-304, 307

Enzyme 109-111

Excimer Laser 181, 183

-F-

FIB 181-182

First principles 2, 23-24

Flaw tolerance 139, 141-143, 148

Fracture nucleation 79, 84, 87-88

Friction 45-47, 49-53, 109, 130, 266, 267, 269, 278, 286, 299-303, 305-308

-G-

Gradual wear 299-301, 303, 305, 307

Greenwood-Williamson 278

Griffith condition 141-142, 144, 146-147

-H-

Hydrophobicity 109, 110

Interatomic potential 19, 79-81, 83, 87, 236, 291

-I-

Ion sputtering 191, 197

Lab on a Chip 4, 7, 109

LADI 181-184, 186, 188

Lattice Green's function 91-95

LSGF 91, 94

-M-

Mechanical strength 67-68, 75, 122

MEMS 3-4, 7, 15, 17, 23, 45, 52, 119, 151-153, 155, 157-159, 192, 198, 277-278, 285

Minimum energy path 2, 217-218

Molecular dynamics 14, 19, 24, 32, 56, 58, 65, 67, 78, 89-91, 94, 98, 226-227, 234, 150, 161, 191, 217, 236, 286-287, 289-291, 293

Multiscale modeling 55-56, 61, 64-65, 89-91, 93, 95, 97-98, 225-226, 264, 278

Multiscale roughness 277-278

Multiwalled carbon nanotubes 88, 136, 201, 203

MUMPs process 151

-N-

Nanobelts 76-78

Nanocomposite 55

Nanocrystalline materials 289-290, 294

Nanoindentation 3, 8, 17, 22, 121, 130-131, 133, 136, 171-172, 176, 179-180, 225-227, 229-231, 233-239, 241-243, 263, 267, 268, 270, 275, 282

Nanomechanical 60, 65, 101, 121-122, 130, 243, 274

Nanomechanics 11, 13-14 16, 21, 55, 74, 78, 98, 99, 139-140, 149, 199, 217, 261, 299

Nanorods 23-32, 46, 88

Nanostructures 1-6, 9-12, 16-17, 23, 45, 53, 78, 90-91, 98, 149, 192, 195-196, 181, 199, 263, 265, 270-271, 273-275

Nano-volumes 33

Nanowire 11, 32, 46, 53, 67-77, 136

-P-

Phase field modeling 33, 42

Phase transformation 1-2, 34, 45-46, 67-68, 75-78, 205-206, 265

Plasticity 1, 7-10, 14, 106, 226, 231, 234, 236, 238, 243, 263-265, 274-275, 277-279, 281-283, 285-287, 293, 295

Poisson's ratio 259

PZT 173-178

-Q-

Quantum dot 3-4, 89-90, 92-93, 96-98, 195

Quantum mechanics 14, 64

-R-

Roughness evolution 17, 277, 281
Skeletal 100-102, 106, 108

-S-

Solidification 33-34, 37-42, 181-183, 186, 188

Stress evolution 191-193, 195, 197

Surface plasticity 9, 277-279, 281-283, 285-287

Surface stress 2, 11, 67-71, 73, 75-78, 278

-T-

Tetrahydrofuran 126

-V-

Viscoelastic film 205, 209-210, 212-213

-Y-

Young's modulus 15, 57, 121-122, 125-126, 142, 144, 146, 199, 201, 260, 291

AUTHOR INDEX

-A-

Abermann, S. 197
Abraham, F.F. 222,234
Adamson, A.W. 308
Addadi, L. 107,108
Aizenberg, J. 99-108
Ajayan, P.M. 64
Albeck, S. 108
Albers, R.C. 43
Alexander, L.E. 88, 108, 261
Alexseyev, L. 136
Alisin, V.V. 307
Alivisatos, A.P. 32,53
Allan, R. 52
Allen, M.P. 198
Andelman, D. 254
Anderson, P. 274
Andres, R.P. 78
Andrews, R. 64
Angello, J.C. 135
Aoyama, R. 119
Archard, J.F. 286
Archibald, D.D. 108
Argon, A. 191-196, 222,264
Artemev, V. 43
Arzt, E. 78, 149,203
Ashby, M.R. 52,274
Ashruf, C.M.A. 52
Autumn, K. 149

-B-

Bach, D. 53
Bacsa, R.R. 136
Baeri, P. 189
Baglin, J.E. 189
Bahr, D.F. 274
Bai, Z.G. 54
Barber, J.R. 286
Barralet, J.E. 136
Barth, J.V. 254
Baskes, M.I. 98, 234, 243, 274
Beckermann, C. 43
Belytschko, T. 203
Berman, A. 107-108
Bernstein, N. 234
Bhatia, C.S. 308
Bhushan, B. 22,136,286,308
Bierden, P. 198
Bifano, T.G. 197,198
Biggs, W.D. 107
Biscarini, F. 286
Bischel, M.S. 136
Bishop, A.R. 43
Blackford, B.L. 136
Blakeslee, A.E. 259, 261
Bobek, T. 197
Boettinger, W.J. 43
Bogy, D. 308
Bonard, J.M. 136
Boragno, C. 286
Borel, J.-P. 78
Boresi, A.P. 21, 22
Borodich, F.M. 299-308
Borri-Brunetto, M. 286
Bowden, F.P. 52, 53
Bower, A.F. 161-170, 277

Bower, C. 65
Bressers, P.M.M.C. 52
Briggs, G. 136
Brotzen, F.R. 180
Broughton, J.Q. 234, 274
Bruchez, M.P. 53
Buehler, M.J. 139-150, 222
Buffat, P.H. 78
Bulatov, V. 223, 234
Bullough, R. 275
Burnham, N.A. 136
Buzio, R. 286

-C-

Cagin, T. 286
Carlsson, A.E. 98
Carpinteri, A. 286
Carter, C.B. 108, 263, 274-275
Castro, T. 78
Caswell, K.K. 136
Cerny, R. 189
Cha, P.-R. 287
Chab, V. 189
Chambers, M. 263, 274
Chan, H.W. 53
Chang, J. 119, 180, 223
Chang, J.G. 234
Chang-Chien, A. 119
Chaudhury, M. 119
Chauvet, O. 136
Chen, J. 32
Chen, J.C. 119
Chen, X.F. 223
Cheng, Y.-T. 181, 285, 286
Cheung, K.S. 198
Chevary, J.A. 32
Chew, N.G. 189
Chiaia, B. 286
Chizan, D.C. 275
Chizhik, S.A. 136
Cho, K. 21, 88
Choi, E. 78
Chong, K.P. 13-22, 78
Chou, S.-Y. 182-189
Chou, T.-W. 55-65
Chu, C.C. 159
Chuang, T.-J. 67-78
Chung, Y.-W. 235-242, 307, 308
Ciavarella, M. 286
Clayton, C.R. 52
Cleveringa, H.H.M. 234
Cohen, I. 255, 261
Cook R.E. 32
Coombes, A. 136
Cooper, C.A. 64
Cordier, P. 275
Cordill, M.J. 274
Cahn, J.W. 78, 248, 254
Cai, W. 223, 234
Cammarata, R.C. 78
Cao, G. 32, 43
Crabtree, W.G. 32
Crocker, J.C. 261
Cuenot, S. 136
Cuerda-Correa, E.M. 308
Cuitino, A.M. 275
Cullis, A.G. 189
Cumings, J. 136
Cunningham, A. J. 119
Currey, J.D. 107, 108
Curtin, W.A. 234, 275

-D-

Dai, H. 136
Daniel, S. 119
Danielsen, M. 53
Daw, M.S. 234, 275
de Gennes, P.–G. 149
de la Figuera J. 275
de Melto, A.J. 119
de Mongeot, F.B. 286
de Rooij, N.F. 119
Dearnaley, G. 52
Dekker, C. 78

Demczyk, B.G. 136
Demelio, G. 286
Demenet, J.L. 275
Demoustier-Champagne, S. 136
Deng, S.Z. 32
Derjaguin, B.V. 286
DeVries, A.L. 108
Di Fonzo, F. 275
Diao, J. 78
Dickey, E.C. 53, 64
Dickinson, J.T. 53
Didymus, J.M. 108
Ding, Y. 54, 297
Dittmer, J.J. 32
Domke, J. 136
Donnay, G. 108
Douglas, T. 108
Downes, S. 136
Dragoset, R.A. 254
Duan, X. 53, 78
Dugger, M.T. 308
Dunn, M. 78
Dupuy, L. 231, 234
Duvail, J.L. 136
Dyer, M.J. 88, 203

-E-

Eduljee, R.F. 136
Ellis, W.C. 53
Elovich, S.Y. 299-308
Embury, J.D. 78
Emlet, R.B. 108
Enders, S. 149
Endo, I. 119
Endo, T. 136
Erdemir, A. 307, 308
Eshelby, J.D. 51, 54
Evans, S.D. 254

-F-

Fackso, S. 197
Fan, M.H. 275
Fan, S.S. 32
Fang, T.H. 234
Fang, W. 151-159
Fearing, R. 149
Fehrenbacher, L. 53
Feldman, Y. 64
Felgner, P.L. 53
Feng, S.Q. 54
Ferris, N. 254
Fiolhais, C. 32
Fischer, T.E. 53
Fischmeister, H.F. 234
Fleck, N.A. 274
Foiles, S.M. 234
Fong, W. 308
Forrest, S.R. 287
Forro, L. 136
Frank, F.C. 259, 261
Frankland, S.J.V. 65
Fratzl, P. 78, 149, 203
Frebel, H. 119
French, P.J. 52
Frenkel, D. 198, 261
Freund, J.B. 198
Friak, M. 78
Fuchigami, N. 136
Fujii, T. 119
Full, R.J. 149
Furthmüller, J. 32

-G-

Gadek, T.R. 53
Gähler, F. 150
Gall, K. 76-78
Gao, H. 78, 88, 136, 139-150, 203, 222, 274, 286
Gao, T. 32

Gao, X.Y. 32
Gao, Y.F. 254, 277-286
Garem, H. 275
Garlotta, D. 137
Gasser, U. 261
Gates, T.S. 65
Ge, H. 32, 189
Gelotta, R.J. 254
Gerberich, W.W. 222, 274-275
Gerhard Heinicke 53
Giannaris, S.C. 64
Gidwani, A. 275
Gillespie, J.W. 136
Girshick, S.L. 274-275
Goddard III, W.A. 286
Godfrey, A. 243
Godon, C. 136
Gommans, H.H. 65
Gonzalez, M.A. 275
Gorb, S. 141, 149
Gorbunov, V.V. 136
Goryacheva, I.G. 308
Gosain, D.P. 53
Gosline, J.M. 107
Grant, M. 43
Greenwood, J.A. 134, 137, 278, 286
Griffith, A.A. 141-149, 203, 220
Grujicic, M. 43
Grunlan, J.C. 274
Gu, G. 136
Gu, J. 189
Gumbsch, P. 234
Guo, L. 188
Guthrie, W.F. 22, 180

-H-

Hafner, J. 32
Haggenmueller, R. 65
Hamilton, J.C. 234, 275
Han C.Y. 32
Han, W. 136
Hanneman, R.E. 76, 78
Hansen, W.R. 149
Hanson, J. 108
Hariadi, R. 53
Hauschka, P.V. 108
Hay, J.C. 243
Hay, J.L. 243
He, G. 308
Heberlein, J. 275
Heiman, N. 308
Heimberg, J.A. 301-308
Heinicke, G. 53, 307
Hernandez, C. 98
Hetman, M. 136
Heywood, B.R. 136
Hieda, K. 136
Hiller, J.M. 32
Hilliard, J.E. 248
Hinkley, J. 56, 65
Hirosaki, N. 223
Hirth, J.P. 78, 223, 297
Ho, Y.-P. 159
Hoagland, J.D. 78
Hodgson, R.T. 189
Hoehn, J. 274-275
Hofer, C. 197
Holm, M. 53
Hong, H.S. 52
Hong, J.W. 119
Hong, W. 245-254
Horstemeyer, M.F. 243, 274
Houston, J.E. 274
Hsieh, J. 151-159
Hsu, S.M. 308
Hsueh, C.H. 215
Hu, H.-H. 159
Huang, H. 32, 88
Huang, K. 88, 274
Huang, R.-S. 159
Huang, X.M.H. 65
Huang, Z. 234
Hughes, D.A. 243

Hunt, B.D. 65
Hurtado, J.A. 286
Hutcheson, G.D. 52
Hutcheson, J.D. 52
Hutchinson, J.W. 274
Huynh, W.U. 32

-I-

Ibach, H. 78
Iijima, S. 21, 88
Inai, R. 88
Inamura, T. 243
Ingber, D.E. 135
Iordanoglou, D.I. 275
Iruelaarispe, M.L. 135
Ishii, O. 135
Isono, Y. 136
Israelachvili, J.N. 149

-J-

Jackson, K.A. 32
Jacobsen, K.W. 222, 297
Jaeger, I. 149
Jaeger, I.L. 149, 203
Jahanmir, S. 52
Jain, S.C. 98
Jakeway, S.C. 119
Jang, Y.H. 286
Jayanthi, C.S. 136
Jeng, Y.R. 235-243
Jericho, M.H. 136
Ji, B. 78, 149, 203, 286
Jiang, H. 65, 79-88
Jin, L. 65
Jin, M. 275
Jin, Y.M. 43
Johnson, H.T. 191, 198
Johnson, K.L. 136-137, 275, 286
Johnsson, K.P. 53
Jonsson, H. 222, 297
Jorand, M. 261
Joubert, J. 32
Jungk, J.M. 274-275

-K-

Kalia, R.K. 98
Kalyanasundaram, N. 192-198
Kane, R.S. 119
Kaplan, A.F.H. 189
Karma, A. 43
Kasper, E. 197
Kassner, K. 43
Katz, Y. 223
Kaxiras, E. 234
Keer, L.M. 299-308
Keimei, C. 189
Kelchner, C.L. 234
Kellogg, G. 254
Kelly, J.J. 52
Kelly, T.F. 88, 203
Kendall, K. 286
Kenny, T.W. 149
Khachaturyan, A.G. 43
Khan, M.R. 308
Khil, M.S. 136
Kiely, J.D. 274
Kim, C.J. 119
Kim, G.T. 136
Kim, H.Y. 136
Kim, J. 119
Kim, K.-S. 16, 17, 285, 286
Kim, M-W. 53
Klein, P.A. 88, 234
Klingler, J.F. 254
Klug, H.P. 108
Knap, J. 275
Koetzle, T.F. 108
Kohlert, V 43
Kohlhoff, S. 234
Koller, H.H. 53
Komvopoulos, K. 22, 236, 243

Kong, J. 136
Kong, X.Y. 78
Koning, M. 234
Koslowski, M. 275
Kotaki, M. 135
Kowalchik, M 53
Kragelsky, I.V. 307
Krauss, P.R. 188
Kresse, G. 32
Krim, J. 307
Krumeich, F. 32
Kulik, A.J. 136
Kurz, H. 197
Kuwahara, K. 136
Kvick, A. 108
Kwork, K.W. 32

-L-

Ladd, AJC. 261
Lane, T.F. 135
Langer, R. 135
Langford, S.C. 53
Lanza, R.P. 135
Larsen-Basse, J. 22
Lee, D.R. 136
Lee, K.H. 136
Lee, KYC. 254
Lee, S.H. 137
Leiserowitz, L. 107-108
Lepage, J. 308
Letsinger, R.L. 53
Levitt, A.C. 261
Lewis, S.P. 308
Li, C.Y. 65
Li, D. 135
Li, J. 222-223, 243, 274
Li, X. 135
Lian, G. 53
Liang, H. 45-54
Liang, Y.A. 149
Lieber, C.M. 53,78, 88
Light, T.B. 261
Lii, M.J. 223
Lilleodden, E.T. 274-275
Lim, C.T. 121-136
Limmer, S.J. 32
Lin, H.-Y. 151, 159
Lin, S.C. 119
Lippmann, F. 108
Lips, D. 64
Liu, L. 136
Liu, W.K. 21, 88
Lookman, T. 43
Lordi, V. 56, 65
Louarn, G. 136
Lourie, O. 64, 88, 203
Lowenstam, H.A. 107
Loweth, C.J. 53
Lu, L. 136, 297
Lu, W. 243, 254
Lucas, B.N. 180, 243
Luzinov, I. 136
Lyutovich, K. 197

-M-

Ma, P.X. 135
Ma, Y.X. 135
MacDonald, N.C. 159
Mader, S. 261
Maes, H. 98
Majumdar, A. 286
Mali, R. 198
Mann, S. 108
Mao, L. 43
Mao, Y.Q. 32
Marchon, B. 308
Marhic, C. 136
Martin, M.R. 32
Mase, G.E. 215
Mathias, J.P. 53
Matthews, J.W. 261
Maugis, D. 286
Maultzsch, J. 21
McCafferty, E. 52

McConnell, H.M. 254
McCool, J.I. 286
McGuiggan, P.M. 180, 308
McMurry, P.H. 275
Mehregany, M. 65
Meldrum, F.C. 108
Mele, E.J. 308
Men, De-Sheng 119
Meng, G.W. 32
Merz, R. 52
Meyers, G.F. 22, 180
Mikhin, N.M. 307
Mikos, A.G. 136
Miller, D.J. 32
Miller, I.R. 53
Miller, R.E. 225-234, 263, 275
Miller, R.S. 43
Mills, G. 222
Minor, A.M. 275
Miranda, R. 53
Mirkin, C.A. 53
Misbah, C. 43
Mishin, Y. 223
Misra, A. 78
Molière, V.G. 192,196, 198
Moloni, K. 88, 203
Monteiro, P.J.M. 22
Moody, N.R. 274
Mook, W.M. 261-275
Moore, M.C. 198
Morales, A.M. 53
Morf, W.E. 119
Morgan, J.R. 135
Morris Jr., S.W. 275
Mucic, R.C. 53
Mukherjee, R. 274-275
Mulhern, P.J. 136
Muller, G.M. 274
Muller, J. 43
Muller, V.M. 286
Mullins, W.M. 53
Murakami, H. 203
Murphy, C.J. 136
Murugan, R. 135
Müser, M.H. 308

-N-

Nakano, A. 98
Namazu, T. 136
Navarrete-Guijosa, A. 308
Needleman, A. 234, 274
Nelson, J.C. 274
Nelson, M. 108
Nesper, R. 32
Neumann, D. 275
Newman, B.A. 161,170
Ng, K.-O. 254
Ng, S.Y. 135
Nicholas, E.D. 52
Nielsen, O.H. 32
Nissen, H. 108
Nix, W.D. 180, 274, 282
Northrop, J.P. 53
Nosonosky, M. 286
Nowacki, W. 215
Nysten, B. 136

-O-

Odegard, G.M. 56, 65
Ogata, S. 223
Ohmi, T. 52
Okumura, K. 149
Oliver, P. 108
Oliver, W.C. 180, 243
Opas, M. 135
Ortiz, M. 98, 234, 275
Oudar, J. 52

-P-

Pae, K.D. 161-162,170
Pai, W.W. 275

Pan, E. 98
Pang, Y.T. 32
Park, J.G. 137
Park, N.-S. 53
Park, Y.W. 137
Parthasarathy, T.A. 98
Patzke, R.G. 32
Paulmier, D. 308
Pawson, D.L. 108
Peattie, A.M. 149
Pederson, M.R. 32
Peng, X. 32, 53
Perdew, J.P. 25, 32
Perrey, C.R. 263, 275
Persson, BNJ. 149, 286
Petersen, K.E. 52
Pharr, G.M. 172, 180, 243
Phillips, R. 98, 234
Picu, R.C. 234
Pieranski, P. 261
Plimpton, S. 234
Poate, J.M. 189
Pollock, H.M. 286
Pope, L. 53
Pra, NLDD 136
Preston 53
Prikryl, P. 189
Prinz, F.B. 52
Pugno, N. 199-203
Pusey, P.N. 261
Pykhtin, M.V. 308

-Q-

Qi, Y. 285-286
Qian, D. 21, 64, 88
Quested, D.L. 161, 170
Quinn, T.F.J. 307

-R-

Ra, Y.M. 136
Rabier, J. 265, 275
Rabinowicz, E. 53
Radmacher, M. 136
Rafii-Tabar, H. 243
Ramakrishna, S. 243
Ramamurthy, A.C. 135
Ramaswami, K. 52
Rao, N.P. 275
Rao, S. 98
Rappe, A.M. 308
Rasmussen, K.O. 43
Ravich, D. 64
Reeves, N.J. 108
Reich, S. 21
Reifenberger, R. 78
Ren, Z.F. 64
Retho, P. 136
Rice, J.R. 78
Rigold, G.M. 53
Rinzler, A.G. 65
Ritchie, R.O. 136
Rizzi, S.C. 136
Robbins, M.O. 308
Roberts, A.D. 286
Rodriguez de la Fuente O 275
Roginsky, S.Z. 300, 302, 308
Rojo, J.M. 275
Roman, R. 53
Roth, J. 150
Roth, S. 136
Rothen, F. 261
Rothschild, W. 308
Roukes, M.L. 65
Roytburd, A.L. 33, 43
Rubenstein, L.I. 189
Ruda, H. 53
Rudd, R.E. 234, 274
Ruel, R. 261
Ruoff, R. 199-203
Russel, E.L. 119

-S-

Sage, E.H. 135

Saigal, S. 21
Salvetat, J.P. 136
Sarro, P.M. 52
Saxena, A. 43
Schadler, L.S. 64
Schall, P. 255-261
Scherge, M. 149
Schofield, A. 261
Schultz, J.M. 136
Schultz, P.G. 53
Scoles, G. 254
Seeman, N.C. 53
Seki, M. 119
Sessler, G.M. 254
Seto, C.T. 53
Seul, M. 254
Shan, W.J. 32
Sharma, S. 53
She, J.C. 32
Sheinbein, J.L. 170
Shenoy, S.R. 43
Shenoy, V. 234
Shibutani, Y. 223
Shilkrot, L.E. 234, 275
Shin, M. 135
Shrotriya, P. 286
Shu, J.Y. 274
Shuttleworth, R. 69, 78
Sieradzki, K. 78
Simkiss, K. 107
Simmons, J.P. 98
Singer, I.L. 286, 308
Singh, D.J. 32
Sitti, M. 149
Slutsker, J. 33-43
Smit, B. 198
Snoke, D. 78
Sob, M. 78
Sogo, J.M. 53
Spaepen, F. 255-261
Spolenak, R. 149
Sponberg, S. 149
Srivastava, D. 21, 88
Srolovitz, D.J. 287
Stach, E.A. 274-275
Stillinger, F. 198
Stillinger, F.H. 223
Stitou, M. 308
Stockli, T. 136
Stoneham, A.M. 275
Storhoff, J.J. 53
Stroscio, J.A. 254
Sueda, T. 135
Suh, Nam P. 52
Sumomogi, T. 136
Sun, S.H. 32
Sun, Y. 274
Sundararajan, S. 136
Sunkara, M.K. 53
Suo, Z. 245-254
Suresh, S. 234, 243, 274
Suzuki, H. 243
Swindeman, J.E. 243

-T-

Tabor, D. 52-53
Tadmor, E.B. 98, 234
Takezawa, N. 243
Tan, EPS. 121-137
Tan, T.Y. 189
Teichert, C. 197
Templeton, I. 136
Tenne, R. 64
Terk, M. 52
Tewary, V.K. 89-98
Thomsen, C. 21
Thomson, R. 98, 275
Thostenson, E.T. 64-65
Thumoond, C.D. 53
Tian, Y.T. 32
Tildesley, D.T. 198
Ting, T.C.T. 98
Tokarev, V.N. 189

Tombler, T.W. 136
Tomiya, S. 53
Tomizawa, H. 53
Tomlinson, G.A. 300, 307
Toporov, Y.P. 286
Torrens, I.M. 198
Tour, J.M. 52
Towe, K.M. 108
Trebin, H.-R. 150
Tripp, J.H. 134, 137
Tsai, J.M. 159
Tsai, M.-L. 159
Tseng, F.G. 109-119
Tsong, T.T. 254
Tsu, R. 189
Tsukruk, V.V. 136, 180
Tymiak, N.I. 274, 275

-U-

Udaykumar, H.S. 43
Ugural, A.C. 136
Ulman, A. 254
Urankar, E. 254
Usui, S. 53

-V-

Vacanti, J.P. 135
Valbusa, U. 286
Valenzuela-Calahorro, C. 301, 308
Van Blaaderen, A. 261
Van der Giessen, E. 234
van der Merwe, J.H. 259, 261
Van Vliet, K.J. 234, 274
Vanderbilt, D. 254
Vanderlick, T.K. 287
VanLandingham, M.R. 22, 137, 180
Vashishta, P. 98
Veprek, S. 264, 274-275
Vernon, R.B. 135
Villarrubia, J.S. 22, 180
Vitek, V. 78, 275
Vliet, K.J.V. 234, 243, 274
Vollenweider, H.J. 53
Vosko, S.H. 32

-W-

Wagner, G.J. 21, 88
Wagner, H.D. 64
Wagner, R.S. 53
Wahl, K.J. 22, 308
Wainwright, S.A. 107
Waizmann, U. 136
Wallace, W.A. 136
Wang, H.H. 32
Wang, J. 286
Wang, S. 135
Wang, X. 77, 135, 149
Wang, Y. 43
Wang, Y.L. 136
Wang, Y.M. 136
Wang, Z.L. 77
Warren, J.A. 22, 33-43
Webber, H.C. 189
Weber, T. 198
Weber, T.A. 223
Weeks, E.R. 261
Wei, C. 21
Weiner, J.H. 161-170
Weiner, S. 107-108
Weiss, L.E. 52
Weitz, D.A. 255-261
Welp, U. 32
Wendler-Kalsch, E. 52
Weng, C.I. 234
Wenz, M. 53
Westbroek, P. 108
Westwater, J. 53
Whitesides, G.M. 53
Whitman, L.J. 254
Wilbur, K.M. 107
Willander, M. 98
Williamson, M. 136, 278

Willing, G.A. 32
Willis, J.R. 266, 275
Wilson, T.E. 53
Wiltzius, P. 261
Winer, W. 53
Wise, K. 65
Wohlgemuth, J.H. 52
Wong, E. 21, 88
Woodward, C. 98
Wu, J.J. 286
Wu, M. 159
Wu, S.Y. 136
Wu, W. 189
Wyrobek, J.T. 22, 274

-X-

Xia, Y. 274
Xia, Y.N. 36
Xiao, S.P. 203
Xiao, Z.L. 32
Xie, T. 32
Xu, C.Y. 135
Xu, G 45-54
Xu, N.X. 32
Xu, W. 136

-Y-

Yan, W. 277-286
Yang, B. 98
Yang, F. 135
Yao, H. 149
Yao, N. 56, 65
Yarmush, M.L. 135
Yarusso, D.J. 180
Ye, C.H. 32
Yip, S. 198, 222-223, 234, 243, 274
Yu, D.P. 54
Yu, H.H. 286
Yu, M. 21
Yu, M-F. 88, 203
Yuan, F.G. 98
Yuan, Z.H. 32

-Z-

Zaïdi, H. 303, 307-308
Zettl, A. 136
Zhabrova, G.M. 308
Zhang, C. 32
Zhang, H.Z. 54
Zhang, L.D. 32
Zhang, P. 82, 84, 85, 88
Zhang, W. 189
Zhang, Z.L. 159
Zhao, A.W. 32
Zheng, Q. 65
Zhou, C. 136
Zhou, J. 32
Zhou, O. 65
Zhou, S. 98
Zhou, S.J. 266, 275
Zhu, T. 1, 217-223, 243, 274
Zienkiewicz, O.C. 65
Zimmerman, J.A. 234, 275
Zorman, C.A. 65